Quantum Optics Systems for Long-Distance Cryptography and Quantum Networks

Víctor Román Rodríguez

HAL Id: tel-03872493
https://theses.hal.science/tel-03872493

Submitted on 25 Nov 2022

**Thèse de doctorat de
la Sorbonne Université**

présentée par

Víctor Román Rodríguez

pour obtenir le grade de Docteur de la Sorbonne Université
sur le sujet:

Quantum Optics Systems for Long-Distance Cryptography and Quantum Networks.

Devant le jury composé de:

Pr. Ulrik ANDERSEN	Rapporteur
Pr. Virginia D'AURIA	Rapporteure
Pr. Philippe GRANGIER	Examinateur
Pr. Vladyslav USENKO	Examinateur
Dr. Simon PIGEON	Invité DGA
Dr. Mathias VAN DEN BOSSCHE	Invité Thales
Pr. Valentina PARIGI	Co-encadrante de Thèse
Pr. Eleni DIAMANTI	Directrice de Thèse

Dedication on this page, only for final version.

Résumé

Le domaine de l'information quantique a attiré une grande attention scientifique au cours des dernières décennies, en raison de la variété des questions théoriques ouvertes et des implémentations expérimentales des technologies quantiques dans différentes architectures. Cette thèse est divisée en deux parties, qui visent toutes deux à mettre en œuvre de nouvelles technologies d'information quantique. Dans la première partie, nous avons étudié la faisabilité de la distribution de clés quantiques avec des variables continues (CVQKD) entre un satellite en orbite et une station à la surface de la Terre. L'implémentation en variables continues évite l'utilisation de détecteurs à photons uniques, car les composants de télécommunication courants peuvent être utilisés à la place, ce qui augmente l'applicabilité du protocole. En outre, la liaison avec un satellite en orbite ouvre la porte à la construction potentielle d'un réseau mondial puisqu'elle permet de surmonter le problème de la communication à longue distance. Nous avons donc réalisé une étude théorique où nous avons considéré des paramètres physiques réalistes dans ce scénario afin de montrer les conditions de faisabilité du CVQKD par satellite avec une technologie de pointe.

Dans la deuxième partie du manuscrit, nous décrivons la conception et les résultats expérimentaux montrant les performances d'une source optique pour la génération d'états graph en variables continues aux longueurs d'onde des télécommunications, que nous avons construite à partir de zéro. La préparation d'états graph, également appelés états de clusters, peut être utilisée pour la mise en œuvre de protocoles de cryptographie quantique, de calcul quantique basé sur la mesure (MBQC) ou de simulation quantique. Nous faisons correspondre les nœuds et les liens de l'état du graphe à l'état quantique multimode à partir d'une interaction non linéaire de la lumière dans un guide d'ondes. Après le guide d'ondes, nous obtenons un ensemble d'états de vide comprimés non corrélés, qui peuvent être manipulés dans un graphe souhaité par une transformation unitaire passive appropriée. Nous étudions la quantité de niveaux de compression de l'état de vide comprimé multimode et le nombre de compresseurs, qui sont liés au nombre de nœuds et à la quantité de corrélations EPR dans les états potentiels du graphe après le changement de base approprié. Nous avons préparé une expérience dans laquelle nous avons directement mesuré, par détection homodyne, la compression multimode après l'interaction de la lumière dans le guide d'ondes non linéaire, montrant ainsi la fonctionnalité de la source. Nous donnons enfin les perspectives à court terme pour l'optimisation de la source et certaines de ses potentialités à long terme.

Abstract

The field of Quantum Information has drawn a lot of scientific attention in the last decades, due to the variety of both theoretical open questions and experimental implementations of quantum technologies in different architectures. This thesis was part of two scientific projects, and it is hence divided into two parts, which both aims at implementing new quantum information technologies. In the first part, we investigated the feasibility of performing Quantum Key Distribution with Continuous Variables, (CVQKD) between an orbiting Satellite and a ground station at the Earth's surface. The implementation in continuous variables avoids the use of single-photon detectors, as current off-the-shelf telecommunication components could be used instead, which increases the applicability of the protocol. Furthermore, the link with an orbiting satellite opens the door to the potential construction of a global network since it allows to overcome the long distance communication problem, due to both the inherent losses in the optical fibers and the fact that signal amplification without introducing noise is not possible (no-cloning theorem). We therefore performed a theoretical study where we considered realistic physical parameters in this scenario to show the conditions for the feasibility of satellite CVQKD with state-of-the-art technology.

In the second part of the manuscript, we describe the design and the experimental results showing the performance of a continuous variable optical source for the generation of graph states at telecom wavelengths, that we built from scratch. The preparation of graph states, also called cluster states, can be used for implementing quantum cryptographic protocols, measurement-based quantum computation (MBQC) or quantum simulation. We map the graph state nodes and links to the multimode state from a non-linear interaction of light in a waveguide. After the waveguide, we obtain a set of uncorrelated squeezed vacuum states, than can be manipulated into a desired graph by an appropriate passive unitary transformation, hence multiport interferometry. We study the amount of the squeezing levels of the multimode squeezed vacuum state and the number of squeezers, that are related to the number of nodes and the amount of EPR correlations in the potential graph states after the appropriate basis change. We prepared an experiment where we directly measured, via homodyne detection, multimode squeezing after the light interaction in the non-linear waveguide, hence showing the functionality of the source. We finally give the short-term prospects for the optimization of the source and some of its long-term potentialities.

Contents

Introduction

The discovery of Quantum Mechanics at the beginning of the XXth century completely revolutionized the field of Physics. At the time, it was thought that the equations of motion of the whole universe were already derived, we just needed to know the position and velocity of all the particles in the universe, together with an unimaginable computational power, and we could trace all their past and predict their future. Conceptually, though, there was nothing to improve, the universe was seen like a big deterministic machine. The famous experiments on the black body radiation in 1900, where Max Planck introduced the concept of radiation quanta, the photoelectric effect in 1905, or the famous double slit experiment, serve to start turning upside down this view of the world. Light, classically viewed as an electromagnetic wave, appeared to be nevertheless composed by minimum energy packets, the photons. In parallel, the work on Brownian motion, also in 1905, and the Geiger-Marsden experiments (also known as the Rutherford experiment), showed the existence of atoms, the units of matters, and its constituents, the already known electron and the positively charged nucleus.

At this point, it seems like we were discovering the very limits of the microscopic scale, the fact that one cannot infinitely divide either light nor matter, but that there were some irreducible objects, that we called photons, electrons and nuclei, that cannot be reduced any further. However, probably the most interesting discovery, at least in essence, was not the constituents of light and matter themselves, but the breaking of the usual physical laws that we thought governed the universe when applied to these microscopic objects.

We had to invent a new physical framework to make sense of the weird behavior of these dual particles/waves, that we called Quantum Mechanics. The cost to construct this new framework was nevertheless conceptually revolutionary, since we had to completely abandon the deterministic view of the world. We had to accept that even the word predict was actually in danger; Nature was probabilistic at its very core. Moreover, we had to admit the reality of a highly counter intuitive behavior in order to account for the microscopic world. The view of reality was completely substituted, with all its philosophical implications.

Obviously, the quantum theory got a number of detractors at the time of its development, in the 20's and 30's, that refused to believe the idea of the total abandoning of determinism. Humans are stubborn by nature, but Nature does not care. Until late XXth century,

we examined new phenomena that emerge from quantum theory, revolutionizing fields of Physics, like Astrophysics, Cosmology or Thermodynamics, or even creating new ones, like Nuclear Physics, Particle Physics or Quantum Optics, that can be grouped into Quantum Field Theories, providing new exciting open questions in fundamental Science. At the time of writing, Quantum Field theory is the best experimentally proven description of reality that we know.

In 1981, Alan Aspect *et al* published an experimental article showing the violation of the Bell inequalities, proposed by John Bell in 1964, proving that the nature of reality is non-local. No hidden (deterministic) variables could explain the effect of quantum entanglement. After that, the acceptance of the quantum mechanical behavior was settled. We then started asking ourselves different questions, could we actually use this physical theory to our benefit? In other words, is Quantum Mechanics able to provide solutions to problems that are not solvable with classical physics only? Can we apply this effects to improve technology? We made the logical transition from the understanding of the counter intuitive behavior of quantum particles, to trying to control that behavior in order to perform actual tricks. In 1980, Paul Benioff proposed a quantum mechanical version of the Turing machine, and shortly afterwards Richard Feynman and Yuri Manin suggested that a quantum computer could potentially simulate things that a classical computer cannot. The field of quantum computation was emerging. In 1984, Charles Bennett and Gilles Brassard proposed the first quantum protocol to distribute a secret key between two users, opening the field of quantum cryptography and quantum communication. From the 90's to the current date, a whole variety of theoretical quantum protocols have been proposed for communication, computation and simulation, and giants steps have been taken for their implementation in the lab, in a range of different architectures: photons, trapped ions, superconducting circuits, quantum dots... Even quantum protocols applied to artificial intelligence are now under research, in the field of quantum machine learning. The emergence of all these new research fields, combining engineering, computer science, and physics, gathered in the so-called Quantum Information framework, is sometimes referred to as the second quantum revolution.

This thesis is therefore enclosed in the general field of Quantum Information, and aims to contribute to the scientific research of quantum cryptography and quantum optics, from an application point of view. Both theoretical and experimental original work will be presented in the manuscript.

The thesis is divided into two parts, that correspond to two different projects for quantum cryptography and quantum optics. In the first part we aim to theoretically study a Quantum Key Distribution (QKD) scenario where the two parties that want to share a secret key are in an orbiting satellite and a ground station, respectively. The motivation of that scenario is a limitation in long distance quantum communications due to optical losses in fibers and the impossibility to amplify a quantum signal without adding noise, due to the no-cloning theorem, that can be thus tackled with satellites. An actual satellite link for QKD has already been demonstrated, but in the framework of Discrete Variables. Through out all

this thesis, we will focus in the somewhat less treated framework of Continuous Variables, and their advantages with respect to Discrete Variables will be outlined. This part constitutes the first two Chapters of the manuscript. In Chapter 1 we will give a brief introduction to the physical and mathematical tools used in quantum cryptography, while in Chapter 2 we present our work in the feasibility study of satellite QKD with Continuous Variables.

The second part of the Thesis consists in describing the design and construction, from scratch, of a continuous variable quantum source for graph states of light, that form what we called a Quantum Network. The field of work in the second part can be referred as Multimode Quantum Optics. This source would open the door to the implementation of quantum protocols in continuous variables (including QKD), Measurement-Based Quantum Computation (MBQC), and even quantum simulation. In order to build the source, we use the non-linear interaction of light in waveguide structures that prepares multimode squeezed vacuum states in the frequency domain, and we show why these multimode quantum states can be thought to be directly related to configurable quantum networks.

In Chapter 3, we briefly discuss the multimode character of the electromagnetic field, that leads to introducing Ultrafast Optics, describing ultrashort pulses of light both spatially and temporally. We also describe our characterization of the laser source and the experimental tools we used for pulse manipulation, namely the pulse compressor and the pulse shaper, showing the experimental results. In Chapter 4, we introduce classical non-linear optics, and discuss theoretically the waveguide physical characteristics. We also show a numerical finite-element method simulation we performed for our waveguides for the discretization of spatial modes in the structure, and compare the result with the experimental characterization of the spatial modes in the actual waveguide. In Chapter 5, we present the quantum formalism applied to the calculation of the quantum states after the light interaction in the non-linear waveguide. We show how multimode EPR correlations (entanglement), is related to squeezing, and how a multimode squeezed vacuum state results from the non-linear process. In Chapter 6, we define the quantum networks as graph states in the frequency domain, that can be directly obtained with the results of the previous Chapter. We also show our calculations for the experimental design of the source, and in particular the dependence of the multimode quantum states on the controllable degrees of freedom in the experiment. Finally, in Chapter 7, we show the rest of the experimental results in the thesis. We divide the experiment in six blocks and show the characterization and details of all of them. We show the results of a Phase Sensitive Amplification experiment by constructing an Optical Parametric Amplifier with the waveguides that allows us to show parametric gain, a precondition for squeezing, and give an order of magnitude of the potential squeezing level. To finish the Chapter, we show the multimode squeezing measurement of the source via homodyne detection, characterizing the multimode quantum states. We finish the manuscript with the concluding remarks and the prospects for the near objectives to considerably improve the squeezing measurement, and the long-term potentialities of the constructed quantum source.

Part I

Satellite Continuous Variable Quantum Key Distribution

Chapter 1

Introduction to Quantum Cryptography

"We can only see a short distance ahead, but we can see plenty there that needs to be done"

– Alan Turing, Computing machinery and intelligence

Contents

This Chapter aims to give a brief introduction to the field of Cryptography, and in particular we will set the grounds to introduce Quantum Key Distribution (QKD), as one of the first quantum protocols that is already commercialized in real-world applications and that is able to provide information theoretic security. We will present the main challenge for QKD nowadays, namely the long distance communication problem due to the inherent optical losses and the impossibility to amplify a quantum signal without adding noise due to the no-cloning theorem. We will derive the basic notions and tools needed for Quantum Key

Distribution in the context of Continuous Variables, CV-QKD, defining the main variables and formulas in the GG02 protocol [1], which is a prepare-and-measure protocol with coherent states. Our work in the next Chapter will focus on the feasibility of the GG02 protocol presented here in a satellite-ground station link, tackling the long distance communication problem.

1.1 Introduction to Cryptography

The word Cryptography comes from the ancient Greeks, where $kryptos$ stands for "secret, hidden" and $graphein$ stands for "to write". It is therefore the discipline that tries to conceive secure systems of communication between two parties, that are historically called Alice and Bob, against possibly malicious third parties, called the Eavesdroppers or simply Eve.

There is record of cryptographic codes from the time of Julius Caesar [2], 2000 years ago. With the advent of computers after the Second World War, and the decoding of the nazi's Enigma machine [3], the cryptographic systems started to become increasingly complex.

In cryptography, the message to be communicated is called the plaintext, p, that is encrypted into an unintelligible form called the chiphertext, c, using an algorithm called a cipher. For the message to be communicated secretly a (ideally short) string of characters could be shared between Alice and Bob, the *Key*, that is used for encrypting and decrypting the messages. This type of encryption/decryption algorithms are known as *symmetric-key cryptography*.

Even though many encrypting methods have been invented throughout History, a recurrent process can be identified in the most basic and practical schemes:

- Alice has a box with two inputs: the plain message p and the secret key k. Alice will encrypt the text with the key, resulting in the ciphertext m.

- The encrypted message m is transmitted through a channel to Bob who receives it, but the untrusted Eve can also read and manipulate the message.

- Bob has a box with two inputs: the received encrypted message m and the secret key $k' = k$ (the equality here implies symmetric cryptography). Bob will decrypt m with the key, obtaining the original message, p.

The security of the procedure relies on two factors: the secrecy of the key and the algorithms performed. If the security relies entirely on the design of the boxes for Alice and Bob, the security is said to be "security by obscurity", which is not very recommended in practice since an adversary could get to know the boxes and break the system.

The current trend is to rely only on the secrecy of the key to guarantee confidentiality of the communication, the design of the boxes being public.

Of course the algorithms performed by the boxes must be non elementary because in that case it would be possible for an attacker to guess the key. For example, shift cipher (or

Caesar's cipher [2]) is a simple cryptographic method where the boxes only shift the letters of the alphabet by the value of the key. If the alphabet is known and relatively small, it would be possible for Eve to guess the message trying iterations of the key.

The previous example raises the question of whether some algorithms are more secure than others or even if it is possible to construct a perfectly secure algorithm. In practice, the attacker will need to perform some computation to try to decipher the messages in the channel. We can quantify the attacker's potential, thus, by processing power. In this case, it is possible to run benchmarks on the average number of operations required to decipher a message encrypted by a particular algorithm, which is typically a function of the number of bits used in the key. Most of the modern algorithms require an exponential processing time with respect to the size of the key, which makes them intractable in most cases. The performance of the cryptoanalysis benchmarks for a particular algorithm can improve for two reasons: either a conceptual error is discovered in the cryptography scheme or a better algorithm to treat the problem is discovered.

From all the algorithms invented until now, the most well known symmetric cipher is the AES [4] which is the NIST standard at the moment of writing. As long as no breakthrough discovery happens, it will remain a reliable resource of security.

Even though symmetric cryptosystems are thought to be secure for the short and medium term, their security is always related to the computational resources of the attacker, so the uncertainty about whether a message was decoded cannot be ruled out. Strategies to mitigate this assumption are key refreshment (renew the key every few time units) or the increase of the key size (also affecting the computational requirements for the trusted parties).

It is possible, though, to have a communication scheme in which the security does not depend on the computational resources of the attacker. Those schemes are said to be *information-theoretic secure.*

The paradigm of an information-theoretic secure protocol is the one time pad, (proved information-theoretic secure by Shannon [5] in 1945). However, this protocol presents some practical limitations: the key should be as long as the message, it can only be used once and it should be truly random, which limits its practical use.

More importantly, it has been proven that any other cipher with the property of perfect secrecy must use keys with effectively the same requirements as one time pad keys [5]. Hence, the implementation of these information-theoretic security protocols is indeed not practical for large-scale use.

1.2 Key Distribution

As mentioned before, all current cryptosystems rely on the secrecy of the keys and their renewal. Therefore, if we find a way of distributing the keys without any computational assumption on a potential adversary, prior to the message encryption and decryption by Alice and Bob, we will obtain an information-theoretic secure protocol. The problem of

establishing this key prior to the communication is the *Key Distribution problem.*

It is instructive to give a flavor of the most common key distribution protocol used nowadays: the Diffie-Hellman key exchange protocol [6].

In the Diffie-Hellman key exchange, there is a (big) prime number, p, and a generator $g \in \mathbb{Z}_p^*$, where $\mathbb{Z}_p^*$ is the ensemble of co-primes of p smaller than p. These two values are public. Alice and Bob select privately and randomly additional numbers $a \in \mathbb{Z}_{p-1}^*$ and $b \in \mathbb{Z}_{p-1}^*$ respectively. Alice (resp. Bob) compute $A = g^a \bmod p$ (resp. $B = g^b \bmod p$) and send it to Bob (resp. Alice), making it public. Then Alice computes $K = (g^b \bmod p)^a = g^{ab} \bmod p$ and Bob computes $K = (g^a \bmod p)^b = g^{ab} \bmod p$ which is the secret key shared by them for any information they want to secretly communicate afterwards.

A potential adversary to this protocol, Eve, would know p, g, A and B, since they are public values. However, for Eve to get the key, K, she would need to know either a or b. The only way Eve can get the key (not considering authentication attacks), is inverting the function $f(x) = g^x \bmod p$, i.e. solving $x = \log_p(f(x))$, where $\log_p$ is here the *discrete logarithm* in base p. It is well known that solving the discrete logarithm problem is computationally intractable [7] if p has around 200 or more digits and does not present a number of weakening characteristics, which can be easily chosen since p is a public number. Thus, under this computational assumption, the secrecy of the key is guaranteed.

It is also known that solving the discrete logarithm problem is equivalent to solving the *prime factoring* problem [8], i.e. finding the prime factors of a given number, which is an exponentially hard problem to solve, which means that it would take an exponential computational time to solve it. Thus, the Diffie-Hellman protocol is broken if the prime factorization problem becomes computationally reachable.

This is exactly what happened during the 90's, when Peter Shor proposed a quantum algorithm showing that prime factoring is not exponentially hard for quantum computers [9]. Therefore this is also the case for the discrete logarithm problem, breaking the Diffie-Hellman exchange protocol. Although fault-tolerant quantum computers are still not at the point of solving prime factorization efficiently for practical numbers, it was of primal necessity to come up with a different set of key distribution protocols that are unbreakable even in the event of Eve possessing a universal fault-tolerant quantum computer.

A set of classical cryptographic algorithms that are thought to be resistant even if the attacker has a quantum computer have been developed in the last years. This trend is known as *post-quantum cryptography* and its security lays on the assumption that the set of NP (non-deterministic polynomial time) problems is not fully contained in the BQP (bounded-error quantum polynomial time) complexity class, which contains the problems that could be solved efficiently by a quantum computer. However, there is no proven certainty about the existence of NP problems outside BQP, making the frontier between NP and BQP unclear. For instance, prime factorization does not belong to P (polynomial time) but it belongs to BQP. For a particular problem, we only know that no known quantum algorithms exist at the moment, but they could be discovered in the future. The challenge in post-quantum

cryptography is to discover classical algorithms for which no counter analysis algorithm is known (even within quantum algorithms). This classical nature could make them very flexible, since a simple software update would suffice to deploy them, but their main weakness is that the security might decrease over time, since new algorithms could be discovered. For this reason their security cannot be excluded to be compromised in the future.

Fortunately, quantum physics is the source of these new problems in cryptograpy, but it also proposes a solution. There exist quantum protocols whose security can be proven even for quantum attackers. It is the field of *Quantum Cryptography*, with Quantum Key Distribution (QKD) being one of the most prominent protocols, already in use for commercial applications.

One of the features of QKD protocols is that they heavily rely on the characterization of the communication channel. This fact makes their implementation more challenging with respect to the classical counterparts, because the latter mainly rely on mathematical abstraction and hence can be implemented by software only. In fact, the channel characterization will be one of our main topics for the next Chapter.

In the following section we study the most relevant characteristics of QKD systems.

1.3   Quantum Key Distribution

In QKD, our two familiar users, Alice and Bob, can share information in two different channels. One of the channels is an authenticated classical public channel. Classical here is referring to the fact that the information that can be communicated in this channel presents no quantum correlations. It can be thought as a channel where classical bits of information can be exchanged. For security reasons, it is important that the classical channel is authenticated, i.e. that Bob is confident that the messages exchanged in this channel comes from Alice and viceversa.

Furthermore, Alice and Bob can exchange information using a quantum channel, with which Eve can interact. The quantum channel is therefore defined as the channel in which quantum information can be exchanged. The quantum information is contained in quantum states (typically of light, but not necessarily) that Alice and Bob can share. The Hilbert space of the states could be finite (qubits or qudits states) or infinite (continuous variable states). For this reason, the QKD protocols can be divided into discrete variable and continuous variable protocols, as we will see in the following.

The fundamental principle underlying quantum the key distribution is that any measurement in an individual quantum object leaves a trace. In other words, it is impossible for Eve to read the information from the quantum channel without perturbing it. This perturbation can be detected by Alice and Bob, that can communicate in the classical public channel. We will treat this in more rigorous details in the next sections.

In order to get a flavor about how QKD works, it is instructive to see the first QKD protocol proposed by Charles Bennet and Gilles Brassard in 1984 [10], hence called BB84,
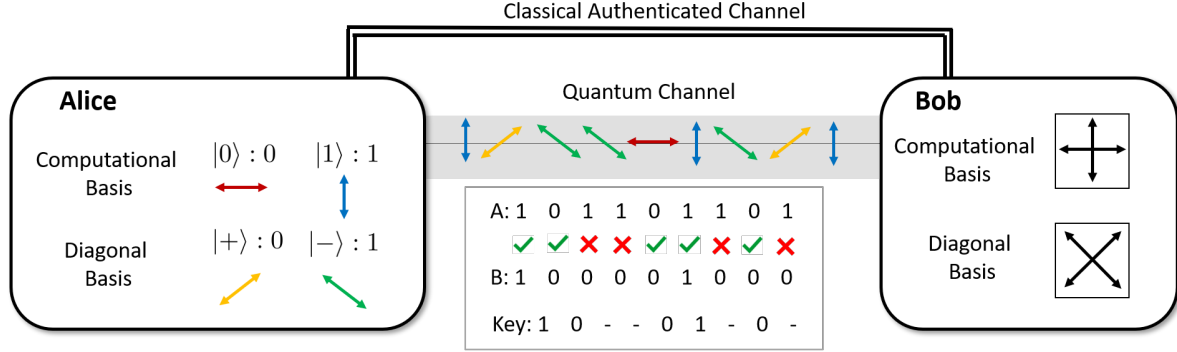
Figure 1.1: BB84 basic scheme. Alice encodes her states in two conjugate basis, here represented by the photon polarization states, and send the states to Bob, who chooses randomly to measure the polarization in either of the two basis. For more details see text.

that encapsulates the basic properties of all QKD schemes that came after.

1.3.1   BB84

The quantum states that are used in the BB84 protocol are qubits, i.e. two-level quantum systems, that can be implemented in different physical platforms, the photon polarization being the most popular.

Hence, we can write the general quantum state shared in the quantum channel as a linear superposition in a given two dimensional Hilbert space basis:

$$|\psi\rangle = \alpha |0\rangle + \beta |1\rangle \tag{1.1}$$

where α and β are two complex numbers that normalizes the state $|\psi\rangle$, $|\alpha|^2 + |\beta|^2 = 1$. The basis $\{|0\rangle , |1\rangle\}$ is usually called the computational base.

We can also write the state in a rotated basis $\{|0'\rangle , |1'\rangle\}$ using its relation to the computational basis, by a rotation in the Bloch Sphere:

$$\begin{pmatrix} |0\rangle \\ |1\rangle \end{pmatrix} = \begin{pmatrix} \cos\theta & -\sin\theta \\ \sin\theta & \cos\theta \end{pmatrix} \begin{pmatrix} |0'\rangle \\ |1'\rangle \end{pmatrix} \tag{1.2}$$

where θ is the rotation angle. In the BB84 protocol we will work with the computational basis and the so-called diagonal basis, $\{|+\rangle , |-\rangle\}$, which is the rotated base with an angle of $\theta = 45^o$. Explicitly:

$$\begin{pmatrix} |0\rangle \\ |1\rangle \end{pmatrix} = \frac{1}{\sqrt{2}} \begin{pmatrix} 1 & -1 \\ 1 & 1 \end{pmatrix} \begin{pmatrix} |-\rangle \\ |+\rangle \end{pmatrix} \tag{1.3}$$

The BB84 protocol starts with Alice choosing randomly the basis in which she encodes her state, preparing correspondingly one of the states between $|0\rangle / |1\rangle$ or $|+\rangle / |-\rangle$ and

sending it to Bob. Bob would also choose randomly the basis in which measuring the state. If Alice and Bob happened to have chosen the same basis, then Bob's measurement would always correspond to Alice's state. If Bob chooses the wrong basis, then his bit of information has a 50% chance of being 0 or 1 and his measurement is completely uncorrelated with the state that Alice sent. A scheme of the protocol is represented in Fig.1.1.

In order for Alice and Bob to know what were the right basis choices, Bob communicates through the classical authenticated channel his basis choice and Alice checks which ones were correct, i.e. which ones corresponded to her choice. This step in the protocol is called reconciliation.

Since their results are completely correlated when the choice of basis was correct, then Alice and Bob keep only those instances, obtaining the key.

For Eve to get information about the states that Alice sent, she would need to interact with the quantum channel and measure the state in a given basis. For her to not be noticed, she should also prepare the same state she has measured and send it to Bob.

However, this attack can be detected by Alice and Bob. Bob would communicate by the classical channel some subset of his measurement results to Alice, who will compare with the states she prepared. There are cases were Eve measures in the wrong basis, getting a completely random result and preparing the state in the wrong basis to Bob. Therefore, half of the times that Bob would measure this state sent in secret by Eve, he would obtain a result that does not correspond to Alice's choice, since Eve has changed the basis after intercepting the state in the quantum channel. Thus, the presence of Eve produces errors in the final string of bits after reconciliation.

In particular, the probability of an error is the probability that Eve measures Alice's state in the wrong basis (50%) times the probability that Bob's gets the wrong result from the state sent by Eve (50%), and so 25%. Therefore, if Alice and Bob are willing to sacrifice n bits from the key by revealing them, they can detect Eve in the channel with probability $1 - (3/4)^n$. Subsequent classical post-processing phases can purify the correlated values of Alice and Bob as a function of the measured errors to obtain a perfectly secret key. The attack described here is a basic intercept-and-resend attack that we are using here to illustrate an example of the security issues in QKD.

Three important remarks from this protocol are:

- The errors are considered to be caused by Eve, even though in practice they can be produced by imperfections in the system.

- Alice and Bob should have available a physical system capable of producing on-demand qubits with sufficiently good fidelity. Single photon emitters are considered at Alice's side.

- Perfect preparation and measurement of the qubits is also considered. In the case of implementation with light, single photon detectors are considered at the Bob's side.

- A certain number of assumptions are used to construct a mathematical framework that will allow the analysis of the security.

Many more QKD protocols have been invented since BB84, but the great majority share all these characteristics. The backbone of QKD is to build a physical model of the communication system and develop a mathematical framework that includes the laws of quantum mechanics. This mathematical framework is usually called *security proof*, that is valid only when the hypotheses of the model are valid. The security of a given model is typically quantified with the probability of success for a potential eavesdropper, that must be arbitrary small within the context of the model for having perfect security.

1.3.2 QKD workflow

Most of the QKD protocols follow a series of steps that are common to all of them:

– **Distribution of quantum states**: Quantum states are prepared, transmitted and measured between the parties. After this step, Alice and Bob share two strings of correlated values.

– **Parameter estimation**: Alice and Bob reveal a random part of their correlated values in order to characterize the quantum channel. The revealed values will not be used in the final key, so there is a trade-off between the quantity of values revealed to have an accurate estimation of the channel and the final key length. The channel estimation includes the possibility of a possible eavesdropper, that will be detected by noticing extra noise due to the perturbation of the quantum states while eavesdropping.

– **Error correction**: Because of the different imperfections in the systems, the correlation in the two sets between Alice and Bob is not perfect and needs to be corrected. Classical error correcting codes can be used for this purpose. After the application of these codes the parties share the same string of values with no errors.

– **Privacy amplification**: Even after the error correction phase, some information could have been leaked to a eavesdropper, so an additional classical protocol is performed in order to increase the secrecy of the key at the expense of reducing the final key length. The remaining shared string after this phase is the final secret key shared between Alice and Bob.

In this thesis, we will be interested mainly on the first two phases, distribution of quantum states and parameter estimation, since they are the only ones that involve quantum mechanics directly, the rest of the steps being completely classical and generally well-known. In fact, in proof-of-principle scenarios, it is common use to complete these two steps, and draw the conclusions from there. More specifically, the security proof will predict the length of the key after the parameter estimation phase. After that phase, the only parameter that is

relevant for the key length is the reconciliation efficiency, that is in turn given by the classical error correction codes. For this reason, in the next Chapter, we will consider a typical value of the reconciliation efficiency from the literature and compute the secret keys taking only into account the QKD protocol until parameter estimation.

1.3.3   Entanglement-based and Prepare-and-Measure Protocols

In 1991 Artur Ekert [11] published E91, a QKD algorithm that was conceptually different from BB84, since the quantum resource assuring security was entanglement. Other protocols based on entanglement, like BBM92 [12] followed soon.

In these types of protocols there is a third untrusted party, Charlie, who prepares a state composed of two subsystems presenting quantum correlations between them (entanglement). This could be two-photon Bell pair states. Charlie distributes each part of the entangled system to Alice and Bob, that perform consecutive measurements in a random basis, as in BB84. Since the system had entanglement, the states at Alice and Bob are completely correlated. After the distribution phase Alice and Bob would communicate their basis choice and compute statistics in the channel of the type of Bell test inequalities [13], which would indicate whether there were real quantum correlations in the states that Charlie sent. The rest of the classical steps proceed the same way as in the BB84 protocol.

Very soon after E91 was proposed, it was proven that entangled and non-entangled based protocols, also called *prepare-and-measure* protocols, are equivalent. For every entanglement-based protocol, there exist a prepare-and-measure protocol that is equivalent in terms of security[1].

Usually, however, the security proofs are easier to show for entanglement-based protocols, while the real implementation of the protocol is performed with the corresponding equivalent prepare-and-measure counterpart.

1.4   Long distance communication

The uncertainty principle in quantum mechanics has as a consequence the impossibility of making a measurement of a quantum system without disturbing it. As we have already seen, this is the theoretical working principle in QKD protocols, since it allows the detection of the eavesdropper. Another way to look at this is via the so-called no-cloning theorem, which came as an evolution of the no-go theorem in [14], and that states the impossibility of perfectly copying a quantum system. This feature, however, comes with the inconvenience that long distance communication becomes a challenging aspect for practical QKD. As the communication channel is longer, the losses in the channel increase. Classically, the signal would be re-amplified using a repeater, but this is not possible in QKD, where the quantum

---

[1]The equivalence referred here do not consider Device Independent protocols, in which entanglement is required, and that are therefore not possible to implement with prepare-and-measure protocols .

signal cannot be copied. The typical optical losses in fiber at the time of writing are around 0.2 dB/km [15], which will limit the communication distance to a value that depends on the sensitivity to losses of the particular QKD protocol to be implemented, but that is no longer than few hundreds of kilometers.

This is a very important constraint in the context of secure quantum networks and for quantum cryptography in general. If we are to build a global network whose links are secured by QKD, we would need to find a way of circumventing the long distance problem.

One of the ways to solve the problem is by the use of trusted nodes, dividing a long communication distance into several shorter point-to-point links. In this way, a network of trusted users could be constructed at the cost of the necessity of trusting each node. There should be also some physical security mechanism to ensure that the intermediate devices are not tampered with. The most extensive trusted node network at the moment of writing expands for more than 2000 km between several major cities in China [16].

Another approach to overcome the distance limit is to divide the channel into pieces and perform entanglement swapping at each step [17, 18]. This approach is known as *quantum repeaters*. The idea behind quantum repeaters consists in extending the classical signal amplifiers to the quantum realm by the use of quantum teleportation, guaranteeing the distribution of entangled photons between two locations. It is a promising but challenging field that would be useful not only for QKD, but for other communication protocols as well.

Finally, there is also the possibility of using satellites to establish link-to-link communication with a ground station. This approach is simply known as *satellite-QKD* [19]. The losses in fiber or free-space on Earth's surface are exponential with the distance, following the optical absorption law, whilst they are only quadratic after the atmosphere, where only diffraction is present. Since the atmosphere effectively covers only 10 km in height, it is possible to establish a QKD key with an orbiting Satellite, pushing the distance limit of repeaterless QKD protocols to link with satellites. One way of setting a quantum network protected by QKD in this way could be to first distribute a QKD key between a ground station and a satellite, then perform yet another QKD protocol between the satellite and another ground station in a different part of the Globe (even passing through a communication phase with other intermediate satellite), so the two points on Earth can share the secure key.

1.5 Secure Key-Rate

The level of security of any QKD protocol depends on the assumptions in the technological capabilities of the potential eavesdropper. In the security proofs, the types of attacks are classified into three different groups [20]:

Individual attacks: Eve performs an independent and identically distributed (i.i.d.) attack on all signals, i.e. she prepares separable ancilla states each of which interacts individually with one signal pulse in the quantum channel. The states are stored in a quantum memory

until the post-processing step, and subsequently measured independently from one another.

Collective attacks: Eve performs an i.i.d. attack with separable ancilla states, stores her states in a quantum memory and performs an optimal collective measurement on all quantum states at any later time (in particular, after post-processing).

Coherent attacks: The most general attack where no (i.i.d.) assumption is made. In particular, Eve may prepare an optimal global ancilla state whose (possibly mutually dependent) modes interact with the signal pulses in the channel and are then stored and collectively measured after the classical post-processing.

Apart from this classification, security proofs can be framed either in the *asymptotic limit*, where an infinite number of symbols is transmitted, or in the case where a finite number of transmitted symbols is considered. The asymptotic limit is useful because it can give an upper bound for non-asymptotic security proofs and the formulas are easier to obtain.

In this manuscript we consider the application of the formulas that are known to be secure against collective attacks in the asymptotic limit. Additionally, in the next chapter we will also compute some corrections for finite-key sizes.

In general, the secure key rate is given by:

$$K = f_{\text{sym}} r \tag{1.4}$$

where f_{sym} is the symbol rate (measured in symbols per second), that depends on the communication speed in the quantum channel, and r is the secret fraction (measured in bits per symbol), i.e. the secure key rate per symbol.

In the asymptotic limit, Devetak and Winter derived a lower bound for the secret fraction considering collective attacks as [21]:

$$r_{\text{col.}}^{\text{asymp.}} \geq I_{\text{AB}} - \chi_{\text{E}} \tag{1.5}$$

where I_{AB} is the *mutual information* between Alice and Bob's strings, which is a quantification of the amount of information obtained in one of their string when observing the other one, and χ_{E} is the *Holevo bound*, which is a bound on the amount of information that Eve can obtain from the key.

In practice, we can add to this bound the fact that the error correction codes do not operate at the asymptotic limit. If we consider that some blocks of the key will fail to be corrected we can multiply the mutual information by an effective number $\beta \in [0, 1]$ that represents this fraction. The number β was mentioned before and it is called the *reconciliation efficiency*. Also, a certain fraction of the key, p, will be revealed for the classical post-processing phase, and so the final bound for the secure key rate in a practical scenario can be written as:

$$r_{\text{col.}}^{\text{asymp.}} \geq (1 - p)(\beta I_{\text{AB}} - \chi_{\text{E}}) \tag{1.6}$$

This formula is taken into account every time a QKD protocol should be analyzed, and compared with actual key obtained from experimental implementations.

In the analysis of a QKD protocol, one usually assumes that Eve can perform the best attack possible, maximizing the Holevo bound, and the equality holds in Eq.(1.6).

1.6 CVQKD

The QKD protocols we have mentioned until now, including our example on BB84, are based on Discrete Variables (DVQKD), in the sense that the quantum information is encoded into systems with a discrete number of degrees of freedom. For instance, in BB84, the quantum states needed are qubits, two-level quantum systems, so the Hilbert Space is two-dimensional.

The use of DVQKD simplifies the analysis of the system, but can make the implementation difficult, since those states can be difficult to generate or detect. Often weak coherent states are employed for generating single-photons at Alice's side, instead of pure single-photon emitters. However, single-photon detectors are necessary at Bob's side, which are expensive and cumbersome for some real-world applications.

Nevertheless, the Hilbert space of the states used in QKD can be extended to infinite dimensions simply by using quantum states derived from a hamiltonian whose eigenvalues take an infinite range of possible values. This type of QKD is called Continuouos Variable QKD (CVQKD). In this case one can use coherent (for prepare-and-measure protocols) or squeezed (for entanglement-based protocols) states of light.

By moving to an infinite Hilbert Space, the security proofs and the classical cryptographic steps (error correction codes and private amplification) are more involved than in the DV case. However, the main advantage of CVQKD with respect to DVQKD is the simplification in the implementation. A laser naturally emits coherent states, and no single-photon detector is needed, so practical QKD system can be envisioned and implemented using only off-the-shelf optical components.

1.6.1 Coherent states

Coherent states of light are eigenstates of the annihilation operator $\hat{a}$. We define the quadrature operators, $\hat{q}$ and $\hat{p}$ as:

$$\hat{q} = \hat{a} + \hat{a}^\dagger \tag{1.7}$$

$$\hat{p} = i(\hat{a}^\dagger - \hat{a}) \tag{1.8}$$

so that any coherent state, $|\alpha\rangle$ fulfills:

$$\hat{a} |\alpha\rangle = \alpha |\alpha\rangle \tag{1.9}$$

where $\alpha = \frac{1}{2}(q + ip)$, and q and p are the eigenvalues of the quadrature operators. Since these eigenvalues are real numbers, the spectrum of possible outcomes in a quadrature measurement is continuous, and hence the use of the name Continuous Variables.

Furthermore, since the quadrature operators do not commute ($[\hat{q}, \hat{p}] = i\mathbb{I}$) then, by the uncertainty relation, there is a minimum value in the product of the quadrature variances:

$$\delta q \delta p \geq 1 \quad \text{(S.N.U.)} \tag{1.10}$$

That is to say, a measurement of these observables cannot be performed with an infinite precision. For a coherent state, the equality in Eq.(1.10) holds, minimizing the uncertainty relation with an equal value of the quadrature variances.

Coherent states can be represented in *phase space*, which is the 2D plane whose axes are the field quadratures values q and p. Since the uncertainty relation is fulfill with equal variances, a coherent state can be represented as a circle-like object in phase-space, centered at the mean value of the quadratures, and with a variance given by 1 shot noise unit.

1.6.2 GG02 Protocol

The specific CVQKD protocol that was studied in this thesis is called GG02[1], after P. Grangier and F. Grosshans. It is of the type prepare-and-measure, using coherent states of light. The protocol goes as follows:

Distribution of coherent states:

The protocol starts with Alice choosing a set of random numbers $Q = \{q\}$ and $P = \{p\}$ following a normal probability distribution with 0 mean and variance V_A:[2]

$$Q \sim P \sim N(0, V_\text{A}) \tag{1.11}$$

V_A is simply called *Alice's variance*. Every pair of the form $\{q_j, p_j\}$ is associated to a coherent state $|\alpha_j\rangle = |q_j + ip_j\rangle$. Hence:

$$\hat{a} |\alpha_j\rangle = \alpha_j |\alpha_j\rangle = (q_j + ip_j) |\alpha_j\rangle \tag{1.12}$$

where $\hat{a} = \frac{1}{2}(\hat{q} + i\hat{p})$ is the annihilation operator and $\hat{q}$ and $\hat{p}$ are the quadrature operators as defined above.

The photon number operator is defined as:

$$\hat{n} = \hat{a}^\dagger \hat{a} = \frac{1}{4}(\hat{q}^2 + \hat{p}^2) - \frac{1}{2} \tag{1.13}$$

and its expectation value for the j-th coherent state is:

$$\langle \hat{n} \rangle_j = \langle \alpha_j | \hat{n} | \alpha_j \rangle = |\alpha_j|^2 = q_j^2 + p_j^2 \tag{1.14}$$

---

[2]Although not necessary for practical cases, Alice should use a Quantum Random Number Generator (QRNG), [22], for assuring the randomness in her sampling of the distributions.

Since these numbers are sampled from the gaussian distribution, then the ensemble mean number of photons, $\bar{n}$ is[3]:

$$\bar{n} = \bar{Q}^2 + \bar{P}^2 = 2V_A \tag{1.15}$$

Alice's Variance V_A is not to be confused with the so-called modulation variance, V_m, that is the total variance in the modulation, and it is defined as the sum of of Alice's variance and the intrinsic noise of the coherent state (1 S.N.U.), i.e. $V_m \equiv V_A + 1$. Note that even in the case of $V_A = 0$ the quadratures still carry a variance of 1 shot noise unit, as required by the uncertainty relation, and hence the total modulation variance is still 1. Eq.(1.15) is therefore the mean photon number in terms of the total Alice's variance. Hence, Alice's variance is directly related to the mean number of photons sent to Bob. We will see in the next chapter that the typical values of the modulation variance is between 2 and 4 shot noise units.

Alice then prepares the modulated states $|\alpha_1\rangle |\alpha_2\rangle |\alpha_3\rangle$ ... and sends them to Bob through the gaussian quantum channel.

Bob receives the states and performs coherent detection, that permits him to retrieve the quadrature values, either by homodyne detection (measuring one quadrature) or heterodyne detection (measuring a pair of conjugate quadratures).

Parameter Estimation:

After the measurements performed by Bob, both Alice and Bob will reveal a random subset of their data in order to estimate the total transmission of the gaussian channel and the excess noise present. They will compute the mutual information, I_{AB} and the Holevo bound for Eve's information, χ_E. As we will see next, we will consider the case of reverse reconciliation, which means that Alice will correct her bit string according to Bob's information. For this reason, from now on we denote the Holevo bound as χ_{EB}, since it is the maximal amount of information that Eve can get from Bob during the reconciliation.

If $\chi_{EB} > \beta I_{AB}$, following Eq.(1.6), then the potential eavesdropper has more information than the one shared by Alice and Bob, and the protocol is aborted. Otherwise, they will proceed with the next steps in the protocol. Note that the protocol abortion could happen even when there is no eavesdropper, if the channel is sufficiently noisy, resulting in a high value in the estimation of χ_{EB}.

Information Reconciliation:

In this step one-way information reconciliation is performed, which is a type of error correction. Typically, low-density parity-check (LDPC) codes are used for this step [23]. In the case in which Alice sends the classical information to Bob in order for him to correct the errors in his string, this is called direct (or forward) reconciliation. However, this necessitates a channel transmittance, T, bigger than 0.5 (or 3 dB), which is hence not practical for long-distance communication [24]. This limitation can be overcome by reverse reconciliation, in which Bob sends the information to be corrected by Alice. In this case, since Alice's information on Bob's measurement is always greater than Eve's, the mutual information

---

[3]Note that here, the symbol $\bar{...}$ means an average over the normal distribution, while $\langle ...\rangle$ is the mean value of the quantum mechanical operator inside the brakets over the state under consideration.

can remain always greater than the Holevo bound during the reconciliation. As mentioned above, we will consider reverse reconciliation for the rest of the text.

Privacy amplification: A brief step of confirmation can be performed, in which Alice and Bob use a family of hash functions [25] that is made public and perform it to their key, communicating the result. In this way, they bound the failure probability of the error correction phase. If the hash is the same for Alice and Bob, they proceed with the protocol, otherwise, they abort it.

At this step Alice and Bob already share identical bit strings with a very high probability, but some information could have been leaked to Eve in the whole process. In order to reduce the probability that Eve could guess a part of the key, they perform a privacy amplification protocol to their bit strings [26]. A secure key with a certain length is finally shared between Alice and Bob and the protocol is finished.

1.6.3 Coherent detection

After the distribution of the quantum states, Bob measures the states sent by Alice to proceed with the parameter estimation phase. In the case of DVQKD, the states are single photons, and therefore Bob should have single photon detectors in order to recover the information from the states. This could be technologically challenging in some cases, which reduces the practicality of the system.

In the case of CVQKD, the information is encoded into the quadratures of the coherent states sent by Alice. In order to recover this information, Bob could perform coherent detection, which does not require any single photon detector, but photodiodes.

The coherent detection used in CVQKD protocols is called *homodyne detection*, and permits to obtain one general quadrature value from the light state. Sometimes, both a specific given quadrature and the corresponding conjugate quadrature (the quadrature rotated by 90 degrees in phase space) are to be measured. In this case, one can simply perform two homodyne measurements in parallel with a phase difference of 90 degrees, which is known as *heterodyne detection* in the literature. We therefore refer to heterodyne detection as double homodyne detection here.[4]

The principle of homodyne detection is to mix the light that is to be measured with a bright coherent state, called the Local Oscillator (LO). The LO serves as the modal reference (frequency, space, and polarization), and can be generated directly at Bob's side. Both the quantum states and the LO are mixed in a beamsplitter and then sent to two photodetectors. The photodetectors convert the optical energy impinging on them into an electronic signal, hence measuring the optical intensity. If both output signals are electronically subtracted, the final signal that remains is proportional to the quadrature that is in phase with the LO.

To see this more precisely, notice that we can treat the LO as a classical coherent state

---

[4]The protocols featuring heterodyne detection are also known as "no-switching" protocols.

with intensity $|\alpha_{\mathrm{LO}}|^2$ and relative phase θ with respect to the signal[5]

$$\alpha_{\mathrm{LO}} = |\alpha_{\mathrm{LO}}|e^{i\theta} \tag{1.16}$$

Recalling the beamsplitter (BS) action in the matrix representation, with $\{\hat{a}_{\mathrm{in1}}, \hat{a}_{\mathrm{in2}}\}$ as input modes to the BS, and $\{\hat{a}_{\mathrm{out1}}, \hat{a}_{\mathrm{out2}}\}$ the output modes[6]

$$\begin{pmatrix} \hat{a}_{\mathrm{out1}} \\ \hat{a}_{\mathrm{out2}} \end{pmatrix} = \frac{1}{\sqrt{2}} \begin{pmatrix} 1 & 1 \\ 1 & -1 \end{pmatrix} \begin{pmatrix} \hat{a}_{\mathrm{in1}} \\ \hat{a}_{\mathrm{in2}} \end{pmatrix} \tag{1.17}$$

By mixing our LO with a quantum signal represented by the operator $\hat{a}_{\mathrm{in1}} = \hat{a}$, the output modes after the BS are therefore:

$$\begin{pmatrix} \hat{a}_{\mathrm{BS1}} \\ \hat{a}_{\mathrm{BS2}} \end{pmatrix} = \frac{1}{\sqrt{2}} \begin{pmatrix} \hat{a} + \alpha_{\mathrm{LO}} \\ \hat{a} - \alpha_{\mathrm{LO}} \end{pmatrix} \tag{1.18}$$

The intensity of an optical field $\hat{A}$ is proportional to the mean number of photons, $\hat{N} = \hat{A}^\dagger \hat{A}$, and therefore the intensity at the beamsplitter outputs are proportional to:

$$\hat{N}_{\mathrm{out1}} = \hat{a}_{\mathrm{BS1}}^\dagger \hat{a}_{\mathrm{BS1}} = \frac{1}{2}\left(\hat{a}^\dagger \hat{a} + |\alpha_{\mathrm{LO}}|^2 + \hat{a}^\dagger \alpha_{\mathrm{LO}} + \hat{a}\alpha_{\mathrm{LO}}^*\right) \tag{1.19}$$

$$\hat{N}_{\mathrm{out2}} = \hat{a}_{\mathrm{BS2}}^\dagger \hat{a}_{\mathrm{BS2}} = \frac{1}{2}\left(\hat{a}^\dagger \hat{a} + |\alpha_{\mathrm{LO}}|^2 - \hat{a}^\dagger \alpha_{\mathrm{LO}} - \hat{a}\alpha_{\mathrm{LO}}^*\right) \tag{1.20}$$

The subtraction of both intensities then gives the following operator:

$$\Delta\hat{N} = \hat{N}_{\mathrm{out1}} - \hat{N}_{\mathrm{out2}} = \hat{a}^\dagger \alpha_{\mathrm{LO}} + \hat{a}\alpha_{\mathrm{LO}}^* = |\alpha_{\mathrm{LO}}|(\hat{a}^\dagger e^{i\theta} + \hat{a}e^{-i\theta}) \tag{1.21}$$

by the definition of the quadratures in Eq.(1.8), one has:

$$\hat{a}^\dagger e^{i\theta} + \hat{a}e^{-i\theta} = \frac{1}{2}\left(\hat{q}\left(e^{i\theta} + e^{-i\theta}\right) + i\hat{p}\left(-e^{i\theta} + e^{-i\theta}\right)\right) \tag{1.22}$$

$$= \hat{q}\cos\theta + \hat{p}\sin\theta \equiv \hat{q}_\theta \tag{1.23}$$

where the defined q_θ is a generalized quadrature, that corresponds to a quadrature rotated θ degrees with respect to $\hat{q}$. Hence, if the phase difference between the LO and the signal is 0 (90 degrees), the difference number operator, which is the output of the homodyne measurement, is proportional to $\hat{q}$ ($\hat{p}$). Therefore, by measuring the homodyne signal we get samples of the quadrature operator that is in phase with the LO.

A scheme of the GG02 CVQKD protocol with the distribution of the states and the coherent detection is shown in Fig.(1.2).

---

[5]Actually, in general, we do not need the LO to be a coherent state, just that its number of photons is much higher than the photons in the signal, and small fluctuations of the operators with respect to the mean field value, so we can treat the LO as a classical object.

[6]Note that we write here the modes as operators since we are dealing with their quantum nature, but the exact relation also holds when the fields are classical, only removing the operator nature.
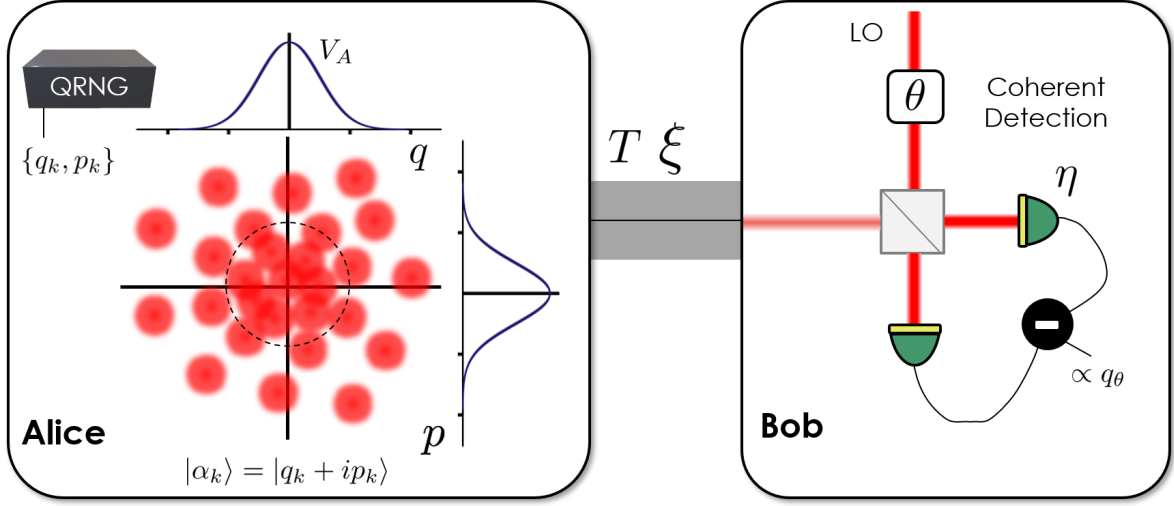
Figure 1.2: GG02 basic scheme. Alice prepares a set of coherent states whose quadratures are obtained from two gaussian distributions with a certain variance. Then she sends the states to Bob, who recovers the information in the quadratures by coherent detection. For more information see text.

1.6.4 Imperfections and excess noise

It is important in these type of protocols to be able to calibrate the imperfections that add noise to the measurement at Bob's. The computation of these errors is performed in the parameter estimation phase. The main parameters to be estimated in a practical scenario are:

- Channel Transmittance, T[27] a characterization of the channel should be performed where the channel losses are treated. This characterization becomes more involved when the losses depend on time, as we will see in the next Chapter. For a fiber-type experiment, the transmittance is fixed. The loss coefficient of the fiber per unit lenght is typically of about 0.2 dB/km [15].

- Detector Efficiency, η, accounting for the detectors's losses when measuring the optical intensity. It is usual to account the detector coupling and measure efficiencies as part of the total channel transmittance.

- The electronic noise, ν_{el}, due to the thermal noise of the detectors even without the presence of any light.

- The modulation variance, V_{A}, known to Alice, when preparing the coherent states.

---

[7]We denote T the transmission coefficient, and $\tau = T^2$ the channel transmittance.

- The excess noise, ξ, that is defined as the rest of noise sources that cannot be calibrated by Alice and Bob[8]. In the security proofs, this noise is assumed to be completely due to the presence of the eavesdropper in the quantum channel. A protocol would be useful whenever the computed key rate after parameter estimation (and therefore after considering the excess noise) is positive. In reality, there could be sources of excess noise that are not known precisely to Alice and Bob that will play a role at the parameter estimation phase. Examples of excess noise are the discretization in the gaussian modulation values, the Raman scattering that is present in the fibers (that can slightly change the light frequency) or phase fluctuations in either the LO or the signal. The excess noise is one of the crucial parameters in a cryptographic Continuous Variable protocol, since it is the parameter perturbed by the action of the eavesdropper [27, 28] during the execution of the protocol.

All the sources of noise have as a consequence the reduction of the signal-to-noise ratio (SNR) when Bob measures the states, hence reducing the mutual information I_{AB}, having an impact on the secure key that can be generated.

In order to compute the actual key rate, one should analyze the variance expected by Bob when measuring the states.

We stress that the total modulation variance, V_m is the sum of Alice's variance when preparing the states, V_{A} and the intrinsic variance of the coherent states, which is 1 shot noise unit, $V_m = V_{\text{A}} + 1$. We can model the noise contribution from the channel, E_c, and from the detectors, E_d, with [20]:

$$E_c = \frac{1 - T^2}{T^2} + \xi \qquad E_d = \frac{1 - \eta}{\eta} + \frac{\nu_{\text{el}}}{\eta} \tag{1.24}$$

where E_c is the loss-induced vacuum noise (due to the channel losses) plus the excess noise, and E_d is the detector and electronic noise. One can furthermore define the noise figure of merit as:

$$E = E_c + \frac{E_d}{T^2} \tag{1.25}$$

where the detector noise is divided by the channel transmittance in order to refer the noise to Bob's output.

The variance measured by Bob can be then computed as:

$$V_{\text{B}} = T^2 \eta (V_{\text{A}} + 1 + E) \tag{1.26}$$

---

[8]There are different scenarios depending on the confidence in the noise sources. The realistic scenario is the one we are describing in this section, in which we assume Alice and Bob laboratories can be trusted, so we can calibrate the noise in Alice's variance and Bob's detectors. One could likewise assume that all sources of noise, including channel losses and detector efficiencies, are also in control of Eve. This is called the untrusted (or paranoid) scenario, and in this case obtaining a secure key is much more challenging given the current technological state-of-the-art.

Using Eq.(1.25) with Eq.(1.24) one arrives to the expression of the variance at Bob's:

$$V_{\mathrm{B}} = T^2\eta(V_{\mathrm{A}} + \xi) + 1 + \nu_{\mathrm{el}} \tag{1.27}$$

We can also include the fact that the coherent detection could be either homodyne (as in our analysis until now) or heterodyne. In the last case one has to divide both T^2 and ξ by a factor of two, since an additional beamsplitter at Bob would be necessary for dividing the signal in order to measure two quadratures at the same time. We can in general write:

$$V_{\mathrm{B}} = \frac{T^2\eta}{h}V_{\mathrm{A}} + 1 + \frac{T^2\eta\xi + \nu_{\mathrm{el}}}{h} \tag{1.28}$$

where $h = 1$ for homodyne detection, and $h = 2$ for heterodyne detection.

In order to compute the secret key of Eq.(1.6), we need to compute the mutual information and the Holevo bound. Here, we are in conditions for already calculating the mutual information, whilst the Holevo bound will be treated in the next Chapter.

First, we define the signal-to-noise ratio as the ratio between the signal power and the noise power. Looking at Eq. (1.28) is clear that the first part of the equation is the actual signal variance, while the extra shot noise unit and the excess noise account for the noise in the state. Thus:

$$\mathrm{SNR} = \frac{T^2\eta V_{\mathrm{A}}/h}{1 + (T^2\eta\xi + \nu_{\mathrm{el}})/h} \tag{1.29}$$

is the signal-to-noise ratio at Bob's output.

The mutual information as defined in Eq.(1.5) can be computed from entropic arguments [29] and it is directly related to the SNR as:

$$I_{\mathrm{AB}} = \frac{h}{2}\log_2(1 + \mathrm{SNR}) \tag{1.30}$$

Using the formula we just found for the SNR we can write:

$$I_{\mathrm{AB}} = \frac{h}{2}\log_2\left(1 + \frac{T^2\eta V_{\mathrm{A}}}{h + T^2\eta\xi + \nu_{\mathrm{el}}}\right) \tag{1.31}$$

Note that the heterodyne measurement ($h = 2$ instead of $h = 1$) increases the proportionality factor by 2, but it also adds an extra shot noise unit to the excess noise, then decreasing the SNR. This extra shot noise unit comes from the uncertainty relation, since we are measuring two complementary observables at the same time, and so at least a shot noise unit should be paid according to the commutator relation between conjugate quadratures. Hence, the performance of homodyne or hetedoryne measurements are dependent on the specific setup.

Often in the literature, the detector's efficiency is accounted inside the transmission efficiency, $T^2 \rightarrow T^2\eta/h$, and the total noise is accounted in a single parameter, $\sigma^2 = 1 + T^2\xi$,

with the new ξ being $\xi \to \xi + \nu_{\mathrm{el}}/(hT^2)$, so that the expression for the mutual information reduces to:

$$I_{\mathrm{AB}} = \frac{h}{2} \log_2 \left(1 + \frac{T^2 V_{\mathrm{A}}}{\sigma^2}\right) \tag{1.32}$$

Eq.(1.32) constitutes our formula for computing the mutual information in the GG02 protocol, that will be applied in the following Chapter.

Chapter 2

Satellite CVQKD: feasibility study

" We choose to go to the Moon in this decade and do the other things, not because they are easy, but because they are hard"

– John F. Kennedy

Contents

With the tools derived in the previous Chapter, we aim to present a feasibility study of Satellite CVQKD developed during this thesis, that can be also found in the publication [30]. We will describe the scenario of a Satellite QKD link with realistic parameters, in which the channel fluctuations will take a central role, and then derive the secret key rate formula in this case and compute it for different configurations.

2.1   Motivation for a Satellite link

As we outlined in the previous Chapter, a fundamental limitation in the implementation of QKD technologies is extending the communication range in which a secure key rate can be obtained. Nowadays, this communication range has evolved from few centimeters to several hundreds of kilometers with modern technology.

However, the realization of an intercontinental QKD link requires covering thousands of kilometers, which would be impossible, given the most advanced technology, due to the exponential attenuation of the quantum signal in optical fibers, i.e. the exponential growth of losses with distance between terrestrial nodes.

One possible solution is the use of quantum repeaters [17, 18], whose functioning relies on entanglement distribution and in most cases on quantum memories. However, despite progress in the field [31, 32], the technology is still far from being applicable to intercontinental quantum communication.

As remarked in the previous Chapter, another possible solution is the use of orbiting terminals to distribute cryptographic keys among ground stations. Studies investigating the feasibility of quantum communication using satellites have been ongoing for a decade, see for example [33], but a milestone was reached in 2017 with the first complete satellite-to-ground QKD implementations realized with the Chinese satellite Micius [34, 35]. Later the same year, QKD from satellite was also implemented by means of a small payload onboard of the Tiangong-2 space laboratory [36]. Soon after these demonstrations, the Micius satellite was used for the realization of the first intercontinental quantum-secured communication [37], thus opening the era of satellite QKD.

Although these results represent a major step in the field, several issues still need to be addressed for the realization of a global QKD network based on satellite communication. To this end, a possible breakthrough may come from the transition from DVQKD to CVQKD protocols. As mentioned in the previous Chapter, these protocols have the main advantage of using standard telecommunication components, since they typically involve the preparation of coherent states and their coherent detection, therefore allowing to exploit the heritage of classical optical communication both in terms of high-speed components and of their space qualification.

Nonetheless, whether this technology can be used for secret key generation in a realistic satellite-based scenario remains an open question. In this Chapter we aim to shine a light on this by considering the GG02 protocol, together with realistic (state-of-the-art) physical parameters for the atmospheric link and the satellite payload.

2.2 Channel characterization

2.2.1 Channel fluctuations

In a satellite scenario, the channel is a free-space link, ranging from some hundreds to tens of thousands of kilometers. A small part of the distance transverses the atmosphere (effectively around 10 km), where different physical phenomena can occur, like absorption or scattering, as we will see in the following. Through the atmospheric part, the losses scale exponentially with distance, as in fiber protocols. The rest of the channel consists in propagation in empty space, where the light is only subject to diffraction. Since the power of light decreases as

the inverse square of the distance, the losses in this path scale only quadratically, making possible the link with a satellite that is potentially one order of magnitude further away than the best QKD implementation on Earth. In this respect, the initial laser waist dictates the amount of divergence that the light would suffer until it reaches the detector. This waist can be quantified with the emitter's *telescope diameter*, or, equivalently, with the *divergence angle*. The divergence angle, denoted θ_d, is defined as the angle between the beam's center spot and the point where the beam's power is reduced to $1/e^2 \approx 13\%$ (see Fig.(2.1)). As the divergence angle increases, the spot size at the receiver also increases, since the laser waist is $W = S\theta_d$, where S is the distance to the Satellite. We note here that the divergence angle is considered constant along the light's path because we are working with traveling distances way bigger than the Rayleigh length of the laser. We use the nominal value of 10 μrad for the divergence angle in our study, which has been demonstrated with a 30 cm aperture telescope on-board of the Micius satellite [34].

The satellite orbits can be approximately divided into three categories with respect to the distance to the Earth's surface: the Low Earth Orbits (LEO), are the closest orbits to the Earth, at a maximum of around 2000 km from sea level. At LEO orbits, the orbital period are 128 minutes or less (with orbital speeds of the order of 7.5 km/s). The majority of satellites fly at LEO orbits. The next altitude orberts are the Medium Earth Orbits (MEO), between 2000 km and 35786 km, where some satellite constellations are placed, like the GPS or the Galileo constellations. At 35786 km, the orbital period of the satellite coincides with the Earth's rotation period, and hence the satellite appears to be still in the sky from any point on the Earth's surface. These are known as the geosynchronous orbits, or also geostationary (GEO) orbits. Finally, orbits beyond GEO are known as High Earth Orbits (HEO). For GEO orbits, since the satellite is not moving with respect to the ground, the channel fluctuations are reduced. However, geostationary orbits occur at very far radius (35786 km from the Earth's surface), and so the losses are typically too large to obtain a secret key rate. We will then not consider them in our study, although this particular situation is of interest for on-going works in Satellite QKD.

While the channel losses are fixed in a QKD scenario between two ground stations, it is clear that this will not be the case in a Satellite to ground link. The channel is not fixed, mainly due to two factors:

- First of all, the satellite is moving, and therefore the distance between Alice and Bob is a function of time during the state transmission. As the propagation takes place in free-space, there exist an error due to the alignment of the satellite with the ground station, that is known as *pointing error*. This error can be quantified with the angle between the straight line linking the satellite with the ground station, and the real angle of the light emitted by the satellite (see Fig.(2.1)). We will denote this angle as θ_p. A pointing error of the order of 1 μrad has been obtained in LEO satellite-to-ground communication links [34]. This is used as the nominal value in our analysis.

- There are several disturbance effects that occur during beam propagation in the at-

29
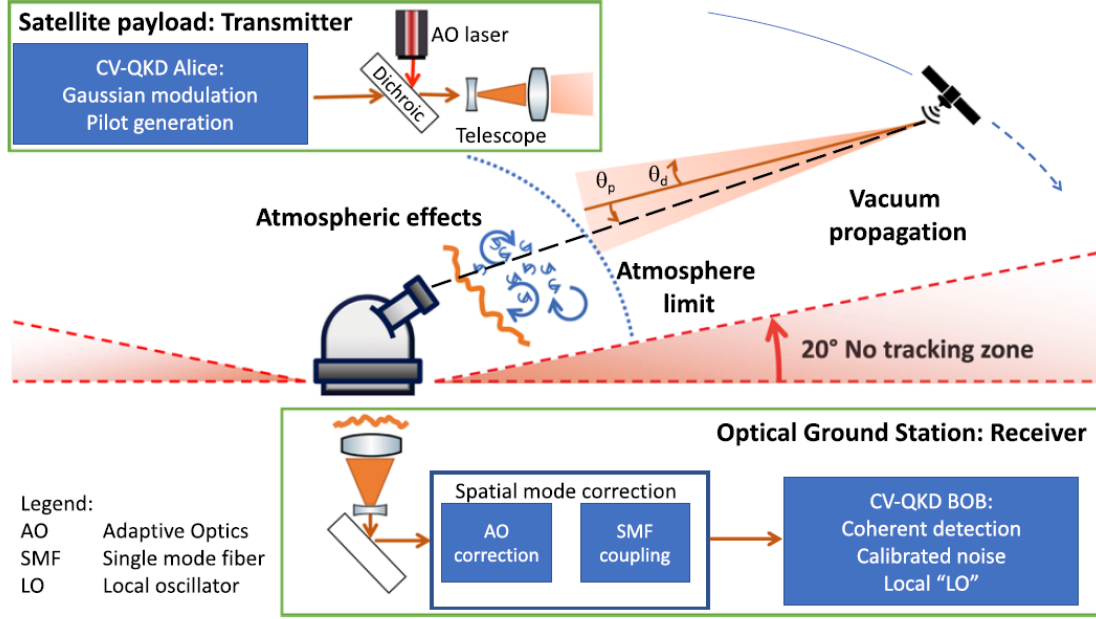
Figure 2.1: Schematic diagram of the CV-QKD communication scheme analyzed in this Chapter. A fixed ground station (Bob) follows the trajectory of a satellite (Alice), equipped with a tracking system, passing over its zenith point. An adaptive optics (AO) system is required in order to correct the wavefront distortions due to the atmosphere and maximize the signal to noise ratio at the receiver. θ_d is the divergence angle, and θ_p is the pointing error.

mosphere, which can be classified as systematic or of random nature.

The systematic effects are theoretically predictable physical processes that perturb and attenuate the signal, and they include the refraction of the beam in the different atmospheric layers and the extinction of light owing to absorption or scattering by air molecules or aerosols. The former is owing to the variation in the optical refractive index of the atmosphere as a function of altitude and it causes the light to deviate from a straight line, resulting in an elongation of its physical path. Reference [38] provides a detailed calculation of the elongation factor (the ratio of the total length of the beam trajectory to the geometric path length) as a function of the apparent elevation angle of the satellite, i.e., the angle with respect to the horizon at which the satellite appears owing to refraction and which differs from the real elevation angle. In this work, we restrict our analysis to elevation angles above 20 degrees, where the elongation factor remains close to 1 and therefore this effect can be neglected . The latter effect, namely extinction owing to absorption and scattering, depends on the link length and on the molecule and aerosol distribution model [38]. It also strongly depends on the sky condition and the transmission wavelength. For elevation angles above 20 degrees, the atmospheric *transmission efficiency* τ_{atm} (which is the square of the atmospheric transmission coefficient), scales as:

$$\tau_{\mathrm{atm}} = \tau_{\mathrm{zen}}^{\mathrm{sec}(\theta_{\mathrm{zen}})} \tag{2.1}$$

where θ_{zen} is the zenith angle and τ_{zen} is the transmission efficiency at zenith [39].

The estimation of the zenith transmission efficiency relies on the MODTRAN code [40], a widely used atmospheric transmittance and radiance simulator. Considering a 1550 nm wavelength, mid-latitude summer atmospheric model with visibility of 23 km (corresponding to clear sky condition), the MODTRAN web app calculator gives $\tau_{\mathrm{zen}} = 0.91$ for both rural and urban aerosol models [41]. We remark that the main parameter that affects the transmission efficiency is the sky *visibility*; in particular, we find $\tau_{\mathrm{zen}} = 0.85,\ 0.75,\ 0.53$ for a 10, 5, 2 km visibility, respectively.

In addition to such systematic effects, random variations in the atmospheric temperature lead to fluctuations in the refractive index that have the statistical properties of turbulent scalar fields. The most important consequence of this *atmospheric turbulence* are intensity fluctuations (scintillation), increased beam wandering and beam broadening, which induce *fading*, namely fluctuations in the received optical power and hence in the transmissivity of the channel. The strength of these effects also depends on the altitude and hence on the elevation angle, as discussed in detail in [38]. The atmospheric turbulence is also responsible for the deformation of the beam profile. This is crucial, especially in the context of CVQKD, where mode matching between the received signal and the phase reference (LO) is important for the coherent detection [42]. To avoid mode mismatch, we assume the use of single-mode fibers as

spatial-mode filters of the incoming beam, together with an advanced adaptive optics system [43] to improve the coupling efficiency of the incoming light into the single-mode fiber core. Acting as a spatial-mode filter, the coupling to a single mode fiber removes components of the signal that would not interact with the LO and contribute to the detected signal. This filtering hence reduces the noise in the detection apparatus and also facilitates the use of components like integrated coherent receivers, which are typically available as commercial off-the-shelf and standardized devices. We remark that recent advances in this field have experimentally demonstrated a coupling efficiency in a single-mode fiber exceeding 50% for a large aperture telescope [44].

Additionally, we will also consider here a *downlink* scenario, with Alice in the satellite, sending the states to Bob, at ground. This is more convenient since the losses in a downlink are smaller with respect to the uplink. The reason is the channel asymmetry with respect to the atmosphere's position. The atmosphere is the main agent of perturbation. In an uplink scenario, the atmosphere affects the light just after the states are sent to the satellite, when the beam starts to diverge, and therefore any deviation would be considerably amplified by the time the light arrives to the receivers in the Satellite. On the other hand, in a downlink scenario, the light is only affected at the end of its path, when the light spot is already bigger than the telescope at Earth, and so the atmospheric effect has a lower impact in the signal. As a consequence, the difference in optical power received (i.e. in losses) between a downlink and an uplink scenario could reach about 20 dB in favor of the downlink, or 100 times less losses.

Without loss of generality, we will consider the satellite trajectory that passes just at the zenith angle with respect to the ground station. Given a satellite, these trajectories are optimal in terms of losses, since the time that the satellite spends in the tracking zone is maximal, and the distance between satellite and ground station is minimal. Generalizing it to any kind of trajectory is also possible. A scheme of the downlink scenario considered is depicted in Fig.(2.1).

2.2.2   Probability Distribution of the Transmission Efficiency

The mathematical function that describes the statistical behavior of the transmission efficiency of our channel, τ, is straightforwardly called the Probability Distribution of the Transmission Efficiency (PDTE). The square root of the transmission efficiency is the channel transmittance, T, used in the previous Chapter of this thesis to derive the mutual information of the CVQKD protocol, Eq.(1.32).

Since our channel has a fluctuating nature, the transmission efficiency τ is a random variable. Here we follow the lines of [45] to calculate the PDTE from first principles.

The situation is depicted in Fig.(2.2) (a). The receiver telescope has an aperture of a, and the light center spot is at a distance r from the center of the telescope and has a waist of W.

Given the definition of the divergence angle θ_d and denoting the distance satellite-ground station as S, we remark that the beam width at the telescope is simply $W = S\theta_d$. For example, in Fig.(2.2) (a), we use $\theta_d = 10$ μrad and $S = 400$ km, which would give a width at the surface of 4 m.

Assuming the beam can be described by a superposition of gaussian beams with different wavenumbers, k, traveling along the $z-$axis, its waveform profile can be written as:

$$U(x, y, z, k) = S(x, y, z, k) \exp(ikz) \tag{2.2}$$

where $S(x, y, z, k)$ is the beam's envelope, that should satisfy the paraxial wave equation from Maxwell's equation.[1]

It can be shown that the envelope solution of the wave equation for a gaussian beam, considering a deflection distance r in the x direction, can be written as:

$$S(x, y, z, k, r) = \sqrt{\frac{2}{\pi W^2}} \exp\left(-\left[\frac{1}{2W^2} - \frac{ik}{2R}\right]\left[(x - r)^2 + y^2\right]\right) \exp(i\Psi) \tag{2.3}$$

where W, R and Ψ are the waist, the radius of curvature and the phase at a distance z. See reference [45] for details of these functions.

Considering the beam travels a distance z_0 from the emitter, the channel transmittance would then be the intensity of the waveform integrated in the joint area between the receiving telescope and the beam at z_0, i.e:

$$T^2(r) = \int\int_A |U(x, y, z_0, k_0, r)|^2 \mathrm{d}x\mathrm{d}y = \int\int_A |S(x, y, z_0, k_0, r)|^2 \mathrm{d}x\mathrm{d}y \tag{2.4}$$

where A is this joined area and we have approximated the superposition of gaussians with wavenumber k to just one gaussian with $k = k_0$. This means we have ignored the signal's spectral width.

Manipulating Eq.(2.4) with Eq.(2.3) and taking into account the geometry of Fig.(2.2) (a), it is possible to write the transmittance in terms of the incomplete Weber integral:

$$T^2(r) = \frac{2}{\pi W^2} e^{-2r^2/W^2} \int_0^a \rho e^{-2\rho^2/W^2} I_0\left(4\frac{r\rho}{W^2}\right) \mathrm{d}\rho \tag{2.5}$$

where ρ is the radial distance from the center of the telescope, and I_0 is the zero-th order modified Bessel function. An approximated solution of this integral is:

$$T^2(r) = T_0^2 \exp\left[-\left(\frac{r}{R}\right)^\lambda\right] \tag{2.6}$$

---

[1]To write this expression, some approximations were assumed, see [45] for the details.

where:

$$T_0^2 = 1 - e^{-l^2/2} \tag{2.7}$$

$$\lambda = 2l^2 \frac{e^{-l^2}\mathrm{I}_1(l^2)}{1 - e^{-l^2}\mathrm{I}_0(l^2)} \left[\log \left(\frac{2T_0}{1 - e^{-l^2}\mathrm{I}_0(l^2)} \right) \right]^{-1} \tag{2.8}$$

$$R = a \left[\log \left(\frac{2T_0}{1 - e^{-l^2}\mathrm{I}_0(l^2)} \right) \right]^{-1/\lambda} \tag{2.9}$$

$$l = 2\frac{a}{W} \tag{2.10}$$

To summarize, we have derived a formula, Eq.(2.6) giving the transmittance as a function of the deflection distance, r, that depends solely on the quotient between the telescope's aperture and the spatial width of the beam, $a/W = a/(S\theta_d)$.[2]

The functional form of Eq.(2.6) is showed in Fig.(2.2) (b) for $a/W = a/(S\theta_d) = 0.1875$.

All the sources of channel fluctuations we have discussed are translated into fluctuations in the deflection distance r. If we assume that the beam fluctuates in the transversal coordinates x and y following a two-dimensional gaussian function centered at the receiving telescope, with variances σ_x^2 and σ_y^2, then the deflection distance $r = \sqrt{x^2 + y^2}$ follows a Weibull distribution with variance σ_r^2:

$$P(r) = \frac{r}{\sigma_r^2} \exp\left(-\left(\frac{r}{\sqrt{2}\sigma_r} \right)^2 \right) \tag{2.11}$$

In Fig.(2.2) (c) we show the behaviour of the probability distribution as a function of r/a.

If we now substitute Eq.(2.6) into the relation between the transmittance and the deflection angle, Eq.(2.11), and use the chain rule, we would find the probability distribution of the transmittance. Given that the transmission efficiency is $\tau = T^2$ we can use once more the chain rule to obtain the probability distribution of the transmission efficiency, the PDTE, depicted in Fig.(2.2) (d).

The variance in Eq.(2.11), σ_r^2, contains the fluctuations in the channel. We consider here the fluctuations due to the pointing error σ_p^2, and the atmospheric turbulence, σ_t^2. Since they are independent phenomena we can write:

$$\sigma_r^2 = \sigma_p^2 + \sigma_t^2 \tag{2.12}$$

The variance due to the pointing error at a distance S is characterized with a pointing angle θ_p and can be written as $\sigma_p = S\theta_p$.

In the weak turbulence regime, the variance due to atmospheric turbulence can be expressed as $\sigma_t \simeq 1.919C_n^2 z^3(2W_0)^{-1/3}$, [46], and depends on the distance traveled by the beam in the atmosphere, z, and on the beam waist when entering the atmosphere, W_0.

---

[2]Note that all variables T_0, R and λ are only functions of a/W.
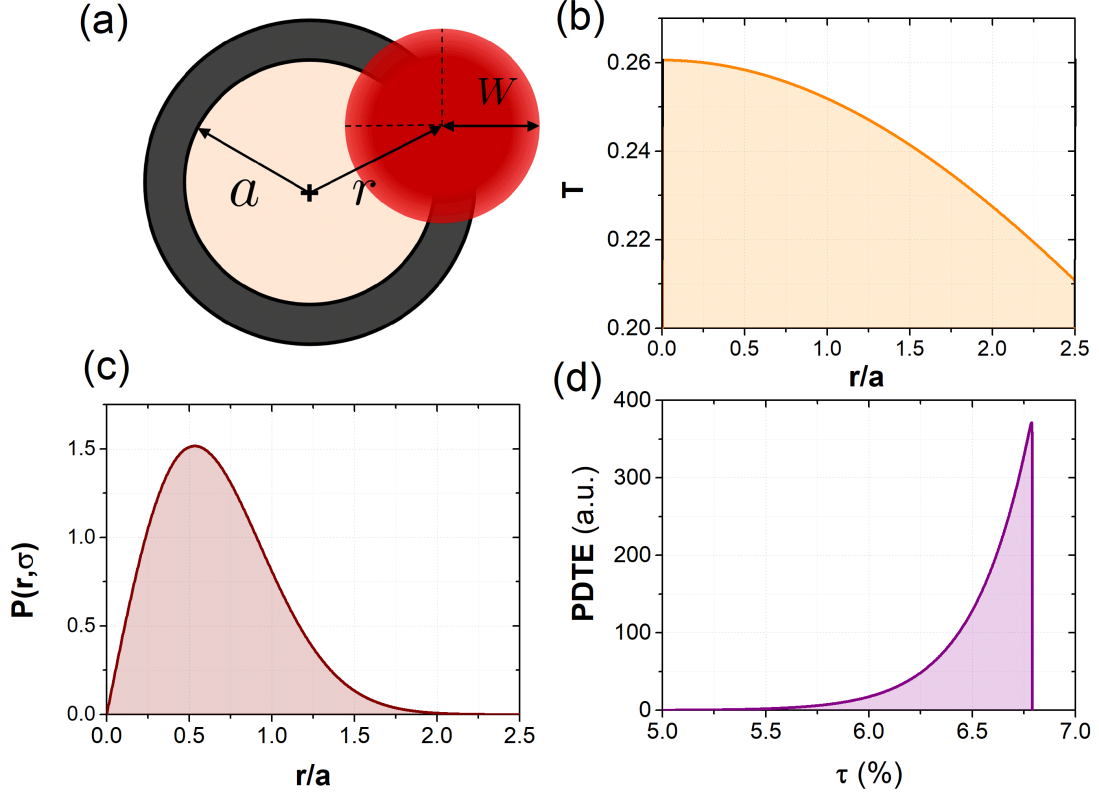
Figure 2.2: Example of the characterization of an atmospheric channel at a fixed satellite-to-ground slant distance of $S = 400$ km. The values for the variables are $\theta_p = 1$ μrad, $\theta_d = 10$ μrad, $a = 0.75$ m. (a) Schematic of the beam and receiver telescope aperture. (b) Transmission coefficient as a function of the deflection distance. (c) Probability distribution of the deflection distance. (d) Probability distribution of the transmission efficiency (PDTE).

For stronger turbulence, this expression represents an upper bound, as σ_t^2 saturates and an increase of the path length or turbulence strength will not increase its value [46]. The parameter C_n^2 is the *refractive index structure* parameter that characterizes the strength of the atmospheric turbulence. In case of moderate turbulence and considering a wavelength of 1550 nm, we have $C_n^2 \simeq (10^{-14} - 10^{-15})$ m$^{2/3}$. In addition, considering the length of the atmosphere to be around 10 to 15 km, and the beam waist coming from a divergence angle of $\theta_d = 10$ μrad, the variance due to turbulence would be maximum of the order of 10^{-4} m^2. Since a pointing error of $\theta_p = 1$ μrad gives a pointing error of the order of 10^{-1} m^2 for a satellite altitude of 300 km and it increases with the altitude, then:

$$\sigma_t^2 << \sigma_p^2 \tag{2.13}$$

therefore, under weak turbulence effects and in our realistic configuration, we see that the pointing error dominates over the turbulence. Hence:

$$\sigma_r^2 \simeq \sigma_p^2 \tag{2.14}$$

The PDTE shown in Fig.(2.2) (d) characterizes the atmospheric link for a fixed satellite-ground station distance, S. During the CVQKD protocol, though, the satellite follows a trajectory with respect to the ground station that can be calculated from the satellite's orbit equation. We therefore need to account for the whole satellite's orbit in order to compute the total PDTE in a satellite pass.

In order to do that, we consider circular orbits that are passing at the zenith of the ground station. We can write the radius of such orbits as $R_O = R_T + h_s$, were R_T is the Earth's radius and h_s the Satellite's altitude with respect to the ground. The angular velocity of the Satellite is then $\omega^2 = GM_T/R_O^3$, where M_T is the Earth's mass and G is the gravitational constant. From the ground station point of view, the satellite's distance during the its visibility time (when the Satellite can be seen at least at 20 degrees from the horizon), is:

$$R(t) = \sqrt{R_T^2 + R_O^2 - 2R_T R_O \cos(\omega t)} \tag{2.15}$$

We then proceed as follows:

☐ The orbit is divided into a set of points defined by the position of the satellite at a certain time, $R(t_i)$ (i runs with the number of points), given by the orbital equation, Eq. (2.15).

☐ For each one of these points, both the PDTE($R(t_i)$) and the time difference between consecutive points of the orbit, denoted $\Delta t_i = t_i - t_{i-1}$, are computed. The PDTE($R(t_i)$) includes as a multiplicative factor the atmospheric transmission efficiency, Eq.(2.1), for the elevation angle corresponding to $R(t_i)$. The value PDTE($R(t_i)$)Δt_i gives the distribution of the times with different transmission efficiencies inside the computed interval.
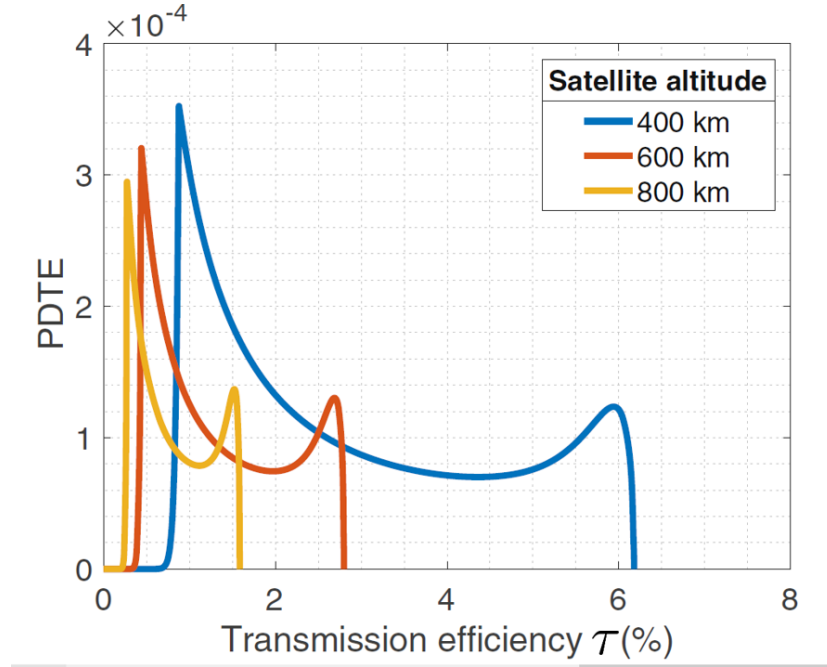
Figure 2.3: PDTE for three different orbits of increasing satellite altitude. The values of the variables for each orbit are the same as in Fig.(2.2).

□ Therefore, if we sum PDTE·Δt_i over all the points we obtain the final distribution for the time spent by the satellite with a certain transmission efficiency, τ. Indeed, we are mimicking the integral over the flight time, FT:

$$\frac{1}{\text{FT}} \sum_i \text{PDTE}(\tau, R(t_i))\Delta t_i \longrightarrow \frac{1}{\text{FT}} \int \text{PDTE}(\tau, t)\mathrm{d}t \qquad (2.16)$$

Because we are considering circular orbits, we can label each orbit with its *altitude*, which is the distance satellite-Earth, and that hence coincides with the distance satellite-ground station when the satellite is exactly above the ground station. For such orbits and following the procedure described above, we show in Fig.(2.3) the PDTE for three different orbits of increasing altitude for a telescope with aperture radius $a = 0.75$ m. We remark that for higher orbits the variance of the distribution decreases, as well as the mean value of the transmission efficiency. The intuitive idea behind this fact is that as the satellite's altitude is higher, the losses due to divergence increases, decreasing the mean transmission. At the same time, the beam width at the receiver telescope is bigger, and, from Eq.(2.6), the transmission is flatter with the deflection distance, i.e. there are less variance in the values of T, which finally translates in having a smaller variance in the PDTE. As described in the following, this fact has an impact on the noise introduced in time-varying channels.
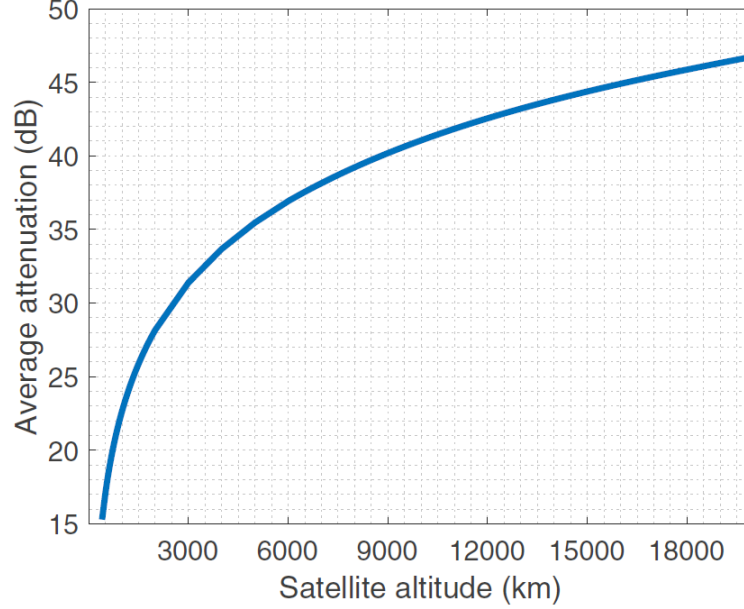
Figure 2.4: Average attenuation per pass as a function of satellite altitude.

For completeness, we show in Fig.(2.4) the average attenuation of a satellite pass as a function of satellite orbit.

2.3   Key rate in a fluctuating channel

One of the questions that arose when preparing this work is how to calculate the secure key rate over a fluctuating (also known as fading) channel. We considered the GG02 protocol with heterodyne detection described in the previous chapter. This theoretical derivation was done by our collaborator Anthony Leverrier.

For this purpose, recalling Eq.(1.6) from Chapter 1, we need to compute the mutual information I_{AB} and the Holevo bound χ_{EB} over a channel whose transmission efficiency fluctuates following the probability distribution of Fig.(2.3).

It is important to understand how fast the fading process is. The main idea here is that this process, whose timescale is typically of the order of 1–10 ms owing to atmospheric turbulence, is much faster than the time needed to distill a secret key, which in our case corresponds to a complete satellite pass. In other words, the channel transmission coefficient fluctuates significantly over N uses of the channel, but this coefficient is relatively stable over consecutive uses of the channel, which occur with ns separation. As a consequence, Alice and Bob can exploit classical signals to roughly monitor the current transmission value of the channel and adapt their error correction procedure accordingly. This implies

notably that for the error correction procedure, we can assume that Alice and Bob know (approximately) the value of T for every k-th use of the channel (for every symbol sent from Alice to Bob). This allows them to use good error-correcting techniques developed for the fading channel where the fading process is known to the receiver. We can therefore compute the mutual information as an average of the usual I_{AB} over the PDTE. That is to say, we can take the expectation value of Eq.(1.32) for the mutual information:

$$I_{\text{AB}} = \left\langle \log_2 \left(1 + \frac{T^2 V_A}{\sigma^2} \right) \right\rangle_{\text{PDTE}} \tag{2.17}$$

On the other hand, the Holevo bound can be estimated with the covariance matrix calculated in the entanglement-based protocol. The covariance matrix is a matrix containing the variances of the quadratures operators of a given quantum optics state in its diagonal entries, and the covariances between quadratures in its non-diagonal entries. The covariance matrix, here denoted Γ, completely describes any gaussian quantum state, like the ones typically considered in CVQKD (coherent or squeezed states).

The Holevo bound is a function of the covariance matrix as [47, 48]:

$$f(\Gamma) = g(\nu_1) + g(\nu_2) - g(\nu_3) - g(\nu_4) \tag{2.18}$$

where g is an entropic function of the form:

$$g(x) = \frac{x+1}{2} \log_2 \left(\frac{x+1}{2} \right) - \frac{x-1}{2} \log_2 \left(\frac{x-1}{2} \right) \tag{2.19}$$

and ν_i, $i = \{1, 4\}$ are known as the symplectic eigenvalues [49] of the covariance matrix, Γ.

In the entanglement-based version of the protocol, the covariance matrix of the bipartite state shared by Alice and Bob can be written as:

$$\Gamma(T) = \begin{pmatrix} V\mathbb{I}_2 & \sqrt{T}\sqrt{V^2 - 1}\sigma_z \\ \sqrt{T}\sqrt{V^2 - 1}\sigma_z & (T(V-1) + \xi)\mathbb{I}_2 \end{pmatrix} \tag{2.20}$$

where $V = V_A + 1$, $\mathbb{I}_2$ is the two-dimensional identity matrix and σ_z is a the Pauli z matrix, $\sigma_z = \text{diag}(1, -1)$.

As observed in [48], when the fluctuation of the transmission efficiency is considered, the resulting state is a mixture of the individual fixed-transmission states, giving an overall covariance matrix equal to:

$$\Gamma = \langle \Gamma(T) \rangle = \begin{pmatrix} V\mathbb{I}_2 & \langle\sqrt{T}\rangle \sqrt{V^2 - 1}\sigma_z \\ \langle\sqrt{T}\rangle \sqrt{V^2 - 1}\sigma_z & (\langle T \rangle (V-1) + \xi)\mathbb{I}_2 \end{pmatrix} \tag{2.21}$$

Comparing the covariance entries for the fixed channel, Eq. (2.20) and the fluctuating channel, Eq.(2.21), we can identify an effective transmission for the fading channel equal to $\langle T \rangle$. In particular, the variance of Bob's system can be written:

$$\langle T \rangle (V^2 - 1) + \xi = \langle\sqrt{T}\rangle^2 (V^2 - 1 + \xi_f) + \xi \tag{2.22}$$

where we have defined an extra excess noise due to the fact that the channel is fluctuating, ξ_f, apart from the excess noise from a fixed channel, ξ:

$$\xi_f = \frac{\langle T \rangle - \left\langle \sqrt{T} \right\rangle^2}{\left\langle \sqrt{T} \right\rangle^2}(V^2 - 1) \tag{2.23}$$

In other words, Eve's information in the presence of fading corresponds to her information for a fixed Gaussian channel with transmission efficiency $\left\langle \sqrt{T} \right\rangle^2$ and an added noise given by $\frac{\langle T \rangle - \left\langle \sqrt{T} \right\rangle^2}{\left\langle \sqrt{T} \right\rangle^2}(V^2 - 1)$. This extra noise will be detrimental to the performance of the QKD system unless $\langle T \rangle - \left\langle \sqrt{T} \right\rangle^2 << \frac{1}{V-1}$. By re-writing the fading case as a fixed case with an effective transmission efficiency and excess noise, it is possible to calculate the symplectic eigenvalues of Eq.(2.18) using reference [50].

To summarize, the equation for the key rate in a fluctuating channel, that is secure against collective attacks in the asymptotic limit is:

$$K_f = \beta \left\langle \log_2 \left(1 + \frac{T^2 V_{\mathrm{A}}}{\sigma^2}\right) \right\rangle_{\mathrm{PDTE}} - f\left(\langle \Gamma(T) \rangle_{\mathrm{PDTE}}\right) \tag{2.24}$$

that is the secure key rate formula used in the results of the next section.

2.4 Key rate in Satellite CVQKD

2.4.1 Asymptotic key

We are now ready to use the results derived above to estimate the expected key rate achievable for a satellite-to-ground CV-QKD link under our assumptions. To properly account for the expected noise, we include in our modeling the noise contribution related to the phase recovery between the signals generated by Alice and measured by Bob. The technique that we consider here has been proposed in [51, 52] and consists in sending periodic reference symbols (pilots) along with the quantum signal. At the receiver side, Bob uses a free running LO, which must be tuned to compensate for the Doppler frequency shift introduced by the satellite motion, to measure both the pilot and the quantum signals, in a so-called "local" LO configuration. Two noise contributions arise from this technique, which are due to laser instability and shot noise.

We remark that at telecom wavelength, the Doppler shift ranges from several GHz for LEO to several hundreds of MHz for MEO [53]. This problem is well known in classical laser communication and several solutions have been proposed, such as optical [54] or digital [55] phase-locked loops. With these techniques, it is possible to achieve an a posteriori determination of the satellite velocity with a precision of <1 mm/s, which would correspond

Parameter	Symbol	Reference Value
Pointing Error	θ_p	1 μrad
Divergence Angle	θ_d	10 μrad
Fixed Attenuation	Att	3.8 dB
Zenith Transmittance	τ_z	0.91
Electronic Noise	ν_{el}	10% S.N.U.
Detection Efficiency	η	0.4
Fixed Excess Noise	ξ	1-5 % S.N.U.
Classical beacon symbol energy	E_{ref}	0.1 nJ
Reconciliation Efficiency	β	0.95
Transmission symbol rate	f_R	1 Gsymbol/s
Receiving Telescope Radius	a	0.75 m

Table 2.1: Summary of the main simulation parameters used in our study, together with their reference values.

to a residual frequency shift of <1 kHz [56]. Moreover, in the case of "local" LO CV-QKD, an alternative solution is to exploit the pilots to measure the residual Doppler shift.

According to the previous section in this chapter, the overall excess noise is composed by the the fading noise and an additional fixed contribution owing to experimental imperfections, which includes all other possible sources of noise contribution.

Table 2.1 summarizes the main experimental parameters that influence the key rate generation , together with their reference values, which represent a high-performance satellite optical communication system. A detailed analysis of the effect of individual parameters on the key rate is given in Appendix A.

We remark that in our simulations, the signal variance V_A is optimized over the key rate for every satellite orbit. Recall that a big signal variance (or equivalently a greater number of photons per symbol sent by Alice) implies an increasing mutual information, but also an increase in the Holevo bound. Intuitively, this is because an intense signal increases the signal to noise ratio at Bob's, but also increases the amount of information that can be leaked to an eavesdropper. The optimized values of V_A in our study are in general between 2 and 4 shot noise units (S.N.U.), depending on the specific orbit.

In Fig.(2.5) we show the fading noise given by the PDTE that we obtain for orbits going from 400 km to 22000 km. As we see, an increase of the noise is present for LEO orbits, since the variance of the channel transmission is bigger for closer orbits, as discussed above and seen in Fig.(2.3). Moreover, it is worth noting that when the pointing error is much smaller than the beam divergence, the fading effect is mainly due to the variation on the satellite distance.

Binning:
To reduce the effect of fading excess noise, a natural strategy is to reduce the variance of the
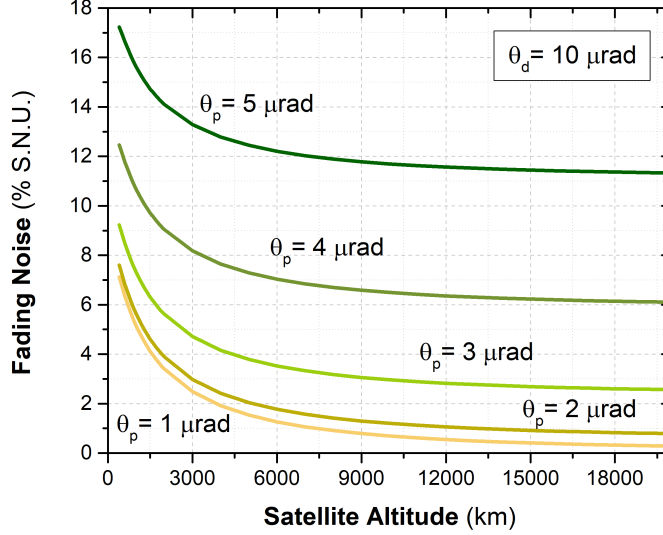
Figure 2.5: Fading excess noise trend, ξ_f, in percentage of the shot noise units, as a function of the satellite altitude for several values of pointing error and a fixed value of the divergence angle.

transmission efficiency. This can be achieved as follows: Alice and Bob can approximately monitor the value of the transmission efficiency of the channel, seen by the quantum symbols τ_k, by multiplexing in some degree of freedom an intense optical signal that serves as beacon and experiences a transmission efficiency τ_b. An intensity detection of the beacon at Bob's, sampled at rates higher than the atmospheric coherence time (typically 1 kHz), can provide an accurate estimation of the channel transmittance evolution with time $\tau_b(t)$. This information can be used to classify the detected quantum symbols in groups as a function of the expected transmittance so that for each group g the PDTE is reduced to a transmittance interval $\mathrm{PDTE}(g)$ for which the contribution of the fading is less detrimental. The CVQKD protocol can be performed independently for each of these groups to obtain a secret key rate per symbol $K_f(\mathrm{PDTE}(g))$ and an aggregated secret key rate per symbol of:

$$K_{\mathrm{agg}} = P(\tau \in \mathrm{PDTE}(g)) K_f(\mathrm{PDTE}(g)) \tag{2.25}$$

This technique is known as *binning*.

It is clear that in order to reduce the effect of fading, narrow PDTE intervals are desirable, but this can magnify finite-size effects[3], since the number of symbols per group will be reduced. This compromise between PDTE interval width and the number of symbols per

---

[3]Recall that our key rate formula assumes an infinite amount of symbols transmitted from Alice to Bob.
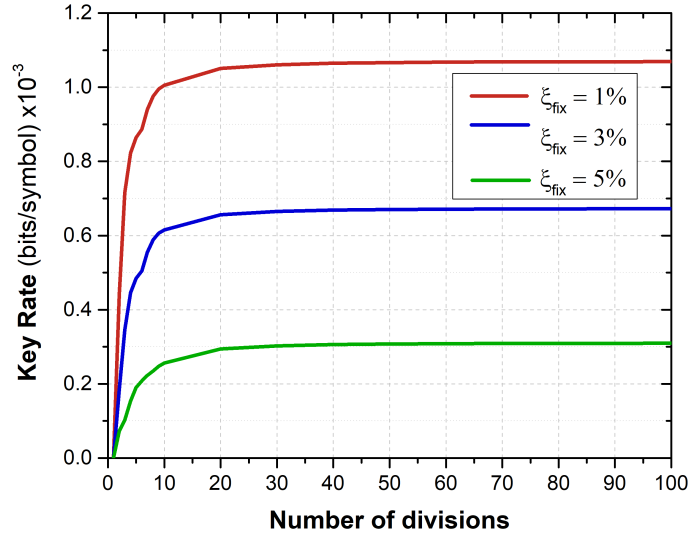
Figure 2.6: Asymptotic key rate vs group factor. Secret key rate for channel subdivision from 1 to 100 equally spaced intervals for a 400 km altitude satellite. The fixed excess noise, ξ, is, in S.N.U, 1 % (red), 3% (blue) and 5% (green), respectively.

group can be taken into account in order to optimize the division of the PDTE so that K_{agg} is maximal for a given PDTE and orbit duration.

In our analysis, we chose a uniform division of the PDTE, hence dividing the whole range of transmission values in equally spaced intervals, going from a single group (corresponding to analyzing the data altogether) to 100 intervals (i.e., close to the asymptotic limit). The results are reported in Fig.(2.6) for a satellite at 400 km and for three values of fixed excess noise. We note that without channel subdivision no key would be possible for a 400 km orbit due to the fluctuations of the channel. To analyze the effect of the channel subdivision for all the orbits, we selected subdivisions of 3, 10, and 100 intervals for all the satellite altitudes. As shown in Fig. 2.7, the division of the channel transmission efficiency in 10 groups gives a total rate close to the asymptotic limit for all satellite altitudes. We underline that for this simulation the same values of beam divergence and pointing error have been used in all cases, to emphasize the impact of the orbit altitude on the key generation rate. However, owing to the different satellite size and environmental disturbance, MEO satellites could in general reach better performance in terms of beam quality.

We note here that Fig.(2.7) constitutes the main result of this work, since it states clearly the feasibility of performing the GG02 CVQKD protocol in the conditions discussed in this chapter, justifying the implementation of Satellite CVQKD.
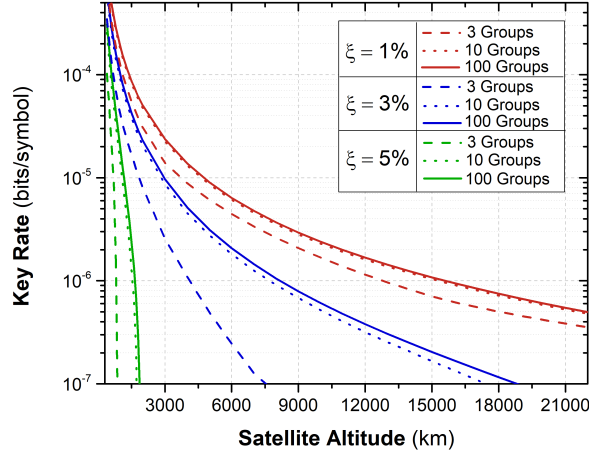
Figure 2.7: Asymptotic key rate vs satellite altitude. Secret key rate for channel subdivision in 3, 10, and 100 groups and different values of the fixed excess noise, ξ: (in S.N.U), 1% (red), 3% (blue), and 5%(green). The key rate in bits/s can be calculated by multiplying by the transmission symbol rate.

2.4.2 Finite key

For completeness, it is worth modifying the statistics of the parameters for accounting possible finite size effects due to the limited amount of symbols transmitted from Alice to Bob. It is worth noting that in satellite communication the maximum amount of time for transmission is given by the orbital parameters and can range from a few minutes to hours, depending on the satellite altitude. As the satellite altitude increases, the amount of time the satellite is in the tracking zone of the ground station also increases, and the channel transmission variance decreases. Both of these effects make the finite size effects to be reduced. The problem of finite size effects is hence important when considering LEO orbits. If also a highly dense subdivision of the channel transmission efficiency is desired in order to mitigate the fading effects, the number of symbols per group will decrease, increasing the finite size effects.

Following [57], it is possible to account for finite size effects by considering a lower bound on the transmission coefficient $T = \sqrt{\tau}$ and an upper bound of the parameter $\sigma^2 = 1 + \tau\xi$:

$$T_{\min} \simeq \sqrt{\tau} + z_{\epsilon_{\mathrm{PE}/2}} \sqrt{\frac{1 + \tau\xi}{mV_A}} \tag{2.26}$$

$$\sigma^2_{\max} \simeq 1 + \tau\xi + z_{\epsilon_{\mathrm{PE}/2}} \frac{(1 + \tau\xi)\sqrt{2}}{\sqrt{m}} \tag{2.27}$$
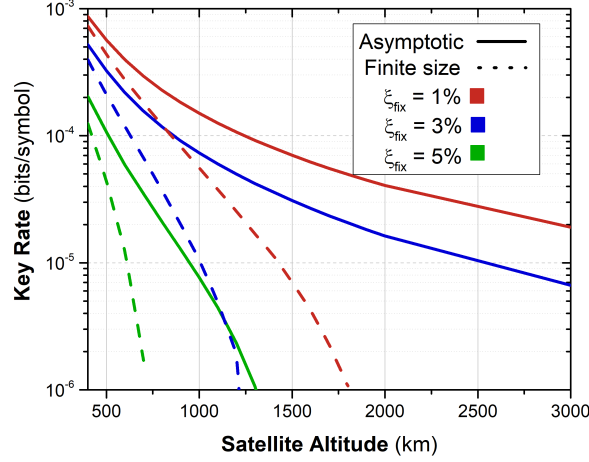
44

Figure 2.8: Finite-size vs asymptotic key rate. Comparison of the key rate for LEO between the asymptotic regime (solid line) and considering finite-size effects (dashed line), which have been calculated for a symbol rate of 1 Gsymbol/s. The fixed excess noise, ξ, is 1% (red), 3% (blue) 5% (green).

where m is the number of symbols used for parameter estimation and $z_{\epsilon_{\mathrm{PE}/2}}$ is a parameter related to the failing probability of the parameter estimation, denoted ϵ_{PE}. Here we consider $\epsilon_{\mathrm{PE}} = 10^{-10}$ which gives $z_{\epsilon_{\mathrm{PE}/2}} = \sqrt{2}\mathrm{erf}^{-1}(1 - \epsilon_{\mathrm{PE}}) = 6.5$, where erf^{-1} is the inverse error function.

The results for the given parameters are shown in Fig. (2.8) and highlight how the finite-size effects have a remarkable impact on higher orbits, effectively precluding CV-QKD operation beyond 2000 km when the key distillation is performed on a single satellite pass. For lower orbits, below 800 km, the effect is only limited to a drop in the key rate. The finite-size effects could be reduced by increasing the transmission rate and optimizing the orbit subdivision, as well as accumulating multiple satellite passes.

2.5 Conclusions about the Feasibility study

To summarize the this Chapter, we presented a study analyzing the feasibility of CV-QKD from a satellite to a ground station. First we characterized the transmission channel by calculating the Probability Distribution of the Transmission Efficiency, taking into account realistic values for pointing error, divergence angle, and considering favorable atmospheric turbulence conditions. We then integrated the satellite orbit to obtain the PDTE of the whole satellite pass. We calculated the secret key formula in the asymptotic case, taking into account the fluctuating nature of the channel, and identified an extra excess noise in

this case that is related to the variance in the PDTE, i.e. in the strength of these fluctuations. Using the PDTE and the key rate formula, we computed the secret key for different satellite altitudes. To cope with channel fluctuations, we proposed a method of data analysis based on orbit subdivision and proved its effectiveness in improving secret key generation. This subdivision makes the finite size effects to become important in some cases, so we modified the secret rate formula for taking them into account for our analysis.

The simulations provide an estimate of the expected key rate of satellite-to-ground CV-QKD and allows to constraint of the experimental parameters for its realization. The obtained results show that coherent state modulation and detection is a viable option for quantum communication with LEO satellites. The communication with higher orbits, achievable in the asymptotic limit, can be affected by finite-size effects if the transmission rate is low or the orbit subdivision is not optimized. We note however that by merging multiple satellite passes, or with the implementation of higher repetition rate systems, it would be possible to extend the communication range beyond 2000 km.

Part II

Continuous Variable Graph States at Telecom Wavelengths via Non-linear Waveguides

Chapter 3

Ultrashort Light Pulses in Linear Media

"If you want to find the secrets of the Universe, think in terms of energy, frequency, and vibration. "

– Nikola Tesla

Contents

This Chapter introduces concepts from classical optics that will serve as theoretical and experimental tools for the experiment performed during this thesis. In particular, we will develop a modal analysis of the electromagnetic field, that is, we will find solutions to Maxwell's equations, defined in a base of electromagnetic modes, in the case of a linear, isotropic and homogeneous medium. The resulting spatial and temporal modes are able to describe the ultrashort pulses of light that we aim to manipulate in the laboratory.

Then, we will apply the theoretical concepts to show the experimental characterization of our laser source (that is a broadband pulsed source in the femtosecond regime, at telecom

wavelengths). To finish the Chapter, we will provide the experimental tools that we will need for pulse manipulation, namely the pulse compressor and the pulse shaper, and their characterization in the laboratory.

3.1 The Wave Equation

We define a *mode* of the electromagnetic field as a spatio-temporal vector function $\boldsymbol{u}(\boldsymbol{r}, t)$ that is a normalized solution to Maxwell's equations [58]. A set of modes $\{\boldsymbol{u}_m(\boldsymbol{r}, t)\}$, with m an integer number, can form an orthogonal basis, so that any electric field $\boldsymbol{E}(\boldsymbol{r}, t)$ can be written as a linear superposition of the family modes with different weights:

$$\boldsymbol{E}(\boldsymbol{r}, t) = \sum_m \mathcal{E}_m \boldsymbol{u}_m(\boldsymbol{r}, t) \tag{3.1}$$

with $\mathcal{E}_m$ the electric field value associated with the m-th mode.

In this Chapter, we are concerned with the modal solutions to Maxwell's equations in the context of a linear, homogeneous and isotropic medium, while in the next Chapter, we will consider the case of non-linear media.

We write Maxwell's equations for a linear, isotropic and dielectric media, in the absence of charges, with scalar electric permitivity ϵ and magnetic permeability μ_0, and in terms of electric and magnetic fields, $\boldsymbol{E}(\boldsymbol{r}, t)$ and $\boldsymbol{H}(\boldsymbol{r}, t)$, as:

$$\nabla \cdot \boldsymbol{E}(\boldsymbol{r}, t) = 0 \qquad\qquad \nabla \cdot \boldsymbol{H}(\boldsymbol{r}, t) = 0 \tag{3.2}$$

$$\nabla \times \boldsymbol{E}(\boldsymbol{r}, t) = -\mu \frac{\partial \boldsymbol{H}(\boldsymbol{r}, t)}{\partial t} \qquad\qquad \nabla \times \boldsymbol{H} = \epsilon \frac{\partial \boldsymbol{E}(\boldsymbol{r}, t)}{\partial t} \tag{3.3}$$

Using the vector identity and the first equation we have that $\nabla \times \nabla \times \boldsymbol{E} = \nabla(\nabla \cdot \boldsymbol{E}) - \nabla^2 \boldsymbol{E} = -\nabla^2 \boldsymbol{E}$. Adding further the Maxwell equation for the curl of $\boldsymbol{E}$, we arrive to the equation:

$$\nabla^2 \boldsymbol{E}(\boldsymbol{r}, t) + \frac{1}{c^2} \frac{\partial^2 \boldsymbol{E}(\boldsymbol{r}, t)}{\partial t^2} = 0 \tag{3.4}$$

which is known as the *Wave Equation* [59] (there is an identical equation for the magnetic field $\boldsymbol{H}$). Here, c is the speed of light in the medium, $c = 1/\sqrt{\mu_0 \epsilon}$. By use of Eq.(3.1), it is clear that any modal component of the electric or magnetic field, that we denote here just as $u_m(\boldsymbol{r}, t)$, also follows the wave equation:

$$\nabla^2 u_m(\boldsymbol{r}, t) + \frac{1}{c^2} \frac{\partial^2 u_m(\boldsymbol{r}, t)}{\partial t^2} = 0 \tag{3.5}$$

This equation is at the heart of the rest of this Chapter, since its solution in different physical contexts and boundary conditions provides the framework to write the spatio-temporal modes describing the ultrashort pulses of light that we will manipulate in the laboratory.

3.2 Spatial Modes: the Hermite-Gauss Beam

We first investigate the spatial solutions of the Wave equation. To this end, let's write the electric and magnetic field modes in terms of a complex amplitude in the form:

$$u_m(\boldsymbol{r}, t) = \text{Re}[U_m(\boldsymbol{r}) \exp(i\omega t)] \tag{3.6}$$

that is to say, we are reducing for now the temporal part to a monochromatic plane wave of frequency ω. This assumption will be relaxed later in this Chapter.

Substituting Eq.(3.6) into Eq.(3.5) it is easy to arrive to:

$$\nabla^2 U_m(\boldsymbol{r}) + k^2 U_m(\boldsymbol{r}) = 0 \tag{3.7}$$

where $k = \omega/c = 2\pi/\lambda$ is the *wavevector*, (λ being the *wavelength*). Eq.3.7 is known as the *Helmholtz equation.*

As we are going to consider waves propagating in a certain direction, we now write the solutions to the Helmholtz equation in the form of a plane wave propagating along z and modulated by a complex envelope $A_m(\boldsymbol{r})$:

$$U_m(\boldsymbol{r}) = A_m(\boldsymbol{r}) \exp(-ikz) \tag{3.8}$$

If we assume that the complex envelope, $A_m(\boldsymbol{r})$, varies slowly within a wavelength step, λ, then it follows that:

$$\frac{\partial A_m(\boldsymbol{r})}{\partial z} << k A_m(\boldsymbol{r}) \Rightarrow \frac{\partial^2 A_m(\boldsymbol{r})}{\partial z^2} << k^2 A_m(\boldsymbol{r}) \tag{3.9}$$

which is known as the *paraxial approximation.* By substituing Eq.(3.8) into Eq.(3.7) and neglecting the $\partial^2 A_m(\boldsymbol{r})/\partial z^2$ by virtue of the paraxial approximation, one arrives to the so-called *paraxial Helmholtz equation*:

$$\nabla_\perp^2 A_m(\boldsymbol{r}) - 2ik \frac{\partial A_m(\boldsymbol{r})}{\partial z} = 0 \tag{3.10}$$

where $\nabla_\perp = (\frac{\partial}{\partial x}, \frac{\partial}{\partial y}, 0)$ is a transversal differential operator. The solutions to this equation are the so-called *paraxial waves* [60]. Paraxial waves are waves in which the wavefront normals are paraxial rays, i.e. they follow the optic axis with small angle deviations.

It can be shown, [60], that the family of *Hermite-Gauss functions*, that will appear recurrently in this manuscript, is a complete set of solutions to the paraxial Helmholtz equation. This means that any solution of Eq.(3.10), and hence any paraxial wave, can be expressed as a linear superposition of different Hermite-gauss functions. Since they obey Maxwell's equations, these functions constitute a set of *spatial modes* of the electromagnetic field. They
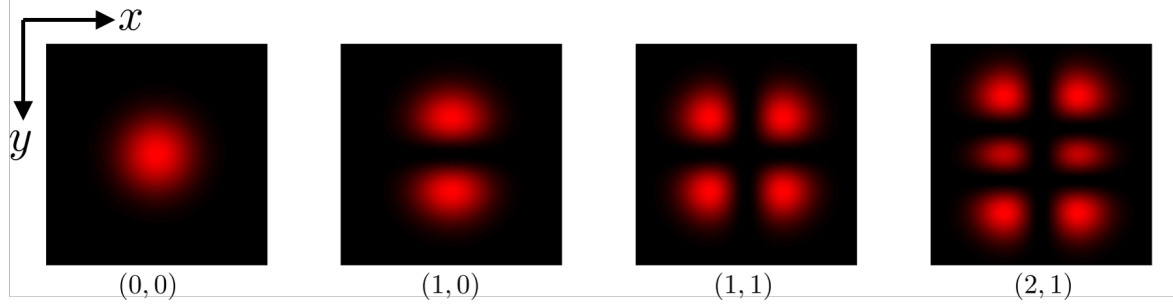
Figure 3.1: Spatial intensity profile of some beams in pure Hermite-gauss modes. The numbers refer to the respectives mode orders (l, n).

can be explicitly written as:

$$
A_{ln}(x, y, z) = \left(\frac{W_0}{W(z)} \right) \text{HG}_l \left(\frac{\sqrt{2}x}{W(z)} \right) \text{HG}_n \left(\frac{\sqrt{2}y}{W(z)} \right)
$$
$$
\exp \left(-ik \frac{x^2 + y^2}{2R(z)} + i(l + n + 1) \tan^{-1}(z/z_0) \right)
\tag{3.11}
$$

where the modal subscripts $l, n = 0, 1, 2...$, that we denoted until here with a single subscript m, are known as the *mode orders*, are used to label the family of Hermite-Gauss functions $\text{HG}_{l/n}(x)$. Here, z_0 is the *Rayleigh length*, W_0 is the *beam waist*, and the functions $W(z)$ and $R(z)$ are the beam waist and the beam *radius of curvature* at position z. They are defined as:

$$
W(z) = W_0 \sqrt{1 + \left(\frac{z}{z_0} \right)^2}
\tag{3.12}
$$

$$
R(z) = z \left[1 + \left(\frac{z_0}{z} \right)^2 \right]
\tag{3.13}
$$

where the beam waist W_0 is related to the Rayleigh length z_0 via the wavelength, λ, as $z_0 = \pi W_0^2 / \lambda$.

The Hermite-Gauss functions are defined here as:

$$
\text{HG}_l(x) = \frac{1}{\sqrt{\pi 2^{l+1} l!}} H_l(x) \exp \left(-x^2 / 2 \right)
\tag{3.14}
$$

and $H_l(x)$ is the l-th order Hermite polynomial.

The spatial intensity of the field can be obtained from $|U_{ln}(\boldsymbol{r})|^2 = |A_{ln}(\boldsymbol{r})|^2$ from Eq.(3.8). An example of different field intensities in the transversal plane to the propagation direction z, for pure Hermite-gauss spatial modes, is depicted in Fig.(3.1).

The first Hermite-gauss mode, of order ($l = 0, n = 0$), is a two-dimensional gaussian function with the same width in both transversal directions x and y. This solution is known as the *gaussian beam*, and it is the most relevant in the context of this thesis, since it is approximately the spatial mode provided by current cavity-based laser sources, including ours, as we will characterize later in this Chapter.

The description of a gaussian beam propagating in a certain direction is therefore complete with two parameters among (W_0, λ, z_0), from which the beam waist, the intensity profile and the radius of curvature at any given point can be calculated. More explicitly, we can plug Eq.(3.11) with $l = n = 0$ into Eq.(3.8) and obtain the explicit paraxial spatial mode for the gaussian beam:

$$U_0(x, y, z) = \left(\frac{W_0}{2\pi W(z)} \right) e^{- \frac{x^2+y^2}{W^2(z)}} e^{-ik\left(\frac{x^2+y^2}{2R(z)} + z + \tan^{-1} \frac{z}{z_0} \right)} \tag{3.15}$$

which is completely defined by z_0 and $\lambda = \pi W_0^2 / z_0$. The description of the gaussian beam that we have just derived, together with the transformation of the gaussian beam waist and Rayleigh length through a thin lens (that will be shown later in this Chapter), will serve as our experimental tool for controlling the spatial properties of our light pulses in the laboratory.

3.3 Temporal Modes: Ultrafast Optics

Until now we have only considered the spatial characteristics of the electromagnetic field, assuming a temporal dependence of $\exp(i\omega t)$ in Eq.(3.6) that can be approximately accomplished by Continuous Wave (CW) laser sources. However, there are two main reasons why the use of pulsed laser sources is needed in our context. First of all, our experiment will be based on the nature of the temporal modes of the light field, rather than the spatial ones, since we will encode the quantum information into those modes. The pulses of light guarantee optical power to be shared between different wavelengths by virtue of the Fourier transform, which implies a frequency broadband spectrum. Secondly, as we will derive in the next Chapter, one of the constraints for producing considerable non-linear optical effects is high field amplitudes. Compared to the CW case, in pulsed lasers the mean optical energy is condensated into the short pulses, and hence the optical peak powers are high enough to produce measurable non-linear effects both in bulk crystals and waveguide structures.

3.3.1 Decoupling of the spatial and temporal degrees of freedom

As we are now dealing with light pulses propagating in the z direction, following the same arguments that were given in the paraxial approximation, Eq.(3.9), we write the more gen-

eral complex field amplitude as:

$$U_m(\boldsymbol{r}, t) = A_m(\boldsymbol{r}, t) \exp(-ik_0 z) \exp(i\omega_0 t) \qquad u_m(\boldsymbol{r}, t) = \text{Re}[U_m(\boldsymbol{r}, t)] \qquad (3.16)$$

where now we have to specify the carrier frequency ω_0 associated with the wavevector k_0. If we now consider that the complex envelope $A_m(\boldsymbol{r}, t)$ is slowly varying in propagation distance[1], z and in time[2], t, then it should be the case that:

$$\frac{\partial^2 A_m(\boldsymbol{r}, t)}{\partial z^2} << k_0^2 A_m(\boldsymbol{r}, t) \qquad \frac{\partial^2 A_m(\boldsymbol{r}, t)}{\partial t^2} << \omega_0^2 A_m(\boldsymbol{r}, t) \qquad (3.17)$$

which is known as the *slowly varying envelope (SVE) approximation*. By substituing Eq.(3.16) into the Wave Equation, Eq.(3.5), and making the SVE approximation of Eq.(3.17), we arrive to the *Paraxial SVE Equation*:

$$\nabla_\perp^2 A_m(\boldsymbol{r}, t) - i2k \left(\frac{\partial A_m(\boldsymbol{r}, t)}{\partial z} + \frac{1}{c} \frac{\partial A_m(\boldsymbol{r}, t)}{\partial t} \right) = 0 \qquad (3.18)$$

Note that for a CW laser, the envelope would be time-independent and we would recover the paraxial Helmholtz equation from the section before, Eq.(3.10).

It can be seen by direct substitution that Eq.(3.18) is satisfied for any function of the form $f(t - z/c)A_0(\boldsymbol{r})$, where f is an arbitrary function. Thus, $A_0(\boldsymbol{r})$ should itself satisfy the paraxial Helmholtz equation. Therefore, in this approximation, any spatial paraxial wave with envelope $A_0(\boldsymbol{r})$ can be modulated temporally without disturbation of its spatial behavior. That is to say, under the SVE approximation, we can *decouple* the spatial and temporal modes, where the spatial modes satisfy the paraxial Helmhotz equation, and hence can be written as a superposition of Hermite-Gauss modes. This approximation allow us to analyze the temporal and spatial modes independently.

In our particular case, the frequency bandwidth of our laser source will be around $\Delta\lambda \sim$ 60 nm, and the carrier frequency corresponds to a wavelength of $\lambda_0 = 1560$ nm. On the other hand, the typical beam diameter is of the order of $W_0 \sim 2$ mm. This means that $\Delta\lambda/\lambda_0 \sim 0.029$ and $W_0/\lambda_0 \sim 0.0008$ and the SVE approximation holds.

3.3.2 The gaussian pulse

Focusing hence on the temporal degree of freedom, we can therefore write the pulse waveform, with complex amplitude $U(t)$, as a carrier wave of frequency ω_0 modulated by a complex amplitude $A(t)$:

$$U_m(t) = A_m(t) \exp(i\omega_0 t) = |A_m(t)| \exp(i(\phi(t) + \omega_0 t)) \qquad (3.19)$$

---

[1]The field envelope changes slowly in a wavelength distance λ.

[2]The field envelope changes slowly compared to one cycle of the carrier frequency ω_0.

The pulse intensity is $|A_m(t)|^2$. In ultrafast optics, it is usually easier to work in frequency space by means of the Fourier transform:

$$U_m(\omega) = \int_{-\infty}^{\infty} U_m(t) \exp(-i\omega t) \mathrm{d}t = |V_m(\omega)| \exp(i\phi(\omega)) \tag{3.20}$$

where $|V_m(\omega)|^2$ is the *spectral intensity*, $V_m(\omega)$ is centered at ω_0, and $\phi(\omega)$ is the *spectral phase*.

The typical pulses coming from lasers have a gaussian (or sometimes also sech²) intensity profiles, and a frequency-independent spectral phase $\phi(\omega) = \mathrm{Constant}$. This pulse mode is known as the *gaussian pulse*. The property of a flat spectral phase makes the pulse to be *transform-limited*, which means that the product of pulse duration and frequency bandwidth, the *time-bandwidth* product, is the minimum given by the properties of the Fourier transform. Any gaussian pulse with a different spectral phase would have a longer pulse duration. We can calculate the time-bandwidth product by writting the gaussian pulse, denoted $G(t)$, in the time domain[3]:

$$G(t) = G_0 \exp(-t^2/\tau^2) \tag{3.21}$$

and noticing that the Fourier transforms gives another gaussian function of the form $G(\omega) \propto \exp(-\tau^2 \omega^2)$. The temporal Full Width Half Maximum (FWHM) of the pulse is $\Delta t = \sqrt{2 \log 2}\tau$. The time-bandwidth product for a transform-limited gaussian pulse is hence readily calculated to be:

$$\Delta t \cdot \Delta \omega = 2\pi \Delta t \Delta \nu = 2\pi \cdot 0.44 \tag{3.22}$$

The time-bandwidth product can also be written in terms of the wavelength using the relation $\omega = 2\pi c/\lambda$:

$$\Delta \lambda \simeq \frac{\lambda_0^2}{c} \Delta \nu \tag{3.23}$$

which gives us a way of experimentally verifying how much our pulses are different from a transform-limited gaussian pulse.

At the left of Fig.(3.2) we depict the temporal form of the field for a transform-limited gaussian pulse.

3.3.3 Temporal dispersion

Consider a transform-limited gaussian pulse traveling through a lossless and dispersive medium. Since there are no losses, the pulse amplitude remains constant as the pulse propagates in the z direction. However, at position z, the pulse would acquire a frequency-dependent spectral phase of $\phi(\omega) = k(\omega)z$ according to the dispersion relation $k(\omega)$ in the

---

[3]Note that here we drop the index m since we are considering the particular temporal mode of the gaussian pulse.
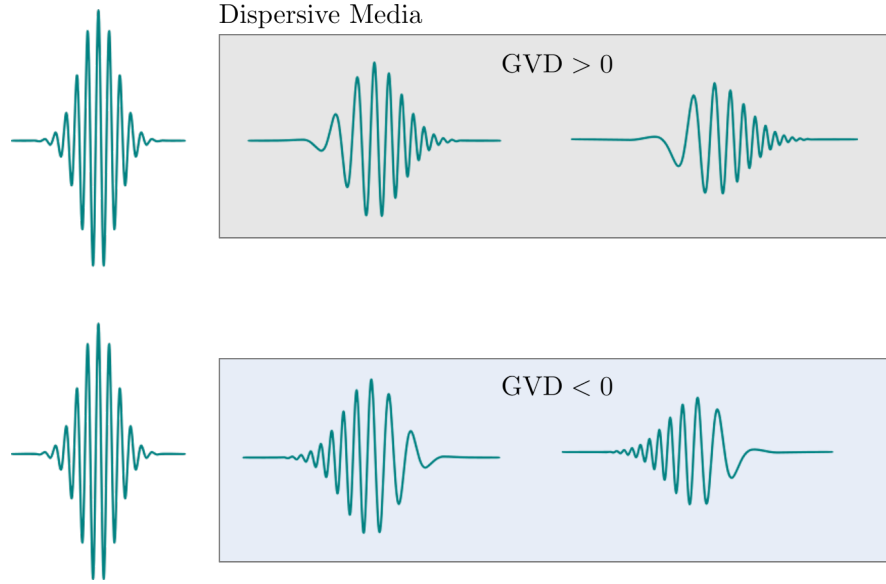
Figure 3.2: Evolution of a transform-limited gaussian pulse through a dispersive medium in the case where the GVD is positive (above), and negative, (below).

medium. At this point in space, the pulse can thus be written as:

$$G(\omega) = G_0 \frac{\tau}{2\sqrt{\pi}} \exp\left(-\frac{1}{4}\tau^2\omega^2\right) \exp(ik(\omega)z) \tag{3.24}$$

which is the product of the gaussian pulse in the frequency domain with the medium response $\exp(ik(\omega)z)$.

We can expand the dispersion relation into a Taylor series in order to understand the different physical effects that play a role in the correction of the spectral phase through the dispersive medium:

$$k(\omega) = k(\omega_0) + \left.\frac{\mathrm{d}k}{\mathrm{d}\omega}\right|_{\omega_0} (\omega - \omega_0) + \frac{1}{2}\left.\frac{\mathrm{d}^2k}{\mathrm{d}\omega^2}\right|_{\omega_0} (\omega - \omega_0)^2 + ... \tag{3.25}$$

By definition, $\mathrm{d}k/\mathrm{d}\omega|_{\omega_0} \equiv (v_g(\omega_0))^{-1}$ is the inverse of the *group velocity* at ω_0, i.e. the speed at which the electric field wavepacket travels in the propagation direction. On the other hand, $\mathrm{d}^2k/\mathrm{d}\omega^2|_{\omega_0} \equiv \mathrm{GVD}(\omega_0)$ is known as the *Group Velocity Dispersion* (GVD) at ω_0. By direct substitution we arrive to:

$$k(\omega) = k(\omega_0) + \frac{1}{v_g(\omega_0)}(\omega - \omega_0) + \frac{\mathrm{GVD}(\omega_0)}{2}(\omega - \omega_0)^2 + ... \tag{3.26}$$

The constant phase $k(\omega_0)z$ is a global phase factor that does not change the pulse in any form. Furthermore, by Fourier transform, the linear frequency dependence in the phase is

mapped to just a time delay for the pulse. This means that the linear term in the Taylor expansion is correcting for the fact that the wavepacket does not travel at the speed of light in vacuum, but with the group velocity $v_g(\omega_0)$, and therefore corresponds to a time delay. The pulse form is therefore not altered by the two first terms of Eq.(3.26).

The last term of Eq.(3.26), however, adds a quadratic phase by means of the group velocity dispersion, that makes the pulse to stretch in time, hence transforming the pulse into a not transform-limited pulse. It can be seen as an effect by which the frequencies that are far away from the carrier frequency travel faster than the ones near it, hence the pulse gets modulated in frequency (also known as getting *chirped*), and the pulse duration increases. This effect is known as *temporal dispersion*. Depending on the sign of $\text{GVD}(\omega_0)$ the pulse can get *up-chirped* ($\text{GVD}(\omega_0) > 0$, high frequencies are faster) or *down-chirped* ($\text{GVD}(\omega_0) < 0$, low frequencies are faster). Fig.(3.2) shows the effect of temporal dispersion on a transform-limited pulse in the time domain, suffering from both up-chirping and down-chirping depending on the sign of the GVD.

Higher order effects can be important if one has either a very dispersive medium, where $\text{d}^3 k(\omega)/\text{d}\omega^3|_{\omega_0}$ is not negligible, or a very wide bandwidth $\Delta\omega = \omega - \omega_0$. In the context of this thesis, however, it will be sufficient to take into account up to the quadratic phase when treating the temporal form of our pulses.

Note that even if the medium is dispersive, due to its linearity, the pulse spectral intensity $|G(\omega)|^2$ does not change as the wave travels through it, as can be seen from Eq.(3.24).

We can deduce the changes in amplitude and temporal duration if we know the dispersion characteristics of the medium. Let's consider an initial transform-limited pulse, with pulse duration τ_1 and amplitude G_1. After some distance, z, we denote b the quadratic coefficient associated with the quadratic spectral phase, $b \equiv \text{GVD}(\omega_0)z$. The pulse can then be written as:

$$G(\omega) = G_1 \frac{\tau_1}{2\sqrt{\pi}} \exp\left(-\frac{1}{4}(\tau_1^2 + ib)\omega^2\right) \tag{3.27}$$

which can also be cast as a chirped gaussian pulse with a new pulse duration τ_2 and a new amplitude G_2. It is clear from Eq.(3.27) that cascading two physical materials with total chirping coefficients b_1 and b_2 has the same effect as considering a unique total chirp of $b = b_1 + b_2$. This fact allows to think about correcting the chirp b_1 of a pulse by exploiting an optical effect that has a total chirp coefficient of $-b_1$, which is the basis of pulse compressors.

Since we can write the general complex envelope of a chirped gaussian pulse in time and frequency as:

$$G(t) = G_2 \exp\left(-\frac{1}{4}(1 + ia_2)t^2/\tau^2\right) \tag{3.28}$$

$$G(\omega) = G_2 \frac{\tau_2}{2\sqrt{\pi(1 - ia_2)}} \exp\left(-\frac{1}{4}\left(\frac{\tau_2^2}{1 + ia_2}\right)\omega^2\right) \tag{3.29}$$

where here $a_2 \equiv b/\tau_1^2 = \text{GVD}(\omega_0)z/\tau_1^2$, then by equating the amplitudes and the exponents

of Eq.(3.27) and Eq.(3.29) we obtain the pulse amplitude and duration after the transmission through the dispersive medium:

$$\tau_2 = \tau_1 \sqrt{1 + \left(\frac{\mathrm{GVD}(\omega_0)z}{\tau_1^2} \right)^2}$$

$$G_2 = \frac{G_1}{\sqrt{1 + i\mathrm{GVD}(\omega_0)z/\tau_1}} \tag{3.30}$$

These equations are important for experimentally controlling the quality of light pulses. A similar calculation can be done if we assume that the initial pulse was already chirped with a certain chirp coefficient. In our case, we have considered that the chirp comes from traveling a distance z though a dispersive medium, and hence $b = \mathrm{GVD}(\omega_0)z$ in Eqs.(3.30), but in general, chirp could also come from different optical effects. Eqs.(3.30) are always correct if we include all those effects into the total chirp parameter b.

We can also derive the explicit dependence of the group velocity and the GVD on wavelength and index of refraction, which are known quantitites in the laboratory, allowing the access to indirect experimental measurements of the temporal dispersion. We start by writing the general relation between the wavevector, $k(\omega)$ and the index of refraction of the material, $n(\omega)$:

$$k(\omega) = \frac{\omega}{c}n(\omega) \tag{3.31}$$

In ultrafast optics, it is usual to work with wavelengths instead of frequencies, that we can interchange by $\omega = 2\pi c/\lambda$. By computing the derivative of Eq.(3.31), and changing the variable to λ, we obtain:

$$v_g(\lambda) = \frac{c}{\left(n(\lambda) - \lambda \frac{\mathrm{d}n(\lambda)}{\mathrm{d}\lambda} \right)} \equiv \frac{c}{N_g(\lambda)} \tag{3.32}$$

$$\mathrm{GVD}(\lambda) = \frac{\lambda^3}{2\pi c^2} \frac{\mathrm{d}^2 n(\lambda)}{\mathrm{d}\lambda^2} \tag{3.33}$$

where $N_g(\lambda)$ is known as the *group index* of the material. Therefore, the dispersion properties of a material can be completely predicted by knowing the dependence of the refractive index on wavelength, $n(\lambda)$. There exist empirical equations fitting this function, known as the *Sellmeier Equations*, that are available in databases for the majority of the materials.
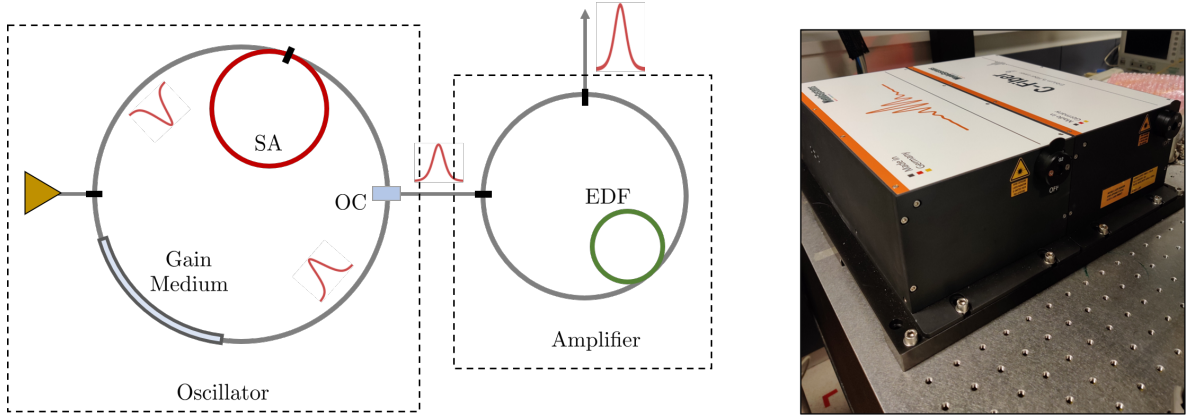
3.4   Laser Characterization

Figure 3.3: Left: Simplified scheme of the laser system. Right: the Laser in our laboratory.

3.4.1 The Laser

The laser source in our experiments is a telecom fiber laser from MenloSystems [61]. The laser can be divided into two main parts: a mode locking system and an optical amplification system.

The mode-locking system consists in a single-mode fiber forming a loop, which is equivalent to a Fabry-Perot cavity in free space. In the fiber there is the laser medium, and a semi-transparent dielectric that couples to an Erbium-doped fiber, that makes the light to present phase shifts due to the phenomenom of self-modulation. This makes this small fraction of the loop to become an artificial saturable absorber i.e. a material in which light is not absorbed after a certain intensity threshold [62]. The presence of the saturable absorber modulates the losses in the cavity, fixing a phase relation between the frequency components that are resonator modes (hence the term mode-locking), and in turn enforcing the generation of ultrashort pulses that circulates in the main resonator in a steady state. The pulse repetition rate can be adjusted with the length of the fiber loop. The technique just described is known as additive-pulse mode locking [63]. This part of the laser is called the "oscillator".

After the pulses leave the oscillator via an output coupler, they pass to a low-noise optical amplifier, consisting in a loop mirror with an Erbium doped fiber amplifier inside (EDFA), [64]. Pulse amplification is obtained thanks to a non-linear interference effect in the loop.

Fig.(3.3) shows a simplified scheme of the laser and a photo of the actual laser from our laboratory.

The output of our laser are free-space ultrashort pulses centered at $\lambda = 1560$ nm, linearly polarized in the vertical direction with respect to the optical table (which we denote as s polarization), and at a repetition rate of $f_r = 100$ MHz. An auxiliary output electrical signal synchronized with the pulses is also provided, which will be useful for the pulse synchronization in the experiment.
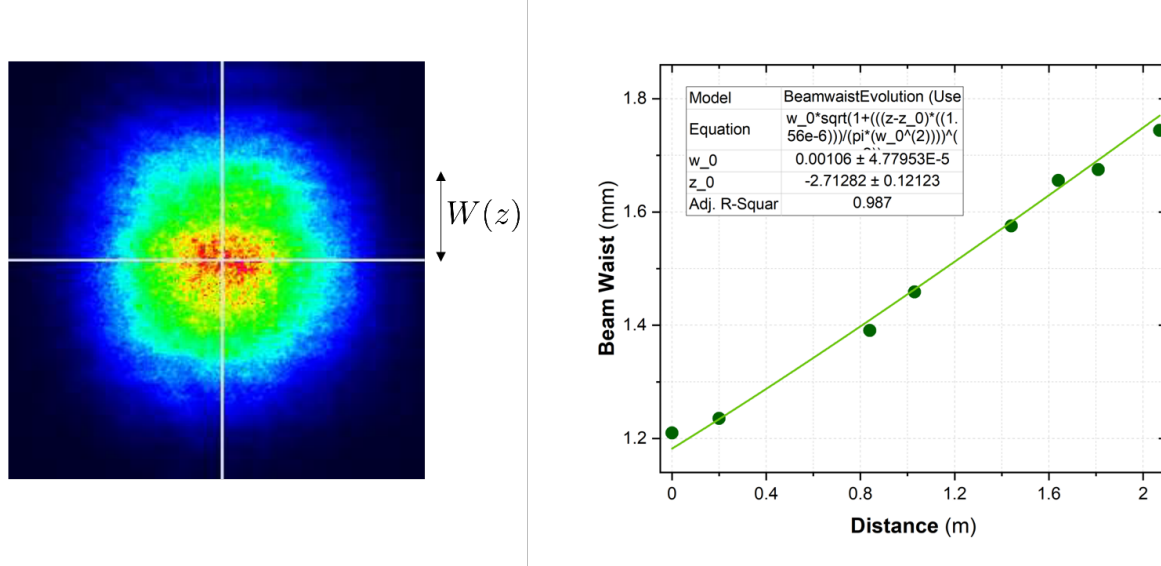
Figure 3.4: Left: Example of a Spatial intensity profile measured for our Fiber femtosecond laser. Right: Beam waist measurement as a function of distance, giving the beam waist and a M^2-factor of around 1.1.

After our discussion about the modal analysis of the electromagnetic field, we are going to mathematically model the output field of our laser source as a train of linearly polarized temporal gaussian pulses, described by Eq.(3.21), propagating in a given space direction, and with spatial amplitudes described by the the gaussian beam of Eq.(3.15).

3.4.2 Spatial characteristics of the Laser

The spatial characterization of our laser can be achieved using an infrared CCD camera and measuring the beam profile in different positions along the propagation direction.

With this aim, in order to find the beam waist W_0, and hence the Rayleigh length z_0, we measured the beam profile at different distances from the laser's output. For every distance, z, we measure the beam radius in the x and y directions (that are approximately equal in all cases) and take the mean value. The data values of these measurements are fitted to Eq.(3.13) giving a beam waist of $W_0 = 1.06 \pm 0.05$ mm, and hence $z_0 = 2.71 \pm 0.13$ m (see Fig.(3.4)). Obviously, we can make this measurement more precise simply by taking more data points at different distances, however, these results were already in very good concordance with the values provided by the manufacturer.

A parameter that quantifies the quality of a beam, i.e. the deviation of the beam's profile from a gaussian form, is the so-called M^2-factor, defined as:

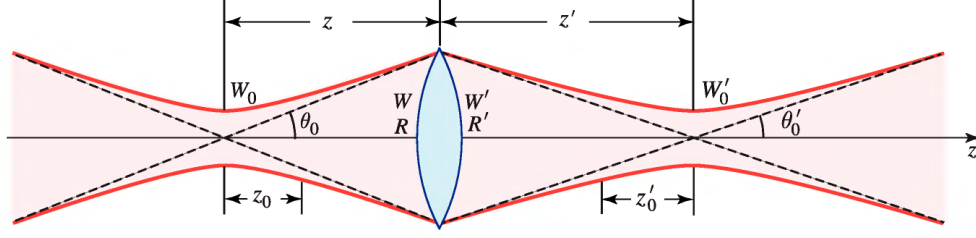$$M^2 = \frac{\pi W_b \theta_b}{\lambda} \tag{3.34}$$

60

Figure 3.5: Transmission of a gaussian beam through a thin lens. Figure taken from [60]. All quantities are defined in the text.

where W_b is the measured beam waist and θ_b is the measured divergence angle, which for a gaussian beam is defined as $\theta_0 = \frac{\pi\lambda}{W_0}$. It is clear that with that definition, $M^2 = 1$ for a perfect gaussian beam. A good quality beam is usually considered from $M^2 < 1.3$. We performed several intensity profile measurements using a CCD camera (optimized for $\lambda = 1550$ nm), in order to obtain the beam waist W_0 and the divergence angle θ_0 of our laser, and hence the M^2 factor, which turned out to be $M^2 = 1.10 \pm 0.05$, see Fig.(3.4).

It is important to be able to control the beam spatial characteristics for any experiment in optics. With regard to the spatial characteristics, the use of thin lenses permits to change the beam waist and the Rayleigh length without changing the gaussian form of the beam profile.

The equations of the beam transformation after passing through a lens system has been extensively studied (see for example [60]). Here we make a summary of the main results for a thin lens of focal length f, depicted in Fig.(3.5). The transformation of the beam follows:

$$\text{New beam waist} \quad W_0' = MW_0 \tag{3.35}$$

$$\text{Waist location} \quad (z' - f) = M^2(z - f) \tag{3.36}$$

$$\text{New Rayleigh length} \quad z_0' = M^2 z_0 \tag{3.37}$$

$$\text{Magnification} \quad M = \left| \frac{f}{z - f} \right| \left(1 + \frac{z_0^2}{(z - f)^2} \right)^{-1/2} \tag{3.38}$$

Fig.(3.5) shows the beam's parameters before and after the thin lens.

With the lens equations and the characterization of our laser we have the basic experimental tools for manipulating the spatial characteristics of the beam in our experiment.

3.4.3 Temporal characteristics of the Laser

The time scale for ultrashort pulses is in the range of femtoseconds, where 1 fs $= 10^{-15}$ s. This time scale is too small compared to the time response of any commercial photodetector. Hence, the pulses are typically too fast to be directly measured with a direct intensity measurement, which would nevertheless provide the average power P_{avg} of the pulses. Since

we know the repetition rate, a direct power measurement allows to calculate the energy per pulse. For instance, our laser has an average power of $P_{\mathrm{avg}} \simeq 500$ mW and a repetition rate of $f = 100$ MHz, thus the corresponding energy per pulse is $E_{\mathrm{pulse}} \simeq 5$ nJ.

A measurement of the time duration of the pulses can be done using an optical autocorrelator [65]. An autocorrelator is an interferometric device where two copies of the pulses interfere in a non-linear crystal. A variable time delay is set in one arm of the interferometer. Autocorrelators commonly measure the intensity of the second harmonic generation in the non-linear crystal as a function of the time delay, T. Our autocorrelator measures instead two-photon absorption intensities in the non-linear crystal, but the basic concept remains the same. The output intensity signal for a given time delay is the autocorrelation signal:

$$\mathrm{Aut}(T) = \int |E(t)|^2 |E(t+T)|^2 \mathrm{d}t \tag{3.39}$$

where the integration limit is the temporal range encapsulating a single pulse. The temporal waveform of the pulse determines the form of the autocorrelation signal, and the corresponding temporal width is related to the width of the autocorrelation signal. The typical pulse waveforms are gaussian, sech^2, and lorentzian.

An important remark is that the temporal dispersion of the optical components should be characterized in order to precisely measure the pulse duration at any given point, since this will cause the pulse to expand temporally, which could lead to incorrect conclusions. This can nevertheless be done by consecutive measurements of the autocorrelation signals in which optical components are added to or subtracted from the optical path. Application of Eq.(3.30) provides the total chirp coefficient, which is the sum of the chirp coefficients of every component[4]. Another way of working is to obtain beforehand the GVD value per unit length of the material from which the optical component is made of, for example from a database like [66], and then compute the chirp coefficient as the product of that value with the thickness of the material. We used ultrafast mirrors and beamsplitters throughout the majority of the experiment, for which the GVD is engineered so that almost no temporal dispersion is present in the pulses.

The autocorrelation signal coming directly from the laser is depicted in Fig.(3.6) (a), giving a pulse envelope of sech^2 (although a gaussian pulse also appropriately fits the data) with a pulse duration of $\tau_{\mathrm{FWHM}} = 57 \pm 1$ fs. The data for the calculation of the GVD of our optical materials also matches very well the GVD per unit length given in the database used in the thesis [66].

The knowledge of the pulse envelope makes it possible to compute the peak power of the pulses, which for a sech^2 (resp. gaussian) pulse is $P_{\mathrm{peak}} \simeq 0.88 E_{\mathrm{pulse}}/\tau_{\mathrm{FWHM}}$ (resp. $P_{\mathrm{peak}} \simeq 0.94 E_{\mathrm{p}}/\tau_{\mathrm{FWHM}}$). Adding the spatial characterization presented above, we can calculate the

---

[4]Technically, we should consider the dispersion of the optical components together with the air dispersion. However, at our wavelength, the GVD of air is around 0.03 fs^2/mm [66], which is several orders of magnitude less than the typical GVD in dispersive materials, and can therefore be ignored.

<div style="text-align:center">(a)</div>

<div style="text-align:center">(b)</div>

Figure 3.6: (a) Autocorrelation signal and (b) spectrum of the ultrashort pulses at the output of the laser.

power density of our laser, which is a relevant parameter for both the non-linear effects that will take place in the experiment, and the components damage threshold that we can handle in the laboratory.

To see if the pulses are approximately transform-limited at the output of the laser, we also measured the spectrum of the signal, shown in Fig.(3.6) (b). We observe a large bandwidth of wavelengths in the spectrum, although the gaussian waveform is not well observed. We fit this data to a gaussian function anyway (with a R^2 fit value of 88%) for having an estimation of the frequency bandwidth, which gives $\Delta\lambda = 75 \pm 1$ nm. However, this is an overestimation in the gaussian fit due to the two spectral "wings" appearing at the end of the spectrum. For this reason, we decided to take as another estimator the spectrum's FWHM ignoring those wings. In this case this gives $\Delta\lambda \simeq 66.0$ nm, which seems more reasonable than the fit, given our spectral data. With this data the time-bandwidth product is estimated to be $\tau_{\text{FWHM}}\Delta\omega = 0.47$, that should be compared with the theoretical value for sech^2 pulses (0.315). Given the form of the spectrum, a bit away from a gaussian, we considered this result close enough for our purposes. From another point of view, the autocorrelator value of the pulse duration, (57 fs) gives a transform-limited bandwidth of around 45 nm for sech^2 pulse-type, which is reasonable from the measured spectrum, Fig.(3.6) (b).

Table 3.1 presents a summary of the results just discussed that characterized the ultrashort pulses of our laser.

Laser Parameter	Value
Central Wavelength	1560 ± 2 nm
Polarization	Linear, s
Average Power	500 ± 10 mW
Repetition Rate	100 MHz
Pulse Duration	57 ± 1 fs
Pulse Envelope	sech^2
Spectral Width FWHM	66 ± 5 nm
Pulse energy	5.0 ± 0.1 nJ
Peak Power	77.2 ± 1.5 kW
M^2-factor	1.10 ± 0.05
Beam waist	1.06 ± 0.05 mm
Peak Power Density	2.2 ± 0.1 MW/cm^2

Table 3.1: Experimental summary of the Laser characterization.

3.5   Tools for Pulse Manipulation

If we are to produce efficient non-linear optical effects in our experiment, it is important to being able to maintain an approximately transform-limited pulse through the whole optical path. As we have seen, the presence of temporal chirp increases the temporal width of the pulses and decreases the field peak amplitude, deteriorating the pulse quality. A lower field amplitude would decrease the effective non-linear interaction. Furthermore, and most importantly, chirped pulses could generate spatio-temporal coupling effects in non-linear processes, reducing the effective interaction strength and complicating considerably the output states of light. The first pulse manipulation tool that we will present, the pulse compressor, will take care of these issues.

Besides that, in our experiment, that will be detailed in the following Chapters, we will need to have some reference pulses, that will act as a Local Oscillator (LO) for homodyne measurements. We will need to shape the temporal spectrum of the LO pulses, for which another pulse manipulation tool, namely the pulse shaper, will come in handy.

3.5.1   The Pulse Compressor

As we have seen, if a transform limited pulse is transmitted through two optical elements with chirp coefficients b_1 and b_2, the total chirp coefficient is simply $b = b_1 + b_2$. If we then manage to construct an optical circuit in which the sign of the chirp coefficient is opposite to the total initial chirp, we would reduce the total dispersion experienced by the pulse ($b = b_1 + b_2 < b_1$) hence decreasing the pulse duration. Ideally, we would want to have $b_1 = -b_2$, so the total chirp is zero and the pulse returns to the transform-limited case,
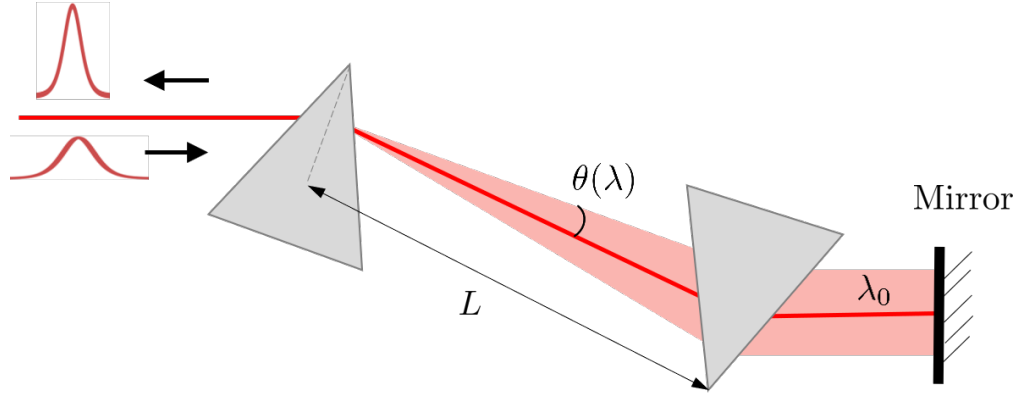
Figure 3.7: Scheme of the pulse compressors built in the lab exploiting angular dispersion in prisms.

where the duration is minimum. This optical circuit is hence called a *pulse compressor*.

There are several ways of constructing pulse compressors, mainly distinguished by the physical mechanism in which a desired chirp coefficient can be obtained, i.e. by exploiting a wavelength-dependent physical quantity or effect. Examples of wavelength-dependent phenomena are material dispersion, angular dispersion, non-linear dispersion or polarization dispersion, among others.

For our experiment, we constructed pulse compressors exploiting angular dispersion in prisms. A scheme of the pulse compressor is depicted in Fig.(3.7), and a photo of an actual pulse compressor in the lab is shown in Fig.(3.8). The first prism disperses the light with a wavelength-dependent angle $\theta(\lambda)$, measured with respect to the angle made by the central wavelength, λ_0, so that $\theta(\lambda_0) = 0$. The second prism collimates the beam, and the mirror makes the beam to pass back through both prisms, undoing the operations, such that the beams entering and leaving the compressor are spatially identical.

To minimize the losses, the apex angle of the prisms is near the Brewster angle for the given wavelength and the beam should enter both prisms at the Brewster angle.

It can be geometrically shown that the wavelength-dependent path after the first prism is:

$$l(\lambda) = L\cos(\theta(\lambda)) \tag{3.40}$$

where L is the distance between the apex of both prisms. Therefore, the phase shift encountered by the wavelength λ is:

$$\psi(\lambda) = \frac{2\pi}{\lambda}l(\lambda) = \frac{2\pi L}{\lambda}\cos(\theta(\lambda)) \tag{3.41}$$

By expanding $\psi(\lambda)$ in a Taylor series we obtain the linear coefficient, associated with a time delay, and the quadratic coefficient, associated with a temporal chirp. The linear
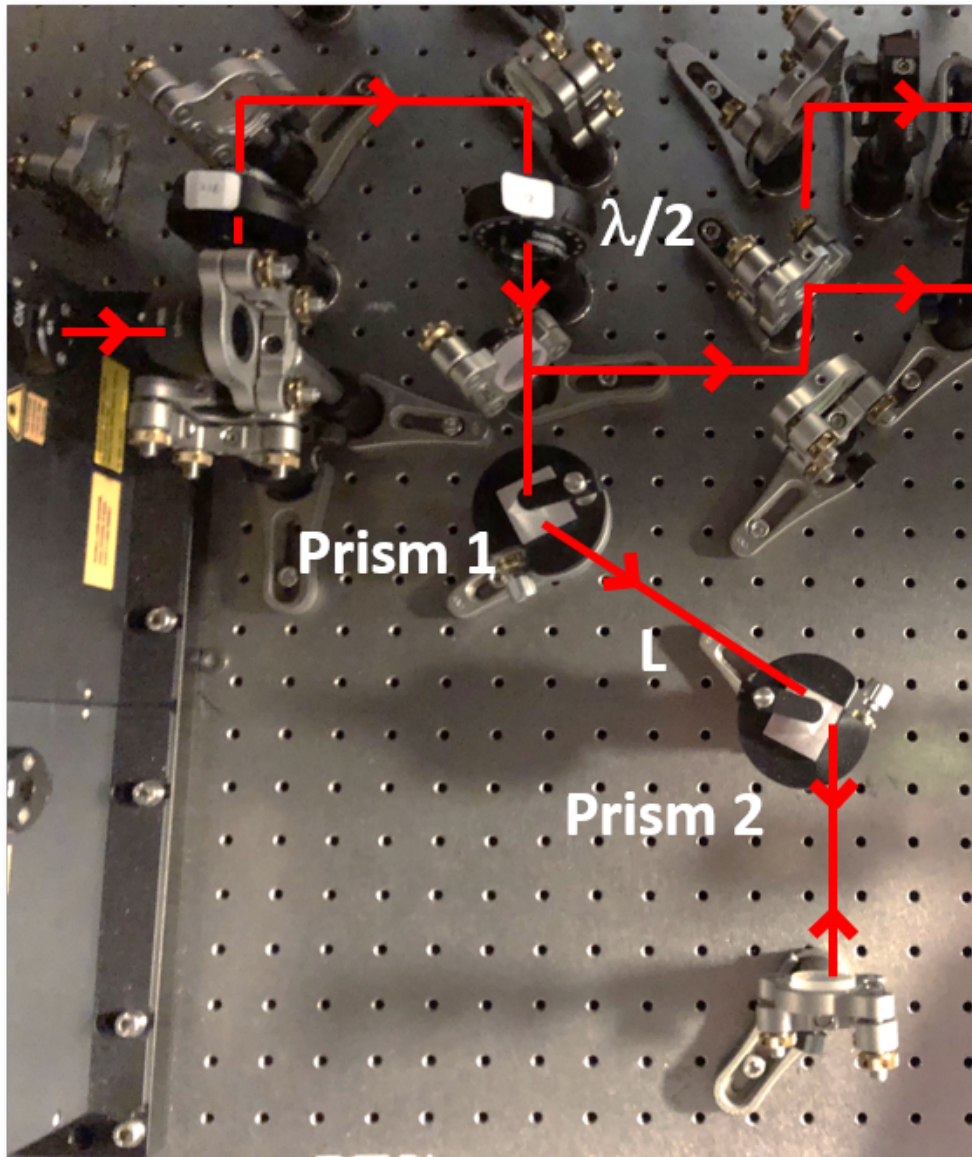
Figure 3.8: Photo of a prism Pulse Compressor mounted in the laboratory.

coefficient trivially corresponds to a time delay of L/c, and the second coefficient reads:

$$\left.\frac{\mathrm{d}\psi(\lambda)}{\mathrm{d}\lambda}\right|_{\lambda_0} = \frac{\lambda_0^3}{2\pi c^2}\left(\left.\frac{\mathrm{d}^2 l(\lambda)}{\mathrm{d}\lambda^2}\right|_{\lambda_0}\right) \tag{3.42}$$

Following the approach of [67], the above second derivative can be written as:

$$\left.\frac{\mathrm{d}^2\psi}{\mathrm{d}\lambda^2}\right|_{\lambda_0} = \frac{\lambda_0^3}{2\pi c^2}\left[4L\left(\left(\left.\frac{\mathrm{d}^2 n(\lambda)}{\mathrm{d}\lambda^2}\right|_{\lambda_0} + \left(2n(\lambda_0) - \frac{1}{n^3(\lambda_0)}\right)\left(\left.\frac{\mathrm{d}n}{\mathrm{d}\lambda}\right|_{\lambda_0}\right)^2\right)\sin\beta\right.\right.$$
$$\left.\left. - 2\left(\left.\frac{\mathrm{d}n}{\mathrm{d}\lambda}\right|_{\lambda_0}\right)\cos\beta\right) + 16\left(\left.\frac{\mathrm{d}^2 n(\lambda)}{\mathrm{d}\lambda^2}\right|_{\lambda_0}\right)^2 W_b\right] \tag{3.43}$$

where $\beta \simeq -2\frac{\mathrm{d}n}{\mathrm{d}\lambda}\Delta\lambda$ and W_b is the beam waist at the input prism assuming collimated beams. We have measured $\Delta\lambda \simeq 66$ nm and $\mathrm{d}n/\mathrm{d}\lambda(1560\,\mathrm{nm}) \sim -0.01\,\mu\mathrm{m}^{-1}$ for the two prism materials we are considering, which are SF10 and fused silica. This data gives a dispersion angle of $\beta \sim (10^{-10})^o$, that allows us to approximate $\sin\beta << \cos\beta$ and $\cos\beta \simeq 1$. This approximation simplifies considerably the above expression:

$$\left.\frac{\mathrm{d}^2\psi}{\mathrm{d}\lambda^2}\right|_{\lambda_0} = \frac{\lambda_0^3}{2\pi c^2}\left[-8L\left(\left.\frac{\mathrm{d}n}{\mathrm{d}\lambda}\right|_{\lambda_0}\right) + 16\left(\left.\frac{\mathrm{d}^2 n(\lambda)}{\mathrm{d}\lambda^2}\right|_{\lambda_0}\right)^2 W_b\right] \tag{3.44}$$

The first term of this equation is the actual negative chirp added by angular dispersion in the pulse compressor, while the second term takes into account the material dispersion within the prisms. In normal conditions, the first term dominates over the second. Since this term is always negative, pulse compressors built in this way can only compress initial up-chirped pulses, i.e. pulses with a positive initial chirp coefficient.

Furthermore, the chirp added by the compressor is *adjustable* via the proportionality dependence of Eq.(3.44) with the distance between the prisms, L.

We built and tested prisms compressors made both in fused silica and SF10. In order to obtain the experimental amount of compression, we measured the pulse duration as a function of the distance between the two prisms. Fig.(3.9) (a) shows the experimental results for fused silica. We observed a minimum of pulse duration corresponding to the point in which the compressor compensates all the initial chirp from the pulse. From this measurement we can infer the chirp coefficient added by the compressor using Eq.(3.30), and compare them to the theoretical values obtained from Eq.(3.44). The result is shown in Fig.(3.9) (b) again for fused silica. A compression of 85 ± 7 fs^2/cm is obtained from this experimental data, in agreement with the theoretical value. Similar results are obtained with SF10 prisms, the compression being 143 ± 8 fs^2/cm at $\lambda_0 = 1560$ nm.

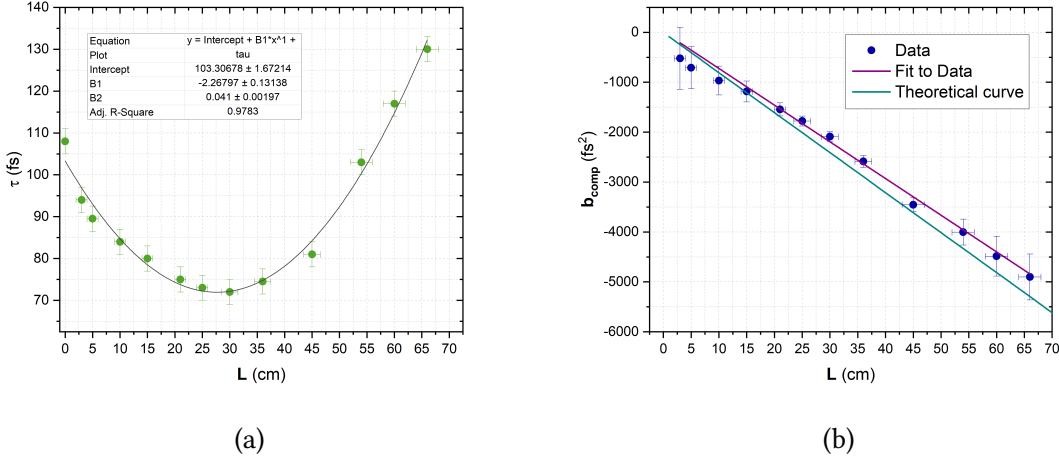(a)   (b)

Figure 3.9: (a) Pulse duration as a function of the distance between the fused silica prisms. Central wavelength: 1560 nm. (b) Chirp coefficient added by the compressor as a function of the distance between the fused silica prisms and comparison with the theoretical model described in the manuscript.

This characterization permits us to add the pulse compressor as the first pulse manipulation tool in our experiment, that will constitute one the main blocks in which we divided the main experiment, to be presented in Chapter 7.

3.5.2 The Pulse Shaper

The pulse shaper, as the name suggests, allows for the manipulation of the amplitude and phase of the different wavelengths present in a given light field. It was originally introduced for picosecond lasers, [68], and later extended to femtosecond lasers [69].

The pulse shaping technique we use in this work is often referred to as Fourier Optical Processing [70]. The working principle is the following: using a diffracting element, we spatially separate the different wavelengths composing our beam and collimate them using an appropriate lens. The beam is sent to the screen of a Spatial Light Modulator (SLM), where each pixel of the screen (corresponding to a small interval of wavelengths) can be addressed independently. The phase of each pixel is modified and the resulting beam is recombined with another diffracting element. This modulation in the phase can also change the amplitude of each pixel with a trick that will be detailed below. The result is a pulse that has been spectrally (and hence also temporally) shaped. The general principle is schematized in Fig.(3.10). For us, the diffraction elements are diffraction gratings, and we will use a single
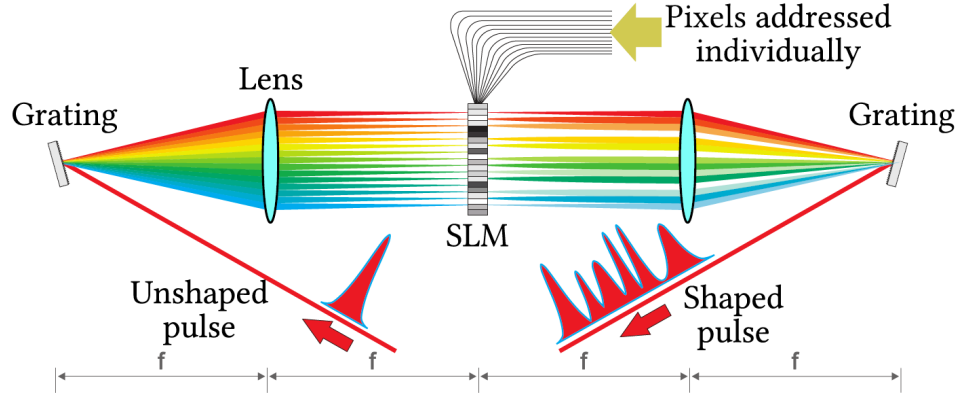
Figure 3.10: General scheme of a Pulse Shaper. A Spatial Light Modulator changes independently the amplitude and phase of the frequency components that arrive spatially diffracted from a diffraction element. After the SLM, the beam is recombined with the final lens and grating. Figure taken from [71].

cylindrical mirror to collimate the input beam and recombine the shaped beam. Fig. (3.11) shows a photo of the actual shaper mounted in our experiment.

3.5.3 Pulse shaper characterization

The diffraction grating is an optical element that presents a fine surface structure with a characteristic size of the same order of magnitude than the wavelength, known as the *grating pitch*, d. Constructive interference after hitting the structure is achieved when the phase difference between the incident rays is a multiple of the wavelength, λ:

$$\sin \theta_i(\lambda) + \sin \theta_d(\lambda) = m\frac{\lambda}{d} \qquad m \in \mathbb{Z} \tag{3.45}$$

where θ_i is the incident angle and θ_d is the diffracted angle.

The different values of m for which we have constructive interference are known as the *diffraction orders*. The zero-th order $m = 0$ corresponds to the standard reflection law. The particular shape of the grating pattern will determine the repartition of light between the various diffraction orders. Our particular grating is optimised to diffract maximally in a single diffraction order, that corresponds to $m = -1$; this type of gratings are called *blazed grating*. Moreover, it is also designed to be more efficient when the diffraction angle coincides with the incidence angle, this is called the *Littrow configuration*. In our experiment we use a $d = 800$ gr/mm holographic grating model PC 0800 50x50x10 NIR from Spectrogon [72]. The order -1 diffracted angle is readily found from Eq.(3.45):

$$\theta_d(\theta_i, \lambda) = -\arcsin\left(\frac{\lambda}{d} + \sin \theta_i\right) \tag{3.46}$$
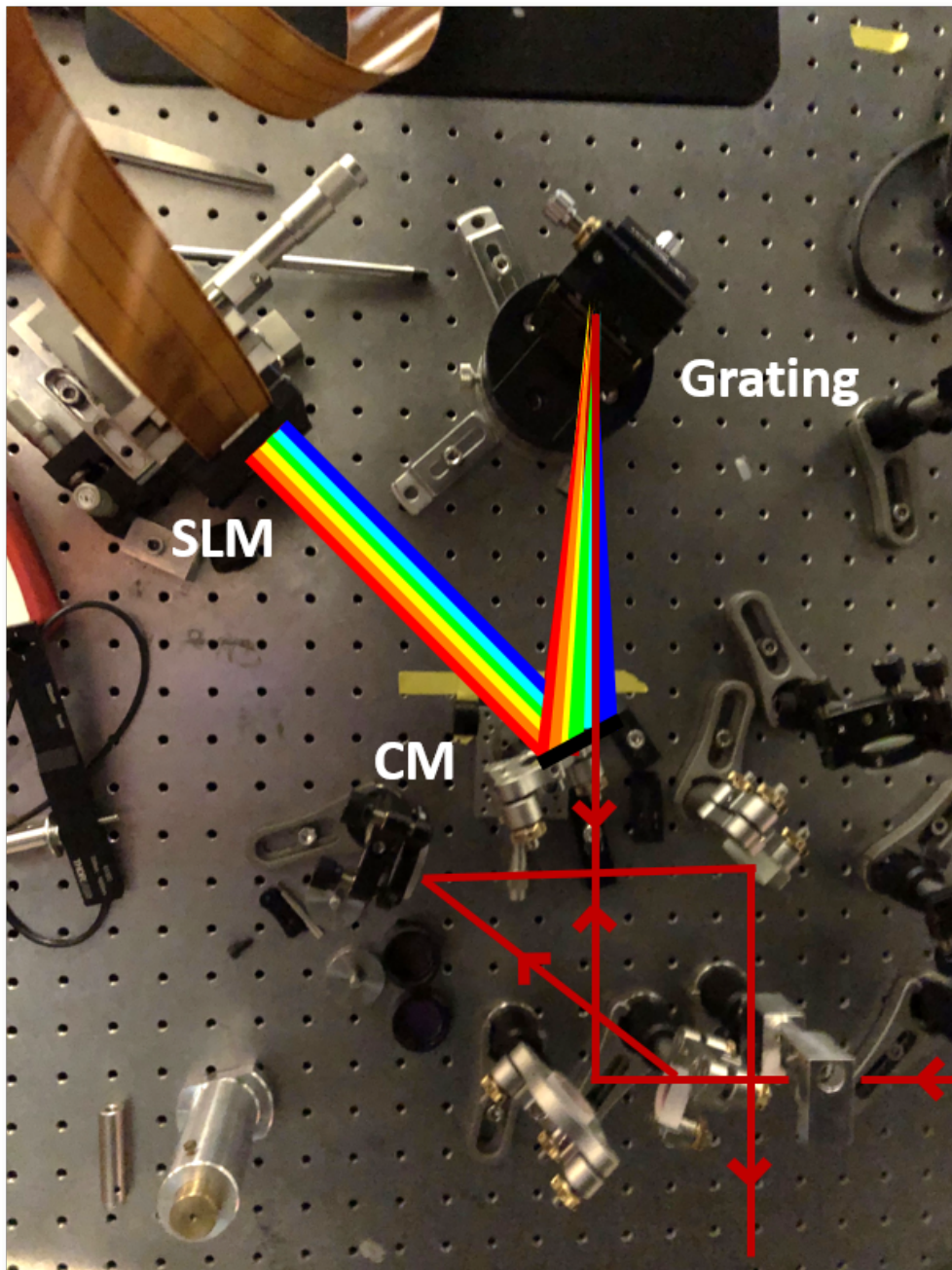
69

Figure 3.11: Pulse Shaper photo from the experimental lab. CM: Cylindrical Mirror, SLM: Spatial Light Modulator.

On the other hand, our Spatial Light Modulator was a liquid crystal SLM (LCOS-SLM model X15213-08 from Hamamatsu [73]), which is a 2D array of liquid crystals that can be individually addressed with an electrical signal. The liquid crystals act as tunable wave-plates that change the phase of light reflected by the SLM surface without any intensity change. The SLM has 1272 × 1024 square pixels of size $\delta x_{\text{px}} = 12.5\ \mu$m.

In principle, therefore, the SLM affects the phase but not the amplitude of the incoming beam. However, in our experiment we used a trick to also be able to affect the amplitude of our pixels. Since light is diffracted horizontally by our grating, using a vertical sawtooth structure in the SLM, the light is only diffracted in orders 0 and 1 from the SLM. If we fix the grating pitch and make sure we filter the first order on the output, we can then tune the amplitude of each spectral component by modulating the magnitude of the vertical grating pattern. Additionally, the relative phase between horizontally adjacent components can be tuned by shifting vertically the grating pattern (see [74, 75] for more details).

The effects of geometrical and optical limits in the resolution of the pulse shaper can be found in [71]. Here, we limit ourselves to the application of those results in our particular case. The quality of a pulse shaper is often expressed in terms of its *complexity*, that is the maximum number of features one can imprint on a given spectrum. The complexity due to the geometry of our setup is given by:

$$\eta_{\text{px}} = \frac{\Delta\lambda}{\delta\lambda_{\text{px}}} = \frac{f\Delta\lambda}{d\delta x_{\text{px}}\cos(\theta_d(\lambda_0))} \tag{3.47}$$

where f is the focal length of the cylindrical mirror, $\Delta\lambda = 66$ nm is the spectral width of our pulses and $\delta x_{\text{px}} = 12.5\ \mu$m is the pixel size. We used a cylindrical mirror with focal length $f = 200$ mm, $\theta_d(1560\ \text{nm}) = 38.6\ ^o$, and a groove density of $1/d = 800$ gr/mm. The geometrical complexity is then computed to be $\eta_{\text{px}} = 1081$.

Eq.(3.47) considers the beam to be formed by polychromatic planes waves, which would be vertically focused to a single point in the SLM. In practice, this is not true, and we would have a finite vertical spot in the SLM, which limits the complexity of the pulse shaper. The spot size after the grating, w', can be calculated with:

$$w' = \frac{\cos\theta_d(\lambda_0)}{\cos\theta_i(\lambda_0)}w_i \tag{3.48}$$

where ω_i is the input waist to the grating. Given the difraction of the gaussian beam, derived in section 3.2, during a distance f, we find that the corrected pixel size, δx_{opt}, is:

$$\delta x_{\text{opt}} = 2\frac{\lambda_0 f}{\pi w'} = 2\frac{\cos\theta_i(\lambda_0)}{\cos\theta_d(\lambda_0)}\frac{\lambda_0 f}{\pi w_i} \tag{3.49}$$

which gives a wavelength resolution of:

$$\delta\lambda_{\text{opt}} = 2\frac{d\lambda_0\cos\theta_i(\lambda_0)}{\pi w_i} \tag{3.50}$$

and a corresponding complexity of:

$$\eta_{\mathrm{opt}} = \frac{\pi w_i \Delta\lambda}{2d \cos\theta_i(\lambda_0)\lambda_0} \tag{3.51}$$

In our experiment, $\lambda_0 = 1560$ nm, $w_i = 2$ mm, $1/d = 800$ gr/mm and $\theta_i(1560 \text{ nm}) = 38.6\,^o$, giving a complexity of $\eta = 136$.

The value of the real complexity is the smallest value between the pixel and the optical complexities, η_{px} and η_{opt}. In our configuration, we are limited by the complexity due to the optical features of our beam and optical elements. In any case, we are able to shape our pulses with 136 "features", which is more than enough for the purpose of the experiment.

It can also be shown [71] that a misalignment in the distance between the cylindrical mirror and the SLM produces both temporal and horizontal chirp to the beam. In the ideal case, when the distance is exactly f, the total dispersion is compensated due to the 4f configuration of the setup (free dispersion line). If the distance between the cylindrical mirror and the SLM is instead $f + \alpha$, then there is an effective chirp coefficient added to the optical circuit of:

$$b_{\mathrm{PS}} = \frac{\alpha\lambda_0^3}{2\pi d^2 c^2 \cos^2(\theta_d(\lambda_0))} \tag{3.52}$$

Giving an order of magnitude, if we have a misalignment of the cylindrical mirror - SLM distance by $\alpha = 3$ mm, then the corresponding chirp coefficient for our experimental values would be $b_{\mathrm{PS}} = 21104$ fs^2, which is pretty high at the femtosecond scale.

For this reason, we measured the duration of our pulses with the autocorrelator at the ouput of the pulse shaper, and moved the cylindrical mirror with a precision translation stage, so that we minimize the pulse duration and hence the temporal dispersion due to the misalignment. We can nevertheless alternatively correct some of the temporal chirp by using a correction mask in the SLM interface.

On the other hand, an incorrect distance between the cylindrical mirror and the SLM would make the beam to get away from collimation, and therefore create an angle between the different frequency components after hitting the SLM, that would deteriorate the recombination in the grating, and therefore different parts of the beam would present different spectrum[5]. This effect is known as *spatial chirp*. An experimental feature of spatial chirp is seen in the lab as ellipticity in the beam profile. We controlled the spatial chirp by measuring the spatial profile with the CCD camera after the pulse shaper and adjusting the position of the SLM with its corresponding precision screws.

3.5.4 Hermite-gauss frequency modes

In this thesis, we were interested in shaping the LO temporal pulses into the family of time/frequency Hermite-Gauss modes. After the pulse shaping alignment, we applied the

---

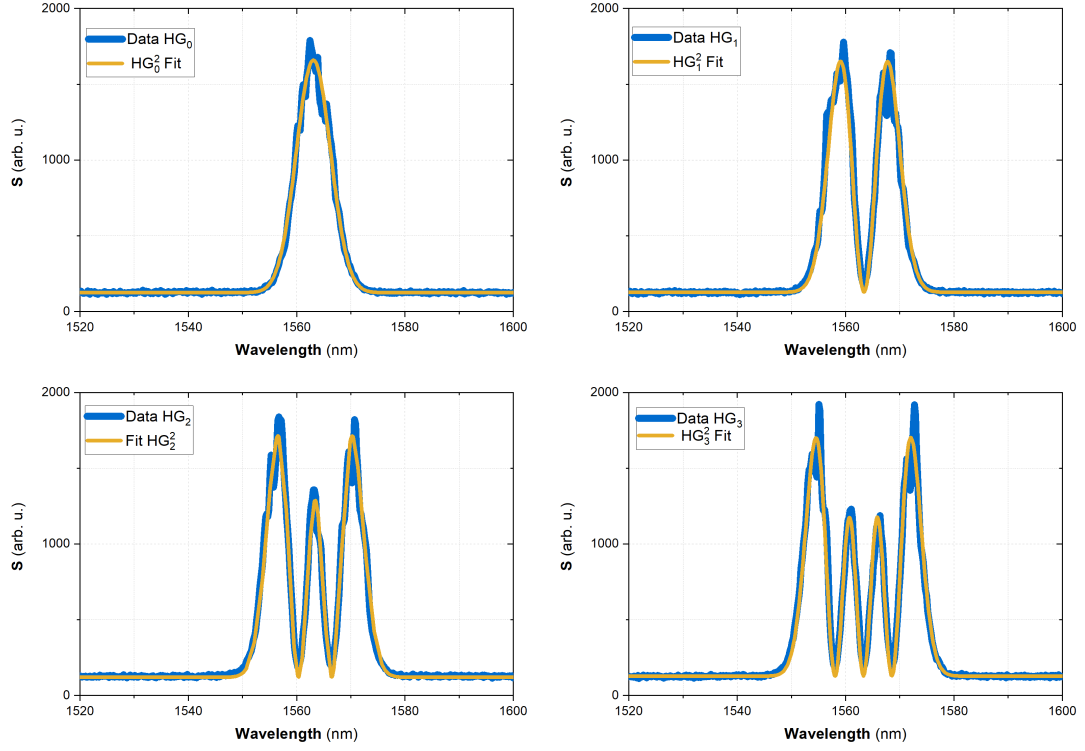[5]Typically, the spectrum at the extremes of the beam is narrower than in the center.

Figure 3.12: Spectrometer data from the first 4 Hermite-Gauss masks after the pulse shaper and corresponding fits to the Hermite-Gauss functions.

corresponding mask to the SLM through our prepared interface and measured the resulting spectrum with a spectrometer. The result is shown in Fig.(3.12), together with the Hermite-gauss fits.

As we can see, the measured spectra are in excellent agreement with the corresponding fits to the Hermite-Gauss modes as defined in Eq.(3.14). Even though we showed here the first 4 modes, our interface can reach up to the last order Hermite-Gauss mode compatible with the pulse shaper complexity.

Chapter 4

Non-Linear Optics in Waveguides

" It does not say in the Bible that all laws of nature are expressible linearly! "

– Enrico Fermi

Contents

After introducing the theory on ultrashort pulses of light and the experimental tools characterized in the lab for their manipulation, we are ready to present the theoretical tools needed for the non-linear components of the experiment. In this Chapter, we present the basic notions in classical non-linear optics needed for the understanding of the quantum mechanical description, that will be presented in Chapter 5. We will consider the case of waveguide structures, and will perform simulations of the characteristic spatial modes of our waveguides given our experimental parameters. Finally, we will show the actual spatial mode characterization of our waveguides in the laboratory and compare with the numerical simulations.

4.1 Non Linear Optics

When an external electric field is applied to a dielectric medium, the atoms composing the medium get polarized, and, to a first approximation, electric dipoles are created. These dipoles oscillate in response to the electric field and hence emit electromagnetic radiation themselves. The electromagnetic radiation emitted by the material can interfere with the original external electric field. If the external field amplitude or the susceptibility of the material is small, the oscillations are harmonic and the response of the medium is linear. We then recover the effects of refraction, diffraction or dispersion, described by the Wave Equation, Eq.(3.5). However, when the material's susceptibility and/or the field amplitudes are high enough, as it is the case in waveguides due to the strong light confinement, the field can drive the dipoles into the anharmonic regime, where non linear optical effects emerge.

4.1.1 Non-linear Polarization

If we denote by $\boldsymbol{E}$ the external electric field, the dipole moment per unit volume, $\boldsymbol{P}$, induced in the medium is:

$$\boldsymbol{P} = \epsilon_0 \chi \boldsymbol{E} \tag{4.1}$$

where ϵ_0 is the permittivity of free space and χ is the *electric susceptibility*. In order to understand the whole variety of non-linear effects that can arise it is advisable to expand Eq.(4.1) into a *power series* of the electric field:

$$\boldsymbol{P} = \epsilon_0 \left(\chi^{(1)} \boldsymbol{E} + \chi^{(2)} \boldsymbol{E}\boldsymbol{E} + \chi^{(3)} \boldsymbol{E}\boldsymbol{E}\boldsymbol{E} + ... \right) \equiv \boldsymbol{P}_\mathrm{L} + \boldsymbol{P}_\mathrm{NL} \tag{4.2}$$

where $\chi^{(n)}$ is the n-th order non-linear susceptibility, which is a $n+1$-rank tensor. We have also defined the linear response, $\boldsymbol{P}_\mathrm{L}$, that corresponds to the first term in the power series, and the non-linear response, $\boldsymbol{P}_\mathrm{NL}$, that comprises all the other terms. It is interesting to give an order of magnitude estimation of the susceptibilities just described. For common dielectric materials, $\chi^{(1)}$ is of the order of unity[1], while the second and third order susceptibilities are[2] [76]:

$$\chi^{(2)} \sim 10^{-12} \text{ m/V} \tag{4.3}$$

$$\chi^{(3)} \sim 10^{-24} \text{ m}^2/\text{V}^2 \tag{4.4}$$

$$\tag{4.5}$$

---

[1]The index of refraction of a non-magnetic linear material is $n = \sqrt{\chi^{(1)} + 1}$, and n is typically between 1 and 3.

[2]We took the case of a specific non-linear material, namely KTP, although the order of magnitude is similar for the materials typically used in non-linear optics experiments.

In this manuscript, our field amplitude inside the waveguides is calculated to be[3] of the order of $|E| \sim 2.5 \cdot 10^5$ V/m. Hence we can compare the order of magnitude of the second and third order terms in the power series, Eq.(4.2):

$$\frac{\chi^{(2)}|E|^2}{\chi^{(3)}|E|^3} = 4 \cdot 10^6 \tag{4.7}$$

which means that the second order term is already 6 orders of magnitude bigger than the third term. This estimation justifies the truncation of the power series of the polarization taking into account only the first two terms. Therefore, in our case, we expect that the non-linear effects are caused by the second order induced polarization:

$$\boldsymbol{P}_{\mathrm{L}} = \epsilon_0 \chi^{(1)} \boldsymbol{E} \tag{4.8}$$

$$\boldsymbol{P}_{\mathrm{NL}} = \epsilon_0 \chi^{(2)} \boldsymbol{E} \boldsymbol{E} \tag{4.9}$$

Due to the presence of the new non-linear term in Maxwell's Equations, the Wave Equation Eq.(3.5) is modified to[4]:

$$\nabla^2 \boldsymbol{E}(\boldsymbol{r}, t) + \frac{1}{c^2} \frac{\partial^2 \boldsymbol{E}(\boldsymbol{r}, t)}{\partial t^2} = \frac{1}{\epsilon_0 c^2} \frac{\partial^2 \boldsymbol{P}_{\mathrm{NL}}(\boldsymbol{r}, t)}{\partial t^2} \tag{4.10}$$

For each component of the fields, these are equations of a harmonic oscillator driven by the non-linear term $\boldsymbol{P}_{\mathrm{NL}}$. The non-linear term can therefore drive the oscillator into the anharmonic regime, creating therefore new frequencies in the system. We thus see that non-linear effects in a dielectric material can give rise to frequency conversion processes.

4.1.2   Three-wave mixing

Since the non-linear polarization depends quadratically on the external field, Eq.(4.9), the generation of new radiation at second order requires the coupling of three electric fields (two from the non-linear polarization and the external field). For this reason, the processes associated with $\chi^{(2)}$ are called *three-wave mixing processes*.

---

[3]The calculation comes from intensity measurements of our pulses before the non-linear material. Considering a gaussian pulse, the electric field amplitude can be estimated with:

$$|E| = \sqrt{\frac{P}{\pi d^2 c \epsilon_0 n}} \tag{4.6}$$

where $n \sim 2$ is the index of refraction of the non-linear material (KTP), P is the mean power, and $d \sim 3\mu m$ is the beam size inside the waveguide. With this data we obtain $|E| \sim 2.5 \cdot 10^5$ V/m.

[4]One can arrive to the new wave equation by rewriting Maxwell's equations with the displacement operator $\boldsymbol{D}$ instead of $\boldsymbol{E}$, and do the same trick that we did in Chapter 3.

To understand the possible three-wave mixing effects, it is instructive to consider first a monochromatic plane wave travelling along the x direction as the external field applied to the material:

$$E(x,t) = E_0 \exp(i(\omega_0 t - k(\omega_0)x)) + \text{c.c.} \tag{4.11}$$

where ω_0 is the wave frequency, $k(\omega_0)$ is its wavevector, and c.c. stands for complex conjugate from now on. The non-linear polarization can be written using Eq.(4.9):

$$P_{\text{NL}} = \epsilon_0 \chi^{(2)} E(x,t)^2 = 2\epsilon_0 \chi^{(2)} |E_0|^2 + \epsilon_0 \chi^{(2)} (E_0^2 \exp(i(2\omega_0 - 2k(\omega_0)x) + \text{c.c.}) \tag{4.12}$$

The first term is responsible for the process of *optical rectification*, that will not be considered in this work, while the second term oscillates at double the original frequency of the external field. This process is known as *Second Harmonic Generation* (SHG), since the field oscillating at double the frequency is known as the second harmonic of the field. We can also see that the phase of the generated second harmonic field has a space dependency of $2k(\omega_0)x$. Since the new wave oscillates at $2\omega_0$, the phase of the SHG waves acquired during propagation is $k(2\omega_0)x$. This generally leads to the cancellation of the Second Harmonic field generated at different positions along the medium due to destructive interference, unless the generated and propagated waves fulfill the condition $2k(\omega_0) = k(2\omega_0)$. This condition is known as the *phasematching condition*, where the SHG builds up along the medium in a coherent fashion.

More generally, consider now the case in which the applied electric field is the sum of two monochromatic waves:

$$E(x,t) = E_1 \exp(i(\omega_1 t - k(\omega_1)x)) + E_2 \exp(i(\omega_2 t - k(\omega_2)x)) + \text{c.c.} \tag{4.13}$$

The non-linear polarization is then:

$$\begin{aligned} P_{\text{NL}} = \epsilon_0 \chi^{(2)} E(x,t)^2 = \epsilon_0 \chi^{(2)} (E_1^2 \exp(i(2\omega_1 - 2k(\omega_1)x) + E_2^2 \exp(i(2\omega_2 - 2k(\omega_2)x) \\ + 2E_1 E_2 \exp(i(\omega_1 + \omega_2) - (k(\omega_1) + k(\omega_2))x) + \\ 2E_1 E_2^* \exp(i(\omega_1 - \omega_2) - (k(\omega_1) - k(\omega_2))x)) + \text{c.c.} \end{aligned} \tag{4.14}$$

Now the two Second Harmonic fields of the original planes waves can be generated, as well as two extra fields at the sum frequency $\omega_1 + \omega_2$ and difference frequency $\omega_1 - \omega_2$. These two extra processes are consequently known as *Sum Frequency Generation* (SFG) and *Difference Frequency Generation* (DFG). Again, for one of these processes to coherently build-up in the medium, a phasematching condition is needed. The phasematching for SFG (resp. DFG) is $k(\omega_1 + \omega_2) = k(\omega_1) + k(\omega_2)$ (resp. $k(\omega_1 - \omega_2) = k(\omega_1) - k(\omega_2)$).

In the general case, all the frequency components of an incident electric field can produce the generation of radiation fields at the respective second harmonics, as well as sum and differences of pairs of frequencies of the field with the condition that the corresponding phasematching condition of the process is fulfilled.

An extensive analysis of the production of the classical SHG, SFG and DFG fields can be performed by studying the amplitudes of the fields with the non-linear Wave Equation,

Eq.(4.10). This is done for example in [77, 78]. As a comment, this approach is useful for finding the quantum counterparts, which are the Heisenberg equations of motion for the quantum operators. In the next Chapter, however, we will consider the hamiltonian approach for going from the classical to the quantum description of the processes.

4.1.3 Quasi-phasematching

In general, the choice of the material under consideration dictates the phasematching conditions for tuples of frequencies following the dispersion relation $k(\omega) = n(\omega)\omega/c$, allowing or not for a specific three-wave mixing process.

A possible solution to tackle this problem is to use the so-called *birefringence phasematching* [79], in which the external and generated fields may not follow the same optical axis. It basically consists in exploiting the dependence of the index of refraction in the incident electric field angle. However, this technique is not very adequate for waveguides, where the coupled external field and the generated fields are naturally collinear along the waveguide direction.

Another technique that allows for perfect phasematching at an arbitrary tuple of frequencies is the *quasi-phasematching technique* (QPM). In this technique, a sign modulation of the second order susceptibility is achieved along the crystal with a certain spatial period, Λ, known as the *poling period*. This modulation can be achieved by applying a high voltage to those regions of the waveguide (or bulk crystal) where the non linearity should be flipped [80]. The modulation makes the uniform non linear coefficient to become:

$$\chi^{(2)} \longrightarrow \chi^{(2)} \sum_{m=-\infty}^{\infty} G_m \exp(imk_{\text{QPM}}x) \tag{4.15}$$

where $k_{\text{QPM}} = 2\pi/\Lambda$ is known as the *grating vector*, m is the quasi-phasematching *order* and G_m are the Fourier coefficients that dictate the strength of a given order.

The modulation of Eq.(4.15) adds an extra term to the wavevector mismatch equations. For example, for SHG:

$$\Delta k_{\text{SHG}} = k(2\omega_0) - 2k(\omega_0) + k_{\text{QPM}} \tag{4.16}$$

hence, by tuning the poling period Λ, one can achieve perfect phasematching ($\Delta k_{\text{SHG}} = 0$) for any frequency ω_0. In practice, the value of Λ providing phasematching for the different three-wave mixing processes is in the order of tens of micrometers (see for example [81]).

Additionally, for obtaining experimental fine tuning of the phasematching, one can use the temperature dependence of the index of refraction, and hence of the wavevectors. This is done by introducing the non-linear material into an oven with a temperature controller.

As we will see, the waveguide allows propagation into a discrete set of spatial modes, each one with a characteristic propagation constant, $\beta_n(\omega)$, $n = 0, 1, 2...$, that are the counterparts of the wavevectors for plane waves. Therefore, both the dispersion relation and the

phasematching condition are in general mode-dependent. All the non-linear materials used in this work rely on QPM and were designed to work with the fundamental spatial mode for all fields generated in the medium.

4.1.4 Anisotropic media

Once we know the non-linear material that will be used, a cartesian coordinate system is set to define the propagation direction (along the waveguide), and the transversal directions (cross section of the waveguide). This is important, since the non-linear materials are *anisotropic*, and the coupling of different non-linear effects are related to the susceptibility tensor $\chi^{(2)}$, which depends on the combination of cartesian coordinates under consideration. In Appendix B we briefly describe the symmetries in the susceptibility tensor that define the cartesian coordinate used along this manuscript.

As we have seen, the intrinsic anisotropic behavior of the material is encoded into the permittivity tensor, ϵ, i.e. into the different indices of refraction along the different spatial directions. Since there always exists a coordinate system where the permittivity tensor is diagonal, we can associate the elements of the diagonal tensor to the permittivity value seen by light polarized in that direction. There will therefore be a maximum of three different indices of refraction for a given non-linear material, provided by the diagonal elements in the appropriate coordinate system. Light linearly polarized in one of the cartesian coordinates will "see" the corresponding index of refraction of that coordinate.

There are two types of non-linear optical crystals, uniaxial crystals and biaxial crystals. For *uniaxial crystals*, the permittivity elements are such that one of them is different from the other two in the diagonal basis. Therefore, we can associate two indices of refraction, called *ordinary* and *extraordinary* indices, for two different polarizations[5]. In *biaxial crystals*, all three permittivity elements are different in the diagonal basis, and so we have three different indices of refraction for every spatial direction, x, y, z. In this thesis, we used Lithium Niobate (LN), that is a uniaxial crystal, for a SHG process, and Potassium Tytanil Phosphate (KTP), a biaxial crystal, for the waveguides.

Taking as an example the KTP case, we define the propagation direction to be x, the vertical direction to be z, and the transversal direction to be y. We therefore associate those directions to three indices of refraction n_x, n_y and n_z, that we will consider functions of wavelength and temperature following specific Sellmeier Equations [6] ($n_j = n_j(\lambda, T)$). The *Kleinman symmetry*, described in Appendix B, allows us to know the non-linear effects allowed by the material, and the corresponding polarizations for input and output optical fields. We can compute the different wavevectors using $k_j(\lambda, T) = 2\pi n_j(\lambda, T)/\lambda$ and hence

---

[5]Since we are considering optical waves traveling in a cartesian coordinate, the index of refraction corresponding to the propagation direction is irrelevant for us.

[6]For the waveguide modelling, we will also consider dependence on the vertical direction, $n_j = n_j(z)$, the so-called *index profile* that will be treated later in this Chapter.

the dispersion properties of the material in that specific process, in particular the wavevector mismatch Δk providing, or not, phasematching.

In the next Chapter, we will derive the quantum states of light due to the non-linear optical effects that we briefly introduced here classically. Even in the quantum regime, our discussion about phasematching, Kleinmann symmetry and material anisotropy are valid and used both in the design of our experiment and in the actual implementation of the non-linear processes.

4.2   Waveguides

Waveguides are structures used to confine optical waves by means of total internal reflection on their surface [82]. They present a core region, surrounded by a substrate and air, the geometry depending on the type of structure. For light confinement to be possible, the index of refraction in the core should be higher than that of the substrate and air. They can be classified into *Planar waveguides* (confining light in two dimensions), and *Channel Waveguides* (confining light in three dimensions).

In the context of this manuscript and the experiment performed in this thesis, we will focus on channel waveguides, although a brief derivation of modal fields in planar waveguides will be shown as well. The first non-linear experiments in optical waveguides were introduced in the 1970's, and since then, extensive research work has been accomplished in waveguide theory, waveguide materials and fabrication, and implementation of a number of passive, active, and functional devices. Examples of such a device are optical couplers, filters or modulators, optical memories or sensors.

The combination of non-linear optics and waveguide technology is somewhat natural. Because of the confinement of light, high optical intensity in a small cross sectional area can be maintained along the waveguide dimensions, removing diffraction and hence obtaining a long interaction length. This gives rise to higher order non-linear optical effects, even when pumping at low or moderate power. A review of research work on waveguide nonlinear optics can be found in [83, 84], and a more modern treatment is given in [85].

4.2.1   General considerations

We are interested in describing the confinement properties of waveguides by the discretization of the spatial modes of light inside the structure, due to its geometry and dimensions compared to the light carrier wavelength, λ_0. The rest of this Chapter will be hence dedicated to the description of those modal fields, that will prove useful in the next Chapter, when we will present the quantum states produced by the non-linear interaction in the waveguide.

First of all, we will consider monochromatic waves with a certain wavelength λ for the calculation of the waveguide's spatial modes. This is justified in Chapter 3, Section 3.3.1,

where we discussed the conditions for the decoupling of the temporal and spatial degrees of freedom. Since the SVE approximation is valid in our case, the spatial modes computed with monochromatic waves will also apply in the case of ultrafast pulses of light with our discussed bandwidth.

The waveguides that we have used for our experiment are fabricated by Rb exchange into a non-linear substrate[7] using a mask, so that only an approximately rectangular region of the substrate suffers the chemical exchange and therefore slightly increases the index of refraction in the waveguide core, allowing total internal reflection, [86].

This fabrication process leaves in general a good homogeneity of the waveguide along the propagation direction (taken here as the x direction). Due to the nature of the exchange process, the Rb atoms will be more diffused near the surface, and hence we expect to have an index of refraction that is in general a function of the cross-section (or transversal) co-ordinates, $n = n(y, z)$. This dependence of the index of refraction is known as the *index profile* of the waveguide. Furthermore, the length of the vertical direction were the Rb exchange is applied depends on the time left for the chemical process to act, and is called the waveguide's *depth*.

Because of the anisotropic properties of materials described in Section 4.1.4, a given polarization of the fields will be associated with a particular index of refraction (ordinary or extraordinary for uniaxial crystals, and $n_{x/y/z}$ for biaxial crystals). Therefore, for each one of those cases, the Wave Equation of Chapter 3 is valid if we substitute the scalar index of refraction n of homogoneous, linear media with the component of the anisotropic index of refraction associated with that particular input polarization.

In order to calculate the spatial modes allowed by the waveguide, we consider monochromatic optical waves with frequency ω_0 travelling in the x axis:

$$\begin{aligned}
\boldsymbol{E}(x, y, z, t) &= \boldsymbol{E}(y, z) \exp(-i\beta x) \exp(i\omega_0 t) \\
\boldsymbol{H}(x, y, z, t) &= \boldsymbol{H}(y, z) \exp(-i\beta x) \exp(i\omega_0 t)
\end{aligned} \tag{4.17}$$

where β is known as the *propagation constant*. By substituing these fields into Maxwell's equations and eliminating the magnetic field $\boldsymbol{H}$ using the identity $\nabla \times \nabla \times \boldsymbol{E} = -\nabla^2 \boldsymbol{E}$ it is easy to arrive to:

$$\nabla_\perp^2 \boldsymbol{E}(y, z) + (k^2 n^2(y, z) - \beta^2)\boldsymbol{E}(y, z) = 0 \tag{4.18}$$

where $\nabla_\perp = (0, \partial/\partial y, \partial/\partial z)$ is a transverse differential operator, $k = \omega_0 \sqrt{\epsilon_0 \mu_0} = \omega_0/c$ is the wavevector of a monochromatic electromagnetic wave in vacuum and we have used that $\epsilon(y, z)/\epsilon_0 = n^2(y, z)$. The resulting equation is the new version of the Wave Equation Eq.(3.5), in which we added the anisotropy of the medium and used the ansatz of Eq.(4.17). The new modal functions solving Eq.(4.18) are therefore the electromagnetic spatial modes in our waveguides.

---

[7]A substrate of KTP, in our case.

When finding the modes of Eq.(4.18) with appropriate boundary conditions, two types of solutions are found. There are solutions where the field amplitude $\boldsymbol{E}(x, y)$ is large in the core and decays exponentially away from it. These solutions are known as *guided modes*, due to the mode confinement in the waveguide. These are the relevant discrete set of modes we want to describe in this manuscript. The other type of solutions do not decay exponentially away from the waveguide, and hence they represent light propagating away from the structure. These modes are known as *radiation modes*, and there is an infinity number of them.

The propagation constant of any specific mode can be written as:

$$\beta = Nk \tag{4.19}$$

and N is the so-called effective index of refraction, or *mode index*.

As we have already discussed, the modes are orthogonal and complete, and therefore any arbitrary field inside the waveguide can be expressed as a weighted superposition of the modal fields.

In the great majority of cases it is impossible to solve analytically Eq.(4.18) for the mode profiles $\boldsymbol{E}(x, y)$ and $\boldsymbol{H}(x, y)$, and numerical methods should be used. However, it is interesting to model the simplest case scenario, in which analytical solutions can be found, in order to get insights into the physics of the modal fields inside the waveguide.

4.2.2 Planar waveguides

Planar waveguides, also known as slab waveguides, are the simplest waveguide structure that can be found. They confine light only over a single transversal direction, here denoted z, as shown in Fig.(4.1). By considering a step index profile of the form:

$$n(z) = \begin{cases} n_\mathrm{a} & z \geq 0 \\ n_\mathrm{c} & 0 \leq z \leq -t \\ n_\mathrm{s} & z \leq -t \end{cases} \tag{4.20}$$

analytical solutions for the modal functions can be found. Here, t is the waveguide thickness, and the constants n_a, n_c and n_s are the values of the index of refraction of air, core and substrate respectively. The solutions for the electric and magnetic fields can be classified into two polarization mode base, because they leave only one non-zero component of either the electric or magnetic field. For this reason they are called *Transverse Electric* (TE) and *Transverse Magnetic* (TM) modes.

TE and TM modes

The Transverse Electric modes can be obtained by setting $H_x = 0$. This condition implies that $E_x = E_z = 0$ and the only non-zero component of the electric field is $E_y(z)$, which
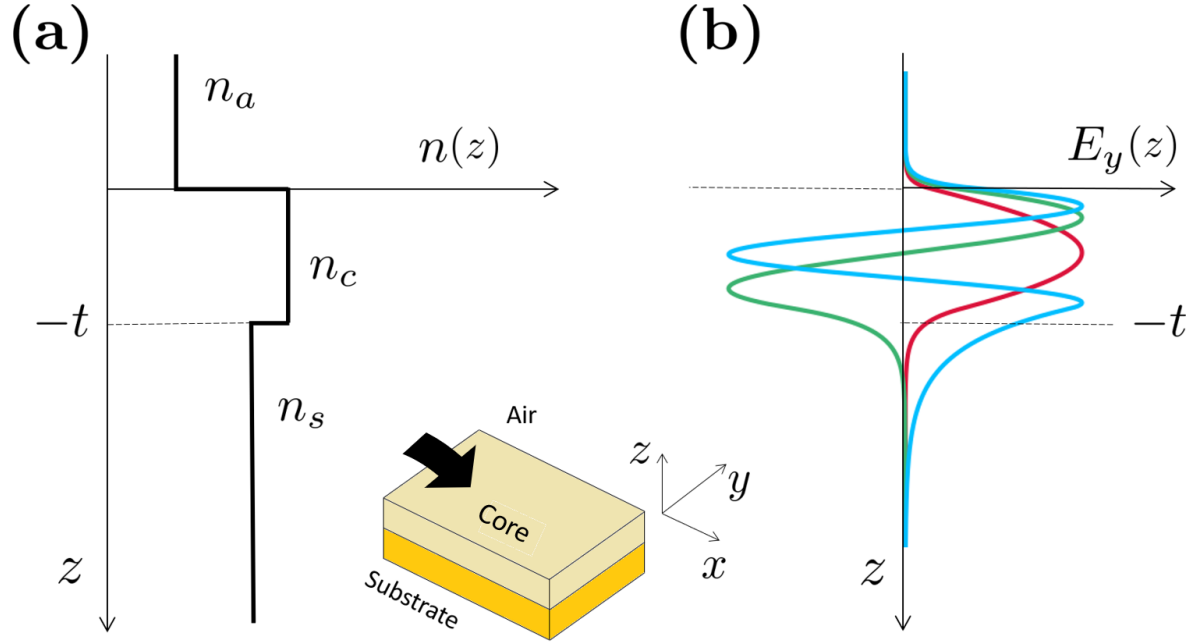
Figure 4.1: Planar waveguide modal fields. (a): The index of refraction profile is considered to be a step function between the air, core and substrates. (b): First three guided TE modal profiles.

follows the wave equation Eq.(4.18). Since we suspect the form of the fields, we make the ansatz for $E_y(z)$ as:

$$E_y(z) = \begin{cases} E_a \exp(-\gamma_a z) & z \geq 0 \\ E_c \cos(\kappa_c z + \phi_a) & 0 \leq z \leq -t \\ E_s \exp(\gamma_s(z + t)) & z \leq -t \end{cases} \tag{4.21}$$

where E_a, E_c and E_s are constants, and:

$$\gamma_a = k\sqrt{N^2 - n_a^2} \qquad \gamma_s = k\sqrt{N^2 - n_s^2} \qquad \kappa_c = k\sqrt{n_c^2 - N^2} \tag{4.22}$$

The solution is completed by the electromagnetic boundary conditions of the fields at $x = 0$ and $x = -t$, that lead to the following condition:

$$\kappa_c t - \phi_a - \phi_s = m\pi, \qquad m = 0, 1, 2... \tag{4.23}$$

$$\phi_a = \arctan(\gamma_a/\kappa_c) \qquad \phi_s = \arctan(\gamma_s/\kappa_c) \tag{4.24}$$

which indeed provides a discrete set of modal fields labeled with the integer m. Eq.(4.24) determines the modal index N of a given mode. Finally, the field amplitudes are related by

$E_a = E_c \cos(\phi_a)$ and $E_s = E_c(-1)^m \cos(\phi_s)$. Fig.(4.1) shows the index profile and the first three modal TE fields solutions.

Since the only non-zero field component is E_y, these guided modes are known as Transverse Electric, or TE, modes, associated with light polarized in the y direction. However, an equivalent set of solutions can be found by setting $E_x = 0$ instead. In this case, the only non-zero component of the magnetic field is H_z, that can also be written as a trigonometric function decaying exponentially at the boundaries. For this reason, these guided modes are known as Transverse Magnetic (TM) modes, and are associated with the orthogonal polarization of the TE modes.

The mode index, N, lies between n_s and n_c, and depends on the wavelength, the core thickness, the polarization and the mode order. It is possible to find configurations in which there is an arbitrary number of guided modes by configuring properly those parameters. Two cases are relevant in general: a *single-mode* waveguide, only supporting one mode, known as the *fundamental mode*, and a *multimode* waveguide, in which more than one solution is found. A useful parameter that quantifies how much a given mode is guided is the *normalized propagation constant*, b, defined as:

$$b = \frac{N^2 - n_s^2}{n_c^2 - n_s^2} \tag{4.25}$$

whose values are between 0 and 1. As the index contrast $(n_c - n_s)$ of the waveguide increases, the light is well confined and $b \to 1$. However, in this case the waveguide would also tend to become multimode, which could not be desired in some applications. The waveguides that we will consider in this thesis are *weakly-guided* waveguides, in which the index contrast is small ($n_c - n_s \sim 0.01$), and so only few modes are supported by the waveguide. Our particular KTP waveguides were designed to be approximately single-mode at telecom wavelengths.

4.2.3   Channel waveguides

As anticipated before, the waveguides used in this thesis confine light over the two transversal directions, y and z, and are called Channel Waveguides.

As with planar waveguides, the modal fields are calculated from Eq.(4.18) and appropriate boundary conditions, where here the index profile $n(y, z)$ is in general a two-dimensional function.

Although no analytical solutions can be found in this case, the physical behavior and analysis for the planar waveguides are conserved for channel waveguides. This can be seen by approximating the channel waveguide as two planar waveguides in the y and z directions. For example, we could take inspiration of the TE modes from planar waveguides, write the electric field as $E_y(y, z) \simeq E_y(y)E_y(z)$ and apply the same ansatz solution to each of these fields, with the presence of two differente mode indices. This way of calculating the modes is known as the *effective index method.*
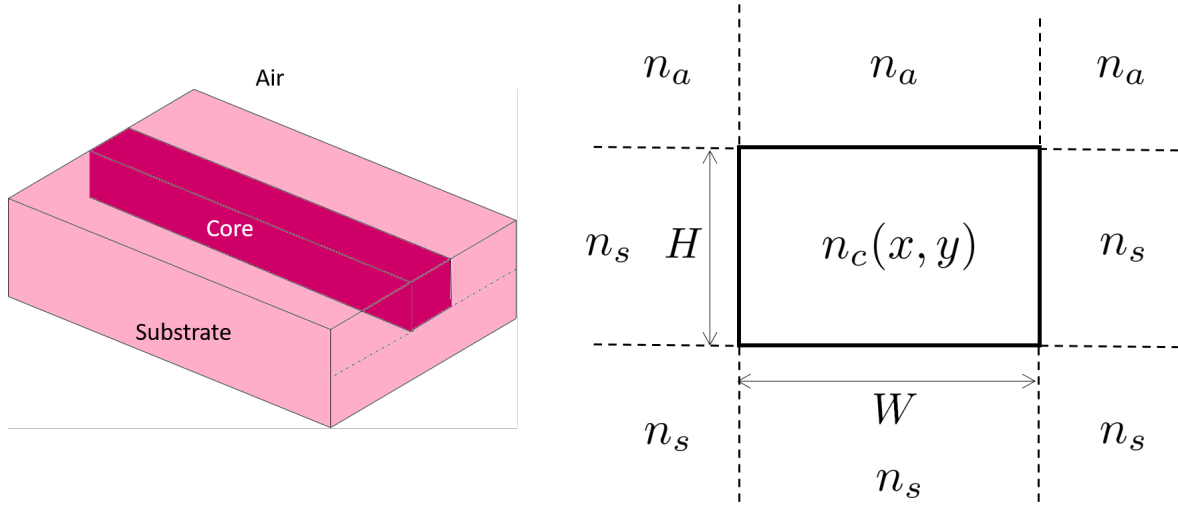
Figure 4.2: Channel waveguide. Left: Rectangular core enclosed by a substrate surrounded by air. Right: Cross section area of the channel waveguide, where W and H are the waveguide width and depth, and $n_{a/s/c}$ is the index of refraction in air/substrate/core.

Another more precise method for the calculation of the modes is *Marcatili's method*, in which the waveguide cross-section is divided as in Fig. (4.2) and the electric field dominant component is decomposed as trigonometric functions inside the core and exponential decay at the core's boundaries [87]. The application of the boundary conditions gives similar characteristic equations to those of the planar waveguide. The modes can be labeled by two integers (m, p) for the depth and width directions, and the modes can then be denoted as $E_{m,p}$ (or $H_{m,p}$ for TM-like modes).

To be precise, the field components that are exactly zero for TE and TM modes in planar waveguides are non-zero in the channel waveguide case. Strictly speaking, the modes in the channel waveguides are hybrid between pure TE and TM modes. However, in weakly guiding structures, as we are considering in this text, the components of the field that are not dominant are small, and therefore these solutions are also referred to as TE and TM modes.

4.2.4 Simulation results

We numerically solved Eq.(4.18) for channel waveguides with the physical parameters of our experiment in order to compute the spatial characteristics of light inside our structures.

The method we used for computing the modes can be found in [88]. It is a *finite difference method*, i.e. the cross-section of Fig. (4.2) is divided into a mesh of points and the differential equations for both electric and magnetic fields, Eq.(4.18), are discretized on the mesh, approximating the derivatives by small differences. The boundary conditions are also con-
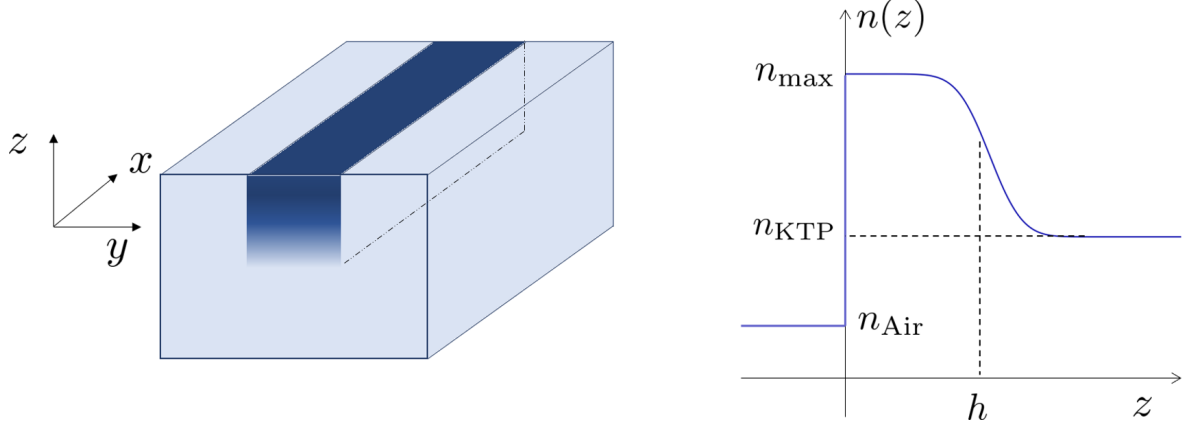
Figure 4.3: Left: Channel waveguide with a grading index profile in the vertical direction. Right: Mathematical form of the index profile using the erf function. Symbols are defined in the text.

sidered, hence obtaining a system of algebraic equations that can be solved computationally.

With the same definition of the cartesian coordinate system that we provided before (propagation along x), the vertical and horizontal polarizations are associated with the TE and TM modes of the channel waveguide. In our particular experiment, however, the polarization of all fields that intervene in the non-linear interaction are polarized vertically (along z) and hence we will focus on the computation of E_{mp}^z modes. The index profile seen by light corresponds in this case to the component of the diagonal permittivity tensor in the z direction, and depends on both transversal directions y and z, i.e. $n = n_z(y, z)$. For generating light at a given wavelength λ we pump with the corresponding second harmonic field, with a wavelength of $\lambda/2$, and we are thus interested in the spatial modes for both the pump wavelength, 780 nm, and the telecom wavelength, 1560 nm.

Furthermore, we will also consider a specific vertical dependence on the index of refraction coming from the fabrication process. The index of refraction depends on the concentration of Rb exchange in the waveguide, that happens vertically. We will therefore consider a uniform index along the horizontal direction (y), that fix the waveguide width, and a gradual index along the vertical direction (z), which defines the waveguide depth. We model the gradual depth as an error function, and define the waveguide depth as the Full Width Half Maximum (FWHM), denoted h, of this distribution. Therefore the index in the waveguide only depends on z and is modelled as:

$$n_z(z) = n_{\max} - \frac{\Delta n}{2}\left(1 + \operatorname{erf}\left(\frac{4(z - h)}{h}\right)\right) \tag{4.26}$$

where $n_{\max}$ is the maximum index of refraction after the exchange and Δn is the index contrast between $n_{\max}$ and the substrate index, n_{KTP}. Hence $\Delta n = n_{\max} - n_{\mathrm{KTP}}$. Eq.(4.26)
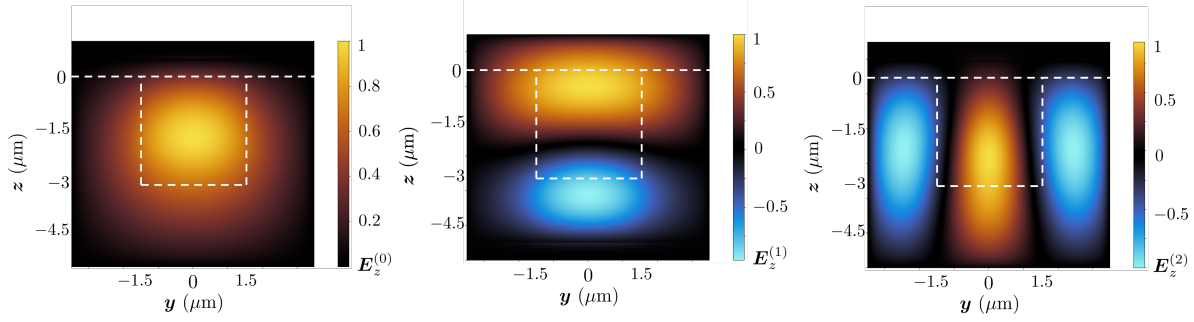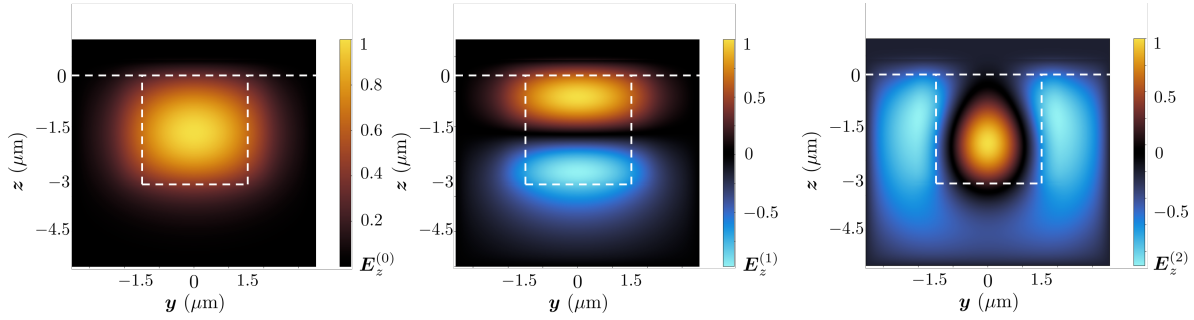
Figure 4.4: First three TE modes (polarization along z) allowed by a KTP waveguide with width 3 μm and depth of 3 μm, for light at $\lambda = 1560$ nm. Computation made based on the finite-element method of [88].

Figure 4.5: First three TE modes (polarization along z) allowed by a KTP waveguide with width 3 μm and depth of 3 μm, for light at $\lambda = 780$ nm. Computation made based on the finite-element method of [88].

is written such that $z = 0$ is the intersection between air and the waveguide, and in $z = h$ the index value is exactly half between the bulk and the waveguide indices. In Fig.(4.3) we show the channel waveguide and the index profile given by Eq.(4.26).

In Fig.(4.4) we show the first three computed TE modes (vertical polarization) allowed by a KTP waveguide with both width and depth of 3 μm using the finite-element method. Similar results are found for the TM modes (horizontal polarization). The dashed lines indicate the surface between the air and the waveguide and the width and depth of the waveguide itself. We see the characteristic waveforms that we expected from the analytic results in planar waveguides. This computation is done at a wavelength of $\lambda = 1560$ nm.

On the other side, in Fig.(4.5) we show the same mode calculation at half the wavelength, $\lambda = 780$ nm. This is done in order to characterize the applied electric field, known as the *pump field*, inside the waveguide.

Together with the modes, we also computed the corresponding mode indices, which allows to obtain the normalized propagation constants of Eq.(4.25). A value of $b = 1$ represents a perfectly guided mode, while $b = 0$ would represent a radiation mode. In Table

$\lambda = 1560$ nm			$\lambda = 780$ nm		
TE Modes (Pol. z)	N	b	**TE Modes** (Pol. z)	N	b
Fundamental Mode	1.83712	0.718	Fundamental Mode	1.85546	0.889
1st Mode	1.82656	-0.343	1st Mode	1.85131	0.547
2nd Mode	1.82109	-0.886	2nd Mode	1.84340	-0.102
TM Modes (Pol. y)			**TM Modes** (Pol. y)		
Fundamental Mode	1.74276	0.806	Fundamental Mode	1.76748	0.650
1st Mode	1.73290	-0.179	1st Mode	1.76441	0.466
2nd Mode	1.72488	-0.976	2nd Mode	1.75499	-0.091

Table 4.1: Numerical modal index and propagation constants for TE and TM spatial modes.

4.1 we summarize the numerical results for both wavelengths and both polarizations. From this data, it is clear that at the telecom wavelength, 1560 nm, only the fundamental mode is allowed. This is because a negative value of the normalized propagation constant, that can occur numerically, represents a non-physical solution and can be discarded. The waveguide is therefore theoretically single-mode at telecom. This is not very surprising since the waveguides were designed for this purpose. For the pump field, however, we find two modal solutions that can be guided inside the structure.

The spatial modes computed in this section are to be compared with the experimental spatial modes measured in the lab when injecting into our actual waveguide chips. In any case, these computed modal fields will serve us in the next Chapter, since they allow to considerably simplify our discussion in the quantum regime.

4.2.5 Experimental waveguide's spatial modes

To finish this Chapter, we present the experimental spatial modes measured both for the pump field and for light at telecom to check that the finite element method employed in the numerical calculation is sufficiently valid for our waveguides.

The actual waveguide KTP chip we used in our experiment was provided by AdvR Inc. [89]. It is 15 mm long and 1.5 mm wide, as can be seen in the chip layout of Fig.(4.6). It containts a total of 30 waveguides, divided in 5 groups. All the waveguides in our chip were 3 μm wide, and their depths vary from one to another following the pattern 2,3 and 4 μm. Therefore, in each group there are two 3x2 μm, two 3x3 μm and two 3x4 μm waveguides, for a total of 6. All groups are identical. We therefore label the waveguides as x.y, where x indicates one of the five groups and y indicates the waveguide number inside the group.

We injected the waveguides with the pump field ($\lambda_0 = 780$ nm, $\Delta\lambda = 2$ nm, pump power in the order of few mW) and measured the spatial modes at the output using an aspherical lens with focal length $f_a = 10$ mm to collimate the beam after the waveguide
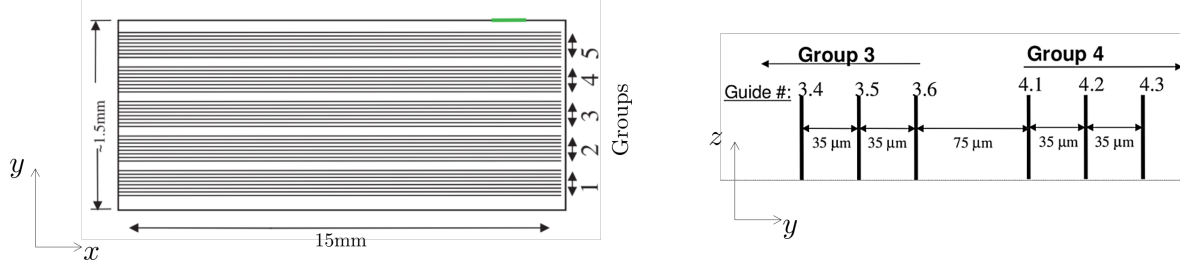
Figure 4.6: Waveguide chip layout, containing a total of 30 waveguides divided in 5 groups. The chips dimensions are also shown.

and an infrared CCD camera. The same procedure was also performed with the light at telecom wavelength ($\lambda_0 = 1560$ nm, $\Delta\lambda = 66$ nm, pump power in the order of few mW). A spectral filter could be placed for telecom light in order to reduce the frequency bandwidth, but we checked that this filter does not alter the measured spatial modes.

The spatial modes depend on some extent on the alignment of the waveguide. In our case, we measured the coupling power (input/output power ratio in the waveguide) and we show here the spatial modes obtained at the maximum value of the waveguide coupling.

In Fig.(4.7) we show six different spatial modes measured at the pump wavelength $\lambda = 780$ nm with a vertical input polarization (TE modes). The measured modes are in good agreement with the numerically computed modes of Fig.(4.5). We observe both the fundamental mode and the first mode in some of the waveguides. We characterized the spatial modes of all 30 waveguides in the chip, that are similar to the modes of Fig.(4.7), for both polarizations.

We performed the same measurement for the spatial modes at telecom wavelength. We show the TE (vertical polarization) modal fields of six different waveguides in Fig.(4.8). Again, we experimentally confirm the approximate single-mode operation of our waveguides at telecom, in good agreement with the numerically computed fundamental mode of Fig.(4.4). Same conclusions are drawn from measurements with the TM (horizontal polarization) modes.

(3x2)μm

1.4

(3x3)μm

2.2

(3x4)μm

3.3
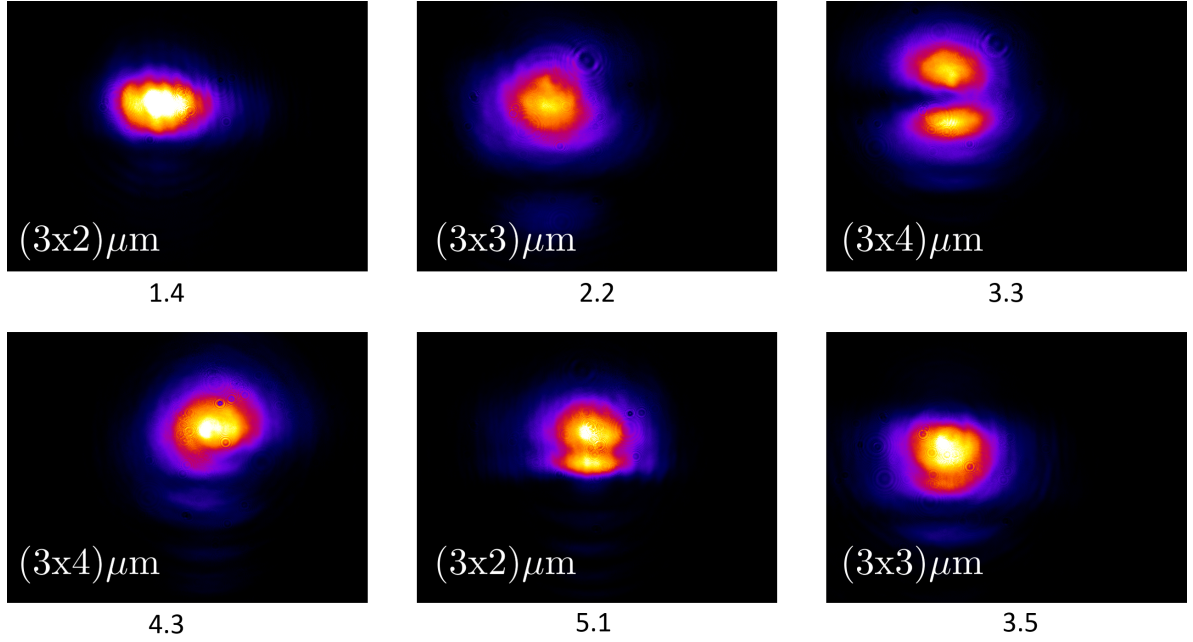
(3x4)μm

4.3

(3x2)μm

5.1

(3x3)μm

3.5

Figure 4.7: Example of 6 experimental spatial modes at the pump wavelength (780 nm) for different waveguide depths. The waveguides are labelled with x.y, where x indicates the group and y numbers the waveguides inside the group.
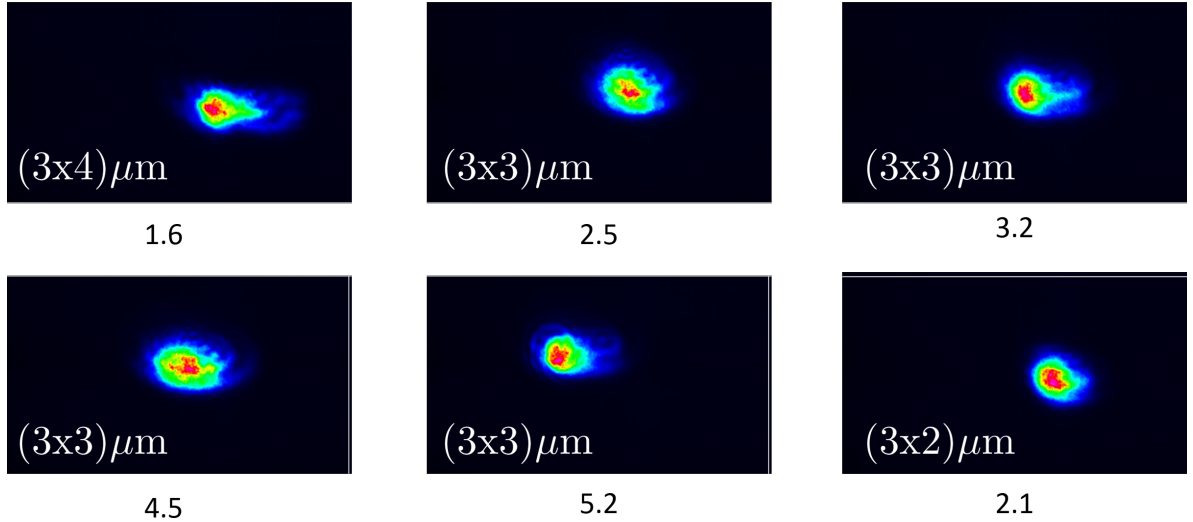
(3x4)μm

1.6

(3x3)μm

2.5

(3x3)μm

3.2

(3x3)μm

4.5

(3x3)μm

5.2

(3x2)μm

2.1

Figure 4.8: Example of 6 experimental spatial modes at telecom wavelength (1560 nm) for different waveguide depths. The waveguides are labelled with x.y, where x indicates the group and y numbers the waveguides inside the group.

Chapter 5

From Classical to Quantum Optics

"See that the imagination of nature is far, far greater than the imagination of man."

– Richard P. Feynman

Contents

In Chapter 4, we have settled the notions needed to understand the frequency conversion processes due to the second order induced polarization in non-linear optics. In this Chapter, we go a step further and bring up the quantum formalism to understand the quantum states of light coming out of non-linear waveguides. In particular, among all the possible second-order effects, we will concentrate in the specific case of Spontaneous Parametric Down Conversion, or SPDC, since it will be the relevant effect for the generation of graph states. The description of the state as graph states will come naturally from the analysis presented in this Chapter.

5.1 The Hamiltonian Approach to Non-linear Optics

5.1.1 Interaction Picture

Usually, there are two approaches taken from Quantum mechanics that allow us to quantize the electromagnetic field in the presence of non-linear interactions. A first possibility is to quantize the field amplitudes from the non-linear Wave Equation, Eq.(4.10) and find the corresponding Heisenberg equations of the quantum operators in the Heisenberg picture, [78]. A second approach, that will be used in this thesis, known as the *hamiltonian approach*, consists in finding a hamiltonian, typically inherited from classical mechanics, and quantize the fields in the hamiltonian from the classical field functions. The interaction picture is adequate in this context, as we will see, and the evolution of the quantum state is given in the form of a Schrödinger equation with the part of the hamiltonian describing the interaction.

In our particular case of an external applied field to a non-linear medium, the classical hamiltonian can be expressed as [90]:

$$H(t) = \frac{1}{2} \int \mathrm{d}\boldsymbol{r}(\boldsymbol{E}^2(\boldsymbol{r},t) + \boldsymbol{B}^2(\boldsymbol{r},t)) - \int \mathrm{d}\boldsymbol{r}\,\boldsymbol{P}(\boldsymbol{r},t) \cdot \boldsymbol{E}(\boldsymbol{r},t) \tag{5.1}$$

where $\boldsymbol{E}$, $\boldsymbol{B}$ and $\boldsymbol{P}$ are respectively the applied electric field, magnetic field, and the induced polarization in the medium. The first term of Eq.(5.1) is a quadratic free hamiltonian[1] describing free propagation of the external field in the medium, denoted H_0, while the second term accounts for the light-matter interaction in the medium and will be denoted as $H_S(t)$.

The phenomenological quantization of this hamiltonian consists in substituing the classical fields by their quantized operators. We obtain thus a hamiltonian of the type:

$$\hat{H}(t) = \hat{H}_0 + \hat{H}_S(t) \tag{5.2}$$

$$\hat{H}_0 = \frac{1}{2} \int \mathrm{d}\boldsymbol{r}(\hat{\boldsymbol{E}}^2(\boldsymbol{r},t) + \hat{\boldsymbol{B}}^2(\boldsymbol{r},t)) \tag{5.3}$$

$$\hat{H}_S(t) = - \int \mathrm{d}\boldsymbol{r}\,\hat{\boldsymbol{E}}(\boldsymbol{r},t)\hat{\boldsymbol{P}}(\boldsymbol{r},t) \tag{5.4}$$

In the interaction picture, the quantum operators evolve following the free hamiltonian $\hat{H}_0$, while the quantum state evolves following the Schrödinger equation on the hamiltonian $\hat{H}_I(t) = e^{i\hat{H}_0 t}\hat{H}_S(t)e^{-i\hat{H}_0 t}$.

The quantum state after the interaction can be calculated by solving the Schrödinger equation with $\hat{H}_I(t)$:

$$|\psi(T)\rangle = \hat{\mathcal{T}} \exp\left(\frac{1}{i\hbar} \int_0^T \hat{H}_I(t)\mathrm{d}t\right) |\psi(0)\rangle \tag{5.5}$$

---

[1]The free hamiltonian H_0 does not depend on time and it is analytically solvable.

Here $\hbar = \frac{2\pi}{h}$ is the reduced Planck's constant and $\hat{\mathcal{T}}$ is the time-ordering operator [91]. We considered that the interaction takes place from time $t = 0$ to $t = T$.

In our particular case of three-wave mixing, we take only the second order non-linear polarization in the light-matter interaction, and hence we can explicitly write the interaction hamiltonian as:

$$\hat{H}_{\mathrm{TWM}}(t) = -\int \mathrm{d}\boldsymbol{r}\, \hat{\boldsymbol{P}}_{\mathrm{NL}}^{(2)}(\boldsymbol{r}, t)\hat{\boldsymbol{E}}(\boldsymbol{r}, t) \tag{5.6}$$

where from now the operators are implicitly assumed to be written in the interaction picture. Recovering our expression of the non-linear polarization from Chapter 4, Eq.(4.9), we have $\hat{\boldsymbol{P}}_{\mathrm{NL}}^{(2)} = \epsilon_0 d_{\mathrm{eff}} \hat{\boldsymbol{E}} \hat{\boldsymbol{E}}$, where d_{eff} is the effective non-linearity (for more information on d_{eff}, see Appendix B). The strategy is therefore to obtain an expression of the electric field operator in the waveguide in order to get a close form of Eq.(5.6) and solve Eq.(5.5) for the quantum state after the interaction.

5.1.2 Field operators in waveguides

For the derivation of the quantized electromagnetic fields in weakly guiding waveguides, we start from associating the electric and magnetic fields to the electromagnetic potential $\hat{\boldsymbol{A}}(\boldsymbol{r}, t)$:

$$\hat{\boldsymbol{E}}(\boldsymbol{r}, t) = \frac{\partial \hat{\boldsymbol{A}}(\boldsymbol{r}, t)}{\partial t} \qquad\qquad \hat{\boldsymbol{B}}(\boldsymbol{r}, t) = \nabla \times \hat{\boldsymbol{A}}(\boldsymbol{r}, t) \tag{5.7}$$

where we also assume the Coulomb gauge, $\nabla \cdot \hat{\boldsymbol{A}}(\boldsymbol{r}, t) = 0$. We divide the vector potential in its positive and negative frequency components:

$$\hat{\boldsymbol{A}}(\boldsymbol{r}, t) = \hat{\boldsymbol{A}}^+(\boldsymbol{r}, t) + \hat{\boldsymbol{A}}^-(\boldsymbol{r}, t) \tag{5.8}$$

Following the lines of [92], we write the quantized vector potential operator derived by Bjorken and Drell for fields propagating in the x direction along a dielectric material as:

$$\hat{\boldsymbol{A}}^+(\boldsymbol{r}, t) = \int \mathrm{d}k_x \mathrm{d}k_y \mathrm{d}k_z \left(\frac{\hbar v_g(\omega)}{16\pi^3 \epsilon_0 c\omega n(\omega)} \right)^{1/2} \hat{a}(\boldsymbol{k}) \sum_{i,j} \boldsymbol{s}_i S'_{i,j}(k_y, k_z) \exp(-i(\omega t - kr)) \tag{5.9}$$

Here $\boldsymbol{k} = (k_x, k_y, k_z)$ is the wavevector of a three-dimensional plane wave, $n(\omega)$ is the index of refraction in the non-linear material, $v_g(\omega) = \partial\omega/\partial k$ is the light's group velocity inside the waveguide, $\boldsymbol{s}_i$ is the unit vector indicating the polarization of the field, and $\hat{a}(\boldsymbol{k})$ is the annihiliation operator of electromagnetic excitations inside the waveguide with associated wavevector $\boldsymbol{k}$. We have also introduced the modal functions $S'_{i,j}(k_y, k_z)$ due to the discretization of the spatial modes allowed by the waveguide structure, defined as:

$$S'_{i,j}(k_y, k_z) = \frac{1}{(2\pi)^2} \int \mathrm{d}y \mathrm{d}z S_{i,j}(y, z) \exp(-ik_y y - ik_z z) \tag{5.10}$$

where $S_{i,j}(y, z)$ are the waveguide's spatial modes that were computed from classical optics in Chapter 4. Therefore, in Eq.(5.10), the index i selects either the set of TE or TM modes in the waveguide, associated with the two possible linear polarizations, while the index j counts the mode order inside the set of TE or TM modes.

The vectorial character of Eq.(5.9) is due to the polarization vector $\boldsymbol{s}_i$, where again, i can take two values, corresponding to horizontal and vertical polarization. However, by symmetry conditions (see Appendix B), the non-linear processes are associated with a specific set of linear polarizations for the three waves involved in the interaction. We can therefore consider in our calculation this single set of TM or TE modes, i.e. specific linear polarizations, fixing the polarization index i, and therefore dropping the vectorial character of the vector potential for the rest of the calculation.

Plugging the definition of the spatial modes, Eq.(5.10), into Eq.(5.9), we find the one dimensional integral:

$$\hat{A}^+(\boldsymbol{r}, t) = 2\pi \sum_j S_j(y, z) \int \mathrm{d}k_x \left(\frac{\hbar v_g(\omega)}{4\pi\epsilon_0 c\omega n(\omega)} \right)^{1/2} \hat{a}(k_x) \exp(-i(\omega t - k_x x)) \quad (5.11)$$

We now transform the integral over k_x into an integral over frequency by the change of variables:

$$\mathrm{d}k_x = \frac{\mathrm{d}\omega}{v_g(\omega)} \qquad \hat{a}(k_x) = \sqrt{v_g(\omega)}\hat{a}(\omega) \qquad (5.12)$$

obtaining:

$$\hat{A}^+(\boldsymbol{r}, t) = 2\pi \sum_j S_j(y, z) \int \mathrm{d}\omega \left(\frac{\hbar}{4\pi\epsilon_0 c\omega n(\omega)} \right)^{1/2} \hat{a}(\omega) \exp(-i(\omega t - k_x x)) \quad (5.13)$$

We note here that, in order to account for propagation in a waveguide, we know from Chapter 4 that the values of k_x are actually the propagation constants $\{\beta_j\}$ associated to the TE or TM set of spatial modes $S_j(y, z)$.

The electric field operator can be obtained by computing the partial derivative of Eq.(5.13) with respect to time:

$$\hat{E}^+(\boldsymbol{r}, t) = i2\pi \sum_j S_j(y, z) \int \mathrm{d}\omega \sqrt{\frac{\hbar\omega}{4\pi\epsilon_0 cn(\omega)}} \hat{a}(\omega) \exp(-i(\omega t - \beta_j x)) \quad (5.14)$$

which is the final expression we need for the electric field operator in the non-linear waveguide, also used in this form in [93].
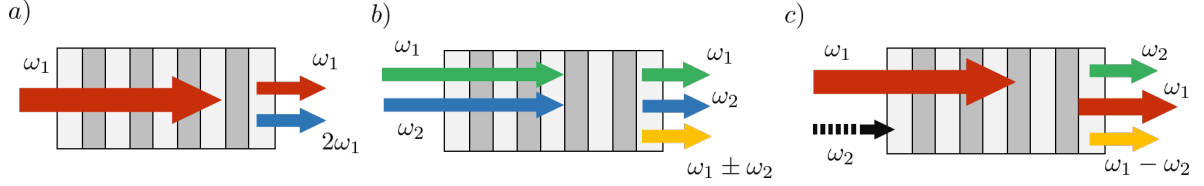
Figure 5.1: Schematics of different $\chi^{(2)}$ processes. a) SHG: In the classical approach, a single monochromatic input field at frequency ω_1 can produce radiation at double the frequency, $2\omega_1$. b) SFG/DFG: if the input field contains two frequency components at ω_1 and ω_2, it can produce radiation at the sum or difference frequencies, $\omega_1 \pm \omega_2$. c) PG: quantum mechanics allows the interaction between the input field and the vacuum field, that has an infinite frequency spectrum. Generation of new frequencies is thus possible even without the presence of a second classical input field.

5.1.3   Three-wave mixing quantum hamiltonian

According to the classical framework that we have developed in Chapter 4, a monochromatic input field in a $\chi^{(2)}$ crystal can only produce a SHG process (see Eq.(4.12)). Furthermore, in order to have SFG or DFG, the input field should contain more than one frequency component (see Eq.(4.14)). The quantum treatment brings a new three-wave mixing nonlinear effect to the list, the *parametric gain* (PG). In essence, a single monochromatic input field can mix with the quantum vacuum fluctuations in the non-linear crystal and therefore produce new frequency components that cannot be classically explained. In other words, the quantum vacuum state can serve as a seed in a DFG process with an input field if the conservation of energy and phasematching conditions are favorable to the process.

The different three-wave mixing effects are depicted in Fig.(5.1) for clarity. In Quantum Optics, the effect of parametric gain is also known as *Parametric Down Conversion* (PDC).

Let's now derive the three-wave mixing hamiltonian starting from Eq.(5.6). First of all, we will consider the input field as a strong classical optical field that does not get depleted during the process and that we will call the pump field, E_p, and an induced polarization in the medium excited by the two quantum fields, $\hat{E}_1$ and $\hat{E}_2$. It is useful to divide each field into the positive and negative frequency components, such that:

$$E_p(\boldsymbol{r}, t) = E_p^+(\boldsymbol{r}, t) + E_p^-(\boldsymbol{r}, t) \tag{5.15}$$

$$\hat{E}_1(\boldsymbol{r}, t) = \hat{E}_1^+(\boldsymbol{r}, t) + \hat{E}_1^-(\boldsymbol{r}, t) \tag{5.16}$$

$$\hat{E}_2(\boldsymbol{r}, t) = \hat{E}_2^+(\boldsymbol{r}, t) + \hat{E}_2^-(\boldsymbol{r}, t) \tag{5.17}$$

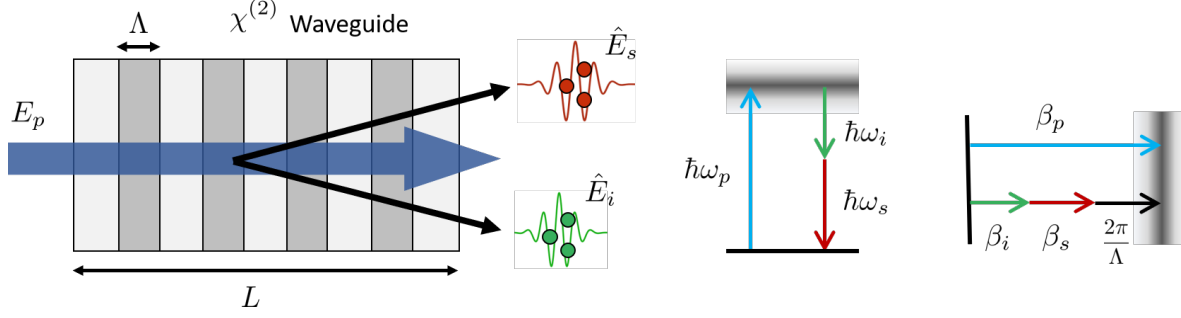Plugging this information into Eq.(5.6) we obtain:

Figure 5.2: Schematics of type II PDC, where two photon fields, called signal and idler, are created at expense of the pump field, here considered a classical object. Conservation of energy, ensuring $\omega_p = \omega_s + \omega_i$, should be fulfilled, while the quasi-phasematching condition $(\beta_p = \beta_s + \beta_i + \frac{2\pi}{\Lambda})$ is also necessary to have an efficient process.

$$\hat{H}_{\text{TWM}}(t) = -\epsilon_0 \int \mathrm{d}\boldsymbol{r} \left(d_{\text{eff}} E_p^+(\boldsymbol{r}, t) \left(\hat{E}_1^-(\boldsymbol{r}, t) \right)^2 + d_{\text{eff}} E_p^+(\boldsymbol{r}, t) \hat{E}_1^-(\boldsymbol{r}, t) \hat{E}_2^-(\boldsymbol{r}, t) \right.$$

$$\left. + d_{\text{eff}} E_p^+(\boldsymbol{r}, t) \hat{E}_1^+(\boldsymbol{r}, t) \hat{E}_2^-(\boldsymbol{r}, t) + \text{h.c.} \right) \quad (5.18)$$

Coming back to the expression of the field operator of Eq.(5.14), we observe that $\hat{E}^+$ is related to the annhilation operator of field excitations, $\hat{a}$, while $\hat{E}^-$ is associated with the creation operator of excitations, i.e. photons, $\hat{a}^\dagger$. This fact helps us to understand the different terms of Eq.(5.18) and associate them to the underlying three-wave mixing effects described before. For instance, in the first term of Eq.(5.18), two identical excitations are created at the cost of destroying a single excitation from the pump field, which corresponds to a PDC process of *type I*[2]. The second term indicates the creation of two different photon fields from the pump field, which will lead to a PDC process of the so-called *type II*. For historic reasons, the two photon fields in the type II case are called *signal* and *idler* fields, and are denoted respectively with the subscripts s and i. Finally, in the last term, a photon field is created from both a pump field and an additional seed field excitations, which corresponds to a SFG or DFG process depending on the frequency of the new field.

5.2 Ultrafast Parametric Down Conversion

5.2.1 Type II Hamiltonian

In this section, we are interested in calculating the quantum properties of light after a Parametric Down Conversion interaction in the waveguides. Given that type I PDC can be

---

[2]Note that the reverse process, contained among the h.c. terms, corresponds to SHG.

formally seen as an specific case of type II, in which the two quantum fields are identical ($\hat{E}_1 = \hat{E}_2$) we will from now on restrict our attention only to the hamiltonian accounting for type II[3], i.e., for us:

$$\hat{H}_{\mathrm{PDC}}(t) = -\epsilon_0 \int \mathrm{d}\boldsymbol{r} d_{\mathrm{eff}} E_p^+(\boldsymbol{r},t) \hat{E}_1^-(\boldsymbol{r},t) \hat{E}_2^-(\boldsymbol{r},t) + \mathrm{h.c.} \tag{5.19}$$

As mentioned above, we consider the pump field to be a classical field that is undepleted by the non-linear effect. Hence, the field E_p is considered an ultrashort train of light pulses traveling along x through the waveguide, that can be written as:

$$E_p^+(x,y,z,\omega_p) = \sum_k A_{p,k} S_{p,k}(y,z) \int \mathrm{d}\omega_p \alpha_k(\omega_p) \exp(-i\omega_p t - \beta_{p,k} x) \tag{5.20}$$

where $S_{p,k}(y,z)$ are the pump spatial modes with corresponding propagation constants $\beta_{p,k}$ and peak amplitudes $A_{p,k}$. Note that this expression is the classical counterpart of our field operator of Eq.(5.14) including more than a single spatial-mode. $\alpha_k(\omega_p)$ is the pump envelope spectrum,[4] and we have accounted for the fact that different spatial modes could have different spectra, hence the index k.

We can substitute the classical pump in Eq.(5.20) and the electric field operators in Eq.(5.14) into Eq.(5.19), obtaining:

$$\hat{H}_{\mathrm{PDC}}(t) = 4\epsilon_0 \pi^2 \left(\sum_{k,j,m} \int \mathrm{d}x\mathrm{d}y\mathrm{d}z \int \mathrm{d}\omega_p \mathrm{d}\omega_s \mathrm{d}\omega_i d_{\mathrm{eff}} A_{p,k} \right.$$

$$S_{p,k}(y,z) S_{s,j}^*(y,z) S_{i,m}^*(y,z) \sqrt{\frac{\hbar\omega_s}{4\pi\epsilon_0 cn(\omega_s)}} \sqrt{\frac{\hbar\omega_i}{4\pi\epsilon_0 cn(\omega_i)}}$$

$$\alpha_k(\omega_p) \exp\left(-i(\omega_p - \omega_s - \omega_i)t + i(\beta_{p,k} - \beta_{s,j} - \beta_{i,m})x\right) \hat{a}_j^\dagger(\omega_s) \hat{b}_m^\dagger(\omega_i) + \mathrm{h.c.} \Bigg) \tag{5.21}$$

where we have introduced the spatial modes of signal, $S_{s,j}(y,z)$, and idler, $S_{s,j}(y,z)$. The labels k,j,m are associated to the spatial modes of pump, signal and idler.

A first simplification to this hamiltonian can be achieved with the Slowly Varying Amplitude (SVE) approximation. If we assume that the carrier frequency (also known as the central frequency) oscillates much faster than the frequency envelope for the rest of the frequencies involved in the spectrum (i.e. the central frequency is much smaller than the frequency bandwidth), then the terms in square roots of Eq.(5.21) are approximately constants

---

[3]In any case, the calculation of the quantum states would follow the same lines for the rest of the three-wave mixing processes.

[4]A Fourier Transform of $\alpha(\omega)$ would give us the expression of the electric field as a function of time instead of frequency.

in the relevant frequency integration limits and can be taken out of the integral, substituting the frequency variables inside the square roots by their respective central frequencies, that will be denoted as $\omega_{s,0}$ and $\omega_{i,0}$ respectively for signal and idler.

Additionally, we define the overlap integral between combinations of spatial modes as:

$$\mathcal{S}_{kjm} = \left(\int \mathrm{d}y\mathrm{d}z S_{p,k}(y,z) S^*_{s,j}(y,z) S^*_{i,m}(y,z) \right)^2 \tag{5.22}$$

Note that these integrals can be computed from the classical spatial mode simulation presented in Chapter 4.

We also define the frequency and phasematching mismatches as:

$$\Delta\omega = \omega_p - \omega_s - \omega_i \tag{5.23}$$

$$\Delta\beta_{kjm}(\omega_s, \omega_i) = \beta_{p,k}(\omega_s + \omega_i) - \beta_{s,j}(\omega_s) - \beta_{i,m}(\omega_i) + \frac{2\pi}{\Lambda} \tag{5.24}$$

Finally, we also note that the integral over the x variable in Eq.(5.21) can already be solved, considering that the interaction is *on* only for the time that the light pulses go from $x = -L/2$ to $x = L/2$, where L is the waveguide's length:

$$\int_{-L/2}^{L/2} \mathrm{d}x \exp(i\Delta\beta_{kjm}x) = L\mathrm{sinc}\left(\Delta\beta_{kjm}L/2\right) \equiv \phi_{kjm}(\omega_p, \omega_s, \omega_i) \tag{5.25}$$

where we have defined the phasematching function $\phi_{kjm}(\omega_p, \omega_s, \omega_i)$. [5]

With all of the considerations, the hamiltonian of Eq.(5.21) reduces to:

$$\hat{H}_{\mathrm{PDC}}(t) = \sum_{k,j,m} \int \mathrm{d}\omega_p \mathrm{d}\omega_s \mathrm{d}\omega_i \mathcal{C}_{kjm} \alpha_k(\omega_p) \phi_{kjm}(\omega_p, \omega_s, \omega_i) e^{-i\Delta\omega t} \hat{a}^\dagger_j(\omega_s) \hat{b}^\dagger_m(\omega_i) + \mathrm{h.c.}$$

$$\tag{5.26}$$

where we have defined $\mathcal{C}_{kjm}$ as:

$$\mathcal{C}_{kjm} = -4\epsilon_0 \pi^2 d_{\mathrm{eff}} L \sqrt{\mathcal{S}_{kjm}} \sqrt{\frac{\hbar\omega_{s,0}}{4\pi\epsilon_0 cn(\omega_{s,0})}} \sqrt{\frac{\hbar\omega_{i,0}}{4\pi\epsilon_0 cn(\omega_{i,0})}} \tag{5.27}$$

Once we have the hamiltonian, the quantum state follows the evolution described in Eq.(5.5), that we rewrite again:

$$|\psi(T)\rangle = \hat{\mathcal{T}} \exp\left(\frac{1}{i\hbar} \int_0^T \hat{H}_{\mathrm{PDC}}(t)\mathrm{d}t \right) |\psi(0)\rangle \tag{5.28}$$

---

[5]Note that the frequency dependence of the phasematching function comes through the dispersion relations $\beta_k = \beta_k(\omega)$.

Firstly, we will ignore the possible effects of the time ordering operator $\hat{\mathcal{T}}$. For more information about time ordering effects see [94, 95, 96, 97, 98]. Secondly, we can extend the boundaries of the time integration in Eq.(5.28) to $\pm\infty$. The argument for doing so is that the state $|\psi(0)\rangle$ is fixed before $t = 0$, as well as $|\psi(T)\rangle$ after $t = T$, since the interaction term is only *on* when light travels through the waveguide.

Furthermore, the initial state $|\psi(0)\rangle$ is the vacuum state, since there are no quantum excitations created before the interaction[6]. Because we are not seeding with any extra input field, this type of Parametric Down Conversion is also called *Spontaneous Parametric Down Conversion* (SPDC) in the literature. Thus, we calculate the quantum state after the interaction, that we denote $|\psi(T)\rangle \equiv |\psi\rangle$, as:

$$|\psi\rangle = \exp\left(\frac{1}{i\hbar}\int_{-\infty}^{\infty}\hat{H}_{\text{PDC}}(t)\mathrm{d}t\right)|0\rangle \tag{5.29}$$

The time integral of this equation can readily be done as the only time dependence in the hamiltonian of Eq.(5.26) is inside the exponential function:

$$\int_{-\infty}^{\infty}\mathrm{d}te^{-i(\Delta\omega)t} = 2\pi\delta(\omega_p - \omega_s - \omega_i) \tag{5.30}$$

where $\delta(x)$ is the Dirac delta function.

This in turn allows us to perform the integration in the pump frequency using the sifting property of the Dirac delta[7], and assures the conservation of energy since we extract the integration function (which is $\alpha_k(\omega_p)\phi_{kjm}(\omega_p, \omega_s, \omega_i)$ evaluated in $\omega_p = \omega_s + \omega_i$). We also define the *joint-spectral amplitude* (JSA) as the following function:

$$J_{kjm}(\omega_s, \omega_i) = \alpha_k(\omega_s + \omega_i)\phi_{kjm}(\omega_s, \omega_i) \tag{5.31}$$

Note that despite its name, J_{kjm} contains not only all the information about the spectral properties of the state, but also about the spatio-temporal coupling, mediated through the indices kjm.

The quantum state after these considerations writes[8]:

$$|\psi\rangle = \exp\left(\sum_{kjm}\mathcal{C}_{kjm}\int\mathrm{d}\omega_s\mathrm{d}\omega_i J_{kjm}(\omega_s, \omega_i)\hat{a}_j^\dagger(\omega_s)\hat{b}_m^\dagger(\omega_i) + \text{h.c.}\right)|0\rangle \tag{5.32}$$

---

[6]Rigorously speaking, the initial state is a classical coherent state in a certain frequency mode and vacuum in the rest of the modes, but the hamiltonian does not affect the classical field, since we are considering it to be undepleted.

[7]The 2π factor gets absorbed into the value of C_{kjm} in Eq.(5.27).

[8]Note that we also absorbed the factor $1/(i\hbar)$ into the constant $\mathcal{C}_{kjm}$.

5.2.2 Schmidt Decomposition

The next step in the derivation of the quantum state is to perform a so-called Schmidt decomposition of the joint-spectral amplitude $J_{kjm}(\omega_s, \omega_i)$. This decomposition was introduced by Everett [99] in 1957 and advanced later [100] in order to study correlations in bipartite quantum systems. In 2000, Law, Walsmley and Eberly transferred the method to the time-frequency degree of freedom [101].

A Schmidt decomposition of a two-dimensional function $f(\omega_s, \omega_i)$ consists in writing the function as a weighted sum of one-dimensional basis functions, $h(\omega_s)$ and $g(\omega_i)$:

$$f(\omega_s, \omega_i) = \sum_l \sqrt{\lambda_l} h_l(\omega_s) g_l(\omega_i) \tag{5.33}$$

The weights are called *Schmidt coefficients*, fulfilling $\sum_l \lambda_l = 1$. There is a unique way of performing a Schmidt decomposition of a given function. This tool is highly powerful in the study of bipartite quantum systems, since the amount of entanglement, (pair-wise quantum correlations) can be derived from the decomposition. For instance, it is clear that if the decomposition yields only one term, the general two-dimensional function can be written as a product of two independent functions, and hence there is no entanglement between the two parts of the bipartite system.

Applying the Schmidt decomposition to the JSA yields:

$$J_{kjm}(\omega_s, \omega_i) = \sum_l \sqrt{\lambda_l} h_{l,kjm}(\omega_s) g_{l,kjm}(\omega_i) \tag{5.34}$$

which leads naturally to the definition of the so-called *broadband* or *time-frequency mode operators*:

$$\hat{A}^\dagger_{l,kjm} = \int \mathrm{d}\omega_s h_{l,kjm}(\omega_s) \hat{a}^\dagger_j(\omega_s) \tag{5.35}$$

$$\hat{B}^\dagger_{l,kjm} = \int \mathrm{d}\omega_i g_{l,kjm}(\omega_i) \hat{b}^\dagger_m(\omega_i) \tag{5.36}$$

where the operator $\hat{A}^\dagger_{l,kjm}$ (resp. $\hat{B}^\dagger_{l,kjm}$) creates a quantum excitation of the electromagnetic field, i.e. a photon, in the frequency mode described by $h_{l,kjm}(\omega_s)$[9] (resp. $g_{l,kjm}(\omega_i)$). Another way of looking at this transformation is as a basis change from the plane-wave basis, in which we create pure plane wave frequency excitations via $\hat{a}_j(\omega_s)$ and $\hat{b}_m(\omega_i)$, to a new basis where the excitations are created by $\hat{A}^\dagger_{l,kjm}(\omega_s)$ and $\hat{B}^\dagger_{l,kjm}(\omega_i)$, and Eq.(5.36) is the relation between the two bases. The basis defined by operators $\{\hat{A}^\dagger_{l,kjm}, \hat{B}^\dagger_{l,kjm}\}$ is also known as the *supermode basis* [102].

---

[9]The photon created in this way is associated with the combination of three spatial modes $S_k(\omega_p)$, $S_j(\omega_s)$ and $S_m(\omega_i)$ for pump, signal and idler.

Plugging the new information into Eq.(5.32), the quantum state in the supermode basis reads:

$$|\psi\rangle = \exp\left(\sum_{l,kjm} \sqrt{\lambda_l} \mathcal{C}_{kjm} \hat{A}^\dagger_{l,kjm} \hat{B}^\dagger_{l,kjm} + \text{h.c.}\right)|0\rangle \tag{5.37}$$

We note that all the information about the state is enclosed in the joint-spectral amplitude $J_{kjm}(\omega_s, \omega_i)$, and this function depends on the Schmidt coefficients and the supermode basis, Eq.(5.34).

5.2.3   Spatial Modes Overlap

In the general case, the spatial and temporal modes are correlated via the mixing of the temporal index l with the spatial mode indices k,j and m. In mathematical form, this fact is translated into having a joint-spectral amplitude that depends on the spatial mode combination, essentially coming from the mismatch in the propagation constants, that are both spatially mode-dependent and frequency dependent. Explicitly, the equations for the joint-spectral amplitude and the mismatch, Eq.(5.24) and Eq.(5.25), are:

$$J_{kjm}(\omega_s, \omega_i) = \alpha_k(\omega_s + \omega_i)\text{sinc}\left(\frac{\Delta\beta_{kjm}(\omega_s, \omega_i)L}{2}\right) \tag{5.38}$$

$$\Delta\beta_{kjm}(\omega_s, \omega_i) = \beta_{p,k}(\omega_s + \omega_i) - \beta_{s,j}(\omega_s) - \beta_{i,m}(\omega_i) + \frac{2\pi}{\Lambda} \tag{5.39}$$

More insights and consequences of these spatio-temporal correlations in bulk crystals are given in [103], and in the waveguide context in [104]. In general, spatio-temporal correlations complicate the theoretical analysis and are detrimental for the experimental state generation, since one typically focuses independently either on the spatial or temporal degree of freedom. This is a reason for the convenience of single(spatial)-mode waveguides.

As we have seen in Chapter 4, our waveguides are approximately single(spatial)-mode for telecom wavelength,which is the central wavelength for our signal and idler fields. The fundamental mode was depicted in Fig.(4.4). Hence, the indices j and m are just $j = m = 0$ in our case, where 0 labels the fundamental mode.

Moreover, for the pump field, at a central wavelength of 780 nm, our calculation gives two spatial modes allowed by the waveguide, which are the two modes at the left of Fig.(4.5), and therefore $k = 0, 1$.

Hence, we are left with only two spatial mode overlap integrals, Eq.(5.22), namely $\mathcal{S}_{0,0,0}$ and $\mathcal{S}_{1,0,0}$. These integrals can be computed given the numerical spatial fields from the finite-element method. Since the field is normalized by the program, the intrinsic value of the integrals is not meaningful, but their ratio tells us the relative contribution to the process of one with respect to the other. We obtain:

$$\frac{\mathcal{S}_{1,0,0}}{\mathcal{S}_{0,0,0}} = 0.0057 \tag{5.40}$$

which means that the second order spatial mode of the pump is practically not relevant in our situation. This result is logical, since the first numerically computed spatial modes are similar for pump and signal/idler fields, and they form an orthogonal basis for every wavelength.

In conclusion, the only expected contribution from the spatial modes in our waveguides is given by the combination of the fundamental modes for pump, signal and idler. We have therefore $k = j = m = 0$ and hence we can drop the spatial indices for the rest of this manuscript.

5.3 Quantum States for Type II SPDC

5.3.1 EPR Correlations

Dropping the spatial mode indices in Eq.(5.37) the quantum state now is simplified to:

$$|\psi\rangle = \exp\left(\sum_l \sqrt{\lambda_l}\mathcal{C}\hat{A}_l^\dagger\hat{B}_l^\dagger + \text{h.c.}\right)|0\rangle \tag{5.41}$$

The scope of this section is to understand this state. In order to do that, let's suppose for the moment that we only have a single frequency pair of modes, $\lambda_l = \lambda = 1$. In that case we can also drop the temporal index l, obtaining the state:

$$|\psi\rangle = \exp\left(\mathcal{C}\hat{A}^\dagger\hat{B}^\dagger + \text{h.c.}\right)|0\rangle \equiv \hat{S}^{(AB)}(\mathcal{C})|0\rangle \tag{5.42}$$

where we have introduced the operator $\hat{S}^{AB}(\mathcal{C})$, called the *two-mode squeezing operator*, for reasons that will be clear in the following.

If we consider the interaction to be weak, we can approximate the operator acting on vacuum as:

$$\exp\left(\mathcal{C}\hat{A}^\dagger\hat{B}^\dagger\right) \sim \mathbb{I} + \mathcal{C}\hat{A}^\dagger\hat{B}^\dagger \tag{5.43}$$

where $\mathbb{I}$ is the identity operator. It is easy to see that this approximated operator applied to vacuum gives the state:

$$|\psi\rangle \simeq \left(\mathbb{I} + \mathcal{C}^*\hat{A}\hat{B} + \mathcal{C}\hat{A}^\dagger\hat{B}^\dagger\right)|0\rangle = \mathcal{N}(|0\rangle + \mathcal{C}|1,1\rangle_{\text{AB}}) \tag{5.44}$$

where $\mathcal{N}$ is a factor introduced for normalizing the state $|\psi\rangle$. By postselection using single photon detectors we can remove the vacuum state from Eq.(5.44). The state vector $|1,1\rangle_{\text{AB}}$ represents a pair of photons associated to the field operators $\hat{A}$ and $\hat{B}$, and therefore in temporal modes $h(\omega_s)$ and $g(\omega_i)$ respectively. The interaction hamiltonian is therefore creating independent photon pairs in defined frequency modes $h(\omega_s)$ and $g(\omega_i)$. This separable

state is widely used in Quantum Optics experiments to create heralded single-photon emitters, where the detection of one photon in mode h heralds the emission of the additional single-photon in mode g.

It is interesting to see what happens in the completely degenerate case, where the two photons are indistinguishable, so $h = g$ as well[10]. If we then make the following basis change to new field operators $\hat{C}$ and $\hat{D}$:

$$\hat{C} = \frac{1}{\sqrt{2}}(\hat{A} + \hat{B}) \tag{5.45}$$

$$\hat{D} = \frac{1}{\sqrt{2}}(-\hat{A} + \hat{B}) \tag{5.46}$$

It is easy to verify that the state in the new basis reads:

$$|\psi\rangle = |11\rangle_{\mathrm{AB}} = \frac{|20\rangle_{CD} - |02\rangle_{CD}}{\sqrt{2}} \tag{5.47}$$

Since the transformation of Eq.(5.46) corresponds to a beamsplitter transformation, this result means that if we make the two single-photons interfere in a balanced beamsplitter (BS), then we will always have both photons at one of the output of the BS, a phenomenon known as the *Hong-Ou-Mandel effect* [105][11]. The process is depicted in Fig.(5.3). The state of Eq.(5.47) is a maximally entangled state that is a type of the so-called *Bell states*. This state presents correlations of the *EPR type*, first proposed by Einstein Podoslsky and Rosen in 1935, [106]. For this reason, these states are also called *EPR states*. Bell states are the cornerstones in a great number of Quantum Optics and Quantum Information experiments. Note that in this description the discrete nature of photons is taken into account for the quantum correlations. Quantum information encoded in those states have a finite number of eigenvalues, and for this reason we talk about *Discrete variable* (DV) entangled states.

In this thesis, however, we are interested in Continuous Variable correlations. Nevertheless, we will see that the essence of the transformation derived for DV also applies in the CV case. The main difference is the fact that we do not work with single-excitations of the fields, but rather with the field properties themselves. In DV, as already stated in Part I of this thesis, the information is encoded in the naturally discrete set of observables (polarization, for instance), while in CV, the information resides in the noise properties of the fields, i.e. in the statistical moments of the quadratures. In fact, the Continuous Variable version of the EPR state can be obtained simply by not approximating the evolution operator of Eq.(5.43) for a weak interaction and looking at the field quadrature correlations

---

[10]In practice, it is experimentally challenging to have a single source giving identical photons. Another way of proceeding is to have two single-photon sources and herald one photon from each of them.

[11]Note that if the two photons are distinguishable, then they would not interfere in the BS and no quantum correlations would be observed in the state. This is why if $h \neq g$, we obtain a separable quantum state from the single-photon source.
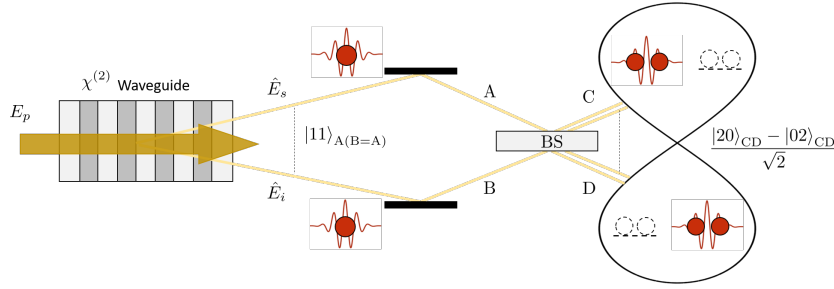
Figure 5.3: Schematics of the generation of entanglement in DV. A degenerate SPDC source ideally generates an indistinguishable pair of photons that are mixed in a balanced beam-splitter (BS). The result is a type of Bell state showing EPR correlations. For more information see text.

of the total output quantum state. We are therefore looking at the correlations in the total signal and idler fields. Since the quadratures have an infinite eigenvalue spectrum, the total Hilbert space in this case is infinite-dimensional, and hence the name Continuous Variables. For clarity, in our current context, we define the quadrature operators associated with the quantum fields $\hat{A}$ and $\hat{B}$ [12] as:

$$\hat{Q}_A = \hat{A} + \hat{A}^\dagger \qquad \hat{Q}_B = \hat{B} + \hat{B}^\dagger \tag{5.48}$$

$$\hat{P}_A = i(\hat{A}^\dagger - \hat{A}) \qquad \hat{P}_B = i(\hat{B}^\dagger - \hat{B}) \tag{5.49}$$

All the statistical moments of our state in Eq.(5.42), and in particular the mean value and the quadratures variances, can be found by the action of the two-mode squeezing operator, $\hat{S}^{(AB)}$, on the field operators $\hat{A}$ and $\hat{B}$. It can be shown [107] that, by defining $|\mathcal{C}| \equiv R$ and $\text{Arg}(\mathcal{C}) \equiv \varphi$, where $\text{Arg}(x)$ means the argument of x, we have the following relations:

$$\hat{S}^{(AB)\dagger}(\mathcal{C})\hat{A}\hat{S}^{(AB)}(\mathcal{C}) = \hat{A}\cosh(R) - \hat{B}^\dagger e^{i\varphi}\sinh(R) \tag{5.50}$$

$$\hat{S}^{(AB)\dagger}(\mathcal{C})\hat{B}\hat{S}^{(AB)}(\mathcal{C}) = \hat{B}\cosh(R) - \hat{A}^\dagger e^{i\varphi}\sinh(R) \tag{5.51}$$

With these relations it is easy to check that the mean quadrature values of $|\psi\rangle$ vanish:

$$\langle\hat{Q}_A\rangle_\psi = \langle\hat{P}_A\rangle_\psi = \langle\hat{Q}_B\rangle_\psi = \langle\hat{P}_B\rangle_\psi = 0 \tag{5.52}$$

and the quadratures variances, defined as $\Delta\hat{Q}_A^2 \equiv \langle\hat{Q}_A^2\rangle - \langle\hat{Q}_A\rangle^2$ (and equivalently for the rest of quadratures) are given by:

$$\Delta\hat{Q}_A^2 = \Delta\hat{P}_A^2 = \Delta\hat{Q}_B^2 = \Delta\hat{P}_B^2 = \cosh^2(R) + \sinh^2(R) \tag{5.53}$$

---

[12]They have been already introduced in the context of Chapter 1, see Eq.(1.8).

The variances found here are always above the quantum limit (which in our units and definition of the quadratures is equal to 1). Therefore, because of the symmetry of the variances in Eq.(5.53), the state, from the point of view of the quadratures of each individual bipartition A and B, is a so-called *thermal state*. If this set of quadratures are measured a number of times, the statistics would show a gaussian centered at the origin with a variance that is always greater than the vacuum noise. Hence, the thermal states are typically represented in phase-space by a ball-like object with a diameter bigger than the quantum limit (of 1, in our units).

However, if we now perform the same change of basis that we have done in the DV case, Eq.(5.46), corresponding to a beamsplitter transformation, we can define the new quadratures $\hat{Q}_C, \hat{P}_C, \hat{Q}_D$ and $\hat{P}_D$ as in Eq.(5.49) with $\hat{C}$ and $\hat{D}$ fields. For our state $|\psi\rangle$, the mean values of the new quadratures are also zero and the respective variances can be readily calculated to be:

$$\Delta\hat{Q}_C^2 = \Delta\hat{Q}_D^2 = \exp(-2R)\cos^2(\varphi) + \exp(2R)\sin^2(\varphi)$$
$$\Delta\hat{P}_C^2 = \Delta\hat{P}_D^2 = \exp(-2R)\sin^2(\varphi) + \exp(2R)\cos^2(\varphi) \tag{5.54}$$

and some of the quadratures go below the Heisenberg limit of 1 (what quadrature depends on the value of φ). When the variance of a field quadrature goes below the Heisenberg limit, at the cost of the variance of the conjugate variable to increase by the same amount, we say that the former quadrature is *squeezed*, and the resulting state is a *squeezed* state (and hence the name we gave to the quantum operator $\hat{S}^{(AB)}$). The amount of squeezing for the given quadrature is given by R, that is known as the *squeezing factor* or *squeezing coefficient*. This result shows that in a two-mode squeezed state, the quadratures themselves are not squeezed, but the correlations between the quadratures are, since, from the point of view of the C and D bipartition, we have two single-mode squeezed states defined by Eq.(5.54).

The correspondence with the EPR-type of correlations in DV is clear if we take the limit of infinite squeezing in the correlations: R $\to \infty$ [13]. Then:

$$\Delta\hat{Q}_C^2 = \Delta\hat{Q}_D^2 \to 0$$
$$\Delta\hat{P}_C^2 = \Delta\hat{P}_D^2 \to \infty \tag{5.55}$$

which means that measurements of the $\hat{Q}_C$ quadrature are completely correlated with measurements of the $\hat{Q}_D$ quadrature, while the conjugate $\hat{P}_{C/D}$ quadratures would yield a completely random result when measured. These are the original EPR correlations described in [106]. In general, the level of squeezing, R, indicates the strength of the EPR correlations.

Therefore, if both modes of a two-mode squeezed state of the form of Eq.(5.42) are sent to a balanced BS, we would obtain two uncorrelated single-mode states with squeezed quadrature variances (of the form Eq.(5.54)). Since the mean value of the quadratures of this state

---

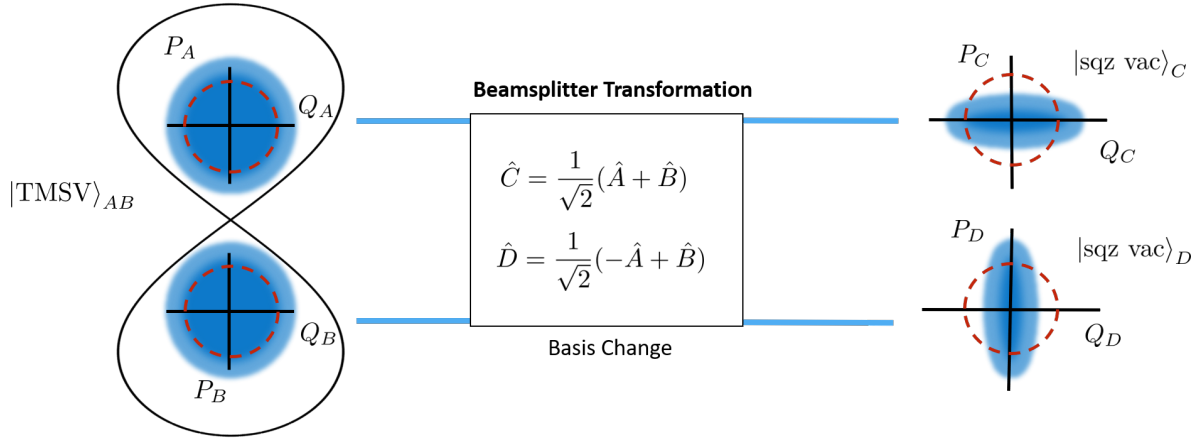[13]Without loss of generality we also suppose that $\varphi = \pi$ radians.

Figure 5.4: Correspondence between a two-mode squeezed state, $|\text{TMSV}\rangle_{AB}$, that is the Continuous Variable EPR-like state, and two single-mode squeezed vacuum states, $|\text{sqz vac}\rangle_{C/D}$ by a beamsplitter transformation. The dotted circles represent the quantum limit in the quadrature variance given by the Heisenberg uncertainty principle on the quadrature operators.

is 0, the single-mode squeezed state presented here is also known as a *squeezed vacuum state*. The reverse process is also true, i.e., two single-mode squeezed vacuum states that are mixed in a beamsplitter produce a two-mode squeezed state with EPR-type correlations. The process is depicted in Fig.(5.4).

This analysis shows the relation between squeezing and entanglement. The beamsplitter transformation, which is a basis change, makes two uncorrelated states presenting squeezing, into a single non-squeezed state presenting quantum correlations in their quadratures. Both squeezing and entanglement are therefore non-classical features that can be interchanged by appropriate basis changes[14].

Note that, as in the DV case, the signal and idler fields should be indistinguishable to have a perfect interference in the BS. If we are to use a single non-linear waveguide, therefore, we need the condition $h(\omega) = g(\omega)$ in our analysis, which is one of the main topics for the next Chapter.

---

[14]This property is however valid only for gaussian states, in the general case of non-gaussian states it's more complicated [108, 109]

5.3.2 Multimode EPR state

The generalization of the EPR state of Eq.(5.42) to the multimode configuration of Eq.(5.41) is straightforward by noting that our state can be written as:

$$|\psi\rangle = \exp\left(\sum_l \sqrt{\lambda_l}\mathcal{C}\hat{A}_l^\dagger\hat{B}_l^\dagger + \text{h.c.}\right)|0\rangle = \prod_l \hat{S}_l^{AB}(\sqrt{\lambda_l}\mathcal{C})|0\rangle \qquad (5.56)$$

For each pair of modes with index l, the state is an EPR state of the form presented above. We could therefore define the quadrature operators associated with each pair of operators $\hat{A}_l$, $\hat{B}_l$ that will present quadrature variances of the type of Eq.(5.54). Note that the squeezing level, and hence the strength of the EPR correlations, for each pair is now mode-dependent, $\sqrt{\lambda_l}\mathcal{C}$. The different EPR pairs of the multimode state are uncorrelated, since they act on the different operators in the supermode basis. The multimode EPR state is depicted in Fig.(5.5).

As in the single two-mode squeezed state, a beamsplitter transformation would mix every EPR pair into two single-mode squeezed states. Since the frequency modes $\{h_l(\omega_s)\}$ form an orthogonal basis, the output of an interference of the two set of frequency modes in the BS would generate a multimode independent squeezed state, where each squeezed state is decorrelated from the rest in the supermode basis. For this interference to perfectly work, though, the signal and idler fields just before the BS should be indistinguishable, and therefore we must have the condition $h_l(\omega) = g_l(\omega) \; \forall l$. This condition will be explored in Chapter 6.

5.4 Quantum States for Type 0/I SPDC

5.4.1 The difference between types of PDC: Field Indistinguishability

The difference between type I and type II PDC processes according to our discussion is the field distinguishability at the output of the waveguide. Following our three wave mixing hamiltonian, type I PDC can be seen as a type II PDC where the signal and idler fields are indistinguishable, i.e. they are the same field. In type I, therefore, there would be only one output field, that will be referred to as the signal field.

The types of PDC are usually defined according to the polarization of the output fields. In type II, the polarization of signal and idler are orthogonal (as shown in Fig.(5.5)), while in type I, the polarization of signal and idler is the same, and orthogonal to the polarization of the classical pump field. The vectorial character of the wavevectors makes possible to fulfill the phasematching condition in a non-collinear configuration, and hence it is possible to generate two non-collinear fields with the same polarization, which would be a type I process by definition but it would be regulated by the hamiltonian of distinguishable fields
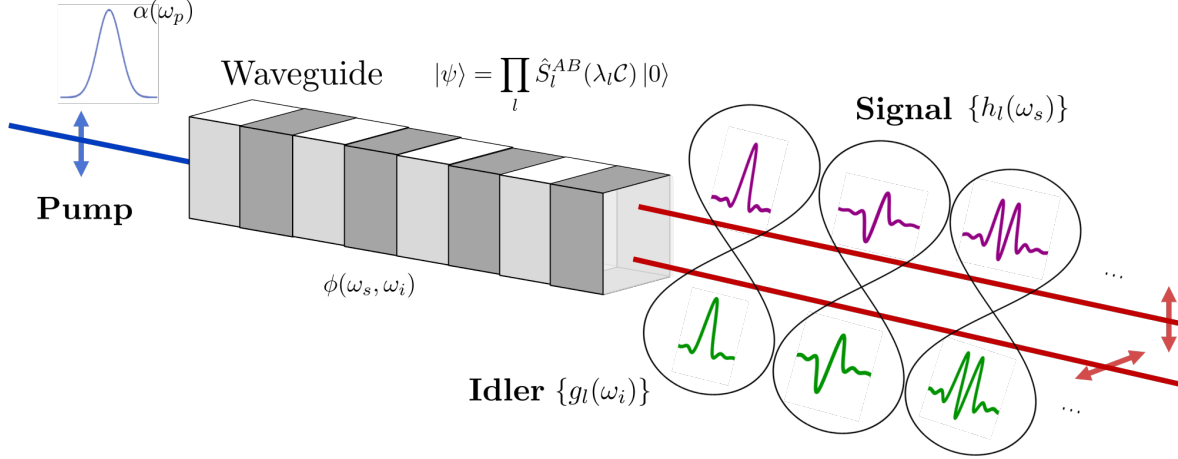
Figure 5.5: Quantum state from a Type II SPDC process, pumping a non-linear waveguide with phasematching $\phi(\omega_s, \omega_i)$ by a laser with spectrum $\alpha(\omega_p)$. The state is constituted by a finite number of uncorrelated EPR pairs in the supermode basis $\{h_l(\omega_s), g_l(\omega_i)\}$. The arrows indicate the pump, signal and idler field polarizations.

(since they are propagating in different directions). In waveguides, the propagation of the generated fields is always collinear with the pump direction.

Furthermore, there is an additional type of PDC, the type 0. In type 0 PDC the polarization of all the fields; pump, signal and idler, is the same. The type 0 case is formally the same as type I, and all the conclusions drawn about the quantum states of type I PDC apply exactly the same for type 0. However, for the non-linear materials considered in this thesis, which are KTP and LN, the effective non-linear coefficient associated with type 0 PDC is about 4 times larger than the corresponding coefficient for type I, presenting therefore a greater light-matter interaction, or equivalently, a greater level of squeezing under the same experimental conditions.

5.4.2 Multimode squeezed vacuum state

As in the case of type II, we start the derivation of type 0/I from the hamiltonian describing this effect, that in this case reads:

$$\hat{H}_{\text{PDC}}(t, \text{type0/I}) = \epsilon_0 \int d\boldsymbol{r} d_{\text{eff}} E_p^+(\boldsymbol{r}, t) \left(\hat{E}_1^-(\boldsymbol{r}, t) \right)^2 + \text{h.c.} \qquad (5.57)$$

Noting that this is the type II hamiltonian that has been analyzed with $\hat{E}_1^-(\boldsymbol{r}, t) = \hat{E}_2^-(\boldsymbol{r}, t)$, all the arguments given to the derivation of the state for type II are also valid here.

When performing the Schmidt decomposition of the joint-spectral amplitude for the type 0/I case, now we obviously find that:

$$\hat{A}_l^\dagger = \hat{B}_l^\dagger \qquad h_l(\omega) = g_l(\omega) \quad \forall l \tag{5.58}$$

where we have already dropped the spatial mode indices because of the dominance of the single(spatial)-mode case, as with the type II process.

Therefore the quantum state after the waveguide for type 0/I is [107]:

$$|\psi\rangle = \exp\left(\sum_l \lambda_l \mathcal{C}\left(\hat{A}_l^\dagger\right)^2 + \text{h.c.}\right)|0\rangle \tag{5.59}$$

As in the case of type II, we can understand this state by considering a single frequency mode in the Schmidt decomposition, i.e, dropping the index l:

$$|\psi\rangle = \exp\left(\mathcal{C}\left(\hat{A}^\dagger\right)^2 + \text{h.c.}\right)|0\rangle \equiv \hat{S}^A(\mathcal{C})|0\rangle \tag{5.60}$$

and now the operator $\hat{S}^A(\mathcal{C})$ is called the squeezing operator. The action of the operator on the creation and annhiliation operator is:

$$\hat{S}^{A\dagger}(\mathcal{C})\hat{A}\hat{S}^A(\mathcal{C}) = \hat{A}\cosh(R) - \hat{A}^\dagger e^{i\varphi}\sinh(R) \tag{5.61}$$

As in the type II scenario, we define the quadratures associated with the field $\hat{A}$; in this case there is only a single pair of quadratures:

$$\hat{Q}_A = \hat{A} + \hat{A}^\dagger$$
$$\hat{P}_A = i(\hat{A}^\dagger - \hat{A}) \tag{5.62}$$

and it is easy to check using Eq.(5.61) that the mean value of the quadratures vanish over the state $|\psi\rangle$:

$$\langle \hat{Q}_A \rangle_\psi = \langle \hat{P}_A \rangle_\psi = 0 \tag{5.63}$$

while the quadrature variances are given by:

$$\Delta\hat{Q}_A^2 = \exp(-2R)\cos^2(\varphi) + \exp(2R)\sin^2(\varphi)$$
$$\Delta\hat{P}_A^2 = \exp(-2R)\sin^2(\varphi) + \exp(2R)\cos^2(\varphi) \tag{5.64}$$

We see that, taking arbitrarily $\varphi = \pi$, the variance of the Q_A quadrature goes below the quantum limit whenever $R > 0$, while the variance of the P_A quadrature increases in the same amount, so that the Heisenberg limit is saturated $\Delta\hat{Q}_A^2\Delta\hat{P}_A^2 = 1$. As we have already discussed, this is the signature of a squeezed mode. Indeed, the variances of Eq.(5.64) are identical to the ones calculated for each single-mode state in the CV EPR pair after the
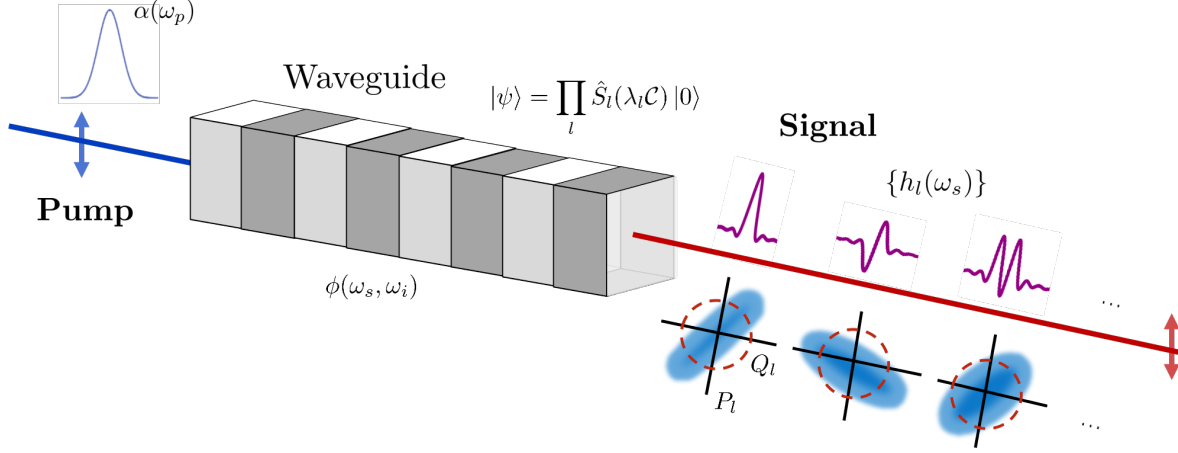
Figure 5.6: Quantum state from a type 0 or type I SPDC process, pumping a non-linear waveguide with phasematching $\phi(\omega_s, \omega_i)$ by a laser with spectrum $\alpha(\omega_p)$. The state is constituted by a finite number of uncorrelated squeezed vacuum states in the supermode basis $\{h_l(\omega_s)\}$. Q_l and P_l are the quadratures associated with the l-th frequency mode.

beamsplitter transformation, which can therefore be identified as two single-mode squeezed states. Therefore the output state is simply a single-mode squeezed state. In particular, since it acts on vacuum (the mean value of the quadratures is 0), it is a single squeezed vacuum state. Again, the value of R determines the level of squeezing in the state.

The generalization to the multimode scenario of Eq.(5.59) is straightforward, since we have multiple uncorrelated squeezing operators acting on vacuum:

$$|\psi\rangle = \exp\left(\sum_l \sqrt{\lambda_l}\mathcal{C}\left(\hat{A}_l^\dagger\right)^2 + \text{h.c.}\right)|0\rangle = \prod_l \hat{S}_l^A(\sqrt{\lambda_l}\mathcal{C})|0\rangle \tag{5.65}$$

and therefore the state is an ensemble of single-mode squeezed states in the frequency modes $\{h_l(\omega_s)\}$. The level of squeezing in each mode is related to the Schmidt coefficients and the intrinsic strength of the interaction, $\sqrt{\lambda_l}\mathcal{C}$. The state is depicted in Fig.(5.6).

Chapter 6

Quantum State Engineering in Waveguides

" Physics is really nothing more than a search for ultimate simplicity, but so far all we have is a kind of elegant messiness. "

– Bill Bryson, A Short History of Nearly Everything

Contents

After calculating the multimode quantum states that appear in a type 0,I and II PDC process, now we are ready to motivate their application in the context of this manuscript. The aim of the project is to prepare clusters states of light, also known as graph states, that can be

abstractly envisioned as quantum networks. They present a great potential as quantum resources for quantum communication protocols, quantum simulation or measurement-based quantum computation (MBQC). In this Chapter, we develop a link between the relevant and controllable physical parameters in a PDC experiment and the theoretical multimode quantum states coming out from the source that we would later shape as graph states. The results of this Chapter motivated the choice of the PDC waveguide used in the experimental setup, that will be described in the next Chapter.

6.1 CV Quantum Networks as Graph States

6.1.1 Definitions

The notion of a *Quantum Network*[1] that will be used in this manuscript is a mathematical abstraction in which an ensemble of nodes are linked in a regular or complex structure.

In a physical context, the nodes are represented by subparts of a physical system, and the edges represent their correlations. If those correlations are from a quantum nature, then the network is, not very surprisingly, called a quantum network. The types of states that resemble the network structure are *cluster states*, also known as *graph states* [111]. Depending on how the quantum information is encoded and the nature of the quantum correlations, the networks can be classified in Discrete Variable (DV) Networks and Continuous Variable (CV) networks.

These states are highly interesting in a wide variety of fields in Quantum Information. Implemented as multimode states, in Quantum Communication and Quantum Computation, they are at the heart of communication protocols [112, 113, 114], Measurement-Based Quantum Computation (MBQC), [115, 116], Quantum Metrology [117, 118] and even Quantum Simulation [119].

Since creating the network involves the preparation of a quantum state with an internal structure that resembles the network, there are different advantages and disadvantages in using DV or CV quantum networks. In optical setups, one can prepare DV states with a better fidelity, but from a probabilistic process. The CV states, on the other side, are more sensitive to losses and noise, but their preparation is deterministic, i.e. the state preparation always succeed. While both types of optical quantum networks are at the edge of our current knowledge, DV networks have been considerably more implemented to the current date, mainly in atomic systems [120, 121, 122, 123], but also in optical ones [124, 125, 126]. Impressive results have been obtained in the recent years also in the optical CV framework [127, 128, 129, 130].

---

[1] In Quantum Information, the concept of quantum networks is often associated with the notion of quantum internet [110]. In this manuscript, the quantum network notion and the graph state are completely interchangeable concepts.

In this thesis, we are interested in constructing, from scratch, an optical quantum source capable of producing configurable graph states of light in the CV regime via non-linear waveguides. The physical system composing the network is the electromagnetic field and hence the name optical graph states. The necessity of the system partition into subsystems that represent the quantum nodes of the network leads naturally to consider the preparation of multimode quantum states of light. Any type of electromagnetic mode can serve as the representation of the nodes, although it seems experimentally natural to take the pure spatial or temporal modes of the light field, under the the spatial and temporal decoupling approximation made in Chapter 3, section 3.3.1.

Spatial modes, in particular, could be used to represent the nodes of the network. However, if different paths are needed for defining the different spatial modes, the network configurability could be compromised, although different solutions to this could be found in the next years. On the other hand, preparing a single beam with correlations between its internal spatial modes would also be possible, but avoiding spatio-temporal couplings with current waveguide or bulk crystal technologies would be in general a difficult task, which in turn would deteriorate the quality of the states and reduce the state fidelity [131].

We will therefore use temporal/frequency modes as the representation of the nodes of the network. As we have seen in Chapter 5, in the context of a waveguide structure, the spatio-temporal coupling can be modelled and discarded if the waveguides are sufficiently single(spatial)-mode. Following the analysis of the states derived in that Chapter, we first associate each node of the network with a frequency mode from the supermode basis:

$$\{\text{Nodes}\} \longrightarrow \{h_l(\omega_s)\} \tag{6.1}$$

6.1.2 Edges

The correlations between the frequency modes constitute the entanglement links in our description of the quantum network. In order to understand the link and the configurability of the network, it is worth to see the basic building block of the network, considering only two nodes. The generalization to N nodes would be straightforward once the 2-node cluster is described.

6.1.3 2-node graph

The simplest version of our quantum network is the case in which we have 2 nodes connected by a single link, corresponding to a 2-mode optical cluster state in our context.

In the 2-node cluster state, two frequency modes $h(\omega_s)$ and $g(\omega_i)$ present CV quantum correlations of the EPR-type[2]. This state is a two-mode squeezed state that was described and analyzed in Chapter 5, section 5.3.1. As we have already seen, the amount of their

---

[2]To be completely rigorous, the CV EPR pair is not exactly the 2-node graph, (they differ slightly in the unitary performed to the single squeezed states), but the nature of its correlation is the same.

entanglement is measured by the amount of squeezing in the quadratures on the mode corresponding to a basis change by the beamsplitter transformation of Eq.(5.46). The quantum state after the beamsplitter is therefore composed by two uncorrelated single-mode squeezed states, Fig.(5.4).

We stress here that the reverse process is also true, as stated above, and hence two single-mode squeezed vacuum states mixed in a balanced beamsplitter generates a CV EPR pair that can be seen as a CV quantum network with two nodes. This fact makes the generalization to generating multiparty EPR-like correlations in N nodes straightforward.

6.1.4   N-node Graph State

Mathematically, an ideal N node Graph state is defined by applying N C_Z entangling gates via the operator $\hat{C}_Z(A)$, where A is the adjacency matrix that defines the edges of the graph, to N infinitely squeezed state modes in the p quadrature, $|0\rangle_p^{\otimes N}$ [132, 133, 134]:

$$|\Psi\rangle = \hat{C}_Z(A) |0\rangle_p^{\otimes N} = \prod_{1 \leq i < j < N} \exp\left(i A_{ij} \hat{q}_i \otimes \hat{q}_j\right) |0\rangle_p^{\otimes N} \tag{6.2}$$

and they are typically studied with the use of the set of nullifier operators, $\{\hat{\delta}_i\}$ [135, 136, 137]:

$$\hat{\delta}_i = \hat{p}_i - \sum_{j \in \text{Ne}(i)} \hat{q}_j \qquad \text{such that} \qquad \hat{\delta}_i |\Psi\rangle = 0 \tag{6.3}$$

In practice, graph states are imperfect, as infinite levels of squeezing are unphysical, and the quality of the graph state is given by the variance of the nullifier operators. Instead of applying C_Z gates, which are experimentally hard to implement, graph states can also be obtained from linear optics and squeezing, as it is the case for every gaussian state due to the Bloch-Messiah reduction [138, 139, 140, 141]. The state can be therefore prepared from a set of N single-mode squeezers and optical interferometry.

In particular, and following our discussion on the 2-mode EPR state, we prepare a state composed of N uncorrelated single-mode squeezed vacuum states with different levels of squeezing $\{\sqrt{\lambda_l}\}$, associated with frequency modes $\{h_l(\omega)\}$, $l = 1, 2, ...N$. We then define the vector $\boldsymbol{h}$ as the column vector containing all the frequency modes:

$$\boldsymbol{h} = (h_1(\omega), h_2(\omega), ..., h_N(\omega))^{\mathrm{T}} \tag{6.4}$$

If we perform a passive unitary operation to the state, represented by the lxl matrix U, then the new frequency modes after the transformation are simply $\boldsymbol{g} = U\boldsymbol{h}$, and we will obtain some quantum correlations (in the form of EPR-like correlations) between some modes in the new basis, forming the particular graph state if its nullifiers are well-defined[3]. This

---

[3]Not all linear combinations of the uncorrelated nodes creates a graph state, since the nullifiers should have a particular mathematical structure. However, the contrary is true, all graph states can be obtain by a certain linear combination of the uncorrelated nodes.
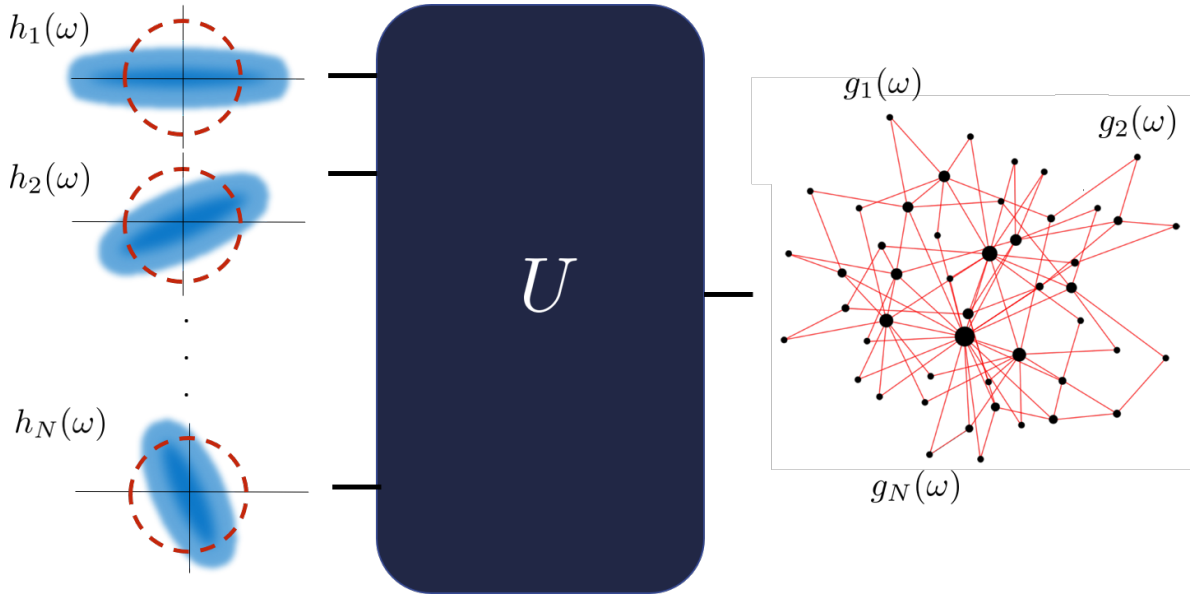
Figure 6.1: Schematics of the generation of a N-mode cluster state from a multimode independent squeezed vacuum state and a passive unitary operation U. For more information see text.

process is depicted in Fig.(6.1).

The topology of the resulting network depends on the unitary U that is applied to the input multimode squeezed state, and the strength of the correlations in the output graph state is a function of the squeezing levels of the original input fields composing the initial state, $\{\sqrt{\lambda_l}\}$.

Physically speaking, a passive unitary operation is implementable by passive linear optics, i.e. by constructing a multiport interferometer. This means that we can experimentally implement any particular network topology by first preparing the multimode squeezed state in the supermode basis $\boldsymbol{h}$ and then making the light pass through the multiport interferometer implementing the unitary U. The final network's nodes can be addressed by measuring the modes in the supermode basis $\boldsymbol{h}$ after the interferometer.

Alternatively, we can equivalently implement the network by preparing the multimode squeezed state and directly measure it in the new basis $\boldsymbol{g} = U\boldsymbol{h}$. This approach is more appealing from the experimental point of view, since the network topology could be easily manipulated because there would be no necessity of constructing different multiport interferometers every time a different network is to be considered, but simply changing the measurement basis. The basis change can be achieved by calculating the new modes $\boldsymbol{g}$ defining the desired network topology and shape accordingly the pulses of a Local Oscillator for homodyne measurements of the network. In this way, a configurable graph state is achieved [142].

This discussion leads to the conclusion that a CV Graph state source in the frequency domain can be implemented by preparing multimode squeezed vacuum states and measure them in a specific mode basis. We have seen that these states can be directly generated from Spontaneous Parametric Down Conversion in non-linear waveguides, which was the topic of Chapter 5. For type 0 and type I, the multimode state is already a set of independent squeezers, (it is already in the supermode basis), while for type II the state is a set of EPR pairs that are uncorrelated between them. For this reason, in the type II case, an extra step of interference between the EPR pairs of signal and idler in a balanced beamsplitter is necessary to recover the supermode basis of uncorrelated single-mode squeezers. For this interference to be perfect, signal and idler fields should then be made indistinguishable.

6.2 Designing the Multimode Quantum States conforming the Graph States

A question that arises naturally from our discussion is what could be the influence of different physical parameters in a realistic experimental setup on the graph states. More precisely, how the features of the graph state depend on the experimentally controllable degrees of freedom of the waveguide and pump field. The tuning of these different degrees of freedom can be referred to as *quantum state engineering*. The theoretical work regarding this issue lead to a publication during this thesis [143].

6.2.1 Multimode quantum state features

The first thing that we want to do is to identify both the relevant degrees of freedom that can be controlled experimentally and the desired intrinsic properties of the generated state.

We recall here that, because of the spatial single-mode approximation in the waveguide (justified in Chapter 5), the output states are multimode frequency modes. The joint spectral amplitude, containing all the information about the spectral properties of the states, can be written in this case as:

$$J(\omega_s, \omega_i) = \alpha(\omega_s + \omega_i)\phi(\omega_s, \omega_i) = \sum_l \sqrt{\lambda_l} h_l(\omega_s) g_l(\omega_i) \tag{6.5}$$

where $\alpha(\omega_s + \omega_i)$ is the pump spectrum, $\phi(\omega_s, \omega_i)$ is the phasematching function, and the sum on the last term is the Schmidt decomposition of the two-dimensional function. The first figure of merit of our graph will be the so-called *cooperativity* or *Schmidt Number* [144], defined as:

$$K = \frac{1}{\sum_l \lambda_l^2} \tag{6.6}$$

This quantity counts the effective number of frequency modes present in the multimode state, i.e. it counts the effective number of supermodes. We call it effective because we take

into account the fact that some pair of modes would present less correlations than others. It is a concept inherited from the entanglement of the photon pairs from the DV point of view [145].

We can intuitively see this by looking at two examples: if the Schmidt number K is equal to 1, then there is only one Schmidt coefficient in the decomposition of Eq.(6.5) that is consequently equal to 1 and it is clear that there is only one pair of frequency modes (in type II) or a single squeezed mode (in type 0/I). The state when $K = 1$ is a separable state and hence presents no correlations. In the case that there is a number N of Schmidt coefficients with equal weight in the decomposition, then $\lambda_l = 1/N$ in order to fulfill $\sum_l \lambda_l = 1$ and therefore the Schmidt number is $K = N$ and every mode is contributing in the same amount to the total state correlation. In any other arrangements of Schmidt coefficients, the Schmidt number K would be smaller according to Eq.(6.6). We therefore have $D \geq K \geq 1$ where D is the dimensionality of the state, i.e. the number of Schmidt coefficient in the sum of Eq.(6.5).

In the case of type 0 or type I SPDC, the two main figures of merit in the simulations are the Schmidt number, K, and the distribution of Schmidt coefficients, $\{\lambda_l\}$. The first accounts for the number of nodes in the network and the second for the distribution of the squeezing levels in the multimode state.

In the case of type II, we need to make signal and idler fields interfere in a beamsplitter in order to recover the single-mode squeezers that can generate the graph states, and hence we have an extra parameter that should account for the similarity of the pairs of frequency modes $\{h_l(\omega_s), g_l(\omega_i)\}$. Naturally, this parameter will be the overlap integral between the frequency mode pairs that we will compute in our simulations, defined as:

$$\mathcal{O}_k = \frac{1}{\mathcal{N}} \left| \int d\omega h_k^*(\omega) g_k(\omega) \right| \qquad \mathcal{N} = \sqrt{\int d\omega \, |h_k(\omega)|^2 \int d\omega \, |g_k(\omega)|^2} \qquad (6.7)$$

where $\mathcal{N}$ is a normalization constant assuring that $\mathcal{O}_k \in [0, 1]$. $\mathcal{O}_k$ therefore measures the similarity of the EPR pairs associated with the modes $h_k(\omega_s)$ and $g_k(\omega_i)$. Only if $h_k(\omega) = g_k(\omega)$ the overlap integral $\mathcal{O}_k = 1$ and the interference between this pair of modes in the beamsplitter would be perfect. In any other case, $O_k < 1$, the visibility in the interference fringes would not be 1, and the fidelity of the final pair of single-mode squeezed states after the beamsplitter would decrease.

6.2.2 Controllable degrees of freedom

For answering the question of what are the main degrees of freedom that are controllable in the experiment we look again at Eq.(6.5). The physical variables appearing in the joint-spectral amplitude are the main relevant quantities that affect the state.

First of all, we will consider a gaussian pump spectrum[4], defined as the (square-normalized) function:

$$\alpha(\omega_s + \omega_i) = \frac{1}{\sqrt{\sqrt{\pi}w_p}} \exp\left(-\frac{(\omega_{p,0} - (\omega_s + \omega_i))^2}{2w_p^2}\right) \tag{6.8}$$

where we have defined the pump central frequency $\omega_{p,0}$ and the *pump spectral width* w_p, that is simply the standard deviation of the gaussian.

Therefore, our first experimental degree of freedom is the pump width w_p, since it completely defines the pump spectrum.

On the other hand, we recall the expression for the phasematching function:

$$\phi(\omega_s, \omega_i) = \text{sinc}\left(\frac{L}{2}\Delta\beta(\omega_s, \omega_i)\right) \tag{6.9}$$

where L is the waveguide length, that will be added as a degree of freedom, and $\Delta\beta(\omega_s, \omega_i)$ is the mismatch in the propagation constants:

$$\Delta\beta(\omega_s, \omega_i) = \beta_p(\omega_s + \omega_i) - \beta_s(\omega_s) - \beta_i(\omega_i) + \frac{2\pi}{\Lambda} \tag{6.10}$$

In our simulations, we will not consider the poling period Λ as a degree of freedom, because we have the additional constraint of fulfilling phasematching for the central frequencies in order to have an efficient process, i.e. the poling period is fixed to the value:

$$\Lambda = \frac{2\pi}{\beta_s(\omega_{s,0}) + \beta_i(\omega_{i,0}) - \beta_p(\omega_{s,0} + \omega_{i,0})} \tag{6.11}$$

where $\omega_{j,0}$, $j = p, s, i$, are the central frequencies for the pump, signal and idler fields. It is easy to check with Eq.(6.10) and Eq.(6.11) that the poling period is such that $\Delta\beta(\omega_{s,0}, \omega_{i,0}) = 0$, i.e. the central frequencies are phasematched.

At this point, we will model the dispersion relations $\beta_j(\omega)$, as :

$$\beta_j(\omega) = \frac{\omega}{c}n_j(\omega) \tag{6.12}$$

where $n_j(\omega)$ is the index of refraction associated with the polarization of pump, signal or idler fields.

Hence, potentially any variable that affects the index of refraction can be a degree of freedom in our calculation. We will consider the wavelength[5], λ, temperature, T and waveguide

---

[4]In general, one could do pump shaping to change the spectrum of the pump and hence change the quantum state after the waveguide. In this work, however, we restricted ourselves to the gaussian pump spectrum, since it is approximately the spectrum directly coming from our laser source.

[5]The frequency dependence and the wavelength dependence are linked by the relationship between the two variables:

$$\omega = \frac{2\pi c}{\lambda} \tag{6.13}$$

characteristics as the main dependences of the index of refraction. The latter includes the waveguide section size, with *height* h and *width* w, and spatial mode order inside the waveguide, defined by two integer numbers n and m (for more details about the spatial modes in waveguides see Chapter 4). For the modelling of the index of refraction with the waveguide characteristics we will use the so-called metallic waveguide approximation [146], in which one assumes the waveguide to be surrounded by perfectly conducting edges. The reason is that in this way we obtain an analytical expression of the index of refraction[6]

$$n_j(\lambda, T, h, w, n, m) = n_j(\lambda, T) + \left(\lambda \frac{n+1}{2h}\right)^2 + \left(\lambda \frac{m+1}{2w}\right)^2 \qquad (6.14)$$

and $n_j(\lambda, T)$ is the index of refraction associated with polarization j in the bulk crystal. For uniaxial crystals, like LN, there will be two indices of refraction and hence two functions of the form of Eq.(6.14), whereas for biaxial crystals, like KTP, there will be three indices of refraction of the form of Eq.(6.14). The functions $n_j(\lambda, T)$ are called the Sellmeier Equations of the material, that are empirical equations whose coefficients are found experimentally under certain conditions. For LN, the Sellmeier equations used in this work can be found in [148], while for KTP, the they can be found in [149]. The association between the indices of refraction in uniaxial or biaxial crystals and the indices for pump, signal and idler are given by the Kleinman symmetry (see Appendix B), allowing only certain configurations of input and ouput polarizations for the different PDC processes.

Furthermore, because of the approximation of single-mode waveguides that we justified in Chapter 5, we will always consider $n = m = 0$ for Eq.(6.14) in our simulations.

In Fig.(6.2) we show the schematics for a single simulation of the graph state from the controllable degrees of freedom considered in this text.

6.2.3 Context for our simulations

In the following sections we will show the numerical simulations performed as a function of the controllable degrees of freedom for SPDC type 0,I and II. These simulations helped us to choose the non-linear waveguides suitable for the expected multimode quantum states. Since we want to characterize the quantum state by the multimode squeezing in the supermode basis, we will study in quite detail the conditions for field indistinguishability, which is necessary to obtain the set of uncorrelated single-mode squeezed states. In the case of type 0 and I, this feature is already given naturally if one works in the degenerate case. For type II, however, signal and idler fields experience different dispersion along the waveguide because of their different polarizations, which results in different supermode spectral widths. To recover indistinguishability, we would need to make the interference between signal and idler fields, and therefore the pairs of supermodes should be as similar as possible

---

[6]As we have stated, other numerical methods can also be used to model the index of refraction, like Marcatili's method [87] or finite-element methods [147].
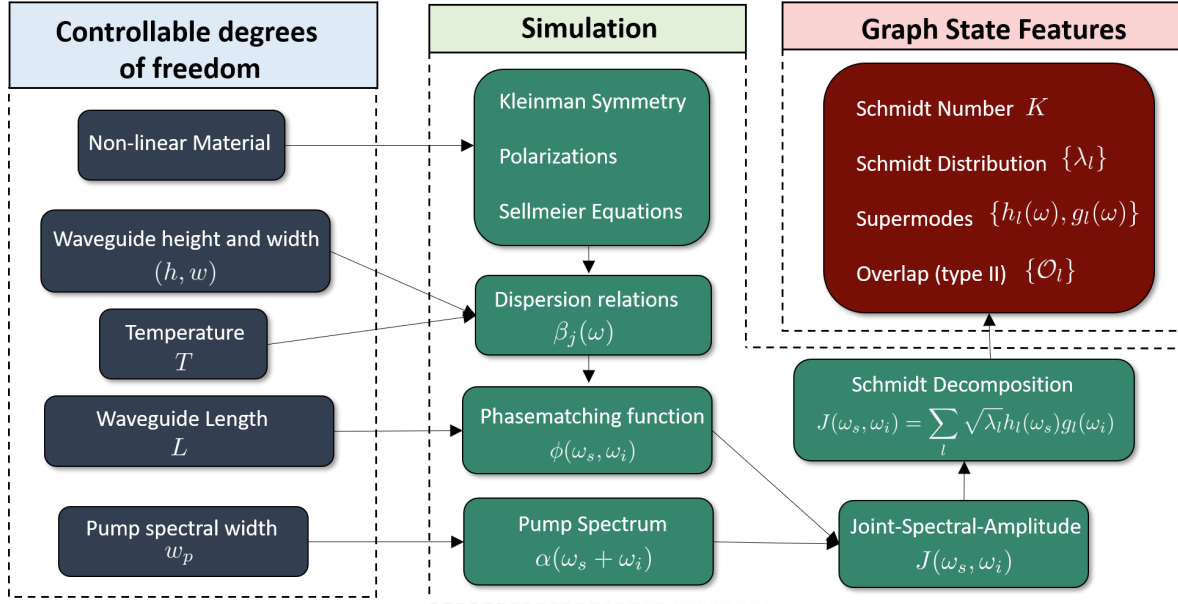
Figure 6.2: Schematics of a simulation of a graph state from the controllable degrees of freedom. For more information see text.

for good visibility, which can be obtained under a certain configuration, that we will call the Symmetric Group Velocity Matching (SGVM) condition. Along these simulations, we will work with PPKTP waveguides at telecom wavelengths ($\lambda = 1550$ nm, although the code is valid for any non-linear material and central wavelength. For practical reasons that will be outlined, the final experimental configuration that we took was type 0 SPDC in a 15 mm long PPKTP waveguide, with dimensions assuring single(spatial)-mode propagation (average waveguide height and width of about 3 μm).

6.3   Type 0 and Type I Simulations

The field indistinguishability discussed in Chapter 5 for type 0 and type I SPDC makes the joint-spectral amplitude to be symmetric under the exchange of signal and idler fields, i.e:

$$J(\omega_s, \omega_i) = J(\omega_i, \omega_s) \tag{6.15}$$

Given the expression of the joint-spectral amplitude of Eq.(6.5), the pump spectrum is already symmetric under the exchange of signal and idler, since it is a function of the sum, $\alpha = \alpha(\omega_s + \omega_i)$. Hence, the condition reduces to $\phi(\omega_s, \omega_i) = \phi(\omega_i, \omega_s)$, and using Eq.(6.9), the mismatch should fulfill $\Delta\beta(\omega_s, \omega_i) = \Delta\beta(\omega_i, \omega_s)$.

To check the dispersion properties, we can expand the mismatch in the propagation

constants in a Taylor series around the central frequencies up to first order:

$$\Delta\beta(\omega_s, \omega_i) = \Delta\beta(\omega_{s,0}, \omega_{i,0}) + \gamma_s(\omega_s - \omega_{s,0}) + \gamma_i(\omega_i - \omega_{i,0}) + ... \tag{6.16}$$

where the coefficients are defined as:

$$\gamma_{s/i} = \left.\frac{\partial\beta_p}{\partial\omega}\right|_{\omega_{p,0}} - \left.\frac{\partial\beta_{s/i}}{\partial\omega}\right|_{\omega_{s,0}} \tag{6.17}$$

Given the definition of the group velocity as $v_g(\omega) = \partial\omega/\partial\beta$, we directly see that the coefficients of the Taylor expansion are directly related to the group velocities of the fields as[7]:

$$\gamma_{s/i} = \frac{1}{v_{g,p}(\omega_{p,0})} - \frac{1}{v_{g,s/i}(\omega_{s/i,0})} \tag{6.18}$$

We recall that since the fields are indistinguishable, in type 0/I it should be the case that $\omega_{s,0} = \omega_{i,0} = \omega_{p/0}/2$ by conservation of energy. Hence, for type 0/I, each linear coefficient is equal for signal and idler by symmetry, $\gamma_s = \gamma_i \equiv \gamma$.

Additionally, as discussed above, the constant term in the Taylor series is $\Delta\beta(\omega_{s,0}, \omega_{i,0}) = 0$ by choosing the poling period of Eq.(6.11).

For femtosecond lasers and typical non-linear materials, the second or higher-order terms in the Taylor series are small compared to the linear leading term in the frequency bandwidth of the laser w_p (see Appendix C for the calculation in KTP), and therefore we can approximate the mismatch as:

$$\Delta\beta(\omega_s, \omega_i) \simeq \gamma(\omega_s - \omega_{p,0}/2) + \gamma(\omega_i - \omega_{p,0}/2) = \gamma(\omega_s + \omega_i) - \gamma\omega_{p,0} \tag{6.19}$$

This means that, for type 0/I, the phasematching amplitude is not only symmetric, but it is also a function of $\omega_s + \omega_i$ up to linear order in the mismatch:

$$\phi(\omega_s, \omega_i) \simeq \phi(\omega_s + \omega_i) \qquad \text{Type 0/I} \tag{6.20}$$

A physical consequence of this mathematical fact is that the supermode's number and bandwidth gets larger for type 0/I with respect to type II, as we will argue in the following:

The joint-spectral amplitude, being a two-dimensional function, can be represented as a surface in the plane defined by the axis ω_s and ω_i. It is useful to separately represent the pump spectrum and the phasematching functions in that plane, since in the intersection of these two functions the JSA would take non-zero values. By reflection symmetry, any function f of the form $f = f(\omega_s + \omega_i)$ would make an angle of -45° with respect to the horizontal axis of the plane. Since we have shown that for type 0/I, both the pump spectrum and the phasematching are functions of the form $f(\omega_s + \omega_i)$, and both are centered at $\omega_{s,0} =$

---

[7]In the same way, the second order coefficients in the Taylor expansion would be related to the Group velocity dispersion.
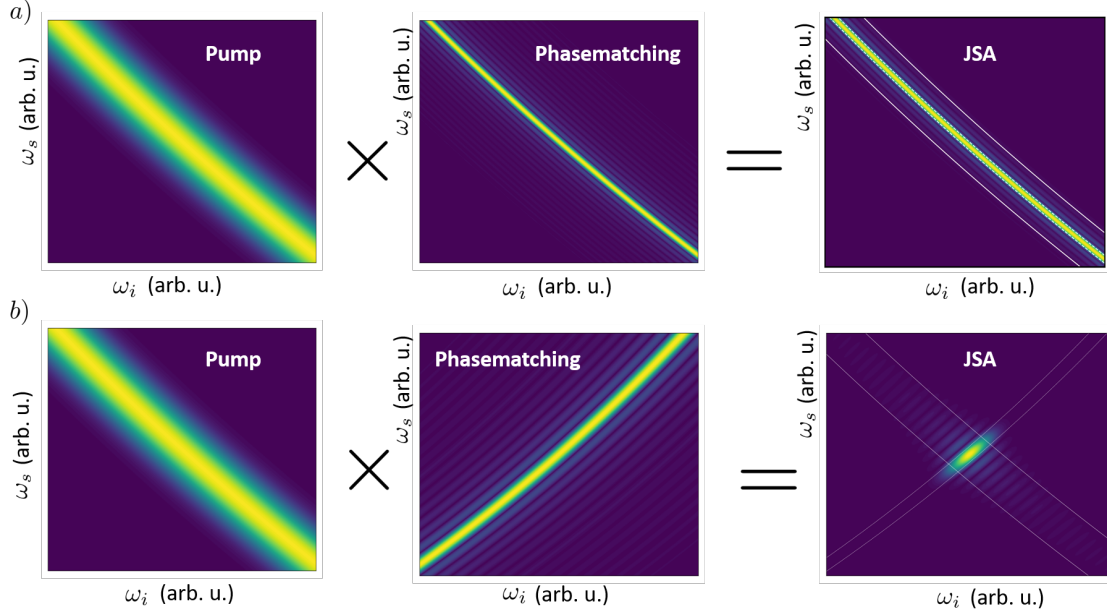
Figure 6.3: General example of the functional forms of pump spectrum, phasematching function and joint-spectral amplitudes in the (ω_s, ω_i) plane. a) Type 0/I case, where the phasematching function is approximately a function of the sum $\omega_s + \omega_i$. This leads to a great intersection area between pump and phasematching and hence a larger number of spectrally wider supermodes. b) Type II in the SGVM condition, where the angle of the phasematching function is reversed and hence the interesection area is smaller, leading to fewer and narrower supermodes.

$\omega_{i,0} = \omega_{p,0}/2$, then they will present a large non-zero value intersection area along the line $\omega_s + \omega_i = \omega_{0,p}$. The pump and phasematching functions starts diverging one from the other when the quadratic term in Eq.(6.16) starts being comparable to the linear term, so the phasematching function acquires some parabolic curvature in the plane. We depicted this situation in Fig.(6.3) a). The curvature of the phasematching function at frequency values far from the central frequency can be better observed in Fig.(6.6).

As a consequence, the number of modes in the Schmidt decomposition is typically large (of the order of hundreds), and the supermode's spectral widths are also large (they should eventually become as large as the projection of the JSA into a given frequency axis). This poses two practical problems: in the first place, only a small fraction of modes will be experimentally accessible from a type 0/I process. This is due to the nature of the homodyne measurements, in which the quantum signal is mixed with a strong local oscillator (LO). Obviously, modes whose bandwidth are bigger than the LO bandwidth will not mix well in the beamsplitter (low visibility), and hence they will eventually become impossible to be addressed experimentally. On the other hand, the total amount of squeezing is shared
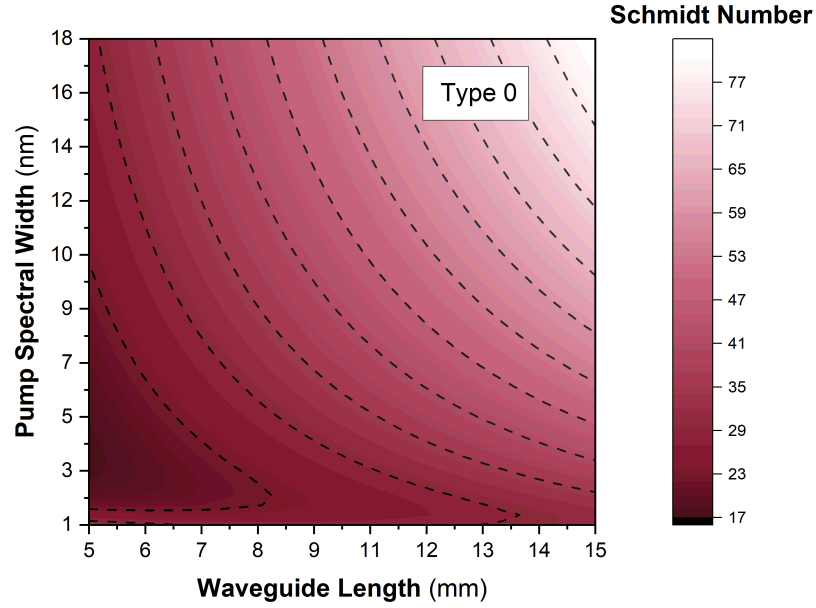
Figure 6.4: Schmidt number as a function of the pump spectral width and waveguide length in type 0 for a (3x3) μm KTP waveguide. Along the dash lines the value of K is constant.

between all the modes, following the Schmidt distribution $\{\lambda_l\}$, and therefore the amount of squeezing per mode could be so low in some cases that the experimental losses would make the quantum nature of the state inaccessible.

Despite this, the typical effective non-linear coefficients in processes of the type 0 are larger than those of type I or II, and so the total amount of squeezing is expected to be larger. For example, in KTP, the non-linearity of type 0 is about 5 times bigger than the non-linearities associated with type I and type II. Additionaly, contrary to the type II case, the output quantum state is already a multimode squeezed vacuum and therefore we do not need to mix the signal and idler fields after the waveguide to recover a single set of squeezed supermodes. The signal/idler interference is an operation that could be considerably lossy depending on the overlaps $\mathcal{O}_l$ defined in Eq.(6.7). This means that we can find some configurations in type 0 and type I that are experimentally more favorable than those of type II in a practical scenario and for our experimental purposes.

6.3.1 Simulations Results

We present here the simulation results for KTP waveguides for the type 0 and type I processes. In the simulations, the temperature was set to $T = 70\ ^o$C, providing poling periods of $\Lambda = 13.4\ \mu$m and $\Lambda = 5.5\ \mu$m for type 0 and type I respectively, giving phasematching at
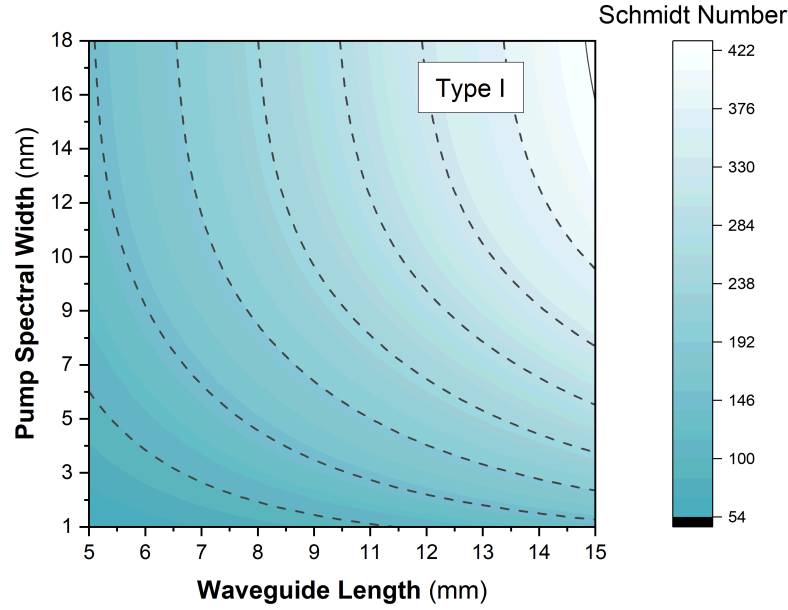
125

Figure 6.5: Schmidt number as a function of the pump spectral width and waveguide length in Type I for a (3x3) μm KTP waveguide. Along the dash lines the value of K is constant.

central wavelengths from $\lambda_{p,0} = 780$ nm to $\lambda_{s,0} = 1560$ nm under the metallic waveguide approximation.

For the simulations shown in this section, the waveguide dimensions were set to $h = w = 3\,\mu$m, since these are the average single-mode waveguide dimensions at telecom wavelengths. In fact, in the experiment that will be shown in the next Chapter, the actual waveguide dimensions took those values.

For KTP and the definition of the x, y, z axis defined along this thesis, the Kleinmann symmetry allows for a type 0 process where all the fields (pump, signal and idler) have vertical polarizations (along z). The type I case corresponds to pump polarized in the vertical direction, and signal and idler fields polarized horizontally (along y).

Fig.(6.4) shows the dependence of the Schmidt number on the waveguide length and the pump spectral width for type 0. We can see that the number of modes grows with both variables in almost all the configurations, except when both are small. This is because the waveguide length controls the phasematching width, that should be compared with the pump width. The interplay between the two provides the symmetry of the JSA that reflects into the Schmidt number value.

Fig.(6.5) shows the same relationship for the Type I case, where the same conclusions can be drawn. Note that the total number of modes is bigger with respect to the type 0 case for KTP. Since the non-linear coefficient is smaller for Type I, the squeezing per mode is

126

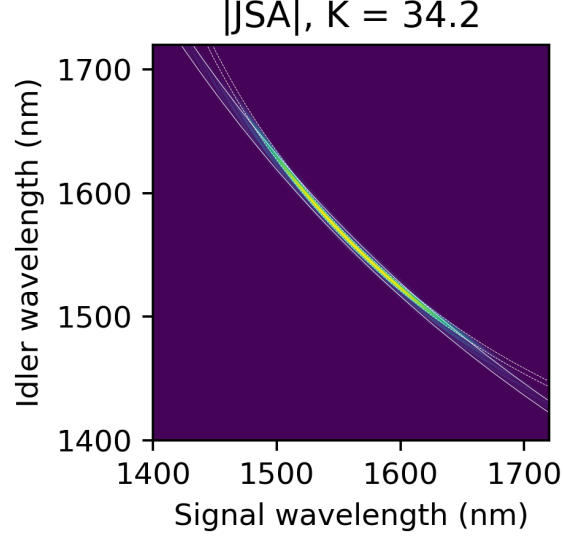expected to be the lowest between all the possible configurations.

Figure 6.6: Simulation of the type 0 joint-spectral amplitude of a non-linear waveguide with the experimental parameters. For more information see text.
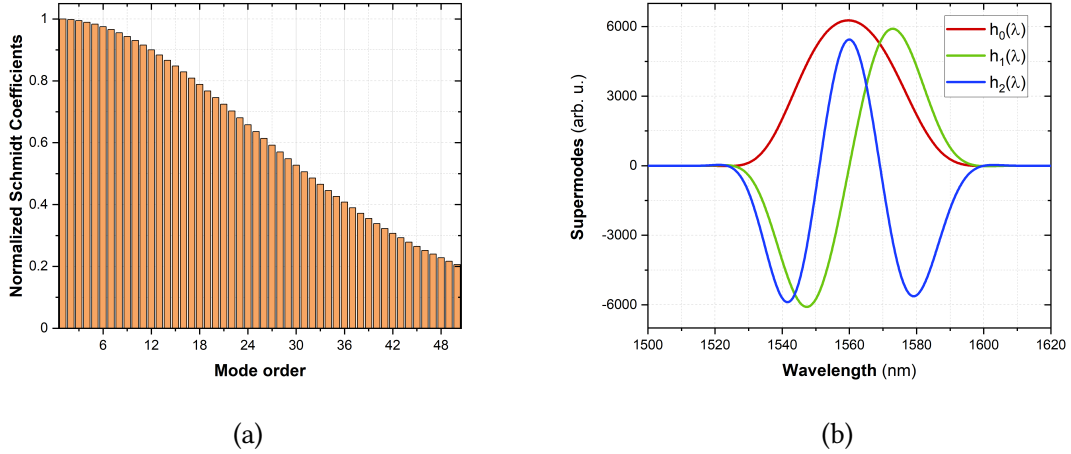

(a)	(b)

Figure 6.7: Simulation of a type 0 waveguide. The experimental parameters where $L = 15$ mm, $h = w = 3\ \mu$m, and $w_p = 2$ nm. (a) Schmidt coefficients distribution. (b) First three frequency modes.

We remark here that it would be interesting to also see how the spectral width of the

supermodes behave under changes of waveguide length and pump width. However, for type 0 and I, typically there is a lot of degeneracy in the Schmidt coefficients. As a consequence, sometimes, the numerical singular value decomposition that performs the Schmidt decomposition do not assign correctly the first mode to the first Schmidt coefficient, and even if we find it along the distribution of coefficients, sometimes the mode is a superposition of different modes due to degeneracy. This is however not the case for the simulation just shown in Fig.(6.7). This numerical problem makes it harder to show a precise plot with the simulation results in those cases. Nevertheless, it can be generally said that we roughly obtained narrower modes with broader pumps and longer waveguides for both type 0 and I.

Finally, we show the simulation with the experimental configuration we have chosen for the experiment described in the next Chapter. We chose a $L = 15$ mm PPKTP waveguide, with dimensions of approximately $h = w = 3$ μm, poling period supporting type 0 SPDC, and pumped with light showing a gaussian spectrum with width $w_p \simeq 2$ nm. The resulting joint-spectral amplitude is depicted in Fig.(6.6), while the Schmidt coefficient distribution and the first three supermodes are shown in Fig.(6.7). We chose those values based on the Schmidt number and supermode's width from a set of numerical type 0 and I simulations like the one shown here.

6.4 Type II Simulations

6.4.1 SGVM Condition

In the type II case, the fields are distinguishable, signal and idler present orthogonal polarizations, and hence their respective dispersion relations are different, $\beta_s(\omega) \neq \beta_i(\omega)$.

Since we need to make an interference between signal and idler after the waveguide in order to recover a single set of supermodes representing the nodes of the graph, we would require that the two fields are the most indistinguishable possible in order to increase their interference visibility. In central frequency, we can reach the degeneration condition when $\omega_{s,0} = \omega_{i,0} = \omega_{p,0}/2$, that can be achieved by quasiphasematching with an appropriate poling period. Assuming the waveguide to be spatially single-mode, we will be spatially limited by the difference between the spatial modes for horizontal and vertical polarization. For the fundamental mode, however, the overlap between the spatial modes for signal and idler is expected to be high (about 97% according to spatial mode simulations of the (3x3) μm KTP waveguides). Furthermore, one can use a PBS after the waveguide in a collinear configuration in order to match signal and idler polarizations.

Therefore, we require the spectral properties of signal and idler to be as close to each other as possible. In particular, the overlap between the supermodes $\{h_l(\omega_s)\}$ and $\{g_l(\omega_i)\}$ should be close to 1.

One can achieve this condition by symmetrizing the joint-spectral amplitude, which in

turn means to symmetrize the mismatch $\Delta\beta(\omega_s, \omega_i)$ under the exchange of signal and idler. Looking at the Taylor expansion of the mismatch of Eq.(6.16), it is clear that the condition $\gamma_s = \gamma_i$ symmetrize the mismatch up to first order, but this condition is obviously physically impossible since $\beta_s(\omega) \neq \beta_i(\omega)$. However, if we impose that $\gamma_s = -\gamma_i \equiv \gamma$, then:

$$\Delta\beta(\omega_s, \omega_i) \simeq \gamma(\omega_s - \omega_i) \tag{6.21}$$

and hence the mistmach is antisymmetric under the exchange of signal and idler, $\Delta\beta(\omega_s, \omega_i) = -\Delta\beta(\omega_i, \omega_s)$ up to first order in the Taylor expansion. Since the phasematching function is an even function on the variable $\omega_s - \omega_i$, (see Eq.(6.9)), then, under this condition, $\phi(\omega_s, \omega_i) = \phi(\omega_i, \omega_s)$, and in turn the joint spectral amplitude is symmetric under exchange of signal and idler fields. The spectral supermodes under this condition are identical and their intereference would be spectrally perfect. The joint-spectral amplitude can be written as:

$$J(\omega_s, \omega_i) = \alpha(\omega_s + \omega_i)\phi(\omega_s - \omega_i) \tag{6.22}$$

Note that the condition we have found for symmetrization of the joint-spectral amplitude, $\gamma_s = -\gamma_i$ can be expressed as a condition on the group velocities of pump, signal and idler, by using the definition of the coefficients in Eq.(6.18):

$$\frac{1}{v_{g,p}(\omega_{p,0})} = \frac{1}{2}\left(\frac{1}{v_{g,s}(\omega_{p,0}/2)} + \frac{1}{v_{g,i}(\omega_{p,0}/2)}\right) \tag{6.23}$$

that is, that the inverse group velocity of the pump is the mean of the inverse group velocities of signal and idler, all of them evaluated at the central frequencies. We call this condition the *Symmetric Group Velocity Matching* (SGVM) condition [150].

This scenario is the complementary case with respect to type 0/I. A function of the form $f = f(\omega_s - \omega_i)$ will make an angle of $+45^o$ with respect to the ω_s axis. Therefore, both functions $\alpha(\omega_s + \omega_i)$ and $\phi(\omega_s - \omega_i)$ are perpendicular in the (ω_s, ω_i) plane, and their interesection area is minimized. Since this area is smaller than the type 0/I case, we therefore expect fewer and narrower supermodes under the same conditions. This situation is depicted in Fig.(6.3) (b).

This configuration is of great interest because it opens the possibility of having a graph state in which all the modes are accessible, and therefore all the squeezing could be shared between experimentally measurable supermodes, making full use of the multimode state.

We remark that, for the anti-symmetrization condition to hold, the higher order terms in Eq.(6.16) should be much smaller than the linear term. This is the case in our non-linear material, KTP, under the typical frequency bandwidths of the experiment. An analysis of the higher order terms in our case can be found in Appendix C.

6.4.2 SGVM wavelength

In general, there is a unique wavelength in which the SGVM condition holds, that we will denote as λ_{SGVM}. For bulk KTP, this natural wavelength is around 1570 nm.
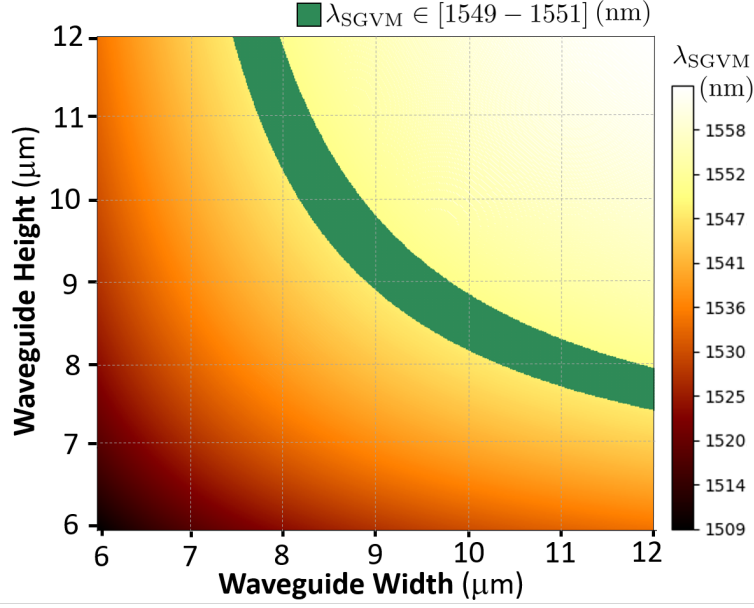
Figure 6.8: SGVM wavelength as a function of waveguide height and width for KTP. The green area indicates the region where $\lambda_{\mathrm{SGVM}} \in [1549, 1551]$ nm. Temperature was set to $T = 70\,^{o}$C.

However, it is evident that we want this wavelength to coincide with the central wavelength of our signal and idler modes, i.e. we want $\lambda_{\mathrm{SGVM}} \simeq 1550$ nm[8].

Since the SGVM condition depends only on the dispersion properties of the material (in particular the group velocities), we can tune it by changing two parameters, the temperature and the waveguide dimensions. Temperature, however, produces very little changes on the SGVM wavelength in our simulations, limiting its effect. In particular, for KTP, our simulations give a change of around 4 nm in λ_{SGVM} for a change of 230 ^{o}C in temperature. We then conclude that it seems more reasonable to fix temperature to the value giving phasematching at central frequencies and then see the tuning that we can obtain with the waveguide dimensions.

Fig.(6.8) shows the SGVM wavelength as a function of the waveguide width and height for KTP in the metallic waveguide approximation [82]. As the waveguide size increases, the surface flattens, making apparent the diminishing impact of the dispersion due to the waveguide characteristics, which is expected looking at Eq.(6.14) and letting $(h, w) \to \infty$.

---

[8]Here, the calculation was done for $\lambda = 1550$ nm instead of $\lambda = 1560$ nm because at that point of the thesis we did not have the precise value of the central frequency of our laser. However, the conclusions drawn in this Chapter are independent of this difference.

	Pump Spectral Width	**Waveguide Dimensions**	**Waveguide Length**
Schmidt Number	Minimum and linear growth	$\sim$ Independent	Directly proprotional
Mode FWHM	Directly proportional	Reverse for signal and idler	Inversely proportional
Overlap	Independent	SGVM condition	Independent

Table 6.1: Columns are input variables, rows are the output features of the graph. Each element expresses the behavior of the output with respect to the input variable.

The green area in this figure marks values of λ_{SGVM} that lie in the interval between 1549 and 1551 nm. Therefore, we conclude that to work at 1550 nm in KTP, the waveguide should have a size of about 9 by 9 μm in width and height under the metallic waveguide approximation.

We emphasize that the precise values of the waveguide dimensions depends heavily on how we model the index of refraction for the waveguides. Better modeling of the waveguides, for example with sophisticated finite element methods [151, 152], would give more precise values. The point of this section, however, is to show that in any case, a change in the characteristics of the waveguide can be found in which the λ_{SGVM} could be engineered to a desired value.

6.4.3 Simulations Results

Table 6.1 shows a summary of the dependencies between input and output variables as defined in this Chapter. It could be used as a guide depending on the type of multimode state that is desired.

All of the results of Table 6.1 can be understood from Fig.(6.9). As mentioned before, the waveguide length controls the width of the phasematching function (the longer the waveguide, the narrower the phasematching). This width has to be compared with the pump width, giving a first figure of merit. The second figure of merit is the angle between the phasematching and the pump, that can be controlled with the waveguide dimensions. If the functions are perpendicular, then the projection on the frequency axis is identical for signal and idler, and we obtain the SGVM condition. This is the reason why the SGVM condition depends on the waveguide dimensions. Furthermore, if the ratio between the pump width and the phasematching width is close to unity, then the number of modes in the Schmidt decomposition will tend to 1 as well.

Note that if one is able to fix the angle with the waveguide dimensions so that we obtain the SGVM condition, then the ratio between the widths will give $K \simeq 1$ when both functions have the same width to higher values when changing the waveguide length or the pump width. Hence, a nice control of the supermodes, and hence on the number of nodes, can be
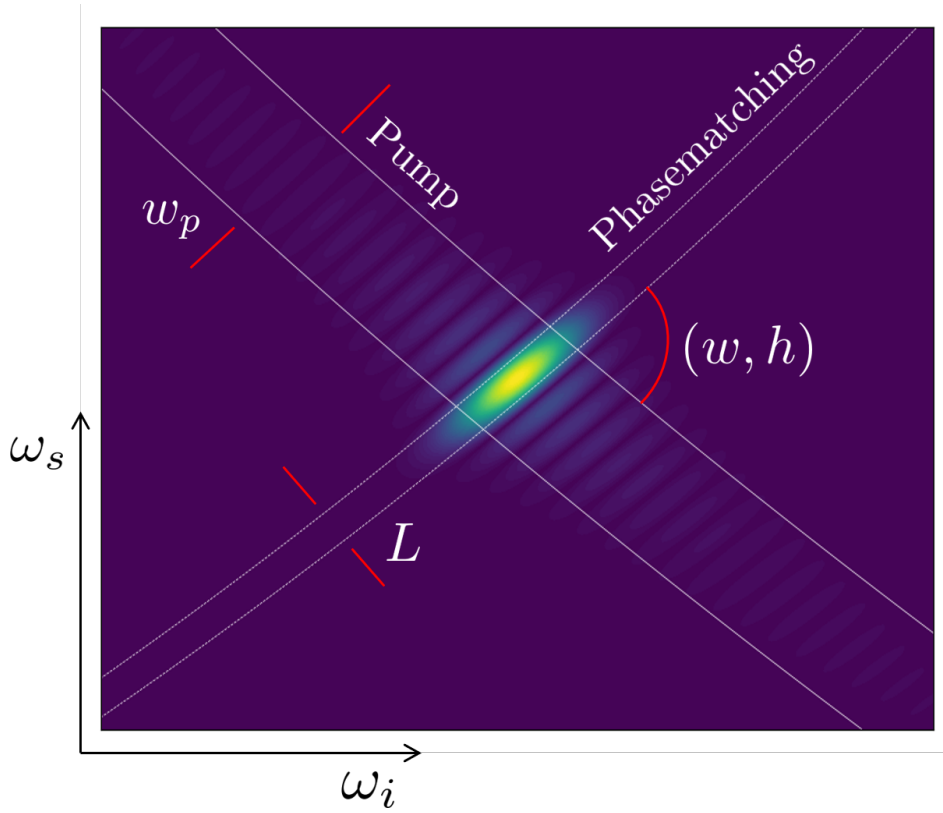
131

Figure 6.9: General example of a JSA function in Type II, highlighting the impact of the waveguide length L, pump spectral width, w_p, and waveguide dimensions (w, h). For more details see text.

performed. If the angle is not perpendicular, the behavior of the number of modes with the ratio between widths will be the same, but the minimum of K would be higher in this case, and the supermodes widths for signal and idler would be different. This is the intuition that allows to understand all the results that will be shown next.

The rest of this section will explore Table 6.1 in detail. The range of values adopted for the input variables is the following: we consider pump widths from 1 to 12 nm, waveguide dimensions between 4 and 10 μm, and waveguide lengths between 5 and 30 mm. The pump width can be modified by tuning the pump field that enters the waveguide, while the waveguide dimensions and length are fixed during the waveguide fabrication process.

For the sake of clarity, we will refer to the elements of Table 6.1 like matrix elements. For instance, the element 2.1 refers to the second row and first column, which corresponds to the dependence of the mode FWHM on the pump width.

First row of Table 6.1, the Schmidt number: Fig.(6.10) (a) shows the Schmidt number as a function of pump width for different waveguide dimensions (elements 1.1 and 1.2 of Table 6.1). The Schmidt number, and thus the number of modes, grows linearly with the pump
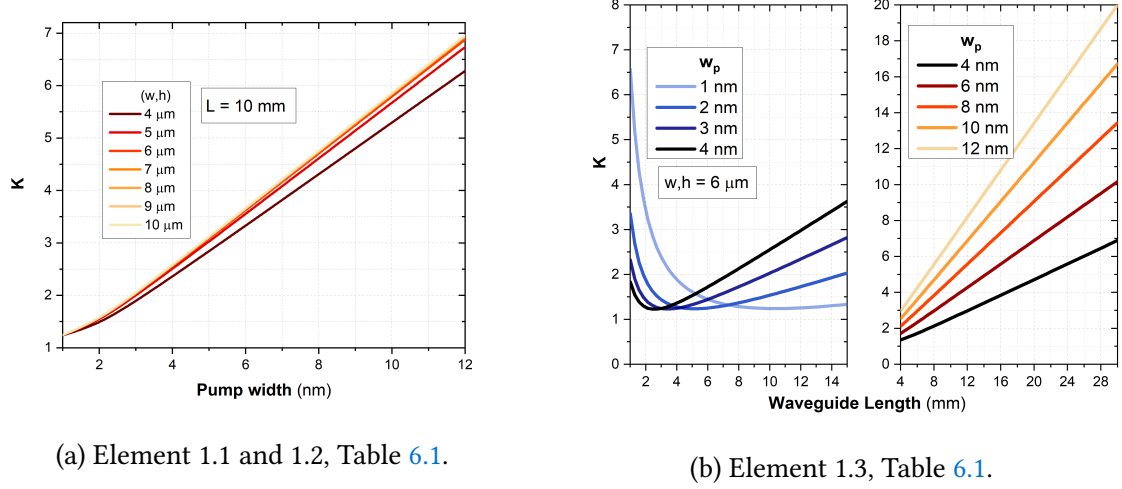
(a) Element 1.1 and 1.2, Table 6.1.

(b) Element 1.3, Table 6.1.

Figure 6.10: Schmidt number as a function of: (a) pump width for different waveguide dimensions, (b) waveguide length for different pump functions.

width, while the waveguide dimensions have almost no influence. The waveguide length was set to L = 10 mm for this simulation. This result can be interpreted in the following way: as the pump width increases, the pump envelope does too, and hence its intersection with the phasematching envelope. This creates frequency correlations between signal and idler fields and hence increases K. This is true because in this set-up the pump envelope is bigger at any time than the phasematching envelope. In general, there would be a minimum value of K when both envelopes have equal widths.

Fig.(6.10) (b) shows the Schmidt number as a function of the waveguide length for different pump widths. In this case we are changing the phasematching envelope, and we observe the minimum value of K when both the pump envelope's and the phasematching envelope's widths are equal. This is why we see that the waveguide length in which the minimum value is reached depends on the pump width. Also, as mentioned above, the minimum value itself would approximately equal 1 when the intersection of α and ϕ was at 90°, that is, at the SGVM condition. This is interesting for applications in single photon sources, where K = 1 ensures maximum purity of heralded single photons (see for example [153]). After the minimum point, increasing the waveguide length decreases the width of the phasematching envelope, and so we are effectively in the same situation as in Fig.(6.10) (a), and we observe the same type of behavior, which is a linear increase in K. It is important to note that in Fig.(6.10) (b) we see that one can control the slope of the increasing linear regime by controlling the pump width, which opens the possibility of modifying the number of modes just by adjusting the pump field. In a realistic scenario, the maximum waveguide length would be limited by the optical losses within the waveguide and the size of the available substrate material. State of the art KTP waveguides have losses of 0.25 dB/cm, which would
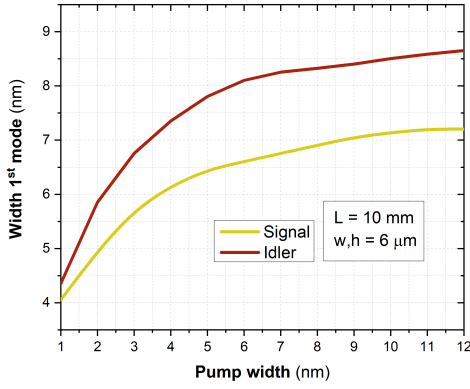
(a) Element 2.1, Table 6.1.
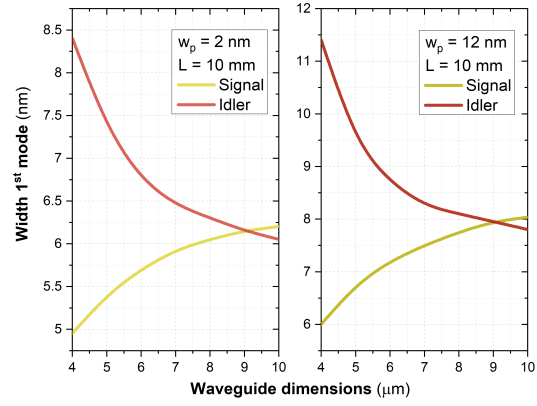
(b) Element 2.2, Table 6.1.
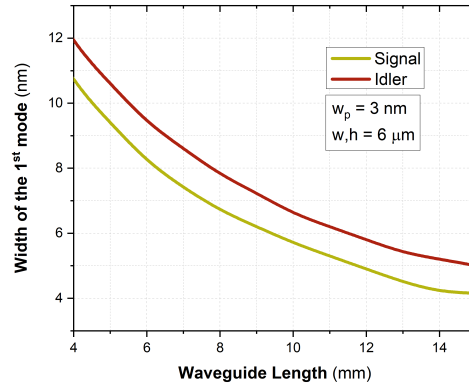
(c) Element 2.3, Table 6.1.

Figure 6.11: First mode FWHM as a function of: (a) pump width, (b) waveguide dimensions, (c) waveguide length.

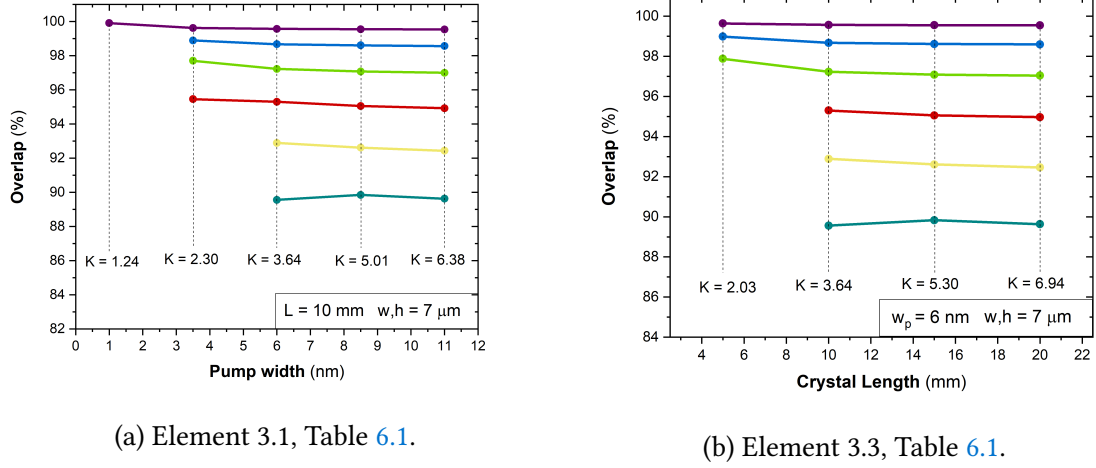(a) Element 3.1, Table 6.1.

(b) Element 3.3, Table 6.1.

Figure 6.12: Overlap of the first 6 Schmidt temporal modes as a function of: (a) pump width, (b) waveguide length.

point toward waveguide lengths in between 10 and 20 mm. This is in accordance with the maximum size of KTP substrates of roughly 30×30 mm^2.

Equivalently, the Schmidt number increases rapidly by decreasing the waveguide length before the minimum, because in that case the 1/L dependence on the phasematching width is more important, creating strong wiggles in the sinc function in Eq.(6.9), and in turn producing strong correlations between the output fields, hence increasing K.

Second row of Table 6.1, the modes bandwidth: we remark that, given that the supermode solutions are approximately a family of Hermite-Gauss modes[9] , it suffices to compute the mode FWHM of the first mode (that is approximately Gaussian), as the rest would grow in width as $\sqrt{n}$, where n is the mode order. Therefore knowing the first FWHM is sufficient to approximately characterize all of them. Fig.(6.11)(a) shows the width of this mode as a function of pump width, which corresponds to the element 2.1 in Table 6.1. The waveguide dimensions were set to $w, h = 6 \ \mu$m, intentionally away from the SGVM condition. We can see that indeed signal and idler modes have different widths for all pump widths and hence their interference would not be perfect with these waveguide dimensions, as expected from the results of the SGVM analysis.

Fig.(6.11)(b) shows the modes FWHM as a function of the waveguide dimensions for pump widths of 2 and 12 nm. Both signal and idler modes coincide at waveguide dimensions near 9 μm (we considered square waveguides), as expected from the SGVM analysis before. We show the plots for two different pump widths to remark again that the similarity of

---

[9]Assuming a gaussian phasematching, the Hermite-Gauss set is exactly the solution. For a sinc phasematching, the modes are close, but in general they present some wiggles at the Hermite-Gauss wings inherited from the sinc function. See the output modes depicted in Fig.(5.5).
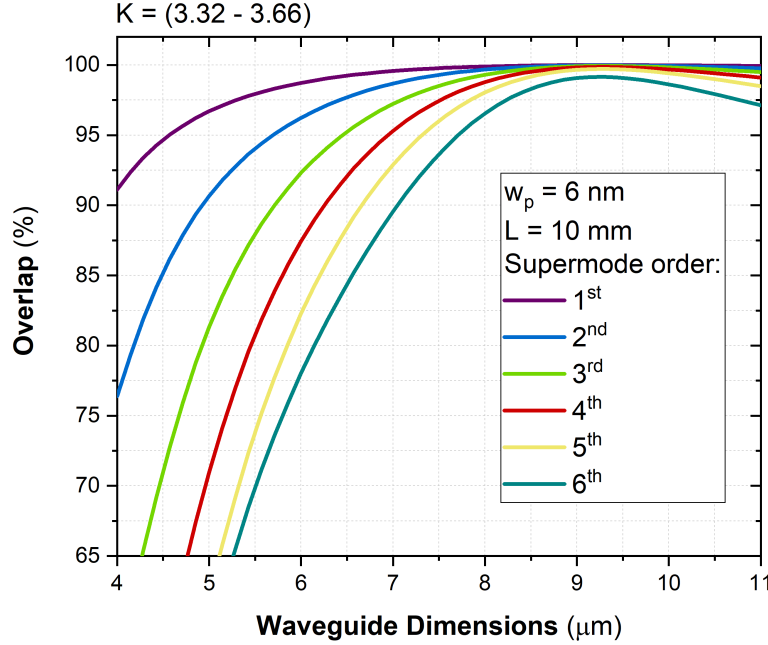
135

Figure 6.13: Overlap of the first 6 Schmidt temporal modes as a function of waveguide dimensions. Element 3.2 in Table 6.1.

signal and idler modes is independent of the pump width, as it is related to the waveguide's phasematching function. These relations correspond to the element 2.2 in Table 6.1.

Finally, Fig.(6.11)(c) shows the modes FWHM as a function of waveguide length for $w_p = 3$ nm and $w, h = 6$ μm, again intentionally away from the SGVM condition. Both widths decrease with length, which would point toward the use of the longest possible waveguide if we are to measure the fields by coherent detection. This relation corresponds to element 2.3 in Table 6.1.

Third row of Table 6.1, the mode overlap: Fig.(6.12) (a) shows the overlap of the first six temporal modes as a function of pump width, leaving fixed the rest of the variables. We can see that the overlap decreases with increasing mode order; the reason is discussed in Appendix D, in which we showed that this effect is due to two factors: the increasing width of the modes with the mode order, and the mathematical properties of the Hermite Gauss modes themselves. The pump width does not change the overlap, even though we have just seen that it changes the relative modes' FWHM by up to 25%. This counter-intuitive behavior arises due to the stability of the relative width of two Gaussian functions when their relative widths change. The mathematical result is that for a relative width difference of 25%, i.e. if the width of one Gaussian is 1.25 times the width of the other, then the change in their overlap does not even reach 1%. This explains why we obtain a constant overlap

136

for different pump widths, although the modes' widths change significantly.

In a similar way, Fig.(6.12 (b) shows that the waveguide length has no effect on the mode overlap. The Schmidt numbers, and hence effective mode numbers, for different lengths are marked in the plot. These two figures correspond to the elements 3.1 and 3.3 in Table 6.1.

Completing Table 6.1, Fig.(6.13) shows the mode overlap as a function of the waveguide dimensions. We observe that the individual temporal mode overlaps have a common maximum at waveguide dimensions around 9 μm, as we computed in the SGVM study. Also, for every waveguide dimension, the similarity between modes decreases as the mode order increases (again the reason for this can be found in appendix D). This dependence corresponds to element 3.2 in Table 6.1.

6.5 Final Experimental Configuration

The simulation results give type II under the SGVM condition as the most controllable quantum state with a few number of modes. This configuration would be adequate, for instance, for implementing quantum information protocols in which few parties are involved, as secret sharing [112], quantum electronic voting [113] or Multiparty Quantum Secure Communications [114]. However, there were some technical problems while trying to obtain type II waveguides. First of all, in order to have a more precise result on the values of the waveguide dimensions that fulfill the SGVM condition, a sophisticated modelling of the index of refraction, specific for a particular non-linear material, should be used. This in turn meant that the specific type II waveguides should be fabricated with a new mask, increasing considerably their fabrication time. Furthermore, the dimensions suggested by the SGVM analysis gives waveguides that are fairly big compared to the central wavelength (9 μm vs 1.5 μm). We expect those waveguides to allow a set of discrete spatial modes, which could create spatio-temporal correlations in the state. The impact of these correlations would be in general difficult to work with experimentally.

For this reason, we decided to perform the generation of the multimode squeezed states with type 0 or type I waveguides, where no signal-idler interference is needed since the fields are indisinguishable in the first place, facilitating the experimental setup. According to our simulations from this Chapter, type I, that has a lower non-linear coefficient, also presents many modes compared to type 0, and we therefore expect the squeezing per mode to be much higher in type 0.

In conclusion, we decided to perform the experimental generation of the graph states via type 0 SPDC in KTP waveguides. The dimensions of the waveguide in which we generated the quantum state were $(h, w) = (3, 3)$ μm, and the waveguide length was $L = 15$ mm. The created states are centered at telecom wavelengths $\lambda_{s,0} = 1560$ nm, and pumped with ultrashort pulses centered at $\lambda_{p,0} = 780$ nm.

Chapter 7

Experimental Generation of CV Multimode Squeezed Vacuum States in the Frequency Domain

"It doesn't matter how beautiful your theory is, it doesn't matter how smart you are. If it doesn't agree with experiment, it's wrong."

– Richard P. Feynman

Contents

In this final Chapter, we aim to show the experimental results of the generation of CV multimode squeezed states performed in the laboratory. For better comprehension, the experiment will be divided into blocks, and we will detail every block separately. Some of the blocks, however, have been already studied in precedent Chapters of this manuscript. The long-term goal of the experiment is to show the generation of the configurable graph state, that is, the experimental demonstration of the quantum source. For this purpose, we first need to measure multimode squeezing in the telecom light coming out from the waveguides, since this is the resource for the graph state generation.
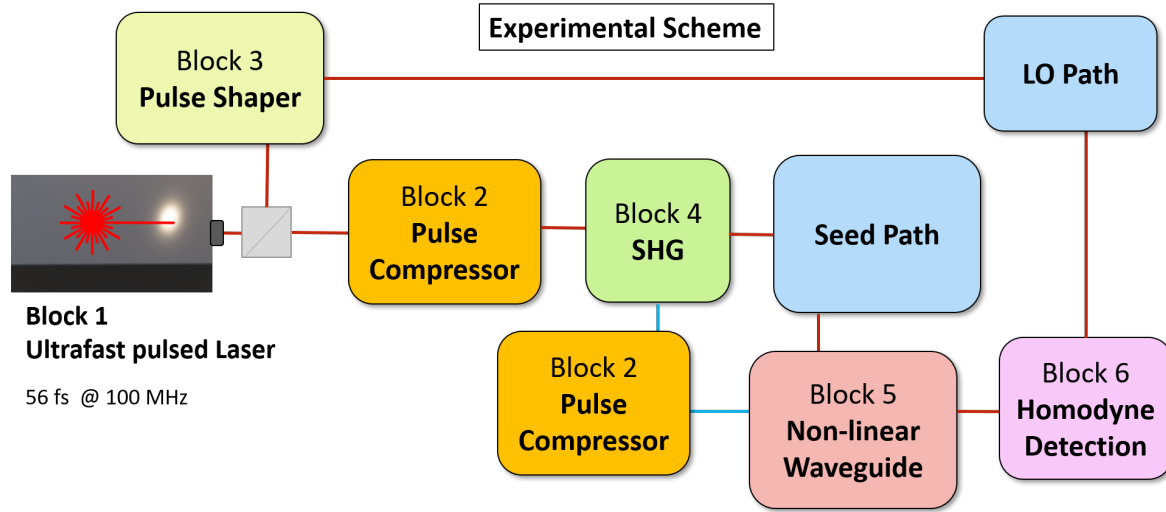
Figure 7.1: Experiment Scheme. The experiment is constituted by six blocks. For more information see text.

7.1 Experimental Scheme

We divided the experiment into a total of 6 blocks. Each block has a purpose and the functioning of all the blocks is necessary for the quantum source to work. In Fig.(7.1) we show the scheme of the blocks constituting the experiment.

The blocks are therefore the following:

○ **Block 1**: Laser source.
The laser serve as the source of ultrafast pulses needed for three-wave mixing interaction in the non-linear waveguides. This block has been already discussed and characterized. The results are in Chapter 3, Section 3.4.

○ **Block 2**: Pulse Compressors.
We used one pulse compressor for compensating the temporal dispersion suffered by the pulses at telecom. Sometimes, another pulse compressor is needed also for the pump wavelength at 780 nm. For the results of this Chapter, this extra pulse compressor was finally not used, but it is depicted in Fig.(7.1) for completeness. Pulse compressors has also been discussed, and the experimental results can be found in Chapter 3, Section 3.5.1.

○ **Block 3**: Pulse Shaper.
At the very beggining of the experiment, we separate the laser's beam, using an unbalanced beamsplitter, into two paths. One path, known as the Local Oscillator (LO), is sent to the pulse shaper, while the rest of the power is used for the non-linear

processes in the experiment. The pulse shaper is needed to manipulate the temporal modes of the LO into the Hermite-Gauss basis, that is approximately the basis of temporal modes after the SPDC in the non-linear waveguides, as seen in Chapter 6. This will allow to perform the homodyne detection in order to access the nodes of the Graph state, to be explained below.

We have also discussed the pulse shaper, the experimental results can be found in Chapter 3, Section 3.5.2.

○ **Block 4**: Second Harmonic Generation.
We realized a Second Harmonic Generation process using a PPLN bulk crystal in order to double the frequency of the original laser source to a central wavelength of 780 nm. This process prepares the pump field for the SPDC in the non-linear waveguides. We take another part of the field with a 90/10 beamsplitter before the SHG crystal to have a telecom field that was used as a seed field. The seed field serve for alignment purposes in the rest of the blocks, since the SPDC light generated by the waveguides is too dim to see it alone, and for the waveguide characterization at telecom light.

○ **Block 5**: Non-linear Waveguide
The waveguides provide the quantum graph states as described in Chapters 5 and 6. The multimode vacuum state is prepared by applying only the pump field at the input facet of the waveguides. Additionally, when introducing the seed field, the PDC process is stimulated via difference frequency generation. This effect produces amplification or deamplication of the seed field at the output of the waveguides, depending on the relative phase between the pump and the seed fields. This effect is known as *Phase Sensitive Amplification* (PSA). A first PSA experiment shows the presence of parametric gain, precondition for squeezing, with a simpler detection mechanism, since no homodyne detection is needed. It also serves for confirming the synchronization of the pulses, that will be discussed later in the Chapter.

○ **Block 6**: Homodyne Detection. Homodyne detection is used to characterize the multimode state, by mixing the LO and the quantum signal to measure the quadrature values of the different temporal modes constituting the total state. By changing the relative phase between the LO and the quantum signal, the quadrature that is measured changes accordingly, spanning the whole phase space after the relative phase goes from 0 to 2π. In the presence of squeezing, we should therefore see oscillations in the noise of the quadrature value that is measured, indicating that a quadrature in phase space has less variance when measured than the conjugate one. By changing the LO temporal mode we measure the squeezing of each supermode independently, therefore characterizing the full quantum available resource.

Apart from the blocks, there are two optical paths, for seed and LO, in Fig.(7.1). In each of these paths we set a delay line, a group of lenses and a piezoelectric mirror. The delay lines

are used for pulse synchronization, given the necessity of the seed to enter the waveguides at the same time than the pump field for PSA, and the necessity of the LO pulses to mix in the balanced beamsplitter of the homodyne detection. The lenses are used for spatial mode-matching, in order to match the spatial profiles of seed, LO and quantum signal. The piezoelectrics are used for changing the relative phases of seed-pump, and LO-quantum signal, respectively.

In this Chapter, we therefore explore Blocks 4, 5 and 6, showing their performance and experimental details. Finally, we will show the final results of the experiment of phase sensitive amplification and multimode squeezing in the quantum signal.

7.2   Second Harmonic Generation

We performed simulations of SHG for predicting the output spectrum given the crystal length and the input spectrum. Finally, we obtained two PPLN crystals, one long, $L = 3$ mm, from HCPhotonics [154], and the other short, $L = 0.3$ mm, from Covesion [155]. Both crystals were introduced in an oven with a temperature controller that allows temperature stabilization in $\pm$ 0.1 ^{o}C in a range of 30 ^{o}C to 200 ^{o}C.

Both crystals contain different *zones* with slightly different values of the poling period. In our case, since our input spectrum is very large in bandwidth, we obtain second harmonic power for every zone, with different power levels, because, for the range of poling periods in the crystal, there is always a wavelength in the input spectrum that is phasematched with that zone. Therefore, the central wavelength in the output spectrum changes with zone and with temperature. Optimization of the SHG for us means that we select the zone with the highest output power and tune temperature to obtain a central wavelength of 780 nm. Alignment of the chip is somewhat important since the input angle could generate spatial chirp in the second harmonic beam.

A shorter crystal will present a smaller conversion efficiency, since the interaction time in the crystal is shorter. However, the phasematching bandwidth, that is inversely proportional to the crystal length, will be consequently larger, and more wavelengths can intervene in the process. The result would be a larger output spectrum in shorter crystals. Temporally speaking, a shorter crystal will generate shorter pulses at the output, which is coherent with the fact of having a larger spectral bandwidth. The pulse duration for long crystals is limited by an effect known as $temporal\ walk-off$ [156]. In long crystals, due to the group velocity difference between the pump wave and the second harmonic wave, the temporal matching of both pulses in the crystal is lost after some interaction length, and no second harmonic is generated after this effective length. This effect can also happen for shorter crystals if the group velocity difference is high enough. The characteristic walk-off time can be obtained as:

$$\tau_{\text{walk--off}} = L \left(\frac{1}{v_{g,p}(\omega_{p,0})} - \frac{1}{v_{g,s}(\omega_{s,0})} \right) \tag{7.1}$$

where $\omega_{p,0}$ is here the pump to the SHG crystal (1560 nm), and $\omega_{s,0}$ is the second harmonic central frequency (780 nm).

For a given crystal length, if the input pulse duration is bigger than the temporal walk-off, the second harmonic pulses will have a duration similar to the walk-off time and the pulse shape will be similar to a square pulse.

In both cases, the SHG process used was type 0, where the polarization of pump and second harmonic are vertical (extraordinary index). Since we know the Sellmeier equations for LN we can compute the group velocities and the walk-off time for both SHG crystals, obtaining[1]

$$\tau_{\text{walk-off}}(\text{Covesion}) = 91.1 \text{ fs} \tag{7.2}$$
$$\tau_{\text{walk-off}}(\text{HCPhotonics}) = 911.2 \text{ fs} \tag{7.3}$$

and this value should be similar to the minimum pulse duration we can have after the SHG crystals.

As a comment, it is possible to reduce significantly the walk-off time in LN by means of the type I process, where the pump is polarized along the ordinary axis and the SHG is polarized along the extraordinary axis. In this case the walk-off time is reduced $\sim$6.5 times with respect to the type 0 case, giving $\tau_{\text{walk-off}}(\text{type I}) = 140$ fs for a 3 mm LN crystal. Nonetheless, the non-linear coefficient associated with type I is about 4 times smaller than for type 0, and so the crystal efficiency is also considerably smaller.

7.2.1 PPLN Covesion

We optimized the SHG from the Covesion crystal, finding the second harmonic signal from the different zones with different poling periods and tuning the temperature so that we obtained a central wavelength of 780 nm and maximum second harmonic power.

In Fig.(7.2) we plot the measured output second harmonic power versus the input telecom power for the selected zone. We could reach up to 265 mW of input power. It is well known that the output power of a SHG process goes with the square of the input power [157]:

$$P_{\text{out}}^{(\text{SHG})} \propto P_{\text{in}}^2 \tag{7.4}$$

which in turn means that the efficiency of the process grows linearly with the input power. We obtain this behavior for the Covesion crystal and measured efficiencies up to $\sim$ 4.5 %. The efficiencies are not very high since the crystal is quite short (0.3 mm).

However, in Fig.(7.3) we see that the spectrum is quite large ($\sim$ 14 nm), and the pulses considerably short, 150 fs.

---

[1]We did this calculation for a temperature of $T = 90\ ^o$C. The temperature dependence is in any case quite weak.
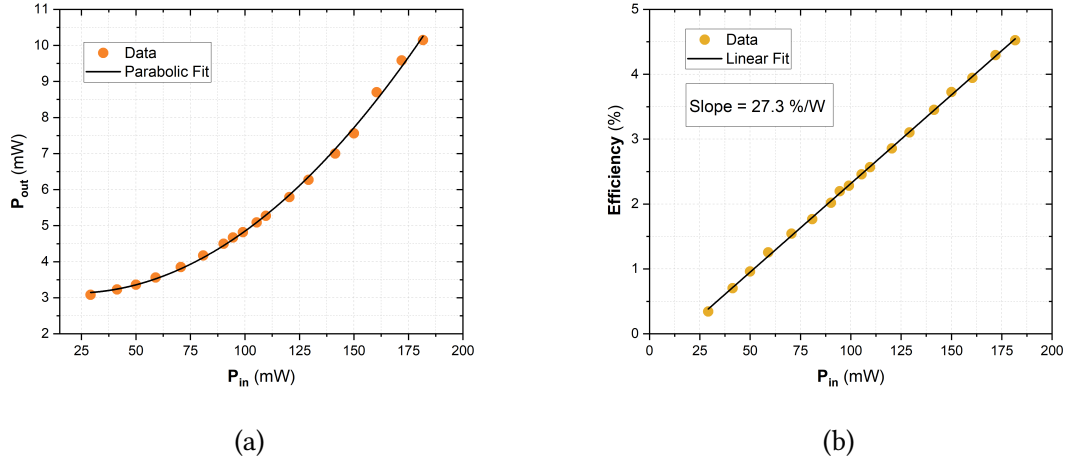
Figure 7.2: Covesion SHG Crystal. (a) Second harmonic power vs input telecom power. (b) Corresponding SHG efficiency.
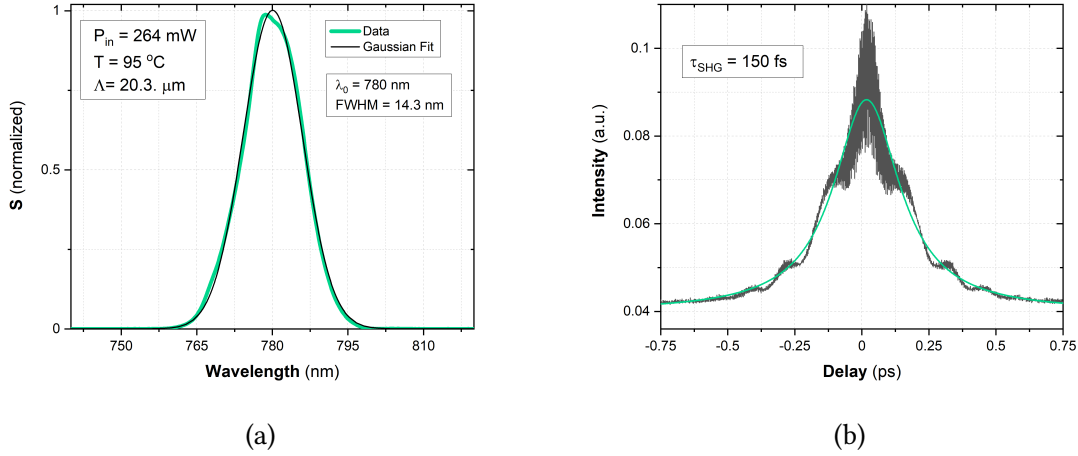

Figure 7.3: Covesion SHG Crystal. (a) Second harmonic Spectrum with a gaussian fit. (b) Autocorrelation signal of the second harmonic, giving a pulse duration of 150 fs.

As we have seen in Chapter 6, a large pump spectrum to a SPDC process in general increases the number of nodes in the Graph state. The spectrally broader pump that we prepare with the Covesion SHG crystal could be particularly useful for a type II waveguide, where the number of nodes is in general small and hence broader spectra are necessary for increasing the multimode character of the states.
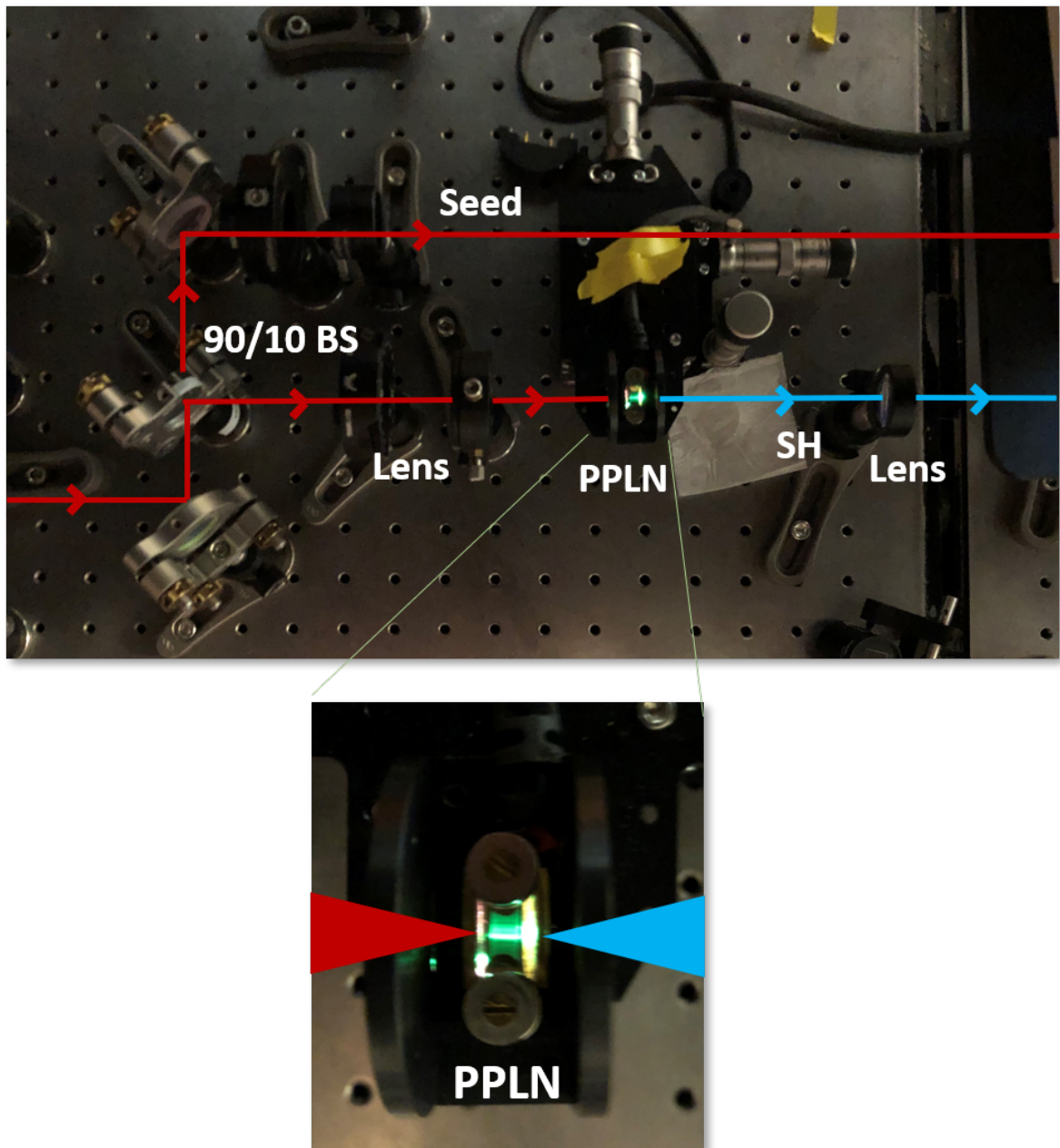
Figure 7.4: SHG photo from the experimental lab. BS: Beam splitter, L_{in}: Input achromatic lens for 1560 nm, L_{out}: output lens at 780 nm.

7.2.2 PPLN HCPhotonics

We performed the same characterization of the SHG crystal provided by HCPhotonics. In this case, the crystal is 10 times longer than before, and so the efficiency is considerably higher, as we can see in Fig.(7.5), reaching up to 30%. We also see saturation of the efficiency, that goes away gradually from the linear regime. We first thought that this saturation behavior was caused by another non-linear effects taking part in the non-linear material. In particular, *Green Induced Infrared Absorption* (GRIIRA), [158, 159], since some green light can be generated in PPLN, by a sum frequency process. This green light, even if quite dim (we cannot resolve it with our spectrometer) induces absorption of telecom light, and hence act as a non-linear source of losses. In Fig.(7.4), that is a photo of the actual SHG in the lab, we can see the green light leading to GRIIRA. The GRIIRA effect depends on the doping elements and concentrations of the LN crystal. However, this effect would be independent of the Second Harmonic Effect, and hence we should also have seen it in the Covesion crystal, since the input powers were very similar, but this is not the case. Although the GRIIRA effect should take part in the phenomenon, the main reason for the saturation of the efficiency is another non-linear effect in the material, namely *two-photon absorption* in the high power regime, see [160, 161, 162]. Here, we empirically modeled this effect as a contribution to the efficiency that goes as P_{in}^{-1}, and the data fits well in our experimental conditions.
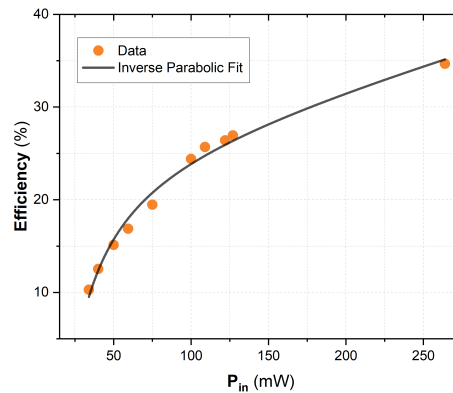

Figure 7.5: HCPhotonics SHG crystal. Efficiency as a function of input telecom power. Saturation due to two-photon absorption effects. See text for more information.

The second harmonic spectrum is hence shorter, $\Delta\lambda_{\mathrm{SHG}} \sim 2\,\mathrm{nm}$, and the autocorrelation signal is triangular, which corresponds to a squared pulse. This is because we are limited by the temporal walk-off in the crystal. The triangular fit gives a pulse duration around $\tau = 850\,\mathrm{fs}$, which is consistent with the numerical calculation we have done for the walk-off in Eq.(7.3). We show both the spectrum and the autocorrelation signal for the SHG of the HCPhotonics crystal in Fig.(7.6). We can see the wiggles in the spectrum due to the sinc
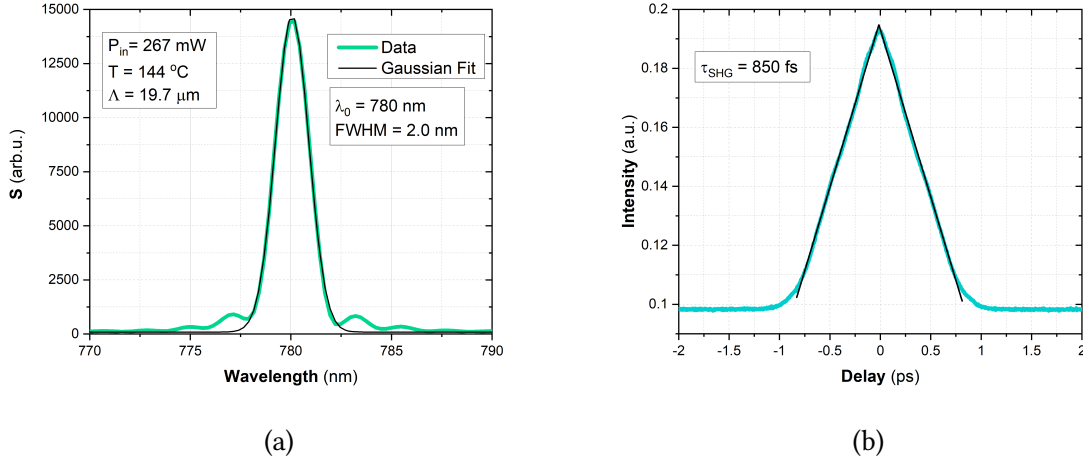
(a)   (b)

Figure 7.6: HCPhotonics SHG Crystal. (a) Second harmonic Spectrum with a gaussian fit. (b) Autocorrelation signal of the second harmonic, giving a square pulse duration of 850 fs.

nature of the phasematching function. The Fourier transform of the sinc function is exactly a square function, which is the pulse waveform.

Finally, we decided to use the HCPhotonics PPLN crystal to prepare our pump field for the waveguides in the experiments presented in this Chapter, due to the higher average optical power. Since the pulse is already quite long temporally, no pulse compressor is needed after the SHG for the pump, since our typical dispersion scale is relevant for shorter pulses. The use of the Covesion SHG implies the potential mounting of an extra pulse compressor before the waveguides. Also, our type 0 simulations in our waveguides suggest that there are fewer modes with the HCPhotonics pump (narrower spectrum), and hence the squeezing per mode is expected to be higher. The Covesion SHG could be nevertheless interesting to test for a near-term experiment, and in particular for a type II waveguide, where the number of modes is smaller than the type 0 or I case.

7.3   Waveguide Characterization

The waveguide chip of our experiment was described in Chapter 4, Section 4.2.5. We recall that the chip, 1.5 mm wide, contains 30 waveguides, divided into 5 groups, that have dimensions of 3x2, 3x3 and 3x4 μm, repeated along the chip in that order, as shown in Fig.(4.6). In that Chapter, we presented the experimental spatial mode characterization, both at pump and telecom wavelengths.

The experimental setup for the waveguides is shown in Fig.(7.7). We used a nanometric 6-axis translation stage from ElliotScientific [163] to be able to precisely manipulate the waveguide alignment. The input lens is achromatic, optimized for pump wavelengths,

with a focal length of $f_{in} = 10$ mm. The ouput lens, used for collecting and collimating light after the waveguide, is an aspheric lens with $f_{out} = 10$ mm. For the waveguide characterization at pump wavelengths, the lens is optimized for wavelengths around 800 nm. For the actual experiment, we use a lens optimized for telecom wavelengths, since the pump wavelength after the single-pass waveguide interaction is irrelevant. We spatially superpose the pump and seed at the input facet with a dichroic mirror, and we filtered the transmitted pump after the waveguide using another dichroic mirror. Finally, the waveguides are mounted in a homemade holder inside an oven connected to a temperature controller, that allow us to tune and maintain the waveguide temperature.
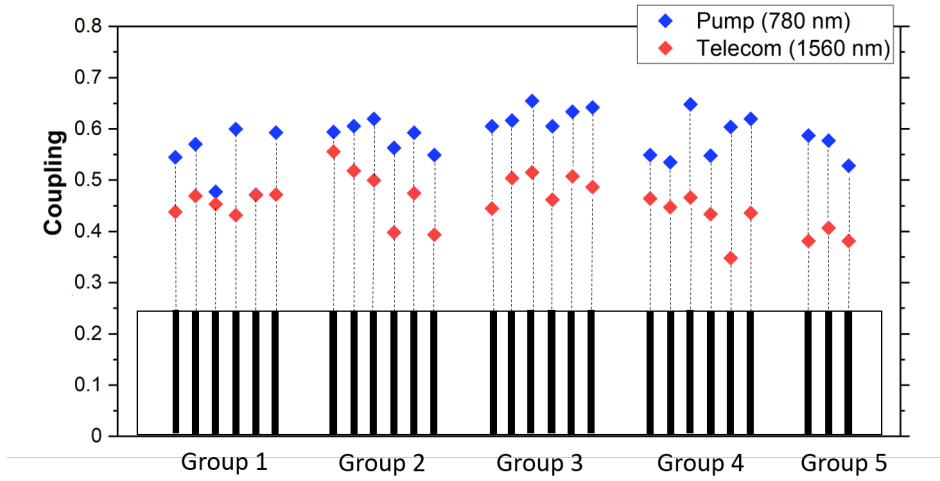

Figure 7.8: Coupling efficiency at pump and seed wavelengths for every waveguide measured along the chip. In all cases the polarization was set to vertical.

We injected the seed and pump fields independently and measured the optical powers and spatial modes after the output lens collimates the beam. Since the light confinement is very high inside the waveguide, we have variable density filters before the waveguide to be able to tune the input pump and seed power. We are interested in injecting with a few mW in order to be sure we do not burn the waveguides. Specifically, for the characterization, we measured the power just before the waveguide chip to be $P_{seed, in} = 11.8$ mW and $P_{pump, in} = 7.1$ mW. Additionally, we control the input light polarization with half-waveplates.

The ratio between the input and output power is known as the waveguide *coupling*. We show the measured coupling for both pump and seed in Fig.(7.8). The couplings shown are for beams polarized along the vertical direction, which is the direction that will be used for squeezing generation. However, similar results are also obtained for horizontal input polarization. The last three waveguides at the chip edge were not measured because the beams clipped due to our geometrical homemade holder setup. We observe good homogeneity in
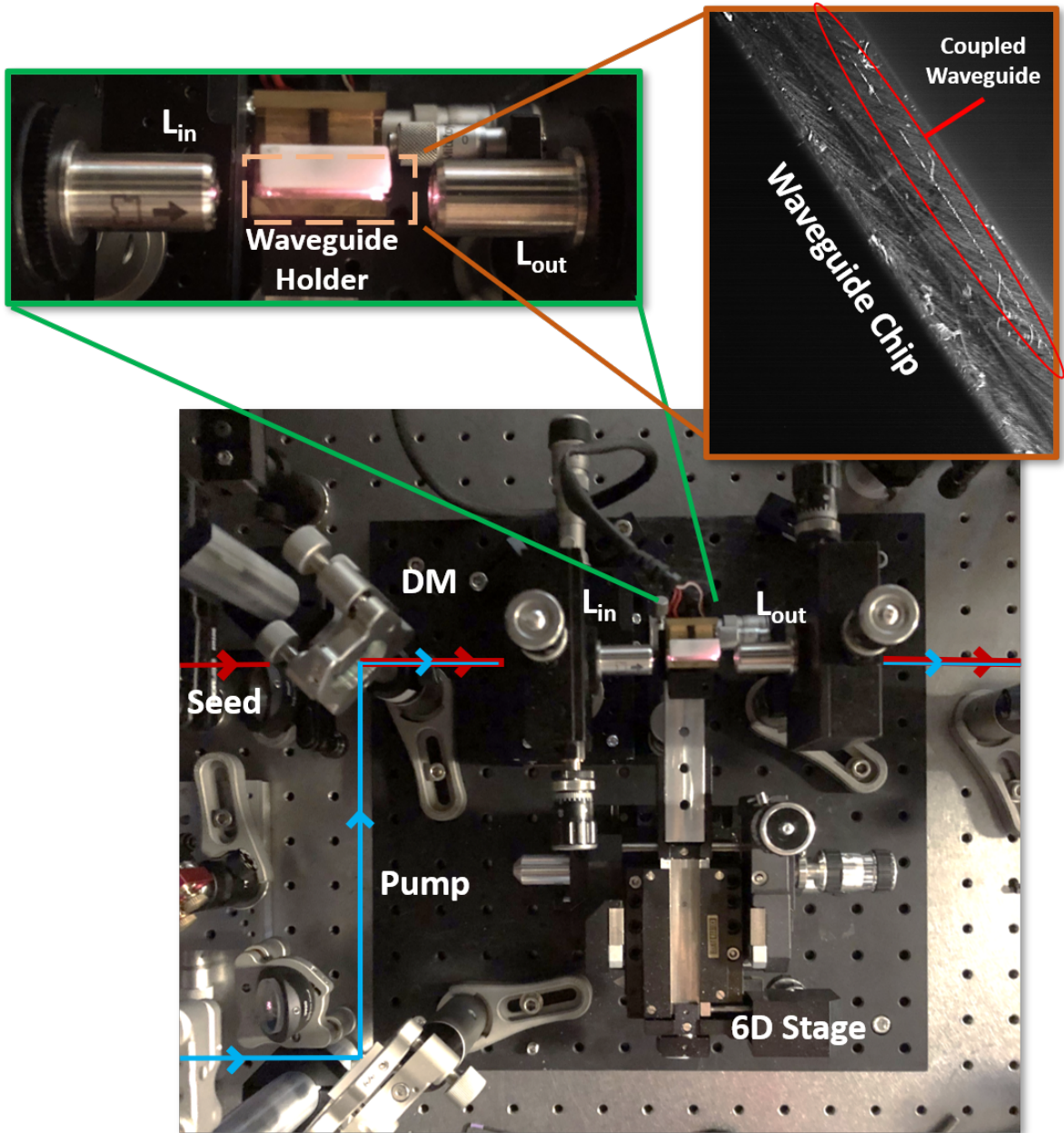
Figure 7.7: Photo of the waveguide chip setup in the experimental laboratory. DM: Dichroic mirror, L_{in}: input achromatic lens, L_{out}: output aspherical lens. Up left: close-up of the homemade waveguide holder and the lenses. Up right: Zoom photo of the waveguide chip, the light coupled to one of the thirty waveguides can be seen and it is rounded in red.
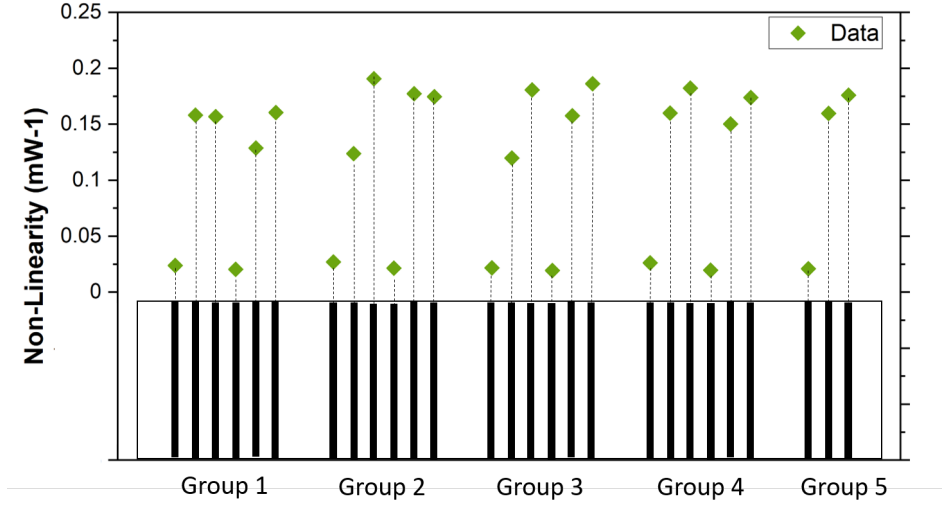
Figure 7.9: Measured waveguide non-linearity as $\eta_{\mathrm{SHG}} \equiv P_{\mathrm{SHG}}/P_{\mathrm{seed}}^2$ along the waveguide chip.

the coupling along the waveguide chip. It is worth to note here that in our experiment we will need to inject both beams at the same time and in the same waveguide. Therefore, the input lens is common for both beams and should focus both. This is the reason why it is important to use an achromatic lens. Otherwise, the light spot at the waveguide facet could be so different that the coupling of one of the two beams could be compromised. In our case we observe good coupling for both the pump and seed.

Since the SHG generation is the reverse process of type 0 PDC, the waveguides are also phasematched for SHG when pumped with the seed field and therefore generate second harmonic light. This is very convenient for a number of reasons:

○ First of all, it allows us to characterize the waveguides non-linearity by measuring the proportion of second harmonic light with respect to the transmitted seed. Since we know that the power relation is quadratic for SHG, we define the quantity $\eta_{\mathrm{SHG}} = P_{\mathrm{SHG}}/P_{\mathrm{seed}}^2$ as a measure of the non-linearity of the waveguides. For a complete measurement of η_{SHG}, several power measurements should be taken and then fitted to the parabolic curve. However, since our objective is to characterize the waveguides, we are only interested in comparing the non-linearities of the different waveguides, which can be done by measuring η_{SHG} once for all the waveguides at the same input power. This measurement is shown in Fig.(7.9). We clearly see that all the waveguides with dimensions 3x2 μm (first and fourth in every group) have a lower non-linearity. The reason for this became clear when we measured the SHG spectrum associated with this waveguides.
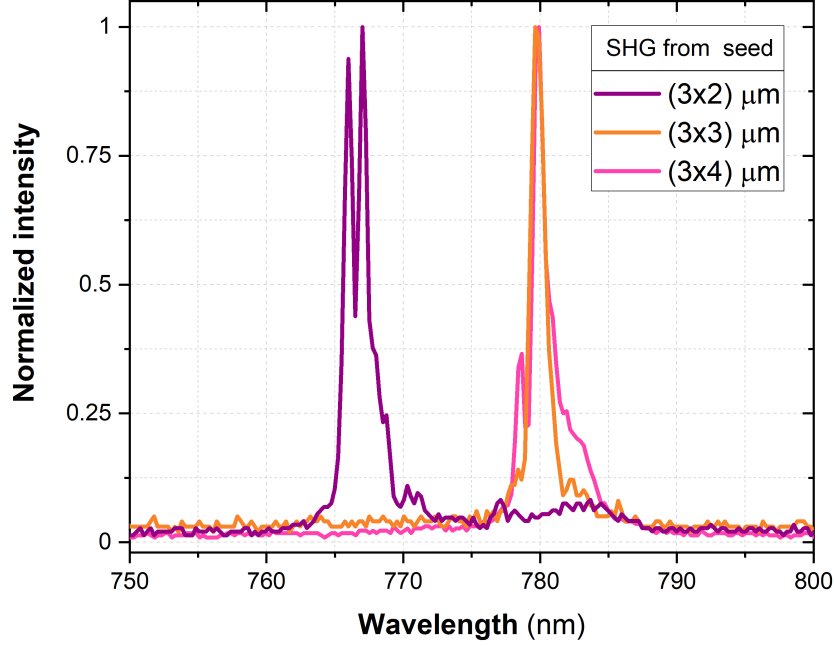
Figure 7.10: Spectra of the SHG's seed in three waveguides (3.1, 3.2 and 3.3). Each waveguide has different depths.

○ Secondly, the spectrum of the generated second harmonic light serve to know if the wavelengths of the PDC process are centered correctly. The SHG central wavelength can be slightly modified by changing the oven's temperature. This method was used to fix the waveguide temperature in the experiment. Additionally, the form of the spectrum also spots if there is any inhomogeneity along the propagation direction. In the absence of inhomogeneities, the SHG spectrum is that of a sinc function (if the phasematching bandwidth is smaller than the seed bandwidth), or that of a gaussian function (if the pump bandwidth is smaller than the phasematching bandwidth). Intuitively, a sinc spectrum means that the waveguide temporal response to the interaction is that of a rectangular step function, which is the case if the waveguide has no inhomogeneity in the second order coefficient along the propagation direction. An example of three SHG spectrums are shown in Fig.(7.10). These spectral forms were nevertheless repeatedly obtained along the whole chip. We see that all the curves are rather gaussian or similar, which indicates good homogeneities along the propagation direction. However, while both the 3x3 and 3x4 μm waveguides are well centered at 780 nm, the 3x2 μm waveguides were systematically centered around 767 nm. This fact indicates that the single fundamental spatial mode allowed by the 3x2 waveg-

uides is indeed centered at 767 nm, and no spatial modes can be guided at 780 nm. This reasoning would also explain why the non-linearity of those waveguides were smaller, since the seed field is not centered at $767 \cdot 2 = 1534$ nm (but it does have a sufficiently broad bandwidth to cover those wavelengths), the power associated with the contributing wavelengths to the SHG is smaller, and hence the non-linearity as well. Seen from another way, if a sufficiently narrow bandpass spectral filter at 1560 nm would be set to the seed beam before the waveguide, no second harmonic would be seen at all, and probably very small coupling efficiency would also be measured for the seed field. This would not be the case for the 3x3 and 3x4 μm waveguides. In the actual experiment, thus, the 3x2 waveguides were not considered.

○ Finally, the second harmonic light will serve us helpful for pulse synchronization, by finding its interference with the pump field, as we will show in the final results section of this Chapter.

We therefore conclude the waveguide characterization with the measurement of the coupling efficiency, the spatial modes, the SHG spectra and the non-linearity coefficients.

7.4 Mode Selective Homodyne detection: device characterization

The quadrature measurement of the output multimode state is performed via homodyne detection. Fig.(7.13) shows the actual optical circuit for homodyne in the laboratory.

The homodyne technique briefly described in Chapter 1, section 1.6.3, that was first introduced by Yuen and Chan, [164, 165] allows us to retrieve the quadrature value of a single-mode optical signal by mixing the quantum signal and a strong and classical Local Oscillator in a balanced Beamsplitter, and then subtracting the photodiode electric signal from each output port of the beamsplitter. The specific quadrature that is measured depends on the relative phase between the LO and the signal.

Here we want to see what happens if the quantum signal is multimode, as it is the case for our set of frequency supermodes. For that purpose we will first assume the LO to be a quantum signal as well. The quantum intensity operator can be written as [107]:

$$\hat{I}(\boldsymbol{r}, t) = 2\epsilon_0 c \hat{E}^-(\boldsymbol{r}, t)\hat{E}^+(\boldsymbol{r}, t) \tag{7.5}$$

and the photocurrent operator from the photodiode, that is measuring its eigenvalues, is therefore:

$$\hat{i}(t) = R \int_{S_{\text{det}}} \mathrm{d}^2\rho \int \mathrm{d}\tau r(\tau)\hat{I}(\boldsymbol{r}, t - \tau) \tag{7.6}$$

where R is the detector responsivity (0.84 A/W in our case), S_{det} is the detector area, and $r(\tau)$ is the detector temporal response, that is inversely proportional to the detector bandwidth, $\tau_{\text{BW}} = 1/\text{BW}$. Since the LO and signal fields are mixed in a balanced BS before

measuring each output port, we can obtain an expression of $\hat{i}(t)$ involving the LO operators $\hat{E}_{\text{LO}}(t)$ and the signal operator $\hat{E}_s(t)$. The homodyne photocurrent is obtained after the two photocurrents from the photodiodes is subtracted. It can be written as:

$$\hat{i}_{\text{hom}}(t) = \hat{i}_1(t) - \hat{i}_2(t) \tag{7.7}$$

$$\hat{i}_1(t) \propto \int \mathrm{d}\tau r(\tau) \left(\hat{E}_{\text{LO}}^-(t-\tau) + \hat{E}_s^-(t-\tau) \right) \left(\hat{E}_{\text{LO}}^+(t-\tau) + \hat{E}_s^+(t-\tau) \right) \tag{7.8}$$

$$\hat{i}_2(t) \propto \int \mathrm{d}\tau r(\tau) \left(\hat{E}_{\text{LO}}^-(t-\tau) - \hat{E}_s^-(t-\tau) \right) \left(\hat{E}_{\text{LO}}^+(t-\tau) - \hat{E}_s^+(t-\tau) \right) \tag{7.9}$$

By direct substitution of the photocurrent operators, the homodyne photocurrent is:

$$\hat{i}_{\text{hom}}(t) \propto \int \mathrm{d}\tau r(\tau) E_s^-(t-\tau) E_{\text{LO}}^+(t-\tau) + \text{h.c.}$$
$$\propto \int \mathrm{d}\tau r(\tau) \hat{a}_s(t-\tau) \hat{a}_{\text{LO}}^\dagger(t-\tau) + \text{h.c.} \tag{7.10}$$

It can be shown that in the Fourier frequency domain, the homodyne signal can be written as [166]:

$$\hat{i}_{\text{hom}} \propto \int \mathrm{d}\omega \hat{a}_s(\omega) \hat{a}_{\text{LO}}^\dagger(\omega) + \text{h.c.} \tag{7.11}$$

For the quantum signal, the bosonic operator $\hat{a}_s(\omega)$ can be written as a sum of bosonic operators $\{\hat{a}_s\}$ associated with the supermodes described by the functions $\{h(\omega)\}$:

$$\hat{a}_s(\omega) = \sum_j \hat{a}_{s,j} h_j(\omega) \tag{7.12}$$

In fact, this decomposition can always be written as long as the frequency modes form a well-defined mode basis.

We will furthermore consider the LO to be much more intense than the quantum signal and we will neglect the LO quantum fluctuations with respect to its mean field. That is to say, the LO is a classical field in a certain frequency mode $g_{\text{LO}}(\omega)$:

$$a_{\text{LO}}(\omega) = \alpha_{\text{LO}} g_{\text{LO}}(\omega) \tag{7.13}$$

where $\alpha_{\text{LO}} = \sqrt{N_{\text{LO}}} e^{i\theta_{\text{LO}}}$ is the LO mean field value, with N_{LO} the number of LO photons and θ_{LO} the relative phase between the LO and the quantum signal.

Substituing Eq.(7.12) and Eq.(7.13) into Eq.(7.11) we obtain:

$$\hat{i}_{\text{hom}} \propto \sum_j \hat{a}_{s,j} \alpha_{\text{LO}}^* \int \mathrm{d}\omega h_j(\omega) g_{\text{LO}}^*(\omega) + \text{h.c.} \tag{7.14}$$

and so the homodyne signal is proportional to the overlap integral between the signal and the LO modes. If we choose the LO mode to coincide with one of the signal supermodes,

$g_{\text{LO}}(\omega) = h_k(\omega)$ for some k; then, by orthogonality, the integral reduces to the Kronecker delta, δ_{jk} and therefore:

$$\hat{i}_{\text{hom}} \propto \alpha^*_{\text{LO}} \hat{a}_{s,j} + \alpha_{\text{LO}} \hat{a}^\dagger_{s,j} \tag{7.15}$$

in terms of the jth mode quadratures:

$$\hat{i}_{\text{hom}} \propto \sqrt{N_{\text{LO}}} \left(\hat{q}_{s,j} \cos\left(\theta_{\text{LO}}\right) + \hat{p}_{s,j} \sin\left(\theta_{\text{LO}}\right) \right) \equiv \sqrt{N_{\text{LO}}} \hat{q}^{\theta_{\text{LO}}}_{s,j} \tag{7.16}$$

where $\hat{q}^{\theta_{\text{LO}}}_{s,j}$ is the generalized quadrature from the frequency mode selected by the relative phase between the LO and the signal.

Eq.(7.16) shows that in a multimode configuration, the homodyne detection filters the quadrature of the mode to be measured according to the overlap with the signal frequency modes. Hence, homodyne measurements are mode selective, and each of the supermodes in the multimode quantum state can be addressed independently by appropiately shaping the LO spectrum. The quality of the homodyne signal depends on the polarization, spatial and frequency matching between the LO and the signal. Since the frequency matching can be manipulated with the pulse shaper, special attention should be put in the spatial and polarization matching in the experiment.

As a consequence of Eq.(7.16), the noise in the homodyne signal is directly related to the quadrature variance, $\Delta \hat{i}_{\text{hom}} \propto N_{\text{LO}} \Delta \hat{q}^{\theta_{\text{LO}}}_{s,j}$. In practice, in order to extract useful information from the noise in the homodyne signal, we will demodulate it over a small frequency bandwidth. There are two main reasons for that. First, the trans-impedance circuit in our homodyne detector has a pass bandwidth around 10 MHz. This means that after that frequency it will be harder to obtain a good signal to noise ratio. The second reason is that classical noise sources dominate the signal at low frequencies. To get the best ratio of quantum signal over classical noise we will therefore restrict our measurement to a band of a hundreds of kHz centered at a frequency compatible with the detector's bandwidth. Specifically, we chose to measure at 2 MHz, in our case, since it is the spot with more clearance, to be defined in the following. See [167] for more details about the spectral analysis of homodyne measurements.

The characterization of our homodyne detector is done without the presence of the quantum signal. We measure first the output homodyne signal without the LO and decompose its frequency components with a spectrum analyzer. The result is the black curve of Fig.(7.11) a), which is the *electronic noise* of the detectors, since there is no light involved. We then input the LO signal and balance the photodiodes. For the balancing, we first make sure that the optical powers in both BS output arms are the closest possible by changing slightly the angle of the 50/50 BS. In our case we had a ratio between the two outputs that is around 1.03 in the best configuration. Once this is done, we measure individually each photodiode response with an oscilloscope and check that the voltage output is the closest as well, tuning the photodiodes alignment with the mirrors at the BS output arms. We again measure the frequency components of the homodyne signal, and repeat the process for dif-
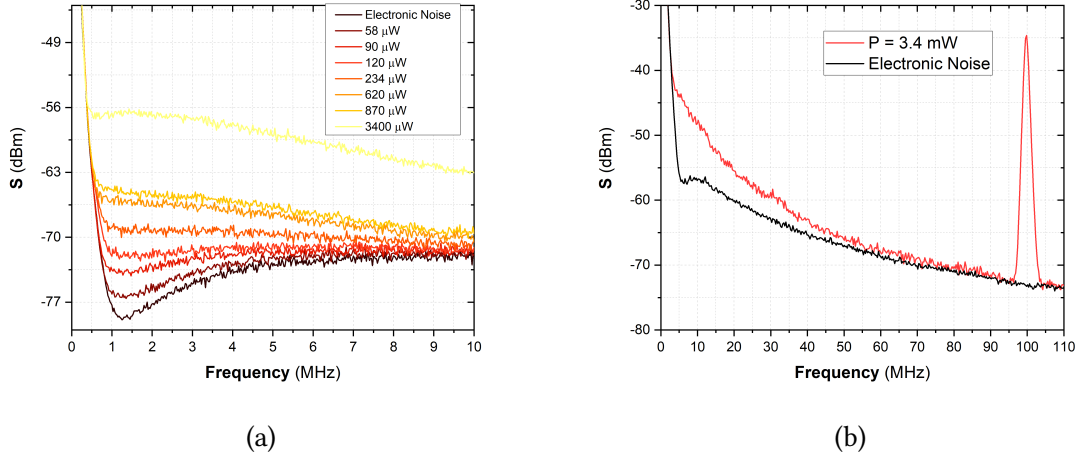
Figure 7.11: Homodyne spectral signal. a) Electronic noise and LO shot noise curves with different optical powers. b) Electronic noise and LO shot noise spanning 110 MHz, showing the peak at the laser repetition rate.

ferent LO powers. These characterization corresponds to the rest of the curves in Fig.(7.11) a).

Due to the LO intrinsic *shot noise*, the noise at a given optical power and frequency should be higher than the electronic noise, and it should grow linearly with the input power. We will notice squeezing as oscillations in the shot noise levels as we change the relative phase ϕ_{LO}. The ratio between the shot-noise, σ^2_{SN}, and the electronic noise σ^2_{el}, at a specific frequency is the Signal-to-Noise ratio (at that frequency). Its value in dB is known as the *clearance*, C:

$$\mathrm{SNR} = \frac{\sigma^2_{\mathrm{SN}}}{\sigma^2_{\mathrm{el}}} \qquad C = 10 \log_{10}(\mathrm{SNR}) \tag{7.17}$$

The electronic noise can be modelled as an additional loss channel [168], with efficiency η_{el}, where:

$$\eta_{\mathrm{el}} = 1 - \frac{1}{\mathrm{SNR}} \tag{7.18}$$

and the total homodyne efficiency, η_{hom} can be written as:

$$\eta_{\mathrm{hom}} = \eta_{\mathrm{PD}} \cdot \eta_{\mathrm{el}} \cdot \eta_{\mathrm{opt}} \cdot \eta_{\mathrm{mod}} \tag{7.19}$$

where η_{PD} is the photodetector efficiencies (conversion photon-to-electron), η_{opt} is related to the total optical losses in the homodyne circuit, and η_{mod} is the mode-matching efficiency, that measures the polarization, spatial and frequency overlap between signal and LO. See [169] for more details about the derivation of these efficiencies.

155

The homodyne measurement could hence be limited by any of these equivalent losses channel. For the electronic noise, we are not limited if the clearance is higher than the amplitude of the oscillations due to squeezing. Fig.(7.12) shows the measured clearance as a function of LO optical power. The photodetector and optical efficiencies η_{PD} and η_{opt} are fixed for us, and depend respectively on the photodiode's responsivity and the optical components characteristics. Finally, η_{mod} will be maximized in the experiment by spatial and temporal mode matching with the seed field after the waveguides. This efficiency can be measured via the square of the *visibility*, a quantity that will be defined in section 7.5.2.

In Fig.(7.11) b) we observe a high peak at 100 MHz, which coincides with the repetition rate of our laser. This peak is precisely due to the fact that the pulses traveling in the two arms after the BS are not synchronized, giving periodic peaks in the temporal homodyne signal, and hence a peak at this frequency component. In case of pulse synchronization, the peaks amplitude is therefore reduced[2]. The level of reduction is known as the *Common Mode Rejection Ratio* (CMRR), which is important is one wants to measure the squeezing *pulse by pulse* [169]. In our specific experiment, our detectors do not have clearance at this frequency. We are interested in measuring at 2 MHz, because of the bandwidth nature of our detectors, that gives the best clearance at this frequency, and so we restrict ourselves to check that the presence of the peak at 100 MHz do not saturate the electronic amplifiers in the homodyne circuit. However, we have developed homemade homodyne circuits, that will be tested in the near-term, able to cover the full bandwidth of the signal, hence opening the possibility of measuring squeezing pulse by pulse (when we measure the frequency component of the noise at the repetition rate).
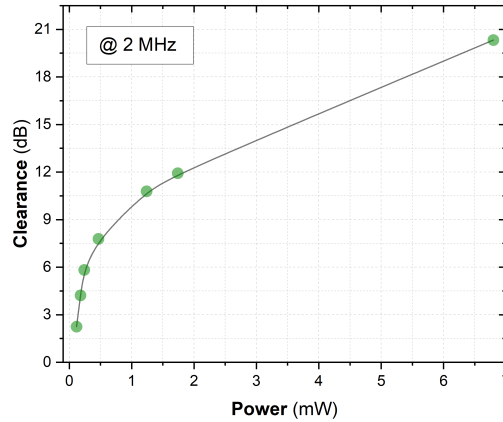

Figure 7.12: Clearance as a function of input power to the photodiodes at a frequency of 2 MHz.

---

[2]The peak is complicated to be completely eliminated even if the synchronization is perfect, since it also depends on the similarity of the two photodiode's response at that frequency.
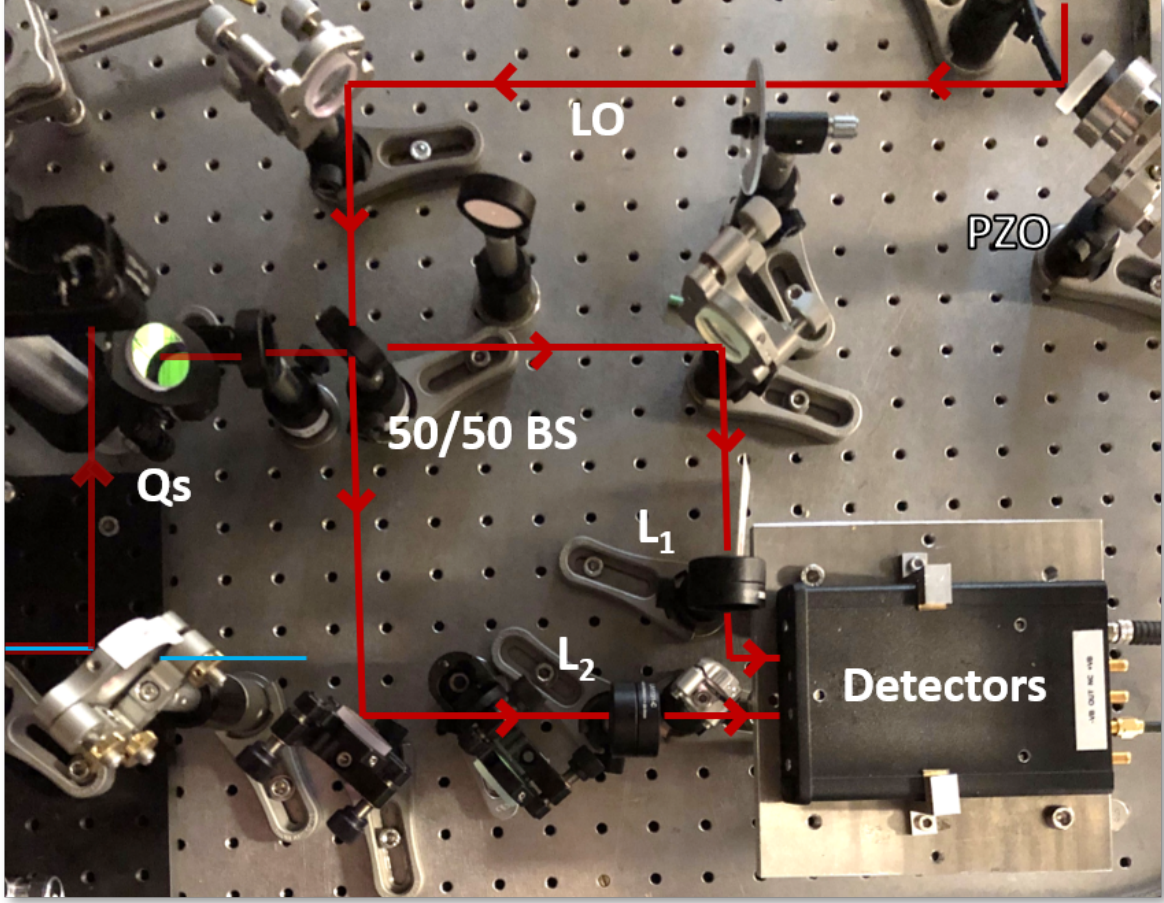
Figure 7.13: Photo of the homodyne detection setup in the experimental laboratory. Qs: Quantum signal, LO: Local Oscillator, L$_{1/2}$: Lenses for the photodiodes, PZO: piezoelectric. The detectors are homemade detectors borrowed from the C2N laboratory at the Université de Paris-Saclay.

7.5 Experimental Results on Multimode Squeezing

We ended up the description of the blocks defined in Fig.(7.1) composing the whole experiment for the demonstration of the quantum source. This final section is dedicated to detail the final results for the multimode squeezing, revealing the implementation of the multimode squeezed vacuum state in the frequency domain.

We performed first an experiment of Phase Sensitive Amplification with the seed field, and finally we implemented the homodyne detection setup for the multimode squeezing measurement that characterizes the multimode quantum state.

7.5.1 Phase Sensitive Amplification

Phase sensitive amplification is a parametric amplification process, that can also be seen as a DFG process, where the signal and idler fields are degenerate, i.e. indistinguishable. In type II, parametric amplification occurs but it is not phase sensitive. The devices that exploit this effect are known as Optical Parametric Amplifiers (OPAs), that open the door to noiseless-amplification [170], that in turn finds applications in fiber communication [171], or quantum-enhanced imaging and spectroscopy [172, 173, 174]. A schematic of phase sensitive amplification is depicted in Fig.(7.14).
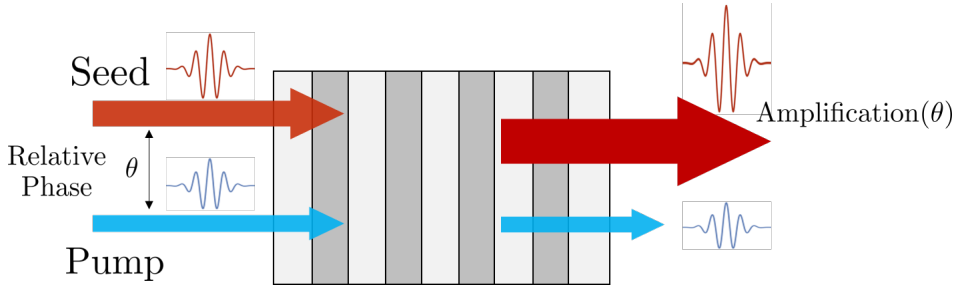

Figure 7.14: Phase Sensitive Amplification scheme. A seed and pump fields are input into the periodically poled waveguide. The seed field is amplified (or deamplified) depending on the relative phase between these two fields.

The PSA experiment allows us to show the existence of parametric gain, precondition of squeezing generation in the waveguide, even though the levels of multimode squeezing cannot be measured in this way. Only an order of magnitude of the total expected squeezing can be inferred from this data, but this will serve us useful for the final homodyne detection.

For the PSA experiment to succeed, we must match the seed beam and the pump in polarization, and spatially and temporally into the waveguide. The spatial matching is naturally achieved thanks to the discretization of the spatial modes in the waveguide, since the same spatial modes for seed and pump are allowed to be guided in the structure at 1560 nm. The polarization matching is trivially obtained using half-waveplates that fix the seed and pump to be vertically polarized.

We are left with the temporal matching, that is, to get pulse synchronization when arriving to the waveguide facet. For this, we built an optical path for the seed that has approximately the same length as for the pump and we measure the pulses with a fast photodiode just before the waveguides. The fast photodiode is not fast enough to "see" the pulses waveform, but it is sufficiently fast to resolve a signal from the individual pulses, since it can measure faster than the laser's repetition rate (100 MHz). We triggered the oscilloscope with the RF signal from the laser, that is synchronized with the pulse generation, and measure, individually, the seed and the pump pulses at the same position. We take the difference in the maximum of the measured photodiode responses as the arrival time difference be-

tween pump and seed pulses. Assuming the pulses travel at the speed of light, we have a rough measurement of the optical path difference that should be corrected in one of the optical paths for synchronizing them. We add a micrometer delay line that allows to tune the seed optical path in a total of 5.0 cm, and therefore match the temporal seed and pump peaks in the fast photodiode.
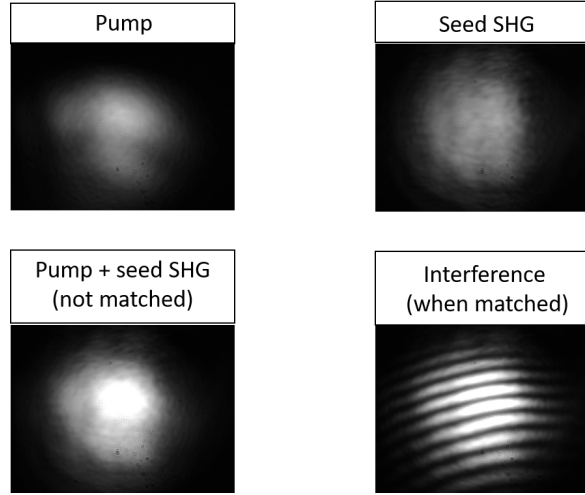

Figure 7.15: Example of the pulse synchornization trick by measuring the interference between the second harmonic from the seed and the pump. For more information see text.

For fine adjustment of the temporal matching, we take advantage of the SHG generated in the waveguide by the seed field. Since the associated SHG process is type 0, the polarization of all fields are also vertically polarized after the waveguide. Therefore the seed's second harmonic and the pump would interfere if they are perfectly temporally matched. We therefore measured the second harmonic and the pump with the 800 nm CCD camera and adjust their power to approximately be equally bright in the camera. Then, we tune the delay line until finding the interference fringes. An example of the result is shown in Fig.(7.15).

As a note, we should inject both the seed and the pump in the same waveguide, which is possible by injecting the pump into the desired waveguide, monitor the output in the CCD camera, and then exclusively tune the alignment of the seed path until we see its second harmonic juxtapose with the pump in the camera, indicating they are traveling through the same guide. Once this is done, we can also move the entire chip with the 6-axis mount so that we can inject both fields into different waveguides. In our case, we used the waveguide labelled as 3.5 (Group 3, waveguide number 5), which has dimensions of 3x3 μm. After seed and pump matching in the waveguide, we filtered the pump from the seed SHG with an output dichroic mirror and measured the optical power at telecom wavelengths using a slow photodiode. We mounted a piezoelectric mirror in the seed path powered with a ramp
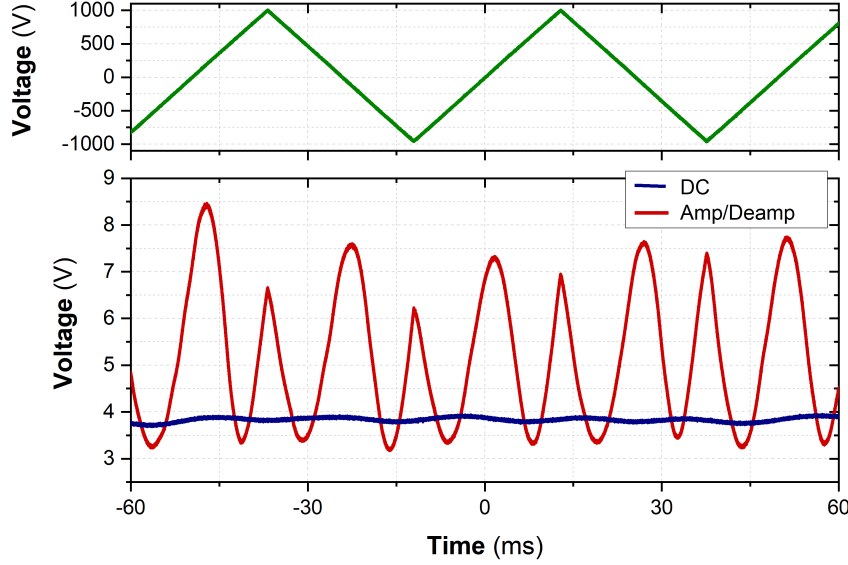
Figure 7.16: Phase Sensitive Amplification. The saw-tooth waveform provides ramps applied to the piezoelectric to linearly change the relative phase between seed and pump. The dark blue line corresponds at injecting only the seed, and the red is when we add the pump field. The amplification and deamplification effect with the phase shows the presence of squeezing in the waveguide.

voltage, shown in Fig.(7.16), so that the relative phase between seed and pump changes linearly. The ramp frequency was around 30 Hz, which is bigger than the natural phase fluctuations in the experiment, that are around 2 Hz, so that the phase can be considered to be only changed by the piezoelectric in a ramp period time.

When we block the pump, we obtain an approximately constant output power, the dark blue line in Fig.(7.16). The small amplitude fluctuations that can be seen in this curve are due to the fact that the piezoelectric is slightly changing the seed alignment, in the range of some μm [3]. The small periodic misalignment modulates the coupling efficiency and hence the output power present those small fluctuations, that are in any case small, with a maximum amplitude of 2% from the mean signal.

When we add the pump field, we observe the phase sensitive amplification in the signal, whose signature are the oscillations at the piezoelectric frequency seen in the slow photodiode, the red curve in Fig.(7.16). We maximized the parametric amplification in the experiment with the waveguide alignment, the temperature and the polarization control.

From the theory on DFG [107, 175], the maximum and minimum gain, $G_{\pm}$ in the single-

---

[3]The piezoelectric range produces translation of the mirror that goes from 0 to 5 μm.
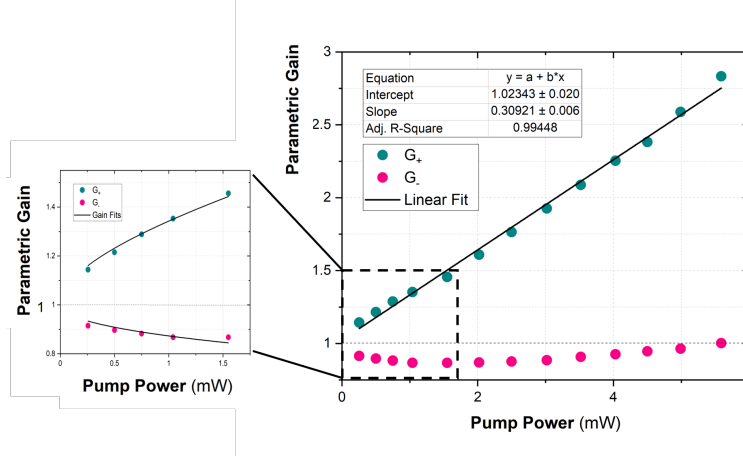
Figure 7.17: Maximum and minimum parametric gain as a function of pump power. At high powers, we report a deviation from the theoretical saturation behavior by a linear growth indicating the presence of another non-linear effect in the waveguide.

mode CW case, are:

$$G_\pm = \exp(\pm 2\sqrt{\eta_{\mathrm{DFG}} P_{\mathrm{pump}}}) \tag{7.20}$$

where η_{DFG} is the waveguide's *non-linear efficiency*, that in theory should be close to the η_{SHG} defined in the waveguide characterization. We measured the maximum and minimum parametric gain as a function of the pump power. The result is given in Fig.(7.17). Losses can also be introduced in the model [176, 177], although we did not include them in these calculations, since we were only interested in the rough behavior (we are not in a single-mode, CW configuration anyway).

We find that, at low pump powers, the gains fit well Eq.(7.20), with a non-linear coefficient from the fit of $\eta = 0.20 \pm 0.01$ mW^{-1}, which is coherent with the value obtained in the waveguide characterization. This linear coefficient gives an estimation of the squeezing parameter of $\sqrt{\eta \cdot P_{\mathrm{pump}}} \simeq 0.44$ at $P_{\mathrm{pump}} = 1$ mW, which would correspond to a squeezing level of 3.5 dB at this power. We note that the parametric gain occurs only within the frequency matching between the seed and the supermodes generated in the waveguide, some frequencies could have not contributed to the process, and hence we expect the value from the PSA experiment to be an underestimation of the actual total parametric gain in the waveguide.

However, at higher powers, we reported that the maximum gain deviates from the fit curve and grows linearly with the pump power. At the same time, the deamplification tends to grow to 1, and even higher values are obtained as we increase further the pump power. We expected the possibility of having other non-linear effects in our waveguides, due to the strong light confinement, that could perturb the gain curve from some input power value. Examples of non-linear effects in the waveguide at high enough powers are two-

photon absorption, second harmonic of the pump field (hence at wavelengths around 390 nm, that corresponds to blue light that we can see at naked eye in the experiment) and GRIIRA effects from green light generated by the seed field. These effects could act as a power-dependent source of losses at telecom and would limit the useful pump power for PDC. However, the addition of losses would reduce the parametric gain, and we actually observe an amplification of the signal above the theoretical curve for the parametric gain. We think that this behavior could be due to the generation of telecom light from a non-linear source in the waveguide, that is not identified for the moment. This amplification will also be important for the multimode squeezing measurements. In any case, a linear fit to the maximum gain curve gives a function of the type $G_+ = 1 + 2\eta' P_{\text{pump}}$ in which we could define a new empirical non-linear coefficient η', that happens to be $\eta' = 0.30 \pm 0.02\text{mW}^{-1}$, higher than the non-linear coefficient at low powers. Further investigations about the behavior of the non-linear effects in the waveguide and the gain curves will be tested in the near-term future to figure out the origin of the extra amplification at higher powers.

In any case, the implemented theoretical gain curves assume a single frequency mode state, which is obviously not the case in our experiment, so the gain fits should be taken with a grain of salt. We nevertheless show the presence of squeezing at telecom wavelengths in the non-linear waveguide, and obtain an estimation of the parametric gain of few dB, which are the main results we desired for the PSA experiment.

7.5.2   Multimode Squeezing

Finally, we performed homodyne detection with the temporally shaped LO for the demonstration of the experimental multimode squeezed state. As explained in the homodyne detection section in this Chapter, we should mix the quantum signal with the LO in a balanced beamsplitter. This interference should have enough visibility for measuring squeezing. The visibility is measured in the lab by an interference measurement with the seed field. We mix the seed and the LO after the beamsplitter, synchronize the pulses with the use of fast photodiodes and a delay line in the LO path, and align the LO field until the interference seen in a CCD camera does not present fringes, but the signal blinks randomly instead. The blinking indicates that the spatial alignment is appropriate, and the random fluctuations are due to the random phase fluctuations in the lab. We add a piezoelectric to the LO path that linearly changes the relative phase of seed and LO faster than the random phase fluctuations and substitute the camera by a slow photodiode. In this way, the interference is seen as sinusoidal oscillations in the oscilloscope. The visibility, V, is then defined as:

$$V = \frac{V_{\text{max}} - V_{\text{min}}}{V_{\text{max}} + V_{\text{min}}} \tag{7.21}$$

where $V_{\text{max/min}}$ are the maximum and minimum values of the voltage obtained from the oscillations in the photodiode. We then maximize V with the alignment, the LO delay line,

optical powers and polarizations. We also add a spectral filter of 12 nm to the seed before the BS, together with a 12 nm gaussian mask to the LO, so that we approximately match spectrally seed and LO. This spectral filter is removed for the squeezing measurements since in that case we spectrally match the LO and quantum signal by changing the pulse shaper mask.

Once a satisfactory visibility is obtained, we block the seed and balanced the homodyne photodiodes. Finally we measure the LO shot noise in the spectrum analyzer while blocking the quantum signal. This measurement is performed at the frequency component of 2 MHz, with a 100 kHz window. Each measurement is done for 1 second and the piezoelectric frequency was set to around 300 mHz. We unblock the quantum signal and observe the noise oscillations around the shot noise due to the presence of squeezing. This value of squeezing is associated to the temporal mode given by the LO mask.

An important remark is that even if the oscillations in the quadrature noise measurements indicates the presence of squeezing, the minimum noise that is measured is at the level of the shot noise itself. This means that we have not measure noise reduction below the shot noise limit, limiting the application of these states in quantum communication and computation protocols. The states that we have measured are known as *Squeezed Thermal* states. The reason for the thermal character of our squeezing measurements is still not clear, but it should be related with the deviation from the PSA curve seen in the section before. An additional non-linear effect is taking place in the waveguides at a certain power that results in generation of telecom light. This extra process is incoherent with the spontaneous parametric down conversion and hence is noisy to the process. The resulting thermal state is squeezed and hence we measure the oscillations above the shot noise characteristic of squeezed thermal states. More tests should be performed to clarify this hypothesis. Understanding the thermal source is a crucial near-term research goal in our experiment.

Fig.(7.18) show the (thermal) squeezing curves of up to 11 temporal modes. Each curve is obtained by changing the pulse shaper mask to successive Hermite-gauss modes and optimize the squeezing amplitude with the spectral width of the specific mask. This is the first time, to the best of our knowledge, that multimode squeezing from a non-linear waveguide at telecom wavelengths is directly measured.

The distribution of squeezing amplitudes from the different modes is shown in Fig.(7.19), which is in agreement with the distribution predicted from the simulations in Chapter 6, section 6.3.1. The total amount of squeezing oscillations is 5.12 dB, which is somewhat in agreement with the PSA experiment results. We stopped measuring at mode number 11 because the variances of the noise starts to be comparable with the spectrum analyzer resolution given the signal fluctuations, but the measurement indicates that there are probably even more frequency squeezed modes in our beam.

On top of that, we also should take into account the optical losses. Optical losses also make the oscillations around the shot noise to diminish. The main source of losses in our case was the imperfect visibility in the homodyne detection, due to the different spatial
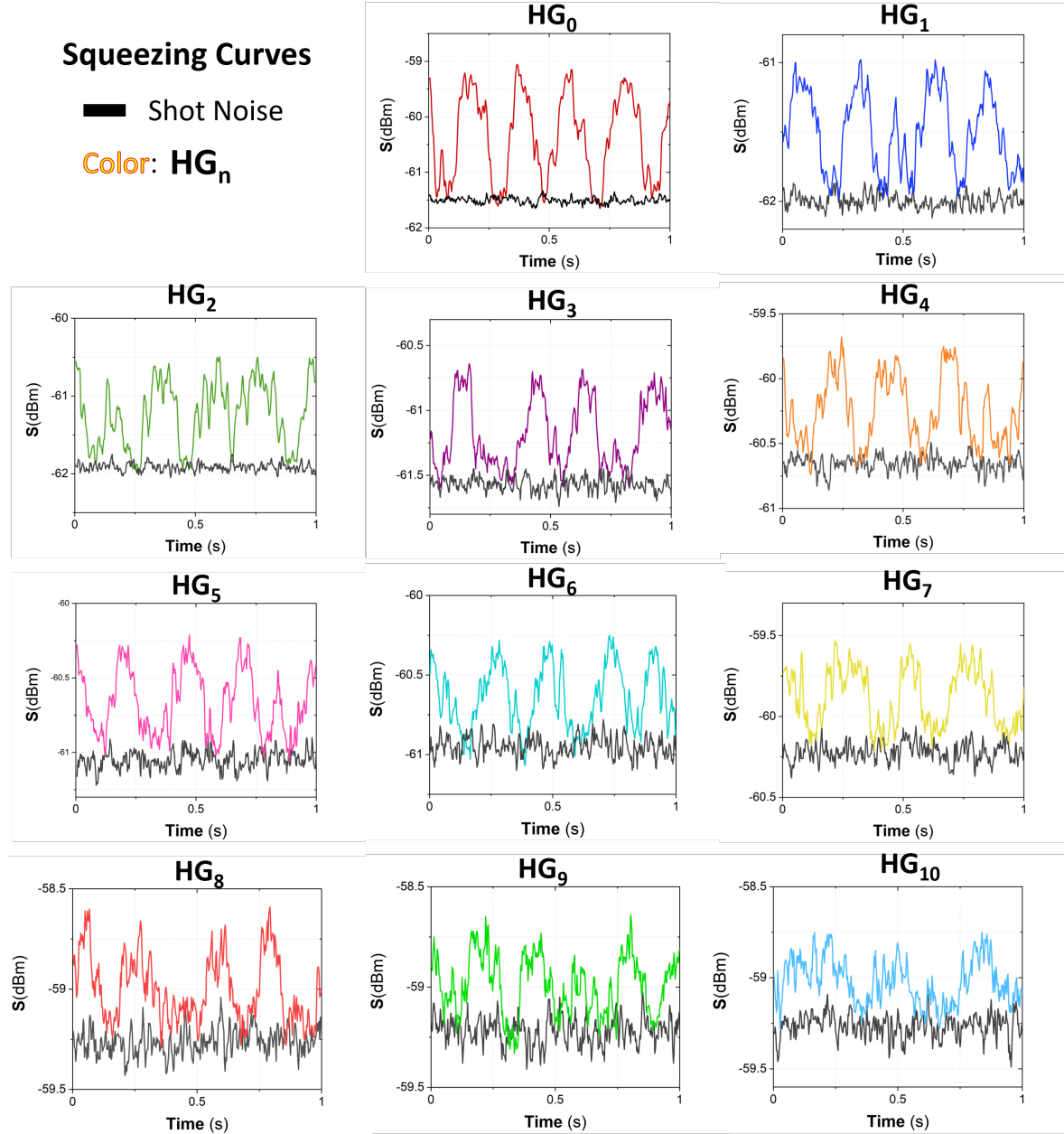
Figure 7.18: Squeezing curves. Multimode oscillations in the quadrature noise is measured in up to 11 Hermite-Gauss modes. These curves correspond to squeezed thermal states, since the oscillations are just above the shot noise level.
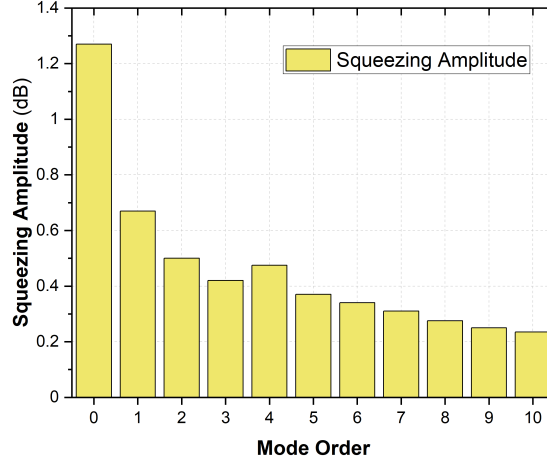
Figure 7.19: Distribution of measured squeezing amplitudes.

mode-matching between the signal and the LO. The efficiency due to the visibility, that we denoted η_{mod} in section 7.4, grows with the square of the visibility [178]. In our case, our visibility was around $V \simeq 50$ %, which is in general a low value compared with typical homodyne measurements.

As mentioned above, the reason for the low visibility in our case must be the low spatial-mode matching between the LO and the quantum signal, since the temporal, spectral, power and polarization matching is well measured and controlled in the experiment. For the spatial matching, however, low control is possible given our current setup, since the only spatial mode-matching in the LO is done using thin lenses, and hence the LO beam keeps gaussian all along, we just change the width of this gaussian to optimize the matching with the quantum signal. However, we have seen that the spatial mode of the quantum signal are not gaussian, but given by functions similar to those of Fig.(4.8). This results in the total 50 % of visibility that we measured in our experiment and that limits the squeezing levels.

A way of solving this issue would be to modify the pulse shaper mask in order to obtain spatial modes specifically similar to those of the waveguide. However, this is a very unpractical solution, because the exact form of the spatial modes are dependent on alignment and other experimental variables, and changes from guide to guide. Furthermore, the behavior of the lenses in the LO path could be in principle different if the spatial beam differs too much from a gaussian form. A more elegant and simple solution is to make the LO pass through a waveguide of the same characteristics as that used for the pump field, so that the waveguide naturally selects the spatial mode and changes spatially the LO accordingly, increasing significantly the visibility in the homodyne interference. This is a prospect for the future in our experiment, that we did not have time to accomplish during the time of
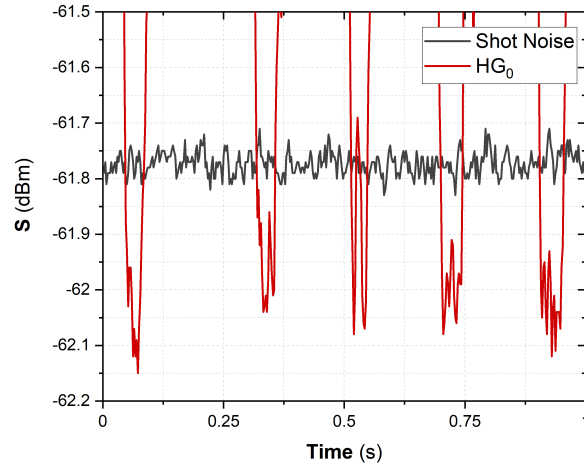
Figure 7.20: Squeezing below the shot noise limit obtained after improvement of the LO-seed visibility.

this thesis, since the experience was moved to another experimental laboratory shortly after finding the results reported here.

In order to show the noise reduction under the shot noise limit, we managed to increase the visibility by just a 6% working on mode-matching using lenses along the LO path. With a visibility of around 56%, we observed reduction of the noise under the shot noise limit for the first few modes. Hence, this is the first time, to the best of our knowledge, that noise reduction below the shot noise limit is directly measured in multimode telecom light coming from non-linear waveguides. In Fig.(7.20) we show the noise reduction, with a mean amplitude of around 0.31 dB for the first Hermite-gauss frequency mode.

This proves our point on the problem in the spatial mode efficiency. We therefore expect to improve the noise reduction amplitude below the shot noise limit with the square the visibility measured between LO and signal.

We therefore conclude this Chapter by showing the measurement of up to 11 squeezed thermal states with different levels of squeezing amplitudes, and showing the noise reduction under the shot noise limit when the visibility was improved. A thermal source from unclear origins is also observed and new tests will be performed to understand its physical origin. Additionally, optimization work in the near future, mainly with the visibility, would unveil larger multimode squeezing below the shot noise at telecom wavelengths.

Conclusion & Outlooks

This thesis was divided into two projects, that were reflected in this manuscript as the two parts that compose the document. Both projects are framed in the field of Quantum Information with Continuous Variables.

In the first project, we studied a particular quantum cryptographic protocol, the prepare and measure CVQKD with coherent states, for its possible actual implementation with satellites. We studied the atmospheric characteristics that are relevant to the transmission of quantum information from a satellite to a ground-station, and the consequences of those physical features to the security proof of the quantum protocol.

We introduced the atmospheric channel from a characteristic rate of change of the transmissivity, which makes the channel to be called a fading channel with a certain probability distribution. From this abstraction, we derived the conditions in which this fading channel is secure against collective attacks in the asymptotic limit, concluding that the protocol is still secure if the equation for the key rate is modified, including a new excess noise term that depends on the probability distribution of the transmissivity, called PDTE.

We therefore studied the behavior of the PDTE on the different time-dependent noise figures that affect the transmisivity of the channel. The most prominent variables for the quantum channel happened to be the divergence angle, that essentially depends on the satellite-ground station distance and emitter telescope's aperture, the pointing error from the satellite, and the atmospheric turbulence. Under good or moderate atmospheric conditions, we concluded that the main source of time-dependent noise comes from the pointing error, given state-of-the-art technologies. With this, we computed the PDTE taking into account an entire circular satellite orbit characterized by its altitude.

With this convoluted PDTE, and adding the noise sources that are accounted in usual CVQKD studies, namely detector efficiency, electronic noise or reconciliation efficiency, we derived the key rate that would be obtained in a real scenario given state-of-the-art instruments, proving the possibility of having non-zero key rates for LEO and MEO satellites if the total excess noise is not bigger than around 5%. We saw the dependencies of the key rate in different mentioned parameters, the most important being, again, the excess noise. We also included the finite size effects that are not accounted in the asymptotic key rate formula, and propose a binning method for improving the key rate for LEO satellites, where the fading noise is most relevant. We concluded that CVQKD with satellites is actually a

feasible near-term option, specially for LEO satellites.

A logical continuation to this project is the actual implementation of a CVQKD experiment in the laboratory, adding an artificial fading channel in which the amplitude and phase of the coherent states are modulated before arriving to Bob. The parameters of the modulation would simulate the actual atmospheric channel. The recovery of the secret key in the experiment and the comparison with our study would prove even more the feasibility of the quantum protocol. This experimental implementation is being currently performed in our laboratories at Sorbonne Université, in Paris, France. If the results end up being positive, one could think in actually performing the protocol with actual satellites in the not so long term.

The second project of this thesis was the design and implementation, starting from scratch, of a quantum source of CV graph states at telecom wavelengths in the laboratory, that would allow to implement quantum protocols in the CV framework. Examples of such protocols are secret sharing, QKD, measurement-based quantum computation, and quantum simulation, among others.

We showed how the graph states can be obtained from a multimode squeezed vacuum state, and outlined the experimental configurability of the potentially generated graphs. The experiment was therefore based on creating the source of the multimode quantum states in a single pass SPDC experiment through a non-linear waveguide.

We first performed a quantum optics theoretical study in which we derive the influence of the controllable degrees of freedom in the experiment on the multimode state, in particular on the number and form of the squeezed supermodes. This study allowed us to design the experiment and choose the particular non-linear waveguide, that happened to be a 15 mm long PPKTP waveguide with transverse dimensions compatible with single(spatial)-mode propagation.

We constructed the multimode quantum source by designing an experiment based on blocks with different functionalities. We tested and characterized experimentally each of the blocks, including a femtosecond laser centered at 1560 nm, pulse compressors, a pulse shaper for the LO, a PPLN SHG crystal for generating the pump to the waveguides, homodyne detection for the multimode squeezing measurement, and the mentioned non-linear PPKTP waveguides. The different frequency modes can be addressed independently by shaping appropiately the homodyne LO with the pulse shaper.

We performed a Phase Sensitive Amplification experiment that showed parametric gain, a precondition for squeezing. We report a deviation from the theoretical curve where the parametric gain grows linearly instead of saturating at sufficiently high powers, indicating the presence of some other non-linear process generating telecom light. We directly measured multimode squeezing in up to 11 expected frequency supermodes and found squeezing oscillations just above the shot-noise level, indicating the presence of multimode squeezed thermal states. The levels of squeezing are in accordance with the expected value from the PSA experiment. The origin of the thermal state is still not clear, and new tests should

be performed to clarify its physical origin. It should be related to the anomalous amplification seen in the PSA experiment by the unidentified extra non-linear process, giving a thermal character to our squeezed states. We also look forward to improving the optical losses, mainly in the mode-matching efficiency when interfering the LO with the quantum signal. Finally, we managed to improve the visibility by mode-matching and we were able to show some noise reduction below the shot noise limit, and hence real squeezing in a few modes. This was the first time, to the best of our knowledge, that multimode squeezing from non-linear waveguides at telecom wavelengths was directly measured.

The first prospect for this experiment is the source optimization, starting from the improvement of the mode-matching efficiency via the visibility, since it would allow us to considerably improve the squeezing amplitudes. The understanding of the thermal source in the near-term is also crucial for the purity of the squeezing levels. Once the squeezing levels will be optimized, the possible applications are certainly wide, as mentioned before. Quantum CV protocols requiring a small number of nodes are the first candidates to be implemented by our source. Another possibility is to prepare a copy of the multimode squeezed state with the use of an extra waveguide and make the two quantum states to interfere, like in [179], so that temporal correlations are added on top of the frequency ones, generating a large cluster. Finally, another more fundamental possibility for the future of the source is to add an extra step of photon subtraction or photon addition that makes the state to become non-gaussian (see for example [180]), in order to understand the properties of these more exotic states and find their potentialities when applied to the field of Quantum Information.

Appendices

Appendix A

Parameter analysis on Satellite CVQKD

In this Appendix we analyze the dependence of the secret key rate on several parameters of our CVQKD study, to obtain a better insight into which parameters affect the most the overall performance and to reinforce our conclusions from Chapter 2. For this multiparameter analysis, we consider the key rate in the asymptotic case for a fluctuating channel, given by Eq.(2.24).

The parameters will be changed one by one, keeping the others to their reference values, expressed in Table 2.1. The color code reflects the value of the fixed excess noise and is the same used in Chapter 2: red, blue, and green for ξ = 1, 3, 5% (in S.N.U.), respectively.
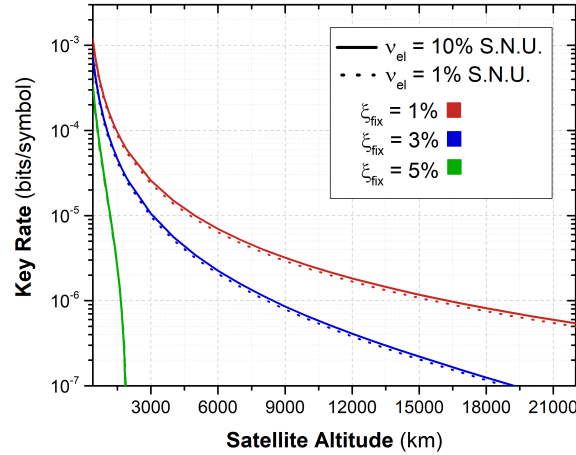

Figure A.1: Impact of the electronic noise on key rate. Comparison of secret key rate for two different electronic noise ν_{el} and three different excess noise values.

In Fig.(A.1), we vary the electronic noise of the detectors from 0.01 to 0.1 S.N.U. We notice that even with one order of magnitude increase in noise, the key rate is almost unaffected
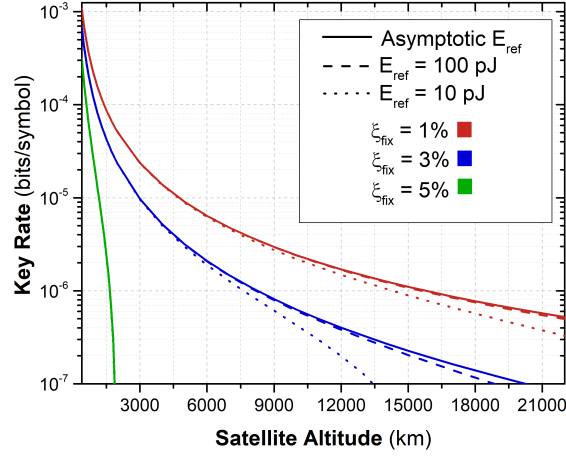
Figure A.2: Impact of the reference pulse energy on key rate. Comparison of secret key rate for different values of the reference symbol energy E_{ref}, for the three different excess noise values considered along Chapter 2 and this Appendix.

for all cases. This is mainly due to the fact that in this analysis we consider the so-called *trusted* or *calibrated* scenario, in which the electronic noise is known to Bob via a constant calibration and cannot be exploited by Eve.

The second parameter we want to consider is the energy of the reference symbols used for phase recovery in the classical pilot pulses. To illustrate the problem: considering a simple phase estimation scheme operating at 1 Gsymbol/s with alternating signal and reference symbols. The time between two such symbols, $\Delta t = 1$ ns, gives rise to a noise contribution $\xi_t = V_A \cdot 2\pi\Delta t\Delta f$, where $\Delta f \simeq 1/(\pi\tau_c) = 10$ kHz is the linewidth of the two lasers and τ_c their coherence time (assumed equal for Alice and Bob). On the other hand, the phase measurement is affected by shot noise, introducing a noise of $\xi_{sn} = V_A/(2\eta n_{\mathrm{ref}}$, where $n_{\mathrm{ref}} = E_{\mathrm{ref}}\tau/E_{\mathrm{photon}}$ is the total number of photons collected, E_{ref} is the energy of the reference symbols and E_{photon} is the photon energy. The effects for different reference symbol energies are shown in Fig.(A.2). Although the effect for LEO satellites is negligible for energies above 10 pJ, for higher orbits stronger values of the reference are required to avoid any detrimental effect owing to the phase alignment uncertainty, which might impose restrictions in the dynamic range of the modulators, as the optimal variance V_A decreases as attenuation increases.

We also consider the impact of the downlink beam pointing error and beam divergence, on the final key rate. This is depicted in Fig.(A.3) for different combinations of θ_p and θ_d. As expected, these parameters have a strong impact en the key, underlying the importance of a high-quality beam propagation for satellite CV-QKD.

Finally, we analyze the role of atmospheric visibility, adding values of 5 km and 2 km,
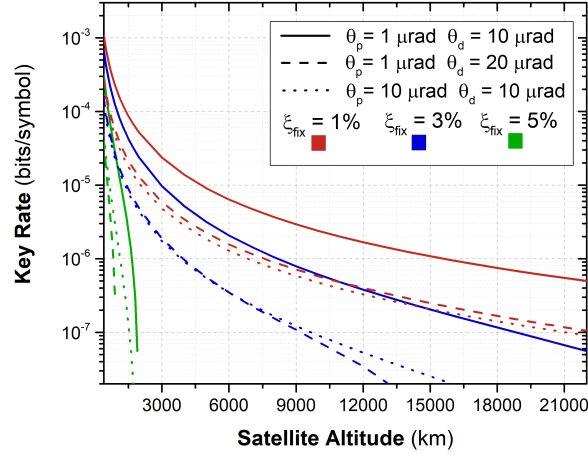
Figure A.3: Impact of the beam quality on key rate. Comparison of secret key rate for different values of pointing error, θ_p, and divergence angle, θ_d at the three excess noise values.
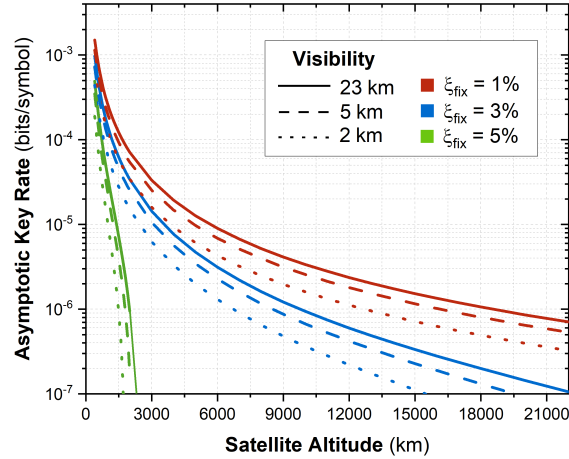

Figure A.4: Impact of the sky visibility on key rate. Comparison of secret key rate for different values of sky visibility at the three excess noise values.

corresponding to haze and mist conditions, respectively, to the 23 km value used in Chapter 2 . In these two cases the atmospheric transmission efficiency at zenith, τ_{zen}, is, respectively, 0.75 and 0.53. The results, reported in Fig.(A.4), show that the key rate is affected slightly by haze condition, but drops significantly for mist condition.

Appendix B

Kleinman Symmetry

In the frequency domain, the second order susceptibility relates all the possible pairs of cartesian components of the electric field, $E_j(\omega)$ and $E_k(\omega)$, to the orthogonal component of the polarization field, $P_i(\omega)$. Furthermore, in general, the associated susceptibility coefficients also depend on frequency, $\chi^{(2)}_{ijk} = \chi^{(2)}_{ijk}(\omega)$. Considering that we have a three-wave mixing process, there will be three frequencies involved in the process, ω_n, ω_m and $\omega_3 = \omega_n + \omega_m$. Explicitly, the relation between the polarization and electric field components is:

$$P_i(\omega_n + \omega_m) = \epsilon_0 \sum_{j,k} \sum_{n,m} \chi^{(2)}_{ijk}(\omega_n + \omega_m, \omega_n, \omega_m) E_j(\omega_n) E_k(\omega_m) \tag{B.1}$$

However, quite often in non-linear optics, and particularly when the external field frequencies do not coincide with any atomic resonance, the second order susceptibility does not depend on frequency. Under this condition (and the approximation of a lossless medium), the third order tensor $\chi^{(2)}$ presents full permutation symmetry. This condition states that all of the frequency arguments of the nonlinear susceptibility can be freely interchanged, as long as the corresponding cartesian indices are interchanged simultaneously. For instance, one can show that:

$$\chi^{(2)}_{ijk}(\omega_3 = \omega_1 + \omega_2, \omega_1, \omega_2) = \chi^{(2)}_{jki}(\omega_1 = -\omega_2 + \omega_3, \omega_2, \omega_3) = \chi^{(2)}_{kij}(\omega_2 = \omega_3 - \omega_1, \omega_3, \omega_1)$$
$$\tag{B.2}$$

This result is known as the Kleinman Symmetry condition, and it allows to rewrite the susceptibility tensor in a contracted form, using a 3 by 6 matrix, usually denoted d_{il}, following:

$$d_{il} = \frac{1}{2} \chi^{(2)}_{i,(jk)} \tag{B.3}$$

$$jk: \quad 11 \quad 22 \quad 33 \quad 23, 32 \quad 31, 13 \quad 12, 21 \tag{B.4}$$

$$l: \quad 1 \quad 2 \quad 3 \quad 4 \quad 5 \quad 6 \tag{B.5}$$

So we end up with the matrix:

$$
d_{il} = \begin{pmatrix} d_{11} & d_{12} & d_{13} & d_{14} & d_{15} & d_{16} \\ d_{21} & d_{22} & d_{23} & d_{24} & d_{25} & d_{26} \\ d_{31} & d_{32} & d_{33} & d_{34} & d_{35} & d_{36} \end{pmatrix} \tag{B.6}
$$

However, due to the symmetry condition, not all the elements of the matrix are linearly independent. For example, $d_{12} = d_{122} = d_{212} = d_{26}$. We finally recover ten independent elements:

$$
d_{il} = \begin{pmatrix} d_{11} & d_{12} & d_{13} & d_{14} & d_{15} & d_{16} \\ d_{16} & d_{22} & d_{23} & d_{24} & d_{14} & d_{12} \\ d_{15} & d_{24} & d_{33} & d_{23} & d_{13} & d_{14} \end{pmatrix} \tag{B.7}
$$

With this notation, we can write the components of the SHG process in the frequency domain as:

$$
\begin{pmatrix} P_x(2\omega) \\ P_y(2\omega) \\ P_z(2\omega) \end{pmatrix} = 2 \begin{pmatrix} d_{11} & d_{12} & d_{13} & d_{14} & d_{15} & d_{16} \\ d_{16} & d_{22} & d_{23} & d_{24} & d_{14} & d_{12} \\ d_{15} & d_{24} & d_{33} & d_{23} & d_{13} & d_{14} \end{pmatrix} \begin{pmatrix} E_x^2(\omega) \\ E_y^2(\omega) \\ E_z^2(\omega) \\ 2E_y(\omega)E_z(\omega) \\ 2E_x(\omega)E_z(\omega) \\ 2E_x(\omega)E_y(\omega) \end{pmatrix} \tag{B.8}
$$

And similar relationships can also be written for SFG and DFG.

The two specific non-linear materials used in this work were Lithium Niobate (LN) and Potassium Titanyl Phosphate (KTP). For both of them, the susceptibility tensor simplifies significantly.

For LN, the susceptibility tensor is:

$$
d_{\mathrm{LN}} = \begin{pmatrix} 0 & 0 & 0 & 0 & d_{15} & -d_{22} \\ d_{22} & d_{22} & 0 & d_{15} & 0 & 0 \\ d_{31} & d_{31} & d_{33} & 0 & 0 & 0 \end{pmatrix} \tag{B.9}
$$

and for KTP:

$$
d_{\mathrm{KTP}} = \begin{pmatrix} 0 & 0 & 0 & 0 & d_{15} & 0 \\ 0 & 0 & 0 & d_{24} & 0 & 0 \\ d_{31} & d_{32} & d_{33} & 0 & 0 & 0 \end{pmatrix} \tag{B.10}
$$

These tensors are important to account for the allowed processes in the crystals. For instance, assume a mixing process of two input frequencies, one polarized along the x axis and the other along the z axis, then the induced polarization would be oriented in the x axis, since only the term d_{15} is coupling this combination. This particular combination is

178

associated with a Type II PDC process, where a pump photon polarized along x is split into two photons, one polarized along x and the other along z. Similar conclusions can be drawn from the rest of field combinations and non-linear effects.

We finally remark the importance of the crystal-cut, since it relates the propagation and transversal directions in the crystal with the cartesian axes that we set when constructing the susceptibility matrix. A different crystal cut implies a change in the position of the coefficients in the d matrix, so it should be taken into account when designing an experiment involving non-linear bulk crystals or waveguides.

The non-linear d coefficients for LN are, taken from [181]:

$$d_{31}(\text{type I}) = 4.4 \text{ pm/V} \tag{B.11}$$

$$d_{15}(\text{type II}) = 4.4 \text{ pm/V} \tag{B.12}$$

$$d_{22}(\text{type 0}) = 2.1 \text{ pm/V} \qquad d_{33}(\text{type 0}) = 25 \text{ pm/V} \tag{B.13}$$

And the non-linear d coefficients for KTP are, taken from [182]:

$$d_{31}(\text{type I}) = 2.54 \text{ pm/V} \qquad d_{32}(\text{type I}) = 4.35 \text{ pm/V} \tag{B.14}$$

$$d_{24}(\text{type II}) = 3.64 \text{ pm/V} \qquad d_{15}(\text{type II}) = 1.91 \text{ pm/V} \tag{B.15}$$

$$d_{33}(\text{type 0}) = 16.9 \text{ pm/V} \tag{B.16}$$

These values are nevertheless wavelength and chemistry composition dependent, so they should be taken only as references.

Appendix C

High order terms in the mismatch

In Chapter 6, we have seen that one of the constraints for the SGVM condition to hold, and hence identical signal and idler supermodes, is that the first order term in the Taylor series of $\Delta\beta(\omega_s, \omega_i)$ should be much larger than the rest of the terms.

We can compute the first order coefficients, γ_s and γ_i, as defined in Eq.(6.17), by using the Sellmeier equations and its derivatives for the index of refraction of KTP, hence computing the group velocities and evaluating them at the corresponding central frequencies of pump, signal and idler. In this way we obtain the linear term, denoted here as $F(\omega_s, \omega_i)$:

$$F(\omega_s, \omega_i) = \gamma_s(\omega_s - \omega_{p,0}/2) + \gamma_i(\omega_i - \omega_{p,0}/2) \tag{C.1}$$

Paralelly, we can numerically compute the mismatch $\Delta\beta(\omega_s, \omega_i)$ by calculating the wavevectors from the relation with the index of refraction:

$$\Delta\beta(\omega_s, \omega_i) = \beta_p(\omega_s + \omega_i) - \beta_s(\omega_s) - \beta_i(\omega_i) \tag{C.2}$$

$$= \frac{1}{c}((\omega_s + \omega_i)n_p(\omega_s + \omega_i) - \omega_s n_s(\omega_s) - n_i(\omega_i)) \tag{C.3}$$

Therefore, the difference between Eq.(C.1) and Eq.(C.3) gives the contribution of all the rest of higher terms in the Taylor series. We call this contribution $H(\omega_s, \omega_i)$:

$$H(\omega_s, \omega_i) = \Delta\beta(\omega_s, \omega_i) - F(\omega_s, \omega_i) \tag{C.4}$$

Fig.(C.1) shows the numerical mismatch, the linear term and its difference as a function of signal and idler wavelength (by changing variables from frequency to wavelength, using $\omega = 2\pi/\lambda$). We compute them around the central wavelength and at the SGVM condition $\gamma_s = -\gamma_i$. We observe that the mismatch function is effectively well described by the first order term at least in the wavelength region considered (that is bigger than the Schmidt modes bandwidth calculated in the paper).

We therefore conclude that, for KTP, and under our configuration, the higher order terms in the mismatch can be discarded in practice and the SGVM condition holds.
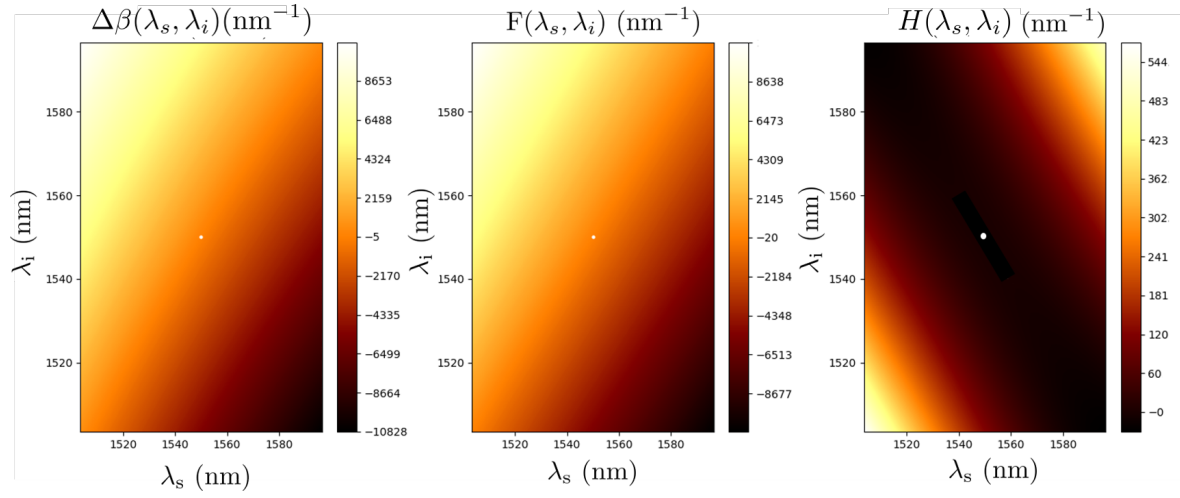
Figure C.1: Left to right: numerical mismatch, $\Delta\beta(\lambda_s, \lambda_i)$, first order term, $F(\lambda_s, \lambda_i)$ and higher order terms, $H(\lambda_s, \lambda_i)$ as a function of signal and idler wavelengths, λ_s, λ_i.

Appendix D

Analytical mode overlap in Type II SPDC

In Fig.(6.12) and Fig.(6.13), we observed that the overlap between the modes decreases as the mode order increases. The aim of this Appendix is to argue deeper this result.

The reason for this fact is two-fold: first, as the mode order increases, their spectral width does too, reaching frequencies further away from the central frequency, where the Taylor expansion of Eq.(6.16) is less precise and hence the modes are expected to present more differences between them. Their overlap is expected to be smaller, as we confirm.

The second reason can be understood by the mathematical structure of the modes. If we approximate the phasematching function (which is a sinc function on its arguments), by a Gaussian function, the supermodes can be calculated analytically, giving two sets of Hermite–Gauss modes of the form[1]:

$$\mathrm{HG}_n(x) = \frac{1}{\sqrt{n!}\sqrt{2^{n+1}\pi}w}H_n(x)e^{-(x-x_0)^2/4w^2} \tag{D.1}$$

where $H_n(x)$ is the n-th order Hermite polynomial and w is the associated width of the zeroth-order function, which is a Gaussian. Our temporal modes are not exactly Hermite–Gauss, but they approximate them fairly well.

If we try to compute the n-th order overlap defined in Eq.(6.7) from two sets of Hermite–Gauss modes with different widths, w and w', we find, using Eq.(D.1):

$$\mathcal{O}_n = \frac{\int_{-\infty}^{\infty} \mathrm{d}x H_n^2(x)e^{-a_1x^2+b_1x}}{\sqrt{\int_{-\infty}^{\infty} \mathrm{d}x H_n^2(x)e^{-a_2x^2+b_2x} \int_{-\infty}^{\infty} \mathrm{d}x H_n^2(x)e^{-a_3x^2+b_3x}}} \tag{D.2}$$

---

[1] The variable x would pysically correspond to the wavelenght λ or equivalently the frequency ω, given that the function describes the temporal modes.

$$a_1 = \frac{1}{2}\left(\frac{1}{w^2} + \frac{1}{w'^2}\right) \quad b_1 = x_0\left(\frac{1}{w^2} + \frac{1}{w'^2}\right) \tag{D.3}$$

$$a_2 = \frac{1}{w^2} \qquad\qquad b_2 = \frac{2x_0}{w^2} \tag{D.4}$$

$$a_3 = \frac{1}{w'^2} \qquad\qquad b_3 = \frac{2x_0}{w'^2} \tag{D.5}$$

and therefore the problem is reduced to finding the integral:

$$L \equiv \int_{-\infty}^{\infty} \mathrm{d}x\, H_n^2(x) e^{-ax^2 + bx} \tag{D.6}$$

For the solution of this integral one can define both the whole family of two variable Hermite polynomials $H_n(x, y)$ and the family of two-indices Hermite polynomials $H_{n,m}(x, y, w, z|\tau)$ [183]. By the method of the generating function, one finds that the solution to the integral L in Eq.(D.6) is an evaluation of the two-index (with the same index n) Hermite polynomial in specific coordinates depending only on a and b.
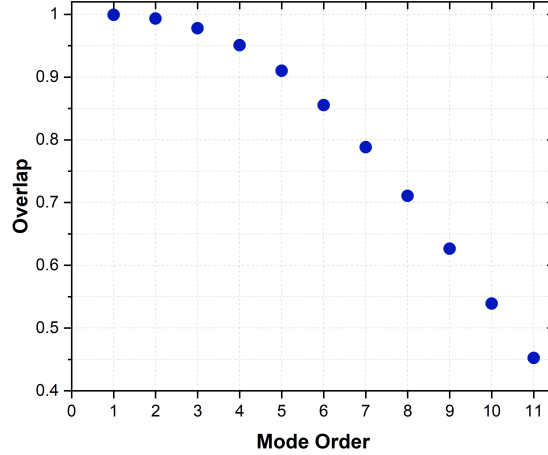

Figure D.1: Temporal modes overlap as a function of the mode order for two sets of Hermite–Gauss modes with relative widths of $w/w' = 0.95$.

For typical values of relative widths for signal and idler temporal modes computed in our simulations, the overlap between modes decreases slightly and linearly. If we also model the fact that our modes are expected to be less similar as the mode order increases, due to their larger spectral width, by making their relative widths to increase with the mode order, then we obtain Fig.(D.1). In this figure, the relative widths for the first modes (Gaussian) is set to $w/w' = 0.95$. From this value, we decrease their relative widths by 2% for every

higher mode order. We observe a decreasing overlap function with the mode order, in very good accordance with the results from the simulations of Chapter 6. We conclude that both the dispersion and the nature of the modes are responsible for the observed behavior of the overlap as the mode order increases.

References

[1] F. Grosshans and P. Grangier. Continuous variable quantum cryptography using coherent states. Physical Review Letters, 88(057902), 2002. (Cited on pages 8 and 19.)

[2] D. Luciano and G. Prichett. Cryptology: From caesar ciphers to public-key cryptosystems. The College Mathematics Journal, 18(1), 1987. (Cited on pages 8 and 9.)

[3] EnigmaHistory. cryptomuseum.com, 2012. [Online; accessed 11-May-2021]. (Cited on page 8.)

[4] Information Technology Laboratory (National Institute of Standards and Technology). Announcing the Advanced Encryption Standard (AES). Federal Information Processing Standards, 2001. (Cited on page 9.)

[5] C. E. Shannon. Communication theory of secrecy systems. Bell System Technical Journal, 28(4), 2021. (Cited on page 9.)

[6] W. Diffie and M. Hellman. New directions in cryptography. IEEE Transactions on Information Theory, 22(6):344–354, 1976. (Cited on page 10.)

[7] K.S. McCurley. The discrete logarithm problem. Proceedings of Symposia in Applied Mathematics, 42:49–74, 1990. (Cited on page 10.)

[8] E. Bach. Discrete logarithms and factoring. Technical report, University of California at Berkeley, USA, 1984. (Cited on page 10.)

[9] P. W. Shor. Polynomial-time algorithms for prime factorization and discrete logarithms on a quantum computer. Siam Journal on Computing, 26(5):1484–1509, 1997. (Cited on page 10.)

[10] C.H. Bennett and G. Brassard. Quantum cryptography: Public key distribution and coin tossing. Proceedings of IEEE International Conference on Computers , Systems and Signal Processing., pages 175–179, 1984. (Cited on page 11.)

[11] A. K. Ekert. Quantum cryptography based on bell's theorem. Physical Review Letters, 67:661–663, 1991. (Cited on page 15.)

[12] C. Bennet, G. Brassard, and N. D. Mermin. Quantum cryptography without bell's theorem. Physical Review Letters, 68:557–559, 1992. (Cited on page 15.)

[13] A. Aspect. Bell's inequality test: more ideal than ever. Nature, 398:189–190, 1999. (Cited on page 15.)

[14] P. James. The concept of transition in quantum mechanics. Foundations of Physics, 1(1):23–33, 1970. (Cited on page 15.)

[15] R. Ursin et al. Entanglement-based quantum communication over 144 km. Nature Physics, 3(7):481–486, 2007. (Cited on pages 16 and 23.)

[16] Q. Zhang et al. Large scale quantum key distribution: challenges and solutions. Optics Express, 26(18):24260, 2018. (Cited on page 16.)

[17] H. J. Briegel, W. Dür, J. I. Cirac, and P. Zoller. Quantum repeaters: the role of imperfect local operations in quantum communication. Physical Review Letters, 81:5932–5935, 1998. (Cited on pages 16 and 28.)

[18] N. Sangouard et al. Quantum repeaters based on atomic ensembles and linear optics. Review Modern Physics, 83(1):33–80, 2011. (Cited on pages 16 and 28.)

[19] R. Bedington, J. M. Arrazola, and A. Ling. Progress in satellite quantum key distribution. npj Quantum Information, 3(30), 2017. (Cited on page 16.)

[20] V. Scarani, H. Bechmann-Pasquinucci, N.J. Cerf, M. Dusek, N. Lukenhaus, and M. Peev. The security of practical quantum key distribution. npj Quantum Information, 81(1301), 2009. (Cited on pages 16 and 24.)

[21] I. Devetak and A. Winter. Distillation of secret key and entanglement from quantum state. Proceedings Royal Society London A, 461(207), 2005. (Cited on page 17.)

[22] Y. Liu, Q. Zhao, MH. Li, et al. Device-independent quantum random-number generation. Nature, 562:548–551, 2018. (Cited on page 19.)

[23] T. Richardson and R. Urbanke. Modern Coding Theory. Cambridge University Press, 1 edition, 2008. (Cited on page 20.)

[24] F. Grosshans, N. J. Cerf, J. Wenger, R. Tualle-Brouri, and P. Grangier. Virtual entanglement and reconciliation protocols for quantum cryptography with continuous variables. Quantum Information and Computation, 3(7):535–552, 2003. (Cited on page 20.)

[25] J. L. Carter and M. N. Wegman. Universal classes of hash functions. Journal of Computer and System Sciences, 18(143), 1979. (Cited on page 21.)

[26] C. H. Bennett, G. Brassard, C. Crepeau, and U. M. Maurer. Generalized privacy amplification. <u>IEEE Transactions on Information Theory</u>, 1, 1995. (Cited on page 21.)

[27] R. Filip. Continuous-variable quantum key distribution with noisy coherent states. <u>Physical Review A</u>, 77(022310), 2008. (Cited on page 24.)

[28] Paul Jouguet. <u>Security and performance of continuous-variable quantum key distribution systems.</u> PhD thesis, UPMC, 2013. (Cited on page 24.)

[29] Thomas M. C. and Joy A. T. <u>Elements of Information Theory</u>. Wiley New Publisher, 2 edition, 2005. (Cited on page 25.)

[30] D. Dequal, L. Trigo-Vidarte, V. Roman-Rodriguez, , G. Valloni, P. Villoresi, A. Leverrier, and E. Diamanti. Feasibility of satellite-to-ground continuous-variable quantum key distribution. <u>npj Quantum Information</u>, 7(3), 2021. (Cited on page 27.)

[31] Z. D. Li et al. Experimental quantum repeater without quantum memory. <u>Nature Photonics</u>, 13(3):644–648, 2019. (Cited on page 28.)

[32] M. K. Bhaskar et al. Experimental demonstration of memory-enhanced quantum communication. <u>Nat. Photonics</u>, 13(580):60–64, 2020. (Cited on page 28.)

[33] G. Vallone, D. Bacco, D. Dequal, S. Gaiarin, V. Luceri, G. Bianco, and P. Villoresi. Experimental satellite quantum communications. <u>Physical Review Letters</u>, 115, 2015. (Cited on page 28.)

[34] S. K. Liao et al. Satellite-to-ground quantum key distribution. <u>Nature</u>, 549(115):43–47, 2017. (Cited on pages 28 and 29.)

[35] J. Yin et al. Satellite-to-ground entanglement-based quantum key distribution. <u>Phys. Rev. Lett.</u>, 119(200501), 2017. (Cited on page 28.)

[36] S. K. Liao et al. Space-to-ground quantum key distribution using a small-sized payload on tiangong-2 space lab. <u>Chin. Phys. Lett.</u>, 34(090302), 2017. (Cited on page 28.)

[37] S. K. Liao et al. Satellite-relayed intercontinental quantum network. <u>Phys. Rev. Lett.</u>, 120(030501), 2018. (Cited on page 28.)

[38] D. Vasylyev, W. Vogel, and F. Moll. Satellite-mediated quantum atmospheric links. <u>Phys. Rev. A</u>, 99(053830), 2019. (Cited on page 31.)

[39] C. Tomasi and B. H. Petkov. Calculations of relative optical air masses for various aerosol types and minor gases in arctic and antarctic atmospheres. <u>J. Geophys. Res. Atmos.</u>, 199:1363–1385, 2014. (Cited on page 31.)

189

[40] A. Berk et al. Modtran6: a major upgrade of the modtran radiative transfer code. Proc. Algorithms and Technologies for Multispectral, Hyperspectral, and Ultraspectral Imagery XX (SPIE), 9088, 2014. (Cited on page 31.)

[41] Inc., S. S. Modtran web app. http://modtran.spectral.com/modtran_home, 2020. (Cited on page 31.)

[42] K. Günthner et al. Quantum-limited measurements of optical signals from a geostationary satellite. Optica, 4(611), 2016. (Cited on page 31.)

[43] R. Tyson. Principles of Adaptive Optics, volume 22. CRC Press, Boca Raton, 3 edition, 2011. (Cited on page 32.)

[44] N. Jovanovic et al. Efficient injection from large telescopes into single-mode fibres: enabling the era of ultra-precision astronomy. Astron. Astrophys., 604(A122), 2017. (Cited on page 32.)

[45] D. Y. Vasylyev, A. A. Semenov, and W. Vogel. Efficient injection from large telescopes into single-mode fibres: enabling the era of ultra-precision astronomy. Phys. Rev. Lett., 108(220501), 2012. (Cited on pages 32 and 33.)

[46] R. Fante. Electromagnetic beam propagation in turbulent media: an update. Proc. IEEE, 68:1424–1443, 1980. (Cited on pages 34 and 36.)

[47] A. Leverrier. Security of continuous-variable quantum key distribution via a gaussian de finetti reduction. Phys. Rev. Lett., 188(200501), 2017. (Cited on page 39.)

[48] V. C. Usenko et al. Entanglement of gaussian states and the applicability to quantum key distribution over fading channels. N. J. Phys., 14(093048), 2012. (Cited on page 39.)

[49] K. Habermann. Introduction to symplectic Dirac operators. Springer, 2006. (Cited on page 39.)

[50] S. Fossier, E. Diamanti, T. Debuisschert, R. Tualle-Brouri, and P. Grangier. Improvement of continuous-variable quantum key distribution systems by using optical preamplifiers. J. Phys. B, 42(114014), 2009. (Cited on page 40.)

[51] D. B. S. Soh et al. Improvement of continuous-variable quantum key distribution systems by using optical preamplifiers. Phys. Rev. X, 5(041010), 2015. (Cited on page 40.)

[52] B. Qi, P. Lougovski, R. Pooser, W. Grice, and M. Bobrek. Improvement of continuous-variable quantum key distribution systems by using optical preamplifiers. Phys. Rev. X, 5(041009), 2015. (Cited on page 40.)

[53] I. Ali, N. Al-Dhahir, and J. Hershey. Doppler characterization for leo satellites. IEEE T. Commun., 46:309–313, 1998. (Cited on page 40.)

[54] Y. Shoji, M. J. Fice, Y. Takayama, and A. J. Seeds. A pilot-carrier coherent leo-toground downlink system using an optical injection phase lock loop (oipll) technique. J. Lightwave Technol., 30:2696–2706, 2012. (Cited on page 40.)

[55] L. Paillier et al. Adaptive optics assisted space-ground coherent optical links: ground receiver performance with digital phase-locked loop. In IEE International Conference on Space Optical Systems and Applications (ICSOS), 2019. (Cited on page 40.)

[56] F. Gao et al. Analysis of hy2a precise orbit determination using doris. Adv. Space Res., 55:1394–1404, 2015. (Cited on page 41.)

[57] A. Leverrier, F. Grosshans, and P. Grangier. Finite-size analysis of a continuous variable quantum key distribution. Phys. Rev. A, 81(062343), 2010. (Cited on page 44.)

[58] C. Fabre and N. Treps. Modes and states in quantum optics. Review in Modern Physics, 92:035005, Sep 2020. (Cited on page 50.)

[59] D. J. Griffiths. Introduction to Electrodynamics. Prentice Hall, 3 edition, 1998. (Cited on page 50.)

[60] B. E. A. Saleh and M. C. Teich. Fundamentals of Photonics. Wiley–Blackwell, 2 edition, 1991. (Cited on pages 51 and 61.)

[61] Menlosystem c-fiber sources. https://www.menlosystems.com/products/femtosecond-lasers-and-amplifiers/c-fiber/. Accessed: 2021-12-18. (Cited on page 59.)

[62] L. F. Mollenauer and R. H. Stolen. The soliton laser. Optical Letters, 9(1):13–15, Jan 1984. (Cited on page 59.)

[63] E. P. Ippen, H. A. Haus, and L. Y. Liu. Additive pulse mode locking. Journal of the Optical Society of America B, 6(9):1736–1745, Sep 1989. (Cited on page 59.)

[64] P. Dipika and V. Mishra. Analysis and review of edfa. International Journal of Computer Science and Network, 4:873– 886, Dec 2015. (Cited on page 59.)

[65] J.C. Diels and W. Rudolph. Ultrashort Laser Pulse Phenomena. Academic Press, 2 edition, 2006. (Cited on page 62.)

[66] Polyanskiy, m. n. 2021 refractive index database. https://refractiveindex.info. Accessed: 2021-12-18. (Cited on page 62.)

[67] R. L. Fork, O. E. Martinez, and J. P. Gordon. Negative dispersion using pairs of prisms. Optics Letters, 9(5):150–152, May 1984. (Cited on page 67.)

[68] J. P. Heritage, A. M. Weiner, and R. N. Thurston. Picosecond pulse shaping by spectral phase and amplitude manipulation. Optics Letters, 10:609–611, May 1985. (Cited on page 68.)

[69] A. M. Weiner, J. P. Heritage, and E. M. Kirschner. High-resolution femtosecond pulse shaping. Journal of the Optical Society of America B, 5:1563–1572, 1988. (Cited on page 68.)

[70] M. B. Danailov and I.P. Christov. Time-space shaping of light pulses by fourier optical processing. Journal of Modern Optics, 36(6):725–731, 1989. (Cited on page 68.)

[71] Thibault Michel. Optimization of the pump spectral shape in a parametric down conversion process to generate multimode entangled states. PhD thesis, Sorbonne Universite and Australian National University, 2021. (Cited on pages 69, 71, and 72.)

[72] Pulse shaper grating. https://www.spectrogon.com/product-services/gratings/pulse-compression-gratings/. Accessed: 2021-12-27. (Cited on page 69.)

[73] Hamamatsu model x15213-08. https://www.hamamatsu.com/us/en/product/type/X15213-08/index.html. Accessed: 2021-12-23. (Cited on page 71.)

[74] J. Albero, I. Moreno, J. A. Davis, D. M. Cottrell, and D. Sand. Generalized phase diffraction gratings with tailored intensity. Optics Letters, 37(20):4227–4229, Oct 2012. (Cited on page 71.)

[75] Cédric Jacquard. A single-photon subtractor for spectrally multimode quantum states. PhD thesis, Sorbonne Universite, 2017. (Cited on page 71.)

[76] A. Mamrashev, N. Nikolaev, V. Antsygin, Y. Andreev, G. Lanskii, and A. Meshalkin. Optical properties of ktp crystals and their potential for terahertz generation. Crystals, 8(8), 2018. (Cited on page 76.)

[77] R. W. Boyd. Nonlinear Optics. Academic Press, 3 edition, 2008. (Cited on page 79.)

[78] Gilbert Grynberg, Alain Aspect, and Claude Fabre. Introduction to quantum optics: from the semi-classical approach to quantized light. Cambridge University Press, 2010. (Cited on pages 79 and 94.)

[79] R. C. Eckardt. Non-linear optics, basics – harmonic generation. In R. D. Guenther, editor, Encyclopedia of Modern Optics, pages 213–223. Elsevier, Oxford, 2005. (Cited on page 79.)

[80] M. Yamada, N. Nada, M. Saitoh, and K. Watanabe. First-order quasi-phase matched linbo3 waveguide periodically poled by applying an external field for efficient blue second-harmonic generation. Applied Physics Letters, 62:435–436, 1993. (Cited on page 79.)

[81] V. Y. Shur, E. V. Pelegova, A. R. Akhmatkhanov, and I. S. Baturin. Periodically poled crystals of ktp family: a review. Ferroelectrics, 496:49–69, 2016. (Cited on page 79.)

[82] K. Okamoto. Fundamentals of Optical Waveguides. Academic Press, 2 edition, 2005. (Cited on pages 81 and 130.)

[83] G. I. Stegeman and C. T. Seaton. Nonlinear integrated optics. Journal of Applied Physics, 58:57–78, 1985. (Cited on page 81.)

[84] N. Bloembergen, D. B. Ostrowsky, and R. Reinisch. Guided Wave Nonlinear Optics. Springer Netherlands, 1 edition, 1992. (Cited on page 81.)

[85] F. Suhara and M. Fujimura. Waveguide Nonlinear-Optic Devices. Springer, 1 edition, 2003. (Cited on page 81.)

[86] L. Padberg, M. Santandrea, M. Rüsing, J. Brockmeier, P. Mackwitz, G. Berth, A. Zrenner, C. Eigner, and C. Silberhorn. Characterisation of width-dependent diffusion dynamics in rubidium-exchanged ktp waveguides. Optics Express, 28(17):24353–24362, Aug 2020. (Cited on page 82.)

[87] E. A. J. Marcatili. Dielectric rectangular waveguide and directional coupler for integrated optics. Bell Syst. Tech., 48, 1969. (Cited on pages 86 and 121.)

[88] A. B. Fallahkhair, K. S. Li, and T. E. Murphy. Vector finite difference modesolver for anisotropic dielectric waveguides. Journal of Lightwave Technology, 26(11):1423–1431, 2008. (Cited on pages 86 and 88.)

[89] Advr, inc. https://advr-inc.com/. Accessed: 2021-12-23. (Cited on page 89.)

[90] F. Dell'Anno, S. De Siena, and F. Illuminati. Multiphoton quantum optics and quantum state engineering. Physics Reports, 428(May):53–168, 2006. (Cited on page 94.)

[91] S. Weinberg. The Quantum Theory of Fields, volume 3. Cambridge University Press, 1995. (Cited on page 95.)

[92] K. J. Blow, R. R. Loudon, and S. J. D. Phoenix. Continuum fields in quantum optics. Physical Review A, 42:4102–4114, 1990. (Cited on page 95.)

[93] B. Brecht, A. Eckstein, A. Christ, H. Suche, and C. Silberhorn. From quantum pulse gate to quantum pulse shaper—engineered frequency conversion in nonlinear optical waveguides. New Journal of Physics, 13, 2011. (Cited on page 96.)

[94] A. Christ, B. Brecht, W. Mauerer, and C. Silberhorn. Theory of quantum frequency conversion and type-ii parametric down-conversion in the high-gain regime. New Journal of Physics, 15(May):53–168, 2013. (Cited on page 101.)

[95] A. K. Ekert and P. L. Knight. Relationship between semiclassical and quantum-mechanical input-output theories of optical response. Physical Review A, 43:3934–3938, Apr 1991. (Cited on page 101.)

[96] I. M. Kolobov. The spatial behavior of nonclassical light. Rev. Mod. Phys., 71:1539–1589, Oct 1999. (Cited on page 101.)

[97] S. Braunstein. Squeezing as an irreducible resource. Physical Review A, 71, May 2005. (Cited on page 101.)

[98] S. L. Braunstein and P. van Loock. Quantum information with continuous variables. Reviews of Modern Physics, 77:513–577, Jun 2005. (Cited on page 101.)

[99] H. Everett. Relative state formulation of quantum mechanics. Reviews of Modern Physics, 29:454–462, Jul 1957. (Cited on page 102.)

[100] A. Ekert and P. L. Knight. Entangled quantum systems and the schmidt decomposition. American Journal of Physics, 63, 1995. (Cited on page 102.)

[101] C. K. Law, I. A. Walmsley, and J.H. Eberly. Continuous frequency entanglement: effective finite Hilbert space and entropy control. Physical Review Letters, 84:3–6, 2000. (Cited on page 102.)

[102] G. Patera, N. Treps, C. Fabre, and G. de Valcarcel. Quantum theory of synchronously pumped type i optical parametric oscillators: characterization of the squeezed super-modes. The European Physical Journal D, 56:123–140, Jan 2010. (Cited on page 102.)

[103] Luca La Volpe. Multimode single-pass spatio-temporal squeezing. PhD thesis, Sorbonne Universite, 2020. (Cited on page 103.)

[104] A. Christ, K. Laiho, A. Eckstein, T. Lauckner, P. J. Mosley, and C. Silberhorn. Spatial modes in waveguided parametric down-conversion. Physical Review A, 80:033829, Sep 2009. (Cited on page 103.)

[105] C. K. Hong, Z. Y. Ou, and L. Mandel. Measurement of subpicosecond time intervals between two photons by interference. Phys. Rev. Lett., 59:2044–2046, Nov 1987. (Cited on page 105.)

[106] A. Einstein, B. Podolsky, and N. Rosen. Can quantum-mechanical description of physical reality be considered complete? Phys. Rev., 47:777–780, May 1935. (Cited on pages 105 and 107.)

[107] R. Loudon. The Quantum Theory of Light. Oxford University Press, 3 edition, 2000. (Cited on pages 106, 111, 152, and 160.)

[108] A. Lvovsky, P. Grangier, A. Ourjoumtsev, V. Parigi, M. Sasaki, and R. Tualle-Brouri. Production and applications of non-gaussian quantum states of light. 06 2020. Preprint. (Cited on page 108.)

[109] M. Walschaers. Non-gaussian quantum states and where to find them. PRX Quantum, 2:030204, Sep 2021. (Cited on page 108.)

[110] H. Kimble. The quantum internet. Nature, 453:1023–1030, 2008. (Cited on page 114.)

[111] M. A. Nielsen. Optical quantum computation using cluster states. Physical Review Letters, 93:040503, Jul 2004. (Cited on page 114.)

[112] F. Arzani, G. Ferrini, F. Grosshans, and D. Markham. Random coding for sharing bosonic quantum secrets. Physical Review A, 100, 2019. (Cited on pages 114 and 137.)

[113] F. Centrone, E. Diamanti, and I. Kerenidis. Practical quantum electronic voting. arXiv preprint quant-ph/2107.14719, 2021. (Cited on pages 114 and 137.)

[114] K. Sutradhar and H. Om. An efficient simulation for quantum secure multiparty computation. Scientific Reports, 11, 2021. (Cited on pages 114 and 137.)

[115] N. C. Menicucci, P. van Loock, M. Gu, C. Weedbrook, T. C. Ralph, and M. A. Nielsen. Universal quantum computation with continuous-variable cluster states. Physical Review Letters, 97, 2006. (Cited on page 114.)

[116] M. Gu, C. Weedbrook, N. C. Menicucci, T. C. Ralph, and P. van Loock. Quantum computing with continuous-variable clusters. Phys. Rev. A, 79:062318, Jun 2009. (Cited on page 114.)

[117] O. Pinel, J. Fade, D. Braun, P. Jian, N. Treps, and C. Fabre. Ultimate sensitivity of precision measurements with intense gaussian quantum light: A multimodal approach. Physical Review A, 85:010101, Jan 2012. (Cited on page 114.)

[118] M. Gessner, L. Pezzè, and A. Smerzi. Sensitivity bounds for multiparameter quantum metrology. Physical Review Letters, 121:130503, Sep 2018. (Cited on page 114.)

[119] J. Nokkala, F. Arzani, F. Galve, R. Zambrini, S. Maniscalco, J. Piilo, N. Treps, and V. Parigi. Reconfigurable optical implementation of quantum complex networks. New Journal of Physics, 20(5):053024, may 2018. (Cited on page 114.)

[120] S. Ritter, C. Nölleke, C. Hahn, et al. An elementary quantum network of single atoms in optical cavities. Nature, 484:195–200, 2012. (Cited on page 114.)

[121] J. Hofmann, M. Krugnorbert, O. Gerardmarkus, W. W. Rosenfeld, and H. Weinfurter. Heralded entanglement between widely separated atoms. Science, 337:72–75, 2012. (Cited on page 114.)

[122] M. Pompili et al. Realization of a multinode quantum network of remote solid-state qubits. Science, 372:259–264, 2021. (Cited on page 114.)

[123] M. Proietti, J. Ho, Grasselli F., Barrowmehul P. M., and Fedrizzi A. Experimental quantum conference key agreement. Science Advances, 7, 2021. (Cited on page 114.)

[124] K. Azuma, K. Tamaki, and H. K. Lo. All-photonic quantum repeaters. Nature Communications, 6:6787, 2015. (Cited on page 114.)

[125] H.S. Zhong et al. 12-photon entanglement and scalable scattershot boson sampling with optimal entangled-photon pairs from parametric down-conversion. Physical Review Letters, 121:250505, Dec 2018. (Cited on page 114.)

[126] D. Istrati, Y. Pilnyak, J.C. Loredo, et al. Sequential generation of linear cluster states from a single photon emitter. Nature Communications, 11:5501, 2020. (Cited on page 114.)

[127] Y. Cai, J. Roslund, G. Ferrini, F. Arzani, X. Xu, C. Fabre, and N. Treps. Multimode entanglement in reconfigurable graph states using optical frequency combs. Nature Communications, 8:373–376, Oct 2017. (Cited on page 114.)

[128] C. Moran, N. C. Menicucci, and O. Pfister. Experimental realization of multipartite entanglement of 60 modes of a quantum optical frequency comb. Physical Review Letters, 112:120505, Mar 2014. (Cited on page 114.)

[129] W. Asavanant, Y. Shiozawa, S. Yokoyama, B. Charoensombutamon, H. Emura, R. N. Alexander, S. Takeda, J. I. Yoshikawa, N. C. Menicucci, H. Yonezawa, and A. Furusawa. Generation of time-domain-multiplexed two-dimensional cluster state. Science, 366(6463):373–376, Oct 2019. (Cited on page 114.)

[130] M. Larsen, X. Guo, C. Breum, J. Neergaard-Nielsen, and U. Andersen. Deterministic generation of a two-dimensional cluster state. Science, 366:369–372, 10 2019. (Cited on page 114.)

[131] L. La Volpe, S. De, T. Kouadou, D. Horoshko, M. I. Kolobov, F. Fabre, V. Parigi, and N. Treps. Multimode single-pass spatio-temporal squeezing. Optics Express, 28(8):12385–12394, Apr 2020. (Cited on page 115.)

[132] J. Zhang and S. L. Braunstein. Continuous-variable gaussian analog of cluster states. Physical Review A, 73:032318, Mar 2006. (Cited on page 116.)

[133] Nicolas Menicucci, Peter van Loock, Mile Gu, Christian Weedbrook, Timothy Ralph, and Michael Nielsen. Universal Quantum Computation with Continuous-Variable Cluster States. Physical Review Letters, 97(11):110501, sep 2006. (Cited on page 116.)

[134] M. Hein, J. Eisert, and H. J. Briegel. Multiparty entanglement in graph states. Physical Review A, 69:062311, Jun 2004. (Cited on page 116.)

[135] N. C. Menicucci, S. T. Flammia, and P. van Loock. Graphical calculus for gaussian pure states. Physical Review A, 83:042335, Apr 2011. (Cited on page 116.)

[136] G. Ferrini, J. Roslund, F. Arzani, Y. Cai, C. Fabre, and N. Treps. Optimization of networks for measurement-based quantum computation. Physical Review A, 91:032314, Mar 2015. (Cited on page 116.)

[137] F. Sansavini and V. Parigi. Continuous variables graph states shaped as complex networks: Optimization and manipulation. Entropy, 22:26, 12 2019. (Cited on page 116.)

[138] C. Bloch and A. M. L. Messiah. The canonical form of an antisymmetric tensor and its application to the theory of superconductivity. Nuclear Physics, 39:95–106, 1962. (Cited on page 116.)

[139] C. J. McKinstrie and M. Karlsson. Schmidt decompositions of parametric processes i: Basic theory and simple examples. Optics Express, 21(2):1374–1394, Jan 2013. (Cited on page 116.)

[140] G. Cariolaro and G. Pierobon. Reexamination of bloch-messiah reduction. Physical Review A, 93:062115, Jun 2016. (Cited on page 116.)

[141] D. B. Horoshko, L. La Volpe, F. Arzani, N. Treps, C. Fabre, and M. I. Kolobov. Bloch-messiah reduction for twin beams of light. Physical Review A, 100:013837, Jul 2019. (Cited on page 116.)

197

[142] G. Ferrini, J. P. Gazeau, T. Coudreau, C. Fabre, and N. Treps. Compact gaussian quantum computation by multi-pixel homodyne detection. New Journal of Physics, 15:093015, 2013. (Cited on page 117.)

[143] V. Roman-Rodriguez, B. Brecht, K. Srinivasan, C. Silberhorn, N. Treps, E. Diamanti, and V. Parigi. Continuous variable multimode quantum states via symmetric group velocity matching. New Journal of Physics, 23, 2021. (Cited on page 118.)

[144] J. H. Eberly. Schmidt analysis of pure-state entanglement. Laser Physics, 16:921–926, 2006. (Cited on page 118.)

[145] M. C. Tichy, P. A. Bouvrie, and Molmer. K. Bosonic behavior of entangled fermions. Physical Review A, 86, 2012. (Cited on page 119.)

[146] Benjamin Brecht. Engineering Ultrafast Quantum Frequency Conversion. PhD thesis, Der Naturwissenschaftlichen Fakultät Paderborn, 2014. (Cited on page 121.)

[147] Li K. S. Fallahkhair A. B. and Murphy T. E. Vector finite difference modesolver for anisotropic dielectric waveguides. Journal of Lightwave Technology, 26, 2008. (Cited on page 121.)

[148] D. E. Zelmon, D. L. Small, and D. Jundt. Infrared corrected sellmeier coefficients for congruently grown lithium niobate and 5 mol. Journal Optical Society of America B, 14:3319–3322, 1997. (Cited on page 121.)

[149] K. Kato and E. Takaoka. Sellmeier and thermo-optic dispersion formulas for ktp. Applied Optics, 41:5040–5044, 2002. (Cited on page 121.)

[150] A. U'Ren, C. Silberhorn, K. Erdmann, R. Banaszek, W. Grice, Walmsley I. A., and M. G. Raymer. Generation of pure-state single-photon wavepackets by conditional preparation based on spontaneous parametric downconversion. Laser Physics, 15:146–161, 2005. (Cited on page 129.)

[151] A. Vaish and H. Parthasarathy. Numerical computation of the modes of electromagnetic wave propagation in a non-homogeneous rectangular waveguide. 09 2006. (Cited on page 131.)

[152] J. Jin. The Finite Element Method in Electromagnetics. IEEE Press, 3 edition, 2014. (Cited on page 131.)

[153] P. J. Mosley, J. S. Lundeen, B. J. Smith, P. Wasylczyk, A. B. U'Ren, C. Silberhorn, and I. A. Walmsley. Heralded generation of ultrafast single photons in pure quantum states. Physical Review Letters, 100:133601, Apr 2008. (Cited on page 133.)

[154] Hcphotonics. https://www.hcphotonics.com/. Accessed: 2021-12-25. (Cited on page 142.)

[155] Covesion. https://www.covesion.com/en/. Accessed: 2021-12-25. (Cited on page 142.)

[156] A. Weiner. Ultrafast Optics. Wiley Publishing, 2009. (Cited on page 142.)

[157] S. Yu, N. E. Kurimura and K. Kitamura. Efficient frequency doubling of a femtosecond pulse with simultaneous group-velocity matching and quasi phase matching in periodically poled, mgo-doped lithium niobate. Applied Physics Letters, 82, 2003. (Cited on page 143.)

[158] Y. Furukawa, K. Kitamura, A. Alexandrovski, R. K. Route, M. M. Fejer, and G. Foulon. Green-induced infrared absorption in mgo doped linbo3. Applied Physics Letters, 78, 2001. (Cited on page 146.)

[159] J. Hirohashi, T. Tago, O. Nakamura, A. Miyamoto, and Y. Furukawa. Characterization of griira properties in linbo3 and litao3 with different compositions and doping. Applied Letter Physics, 82, 2003. (Cited on page 146.)

[160] I. A. Begishev, M. Kalashnikov, V. Karpov, Nickles P., H. Schönnagel, I. A. Kulagin, and T. Usmanov. Limitation of second-harmonic generation of femtosecond ti:sapphire laser pulses. Journal of the Optical Society of America B, 21(2):318–322, Feb 2004. (Cited on page 146.)

[161] Y. Zheng, Y. Wang, V. Petrov, Y.J. Ding, J.B. Khurgin, and W.P. Risk. Ultrafast generation of blue light by efficient second-harmonic generation in periodically poled bulk and waveguide potassium titanyl phosphate. In Conference on Lasers and Electro-Optics, page CTuD4. Optical Society of America, 1998. (Cited on page 146.)

[162] Ben A., E.U. Rafailov, Wilson S., S. Solomon, K. Kaloian, T. Mikael, W. Shunhua, L. Fredrik, B. Philip, F. Tane, R. Tony, and N. Elizabeth. Efficient frequency-doubling of femtosecond pulses in waveguide and bulk nonlinear crystals: design, fabrication, theory and experiment, volume 216, pages 189–227. Springer, 01 2008. (Cited on page 146.)

[163] Elliotscientific precision positioning. https://www.elliotscientific.com/Precision-Positioning/Elliot-Martock-Products. Accessed: 2021-12-29. (Cited on page 147.)

[164] P. Y. Horace and W. S. C. Vincent. Noise in homodyne and heterodyne detection. Optical Letters, 8(3):177–179, Mar 1983. (Cited on page 152.)

[165] G. L. Abbas, V. W. S. Chan, and T. K. Yee. Local-oscillator excess-noise suppression for homodyne and heterodyne detection. Optical Letters, 8(8):419–421, Aug 1983. (Cited on page 152.)

[166] Valerian Thiel. Modal analysis of an ultrafast frequency comb : from classical to quantum spectral correlations. PhD thesis, Sorbonne Universit'e, 2017. (Cited on page 153.)

[167] F. A. S. Barbosa, A. S. Coelho, K. N. Cassemiro, P. Nussenzveig, C. Fabre, A. S. Villar, and M. Martinelli. Quantum state reconstruction of spectral field modes: Homodyne and resonator detection schemes. Physical Review A, 88:052113, Nov 2013. (Cited on page 154.)

[168] R. Kumar, E. Barrios, A. MacRae, E. Cairns, E. H. Huntington, and A. I. Lvovsky. Versatile wideband balanced detector for quantum optical homodyne tomography. Optics Communications, 285:5259–5267, Nov 2012. (Cited on page 155.)

[169] Tiphaine Kouadou. Single-Pass Generation and Detection of Ultrafast Multimode Squeezed Light. PhD thesis, Sorbonne Universite, 2021. (Cited on pages 155 and 156.)

[170] J.A. Levenson, I. Abram, K. Bencheikh, and P. Grangier. Noiseless optical parametric amplification. In Proceedings of 5th European Quantum Electronics Conference, pages 287–287, 1994. (Cited on page 158.)

[171] A. Agarwal, J. M. Dailey, P. Toliver, and N. A. Peters. Entangled-pair transmission improvement using distributed phase-sensitive amplification. Physical Review X, 4:041038, Dec 2014. (Cited on page 158.)

[172] G. Brida, M. Genovese, and Ruo-Berchera I. Experimental realization of sub-shot-noise quantum imaging. Nature Photonics, 4:227–230, 2010. (Cited on page 158.)

[173] N. Samantaray, I. Ruo-Berchera, A. Meda, et al. Realization of the first sub-shot-noise wide field microscope. Light Science Applied, 6:e17005, 2017. (Cited on page 158.)

[174] G. Frascella, R. V. Zakharov, O. V. Tikhonova, and M. V. Chekhova. Multimode optical parametric amplification in the phase-sensitive regime. Optical Letters, 46(10):2364–2367, May 2021. (Cited on page 158.)

[175] D. K. Serkland, M. M. Fejer, Byer R. L., and Y. Yamamoto. Squeezing in a quasi-phase-matched linbo3 waveguide. Optics Letters, 20(15):1649–1651, Aug 1995. (Cited on page 160.)

[176] F. Kaiser, B. Fedrici, A. Zavatta, V. D'Auria, and S. Tanzilli. A fully guided-wave squeezing experiment for fiber quantum networks. Optica, 3(4):362–365, Apr 2016. (Cited on page 161.)

[177] Alexei Ourjoumtsev. Étude théorique et expérimentale de superpositions quantiques cohérentes et d'états intriqués non-gaussiens de la lumière. PhD thesis, Université Paris Sud - Paris XI, 2007. (Cited on page 161.)

[178] L. A. Wu, M. Xiao, and H. J. Kimble. Squeezed states of light from an optical parametric oscillator. Journal of the Optical Society of America B, 4(10):1465–1475, Oct 1987. (Cited on page 165.)

[179] J. Yoshikawa, S. Yokoyama, T. Kaji, C. Sornphiphatphong, Y. Shiozawa, K. Makino, and A. Furusawa. Generation of one-million-mode continuous-variable cluster state by unlimited time-domain multiplexing. APL Photonics, 1, 06 2016. (Cited on page 169.)

[180] Y. S. Ra, A. Dufour, M. Walschaers, C. Jacquard, T. Michel, C. Fabre, and N. Treps. Non-gaussian quantum states of a multimode light field. Nature Physics, 16:144–147, 2020. (Cited on page 169.)

[181] R.S. Klein, G. E. Kugel, A. Maillard, K. Polgár, and A. Peter. Absolute non-linear optical coefficients of linbo3 for near stoichiometric crystal compositions. Optical Materials, 22(2):171–174, 2003. (Cited on page 179.)

[182] United crystals, ktp non-linear coefficients. https://www.unitedcrystals.com/KTPProp.html. Accessed: 2021-12-31. (Cited on page 179.)

[183] D. Babusci, G. Dattoli, and M. Quattromini. On integrals involving hermite polynomials. Applied Mathematics Letters, 25:1157–1160, 2012. (Cited on page 184.)